

UNIVERSITY OF BIRMINGHAM

AN INTEGRATED CRYOGENIC ENERGY SYSTEM WITH COLD ENERGY STORAGE

By

Yunren Li

A thesis submitted to the University of Birmingham for the

Degree of Doctor of Philosophy

School of Chemical Engineering

College of Engineering and Physical Science

The University of Birmingham

September 2021

UNIVERSITY OF
BIRMINGHAM

University of Birmingham Research Archive

e-theses repository

This unpublished thesis/dissertation is copyright of the author and/or third parties. The intellectual property rights of the author or third parties in respect of this work are as defined by The Copyright Designs and Patents Act 1988 or as modified by any successor legislation.

Any use made of information contained in this thesis/dissertation must be in accordance with that legislation and must be properly acknowledged. Further distribution or reproduction in any format is prohibited without the permission of the copyright holder.

Abstract

Environmental concerns due to greenhouse gases emissions from burning fossil fuels call for the development of low or zero carbon technologies, particularly renewable energy sources. Deep penetrations of renewable energy bring in significant challenges in managing the mismatch between fluctuating and intermittent supply and demand. Various energy storage technologies have been proposed and developed to address this challenge. Liquid Air Energy Storage (LAES) has attracted significant attention in recent years due to its high energy density and no geographical constraints.

The round-trip efficiency of a standalone LAES system is limited to 50-60%, one of the major reasons for this is related to the high-grade cold energy storage. Several studies have attempted to address this. However, most of these studies are focused on sensible heat storage (SHS), and little attention has been paid to other storage methods, such as the latent heat storage (LHS) at the cryogenic temperature range, which is also known as the phase change materials (PCMs) based storage. This work aims to develop an integrated sensible and latent heat storage system to store and utilise high-grade cold energy (below -150℃) based on suitable cryogenic thermal energy storage (CTES) materials.

Firstly, this work focuses on the screening and characterisation of suitable CTES materials. In the study of SHS materials, temperature variations were found to have a significant effect on the specific heat values of the glass bead, the Dorset gold gravel and Brittany bronze gravel, decreasing by ~21.7%, ~13.08% and ~20.9% separately at -40℃ compared to that at the room temperature. Borosilicate glass bead is selected as the SHS material due to its better specific heat capacity and thermal conductivity than quartz-based gravels. For the LHS material study, hydrocarbons with C_5 and C_6 were chosen as the LHS material with a phase transition temperature of approximately -160℃.

The results from the DSC and T-history measurements showed that the sample volume has a significant influence on the supercooling degree. To improve the thermal conductivity of the PCMs, expanded graphite (EG) and two different thickeners were used in the formulation to form composite PCMs. Both SiO_2-based (3 wt.%) and SEBS-based (2 wt.%) composites with 0.5 wt.% EG enhance the thermal conductivity by 34.5% and 38.1% in the solid state and 64.2% and 52.3% in the liquid state compared with the pure substance, respectively. Furthermore, the addition of fire retardants was studied and found to be able to inhibit the burning intensity of the PCM with the flammability limits observed to be proportional to the amount of fire retardants added.

An experimental system was then designed based on the CTES materials to store and utilise high-grade cold energy for studying the charging (storage of the cold energy) and discharging (use of the cold energy) processes. The design scheme of the latent heat cold storage (LHCS) device was developed according to the simulation results of the one-dimensional transient tube model with cylindrical fins in terms of fin length, fin thickness, fin gap, and tube material. The simulation results indicated that although the heat transfer coefficients for boiling and condensation varied in different patterns with the proportion of vapour in the two-phase flow, both the inner tube diameter and the mass flow rate were positively related to these coefficients. In addition, the heat transfer rate was significantly influenced by fin thickness, fin gap, fin length and number of fins, but the effect of different tube materials was negligible.

Various experiments were performed using the experimental system, including the high-grade cold energy storage and utilisation processes. The system was found to be able to liquify nitrogen (the working fluid). The charging experiments were conducted at an operating pressure of 13 barg and 8.5

barg, respectively. The CTES devices were found to be completely charged within 10 hours using 110 L of LN_2. In the system discharging experiments, the real-time pressure and temperature of the system were monitored and recorded to evaluate the N_2 liquefaction performance. The results indicate that the total amount of LN_2 produced during the non-phase change period is 1.08 kg at a system pressure of 16.5 barg. During the phase transition period of the PCM, the effective time of N_2 liquefaction is approximately 24 minutes with the mass of the condensed N_2 of 0.72 kg at a system pressure maintained at 17 barg.

Acknowledgements

I would like to express my sincerest gratitude to my esteemed supervisor Professor Yulong Ding for his invaluable supervision, tremendous support and continuous guidance throughout every stage of my Ph.D. study. His unlimited enthusiasm and immense knowledge for energy storage fields constantly inspired me to overcome difficulties not only in my research but also in my career. It has been a great honour and a wonderful experience for me to be a member of the Birmingham Centre for Energy Storage (BCES).

I would also like to express my great appreciation to my co-supervisor Dr. Yongliang Li for his concern and encouragement on my research. I also greatly appreciate to Dr. Boyang Zou and Dr. Abdalqader Ahmad for their selfless help and valuable advice on my experiments and review of thesis. Their suggestions and support are crucial for the completion of my research. I am also deeply grateful to my colleagues and technicians in BCES, Dr. Lin Cong, Dr. Zhu Jiang, Dr. Hui Cao, Mr. Zhen Du, Mr. Xusheng Zhang, Mr. Omar Saeed, Mr. Chyntol Kanhimbe, Ms. Jie Chen. It has been an amazing journey for me to have the opportunity to work with all of you.

I would also like to extend my gratitude to China Scholarship Council (CSC) and UK Department of Business, Energy and Industrial Strategy (BEIS) and Carbon Trust's Industrial Energy Efficiency Accelerator (IEEA) for their financial support on my Ph.D. study.

Last but not least, a special and sincere gratitude from my deep inside to my parents, family and my friends who always support me unconditionally and give me endless love and encouragement.

In a memory of my beloved friend Juno, may there no pain in heaven.

Table of Contents

Abstract ..... **I**

Acknowledgements ..... **IV**

List of Figures ..... **VIII**

List of Tables ..... **XIV**

Abbreviations ..... **XVI**

Nomenclature ..... **XVIII**

CHAPTER 1 INTRODUCTION **1**

1.1 Background **2**

1.2 Aims and objectives **6**

1.3 Novelties **7**

1.4 Thesis layout **7**

CHAPTER 2 LITERATURE REVIEW **10**

2.1 Thermal energy storage (TES) technologies **11**

2.1.1 Classification of TES technologies 11

2.1.2 Criteria for TES material selection 15

2.1.3 Summary 16

2.2 Cryogenic thermal energy storage (CTES) materials **16**

2.2.1 SHS materials 16

2.2.2 LHS materials 20

2.3 PCMs characterisation techniques & methods **30**

2.3.1 Thermal storage capacity determination 30

2.3.2 Thermal conductivity measurements 37

2.3.3 Flammability limits test 41

2.3.4 Summary 45

2.4 CTES devices and applications **46**

2.4.1 Packed bed CTES device 46

2.4.2 Shell-and-tube CTES device 54

2.4.3 Applications of CTES technologies 57

2.5 Summary **62**

CHAPTER 3 MATERIALS AND METHODOLOGIES **64**

3.1 Materials **65**

3.1.1 SHS materials 65

3.1.2 Chemicals 65
3.1.3 Preparation of modified PCM 66
3.2 Characterisation techniques 67
3.2.1 Differential scanning calorimetry (DSC) 67
3.2.2 Temperature-history measurement 70
3.2.3 Thermal conductivity 72
3.2.4 Infrared microscopy (IR) 74
3.2.5 Volume expansion coefficient 75
3.2.6 Thermal cycling performance 75
3.2.7 Flammability limits (FLs) 76
3.3 Mathematical modelling of LHCS tank 78
3.3.1 Geometric model 78
3.3.2 Boiling heat transfer coefficient 81
3.3.3 Condensation heat transfer coefficient 82
3.3.4 Boundary conditions 86
CHAPTER 4 RESULTS AND DISCUSSION: CTES MATERIAL SCREENING AND CHARACTERISATION 88
4.1 Sensible heat storage (SHS) materials 89
4.1.1 Specific heat capacity 89
4.1.2 Thermal conductivity 91
4.2 Latent heat storage (LHS) materials 92
4.2.1 Cryogenic PCM screening 92
4.2.2 Phase transition temperature and enthalpy 93
4.2.3 Thermal conductivity 103
4.2.4 Thermal cycling stability 118
4.2.5 Volume expansion 120
4.2.6 Flammability Limits (FLs) 121
4.3 Alternative cryogenic latent heat storage (LHS) material 132
4.3.1 Phase transition temperature and enthalpy 132
4.3.2 Thermal conductivity 133
4.3.3 Flammability Limits (FLs) 135
4.3.4 Volume expansion 137
4.4 Summary 138
CHAPTER 5 LAB TEST RIG: DESCRIPTIONS, COMPONENTS AND DESIGN 141
5.1 System configuration 142
5.1.1 System charging process 142
5.1.2 System discharging process 143
5.2 CTES components 145
5.2.1 Numerical simulation of the latent heat cold storage (LHCS) tank 145

5.2.2 Design of the LHCS tank 155
5.2.3 Design of the sensible heat cold storage (SHCS) tank 159
5.3 Auxiliary components 161
5.3.1 Data acquisition system 162
5.3.2 Pressure system 167
5.3.3 Gas heating system 169
5.4 Summary 170
CHAPTER 6 RESULTS AND DISCUSSION: TEST RIG EXPERIMENTAL RESULTS 171
6.1 System charging process 172
6.1.1 Charging process at a working pressure of 13 barg 172
6.1.2 Charging process at a working pressure of 8.5 barg 177
6.2 System discharging process 181
6.2.1 Static discharging process 181
6.2.2 Dynamic discharging process 184
6.3 Evaluation of the system condensation capacity 188
6.3.1 System condensation rate of N_2 in the subcooled period of the PCM 189
6.3.2 System condensation rate of N_2 in the phase transition period of the PCM 191
6.4 Summary 194
CHAPTER 7 CONCLUSIONS AND RECOMMENDATIONS 196
7.1 Conclusions 197
7.2 Recommendations and future work 200
Appendix 202
Bibliography 218

List of Figures

Figure 1.1: Share of electricity production from renewables between different countries from 2010 to 2020 [3]. 3
Figure 1.2: The outline of the thesis. 9
Figure 2.1: Schematic diagram of the energy storage process in the LHS system [18]. 12
Figure 2.2: Schematic diagram of the energy storage process in the TCES system [19]. 13
Figure 2.3: Classification of LHS materials for CTES applications [16, 22]. 21
Figure 2.4: Solid-liquid materials being investigated and used as PCMs for sub-zero temperature applications [37-57]. 29
Figure 2.5: Schematic diagram of the T-history experimental rig [65]. 33
Figure 2.6: T-history curves: the PCM with supercooling (a), without supercooling (b), and the water (c) during the cooling process [65]. 34
Figure 2.7: The modified mathematical model of the T-history method: (a) T-history curve with the inflection point b as the boundary; (b) the first derivative of the T-history curve [69]. 36
Figure 2.8: The principle and temperature rise curve of laser flash method [67, 68]. 40
Figure 2.9: Schematic diagram of typical packed bed based CTES device [102]. 47
Figure 2.10: Schematic diagram of modular packed bed high-grade cold storage [15]. 50
Figure 2.11: Schematic diagram of packed bed using cascaded PCMs as TES materials [109]. 51
Figure 2.12: Schematic diagram of some physical phenomena involved in the packed bed storage system [110]. 52
Figure 2.13: Schematic diagram of different degrees of stratification within a packed bed device with the same amount of stored thermal energy: (a) highly stratified; (b) moderately stratified; (c) unstratified storage [115]. 54
Figure 2.14: Schematic diagram of a shell and tube type CTES component. 55
Figure 2.15: Schematic diagram of a shell and tube device with radial fins [122]. 57
Figure 2.16: The use of CTES for cooling and thermal management of the space telescope assembly [127]. 59
Figure 2.17: Schematic diagram of LAES technology [128]. 60
Figure 2.18: Cold energy storage system for LNG cold energy utilisation [129]. 62

Figure 3.1: The preparation procedure of modified PCM.....67
Figure 3.2: (a): Mettler Toledo DSC3+ instrument; (b): Furnace inside of the DSC instrument that contains both sample and reference; (c): 100 μL aluminium crucible; (d) 120 μL stainless steel medium-pressure crucibles; (e) A typical DSC curve of phase transition process.....68
Figure 3.3:(a) Schematic diagram of the test rig configuration for T-history measurement; (b): The setup of the T-history experiment (LN_2 will be held in the middle layer. Thermocouples T_1-T_4 were placed at the same level but at different positions to the centre of the sample cylinder). 71
Figure 3.4: Schematic diagram of NETZSCH LFA 427 instrument with Pt/Rh sample holder.....72
Figure 3.5: (a) Linseis THB-500 instrument; (b) low temperature THB sensor; (c) schematic diagram of the thermal conductivity measurement procedure (The sample was placed into the inner cylinder of the sample holder, and the measurement circuit of the sensor was entirely submerged by the sample. The outer cylinder is filled with LN_2 to cool down the sample).....73
Figure 3.6: OZM FRTA-I instrument: 1. 5 L test vessel; 2. Magnetic stirrer; 3. Magnetic stirrer speed control button; 4. Temperature control panel; 5. High voltage key-switch; 6. Operation control panel; 7. Testing assemblies.....77
Figure 3.7： Schematic diagram of the geometric model of the tube with cylindrical shape fins. 79
Figure 3.8: Two-phase flow regimes in a vertical tube [148]. 83
Figure 4.1:Physical surface morphology (shape and size) of SHS materials: (a) glass bead; (b) Dorset gold gravel; (c) Brittany bronze gravel.....89
Figure 4.2:The average specific heat values of glass bead, Dorset gold gravel, and Brittany bronze gravel at different temperatures were determined by DSC (with a cooling/heating rate of 5 ℃/min, in the temperature range of -40℃ to 20℃).....90
Figure 4.3:The average thermal conductivities of glass bead at different temperatures were measured by LFA (with a cooling/heating rate of 5 ℃/min, in the temperature range of -40℃ to 20℃). 91
Figure 4.4: DSC measurement curve of 1-Hexene with a cooling/heating rate of 1 ℃/min, in the temperature range of -110℃ to -165℃. 95
Figure 4.5: DSC measurement curve of 1-Hexene with a cooling/heating rate of 0.5 ℃/min, in the temperature range of -130℃ to -170℃. 96
Figure 4.6: DSC measurement curves of 2-Methylbutane and its mixture with 5% (v/v) acetone with a cooling/heating rate of 0.5℃/min, in the temperature range of -130℃ to -170℃.....98

Figure 4.7: T-history measurement profile of 1-Hexene PCM, the upper diagram illustrates the freezing process, and the lower one shows the melting process of 1-Hexene. 100
Figure 4.8: T-history measurement profile of 2-Methylbutane PCM, the upper diagram illustrates the freezing process, and the lower one shows the melting process of 2-Methylbutane. 100
Figure 4.9: The comparison of the T-history melting curves of 1-Hexene and 2-Methylbutane under the identical experimental conditions. 103
Figure 4.10: (a) Thermal conductivity measurement results for the solid state of 1-Hexene from -190℃ to -145℃; (b) Thermal conductivity measurement results for the liquid state of 1-Hexene from -135℃ to -25℃.....104
Figure 4.11: (a) Thermal conductivity measurement results for the solid state of 2-Methylbutane from -190℃ to -175℃; (b) Thermal conductivity measurement results for the liquid state of 2-Methylbutane from -155℃ to -35℃.....106
Figure 4.12: Thermal conductivity estimations of 1-Hexene and 2-Methylbutane based on modified Missenard and Pachaiyappan methods [171].....108
Figure 4.13: (a) 1-Hexene with 0.5 wt.% EG mixture; (b) the stability of composite 1-Hexene solutions containing 1 wt.%, 2 wt.%, 3 wt.%, 4 wt.%, 6 wt.% SiO_2 and 0.5 wt.% EG respectively after being stored in a freezer at -45℃ for 48 hours; (c) the stability of composite 1-Hexene solutions containing 1 wt.%, 2 wt.%, 3 wt.%, 4 wt.%, 6 wt.% SEBS and 0.5 wt.% EG respectively after being stored in a freezer at -45℃ for 48 hours. 110
Figure 4.14: Thermal conductivity measurement results of modified 1-Hexene with 3 wt.% SiO_2 and 0.5 wt.% graphite: (a) solid state from -190℃ to -140℃; (b) liquid state from -140℃ to -60℃. ...111
Figure 4.15: Thermal conductivity measurement results of modified 1-Hexene with 2 wt.% SEBS and 0.5 wt.% graphite: (a) solid state from -190℃ to -140℃; (b) liquid state from -140℃ to -60℃. ...112
Figure 4.16: DSC measurement curve of Composite 1 (1-Hexene containing 3 wt.% SiO_2 and 0.5 wt.% EG) with a cooling/heating rate of 0.5℃/min, in the temperature range of -130℃ to -170℃. 115
Figure 4.17: DSC measurement curve of Composite 2 (1-Hexene containing 2 wt.% SEBS and 0.5 wt.% EG) with a cooling/heating rate of 0.5℃/min, in the temperature range of -130℃ to -170℃. 116
Figure 4.18: Infrared spectra of different additives in SEBS-based composite 1-Hexene.....117
Figure 4.19: DSC measurement curves of 1-Hexene after 25, 50, 75, and 100 thermal cycles with a cooling/heating rate of 0.5 ℃/min, in the temperature range of -130℃ to -170℃.....118

Figure 4.20: Thermal expansion determination of 1-Hexene and 2-Methylbutane: (a) PCM in liquid phase under room temperature (25℃); (b) PCM in the solid phase.....121
Figure 4.21: Time series photographs of flame propagation after ignition of a mixture: (a) containing 0.35 mL of 1-Hexene and air at 25℃; (b) containing 0.32 mL of 1-Hexene and air at 25℃.....123
Figure 4.22: Time series photographs of flame propagation after ignition of a mixture: (a) containing 1.5 mL of 1-Hexene and air at 25℃; (b) containing 2.2 mL of 1-Hexene and air at 25℃.....124
Figure 4.23: Pressure change curves in the test vessel after ignition of mixtures consisting of different volumes of 1-Hexene and air. 126
Figure 4.24: Pressure change curves in the test vessel after ignition of mixtures consisting of different volumes of 2-Methylbutane and air. 127
Figure 4.25: Pressure change curves in the test vessel after ignition of mixtures containing 1-Hexene modified with different fire retardants and air. 129
Figure 4.26: Time series photographs of flame propagation after ignition of a mixture containing 0.35 mL of 1-Hexene modified by 5% (v/v) SiO_2 and air at 25℃. 130
Figure 4.27: Pressure change curves in the test vessel after ignition of mixtures containing 2-Methylbutane modified with different fire retardants and air. 131
Figure 4.28: T-history measurement profile of 3-Methylpentane PCM, the upper diagram illustrates the cooling process, and the lower one shows the melting process of 3-Methylpentane.....132
Figure 4.29: (a) Thermal conductivity measurement results of 3-Methylpentane solid phase from -190℃ to -165℃; (b) Thermal conductivity measurement results of 3-Methylpentane liquid phase from -160℃ to -60℃.....134
Figure 4.30: Pressure change curves in the test vessel after ignition of mixtures consisting of different volumes of 3-Methylpentane and air.....136
Figure 4.31: Pressure change curves in the test vessel after ignition of mixtures containing different modified 3-Methylpentane and air. 136
Figure 4.32: Thermal expansion determination of 1-Hexene and 3-Methylpentane: (a) PCM in liquid phase under room temperature (25℃); (b) PCM in the solid phase.....137
Figure 5.1: The flow chart of the experimental system to store and utilise high-grade cold energy through the application of CTES materials.....144
Figure 5.2: (a) The effect of inner tube diameter on the boiling heat transfer coefficient when the mass

flow rate of LN_2 is maintained at 1 g/s; (b) The effect of mass flow rate of LN_2 on the boiling heat transfer coefficient when the inner tube diameter is maintained at 4 mm. 147
Figure 5.3: (a) The effect of inner tube diameter on the condensation heat transfer coefficient when the mass flow rate of LN_2 is maintained at 1 g/s; (b) The effect of mass flow rate of LN_2 on the condensation heat transfer coefficient when the inner tube diameter is maintained at 4 mm. 148
Figure 5.4: The flow pattern determination based on the ratio of We $*$ to 7Xtt0.2 in the condensation process ($We*/7Xtt0.2 < 1$, Slug and bubble flows region; $We*/7Xtt0.2 > 1$, Annular flow region). 149
Figure 5.5: (a) The effect of fin thickness on the boiling heat transfer rate when the fin gap is fixed at 10 mm; (b) The effect of fin gap on the boiling heat transfer rate when the fin thickness is fixed at 1.5 mm. 151
Figure 5.6: (a) The effect of fin thickness on the condensation heat transfer rate when the fin gap is kept at 10 mm; (b) The effect of fin gap on the condensation heat transfer rate when then fin thickness is kept at 1.5 mm. 152
Figure 5.7: (a) The boiling heat transfer rate when the tube material is pure copper; (b) The condensation heat transfer rate when the tube material is pure copper. 154
Figure 5.8: The detailed design layout of the LHCS tank (a: front view, b: three-dimensional vertical section, c: geometric dimensions of the fin stack, unit: mm). 158
Figure 5.9: The detailed design layout of the SHCS tank (a: front view, b: top view, c: three-dimensional view, unit: mm). 160
Figure 5.10: The physical view of the experimental system. 161
Figure 5.11: The distribution of thermocouples in the LHCS tank (a: cross section; b: three-dimensional view, unit: mm). 163
Figure 5.12: The distribution of thermocouples in the SHCS tank (unit: mm). 164
Figure 5.13: Calibration curves of thermocouples at different positions of the system. 165
Figure 5.14: (a) Top view; (b) Front view including 1: Pressure gauge; 2: Bursting disc inner vessel; 3: Relief valve; 4: Vent valve; 5: Level indicator; 6: Pressure building valve; 7: Pressure building regulator; 8: Economizer regulator; 9: Gas use valve; 10: Liquid valve; 11: Bursting disc outer vessel. 168
Figure 5.15: Schematic diagram and dimensions of the water-based heat exchanger (a: front view, b:

cross section view, unit: mm).....169
Figure 6.1: Temperature variation curves of the LHCS tank during the charging process at a system pressure of 13 barg (The distribution of thermocouples is illustrated in the legend).....175
Figure 6.2: Temperature profiles of the SHCS tank during the charging process at a system pressure of 13 barg (The distribution of thermocouples is illustrated in the legend). 175
Figure 6.3: Pressure fluctuations during the system charging process at 13 barg 176
Figure 6.4: Pipeline temperature fluctuations during the charging process at a system pressure of 13 barg. 176
Figure 6.5: Temperature variation curves of the LHCS tank during the charging process at a system pressure of 8.5 barg (The distribution of thermocouples is illustrated in the legend).....179
Figure 6.6: Temperature profiles of the SHCS tank during the charging process at a system pressure of 8.5 barg (The distribution of thermocouples is illustrated in the legend). 180
Figure 6.7: Pressure fluctuations during the system charging process at 8.5 barg.....180
Figure 6.8: Pipeline temperature fluctuations during the charging process at a system pressure of 8.5 barg. 181
Figure 6.9: (a) System pressure variation curves during the static liquefaction process of N_2 at a working pressure of 19.5 barg; (b) Temperature profile of the AS during the static liquefaction process of N_2 at a working pressure of 19.5 barg.....183
Figure 6.10: (a) System pressure variation curves during the dynamic liquefaction process of N_2 at a working pressure of 19 barg; (b) Temperature profiles of the AS and the PCM during the dynamic liquefaction process of N_2 at a working pressure of 19 barg.....188
Figure 6.11: System parameters of LHCS temperature, pressure, and flow rate for N_2 condensation process using the sensible cold energy of PCM at an operating pressure of 16.5 barg.....190
Figure 6.12: The temperature profile of the SHCS tank during the N_2 condensation process at an operating pressure of 16.5 barg using the subcooled period of the PCM. 191
Figure 6.13: System parameters of LHCS temperature, pressure, and flow rate for N_2 condensation process using the latent cold energy of PCM at an operating pressure of 17 barg.....193
Figure 6.14: The temperature profile of the SHCS tank during the N_2 condensation process at an operating pressure of 17 barg using the phase transition period of the PCM.....194

List of Tables

Table 2.1: Some performance data and features of TES systems [19-21]. 14

Table 2.2: Criteria for selecting TES materials [22-24].....15

Table 2.3: Review on solid SHS materials for cryogenic energy storage applications [9, 13-15, 25, 28, 29]. 18

Table 2.4: Comparison of organic and inorganic PCMs for thermal energy storage [36].....21

Table 2.5: Thermophysical properties of salt-water solutions (PCT up to -20^{O}C) [37, 38]. 23

Table 2.6: Thermophysical properties of alkanones for CTES application (PCT up to -30℃) [50]. 25

Table 2.7: Thermophysical properties of commercial PCMs for CTES application (PCT up to -30℃) [54-57]*. 27

Table 3.1: Basic information of SHS materials.....65

Table 3.2: Basic information of chemicals used in this study. 66

Table 3.3: The thermophysical properties of LN_2 at different operating pressures [50]. 87

Table 4.1: Desirable PCM candidates and their thermophysical properties for the cryogenic application [50]. 92

Table 4.2: The phase transition temperature and heat of fusion of 1-Hexene under different measurement conditions.....94

Table 4.3: Thermal conductivity measurement results of 1-Hexene and 2-Methylbutane in both solid and liquid phases.....107

Table 4.4: Thermal conductivity measurement results of modified 1-Hexene in liquid phases. 113

Table 4.5: The phase transition temperature and heat of fusion of modified 1-Hexene. 114

Table 4.6: The phase transition temperatures and heat of fusion values of 1-Hexene under 25, 50, 75, and 100 thermal cycles.....120

Table 4.7: Pressure changes in the test vessel after ignition of the mixtures of 1-Hexene and air.....125

Table 4.8: Pressure changes in the test vessel after ignition of the mixtures of 2-Methylbutane and air.127

Table 4.9: Pressure changes in the test vessel after ignition of the mixtures of PCMs modified with different fire retardants and air. 130

Table 4.10: Thermal conductivity measurement results of 3-Methylpentane in both solid and liquid phases. 134

Table 4.11: Pressure change in the test vessel after ignition of the mixtures of 3-Methylpentane and air. 135

Table 5.1: Basic configuration and parameters on the thermocouples used for system temperature measurement. 163

Table 6.1: Basic information on LN_2 during system charging process. 172

Abbreviations

BOG	Boil-off gas
CAPX	Capital expenditures
CTES	Cryogenic thermal energy storage
COP	Coefficient of performance
DSC	Differential Scanning Calorimetry
EG	Expanded graphite
HDPE	High-density polyethylene
HTF	Heat transfer fluid
IR	Infrared microscopy
LAES	Liquid air energy storage
LFA	Laser flash apparatus
LFL	Low flammability limit
LHCS	Latent heat cold storage
LHS	Latent heat storage
LN_2	Liquid nitrogen
LNG	Liquefied natural gas

MFC	Mass flow controller
N_2	Nitrogen
OPEX	Operating expenses
PBCS	Packed bed cold storage
PCM	Phase change material
PCT	Phase change temperature
PP	Polypropylene
SEBS	Styrene-ethylene-butylene-styrene
SHCS	Sensible heat cold storage
SHS	Sensible heat storage
TA	Thermal analysis
THB	Thermal hot bridge
TCEP	Tris (2-chloroethyl) phosphate
TCES	Thermochemical energy storage
TES	Thermal energy storage
UFL	Upper flammability limit

Nomenclature

A	Surface area (m^2)
C_P	Specific heat capacity (kJ/kg·K)
D_h	Hydraulic diameter (m)
d	Inner diameter of tube (m)
F_{cb}	Convection boiling factor
Fr_L	Froude number
G	Mass flux ($kg/m^2 \cdot s$)
K_{FR}	Correction factor for low Froude numbers
L	Tube length (m)
m	Mass (kg)
P	Pressure (kPa)
Pr	Prandtl number
$Q_{sensible}$	Sensible energy storage capacity (kJ)
Q_{latent}	Latent energy storage capacity (kJ)
q_f	Heat transfer rate through cylindrical fins (W)
q_i	Heat transfer rate from inner fluid to inner tube surface (W)

q_w	Heat transfer rate from inner surface to outer surface (W)
Su_{go}	Suratman number
T	Temperature (℃)
Re	Reynolds number
t	Time (s)
V	Volume (L)
We^*	Modified Weber number
X_{tt}	Lockhart–Martinelli parameter
x	Vapor quality
Δh	Heat of fusion (kJ/kg)
ρ	Density (kg/m^3)
μ	Dynamic viscosity (Pa·s)
λ	Thermal conductivity (W/m·K)
σ	Surface tension (N/m)
η_f	Fin efficiency
$\emptyset_g$	Two-phase pressure drop multiplier

CHAPTER 1

INTRODUCTION

1.1 Background

Fossil fuels (coal, petroleum, and natural gas), as the primary energy sources to meet the world's energy demand, have caused grave environmental issues due to their combustion processes, emitting a huge amount of greenhouse gases, destructing the ozone layer, and leading to excessive acid rains and other pollutions [1]. These have driven the development of energy technologies and energy policies towards decarbonization. The most robust evidence of the development is the increased energy generation from renewable energy sources (solar, wind, hydropower, tide, biomass, geotherm). By the end of 2020, the installed renewable energy capacity reached 2838 GW, which was sufficient to provide an estimated 29% of global electricity generation as reported by the Renewables 2021 Global Status Report [2]. Hydropower and wind power account for 58% and 22%, respectively [2]. The global hydropower generation has a slight growth of 1.5% from 2019, which was an estimated 4370 TWh, or approximately 16.8% of the world's total electricity generation in 2020 [2].

Figure 1.1 shows the share of electricity production from renewable energy sources over the last decade (from 2010 to 2020) [3]. One can see that the renewable share of electricity generation in China increased significantly from 17.81% to 29.02%, considering that the total electricity production was more than doubled over the decade. In the United States, the renewable share increased from 10.23% to 20.44% between 2010 and 2020. The change in the UK was from 6.91% to 42.30%—a big jump. To achieve net zero greenhouse gas emissions of more than three-quarters by 2050 and lead the way in tackling climate change globally, UK Government announced a new ambitious target to reduce the UK's emissions by at least 78% by 2035, compared to 1990 levels [4].

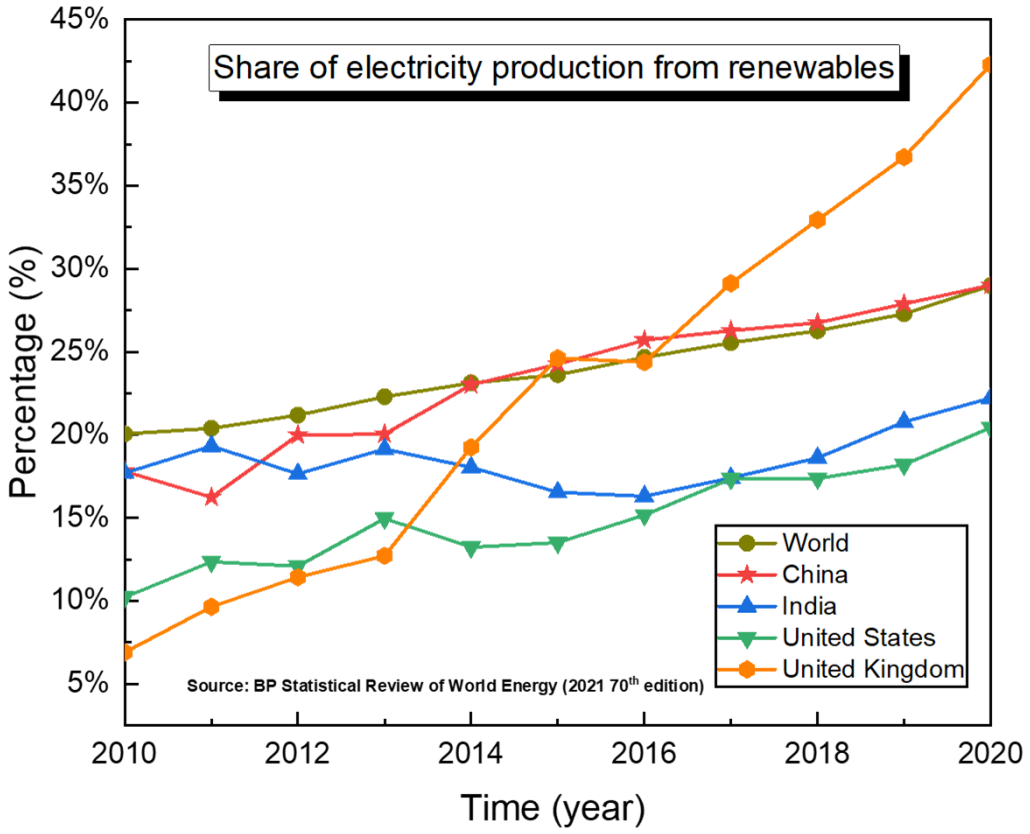


Figure 1.1: Share of electricity production from renewables between different countries from 2010 to 2020 [3].

The significantly increased penetration of renewable energy faces challenges. The main challenge lies in the unpredictable nature of the renewable energy sources, tilting the balance between electricity generation and electricity demand. Another challenge is the effect of the fluctuating renewable energy generation on the frequency of electricity grids, especially when the penetration exceeds 10-20% of the total load [5, 6]. In addition, regional restrictions have a significant impact on obstructing the growth of renewable energy. For instance, tidal energy locations are often far away from industry sites or densely populated areas, and the long-distance power transmission may increase the cost of tidal energy utilisation.

To overcome the intermittent electricity production from renewable sources and reduce the mismatch between renewable energy supply and demand in both time and space, various energy storage

technologies have been developed [7]. These technologies can be classified into the following categories according to their working principles:

- Mechanical energy storage: e.g., flywheel energy storage (FES), compressed air energy storage (CAES), and pumped hydro energy storage (PHES).
- Electrical energy storage: e.g., battery energy storage (BES), flow battery energy storage (FBES), superconducting magnetic energy storage (SMES), and supercapacitor energy storage (SCES).
- Chemical energy storage: e.g., hydrogen, methanol and ammonia.
- Thermal energy storage: e.g., sensible heat storage (SHS), latent heat storage (LHS), and thermochemical energy storage (TCES).

In recent years, Liquid Air Energy Storage (LAES), which is fundamentally a thermal energy storage method, has attracted increased attention due to several advantages, including high energy density, geographical flexibility, environmental friendliness, long lifespan, and a relatively low CAPEX and OPEX [8]. The LAES can be the intermittent renewable sources and/or off-peak electricity to produce liquid air via air liquefaction (charging); while the power recovery process (discharging) occurs in peak times when the liquid air is pumped to high pressure first, then heated by ambient heat and superheated by compression heat before finally expanding in air turbines to produce electricity. The University of Newcastle first was the first to propose the concept of the LAES in 1977 with a theoretical energy recovery efficiency of 72% [9], and the world's first pilot plant (350 kW/2.5 MWh) was established and tested by Highview Enterprises Ltd (now Highview Power) in collaboration with

the University of Leeds from 2009 to 2012. In 2013, the plant was relocated to the University of Birmingham for further study and academic research [10]. Between 2013 and 2018, a pre-commercial scale LAES (5 MW/15 MWh) was designed, built, and tested by Highview Power in Manchester, UK, with Viridor [11]. In 2019, Highview Power started its journey to design and build 50 MW/250 MWh plants in the UK. This was enhanced by an investment of £46m from Sumitomo Heavy Industries, Ltd. (SHI, Japan) into Highview in Feb 2020.

A large-scale standalone LAES system has a relatively low round-trip efficiency, which can be even lower for small-scale systems mainly due to the high energy consumption of the liquefaction process if waste thermal energy (heat and cold) is not recovered [12]. Morgan et al. [13] investigated the integration of high-grade cold storage with quartzite rocks into a LAES pilot plant and showed that the round-trip efficiency of the configuration could be increased by 4.8% compared with the single module configuration. Huttermann and Span evaluated different materials, including metal, ceramic, mineral, and plastic, for use as the TES material in a packed bed [14]. They introduced the average volumetric heat capacity and the temperature-related heat capacity ratio to characterise these storage materials. Their results showed that polypropylene, high-density polyethylene, sodium chloride and quartz achieved the best compromise in terms of storage efficiency, feasibility and costs. Sciacovelli et al. [15] developed a numerical model for the cold thermal storage based on the experimental results of the LAES pilot plant. Their study indicated that the packed bed cold energy storage with quartzite rocks could reduce the energy required in the air liquefaction process by around 25%. So far, most of the studies on the recovery of high-grade cold energy have been focused on the use of sensible heat storage materials, which are characterized by low energy storage density and hence large volume. Little attention has been paid to the high-grade cold energy storage at cryogenic temperature range

(below or around -150℃) with latent heat based phase change materials (PCMs). Although there have been lots of work on cold energy storage using PCMs, the literature work has been mainly concentrated on temperatures not far from 0℃. Studies on cryogenic PCMs far below -100℃ are almost non-existent. These form the dominant motivation for this Ph.D. study.

1.2 Aims and objectives

The aim of this Ph.D. research is to develop an innovative solution for the storage and utilisation of high-grade cold energy (below -150℃) by using suitable CTES materials. The specific objectives are detailed in the following:

i) To understand and screen suitable CTES materials for cryogenic energy storage applications;

ii) To study the thermophysical properties of these CTES materials, including phase change temperature (PCT), latent heat of fusion, thermal conductivity, specific heat capacity, supercooling, flammability, and thermal cycling stability;

iii) To enhance the thermal performance of the most promising cryogenic PCMs;

iv) To design and fabricate a lab-scale test rig based on the CTES materials for high-grade cold energy storage and utilisation;

v) To investigate the system cooling efficiency by using liquid nitrogen (LN_2) as a working fluid, to understand the charging and discharging processes and to study the condensation of nitrogen (N_2) during the discharging process.

1.3 Novelties

The novelties of this work are listed in the following:

i) This work screened and characterised suitable CTES materials for high-grade cold energy (below -150℃) storage and utilisation;

ii) This work extended the research temperature of low temperature PCMs from -100℃ to -160℃;

iii) This work proposed to use a combination of DSC and T-history methods to determine the phase change enthalpies of PCMs with significant supercooling issues;

iv) This work proposed a one-dimensional transient tube model with cylindrical fins to numerically study the effect of fin geometry, material and arrangement on the heat transfer of the working fluid;

v) This work designed and fabricated an integrated laboratory-scale cryogenic energy storage system based on the studied CTES materials to demonstrate high-grade cold energy storage (system charging process) and utilisation (system discharging). This brings a new approach to the N_2 liquefaction via cascading heat exchange with CTES materials.

1.4 Thesis layout

This thesis consists of seven chapters, and they are briefly outlined in the following:

- Chapter 2 summarizes the relevant literature work on CTES materials for cryogenic energy storage applications and methods for evaluating the thermophysical properties of PCMs at very

low temperatures. Potential technical challenges and possible solutions are discussed on the cryogenic PCM candidates. In addition, both numerical and experimental case studies of CTES devices are reviewed to understand the state of the art in the cold energy storage field, including packed bed and shell-and-tube based CTES devices. The applications of CTES technology are also reviewed.

- Chapter 3 details the measurement techniques and instruments for the determination of the thermophysical properties of CTES materials, and the modelling of the CTES device using a mathematical model.

- Chapter 4 investigates the thermophysical properties of potential CTES candidates, and studies the methods to enhance the thermophysical properties of cryogenic PCMs, especially in terms of thermal conductivity and flammability.

- Chapter 5 describes the design and construction of a lab-scale cryogenic energy storage test rig based on the thermophysical properties of the selected CTES materials.

- Chapter 6 presents and analyses the experimental results of the charging and discharging processes using the test rig.

- Chapter 7 summarizes the main findings of this work and provides recommendations for the future work.

To sum up, the outline of the thesis is presented in Figure 1.2.

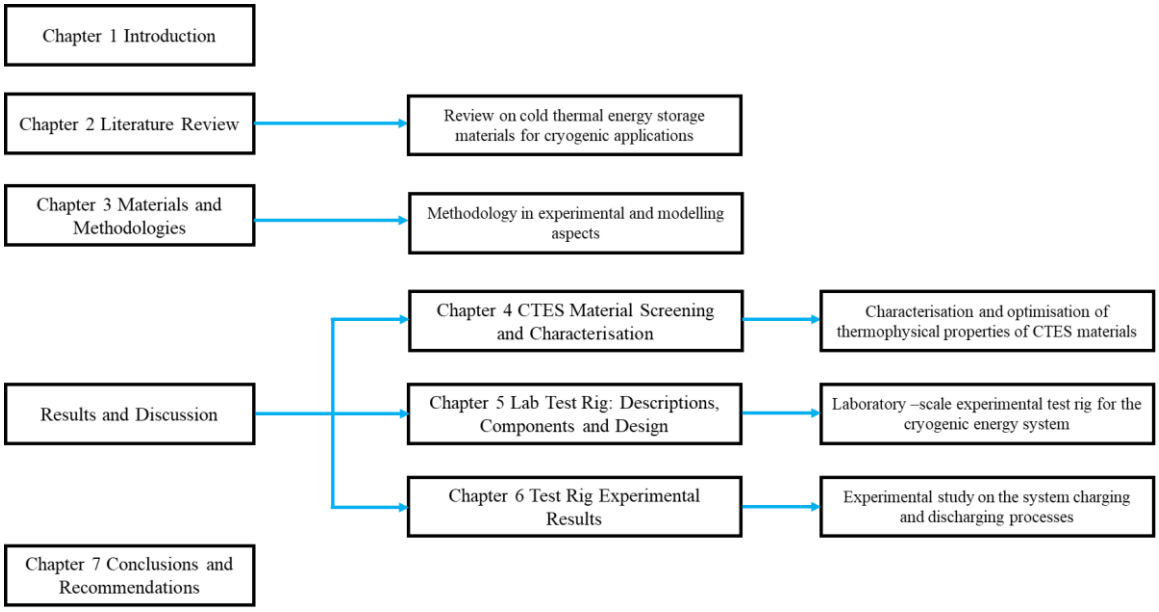


Figure 1.2: The outline of the thesis.

CHAPTER 2

LITERATURE REVIEW

2.1 Thermal energy storage (TES) technologies

TES plays an essential role in reserving excessive energy and coordinating the mismatch between energy demand and supply, as well as improving the performance and reliability of different energy conversion systems, such as renewable energy utilisation, cogeneration, industrial waste heat recovery, etc [16-24]. The classification of TES technologies and the criteria for TES material selection are reviewed in this section.

2.1.1 Classification of TES technologies

It is well known that TES technologies can be categorised as sensible heat storage (SHS), latent heat storage (LHS), and thermochemical energy storage (TCES) according to their material types [16].

The amount of energy stored in a SHS unit is expressed by Equation 2.1 [17], which shows that the specific heat capacity, the temperature change, and the mass of the material determine the upper limit of the energy storage capacity in the SHS system.

$$Q_{sensible} = \int_{T_i}^{T_f} C_P \cdot m \cdot dT \tag{2.1}$$

where $Q_{sensible}$ is the sensible heat stored (kJ), C_P is the specific heat capacity (kJ/kg·K), m is the mass of material (kg), and T is the temperature varying from T_f to T_i (K).

Figure 2.1 [18] illustrates the working principle of storing and releasing thermal energy in an LHS system using PCMs. melting and solidification processes, respectively. The energy storage capacity of a LHS unit, which often includes the SHS part due to temperature variations, can be around 5-14 times higher than that of a SHS unit [16]. The total heat stored by a LHS unit can be given by [17]:

$$Q_{latent} = \int_{T_1}^{T_P} C_s \cdot m \cdot dT + m a_m H + \int_{T_P}^{T_2} C_l \cdot m \cdot dT \quad (2.2)$$

where Q_{latent} is the total amount of sensible and latent heat stored (kJ), C_s is the specific heat capacity of material in solid-state (kJ/ kg·K), C_l is the specific heat capacity of material in liquid-state (kJ/ kg·K), m is the mass of material (kg), a_m is the fraction of material which has melted, H is the latent heat of fusion during the phase change process (kJ/kg), T_P is the PCT (K).

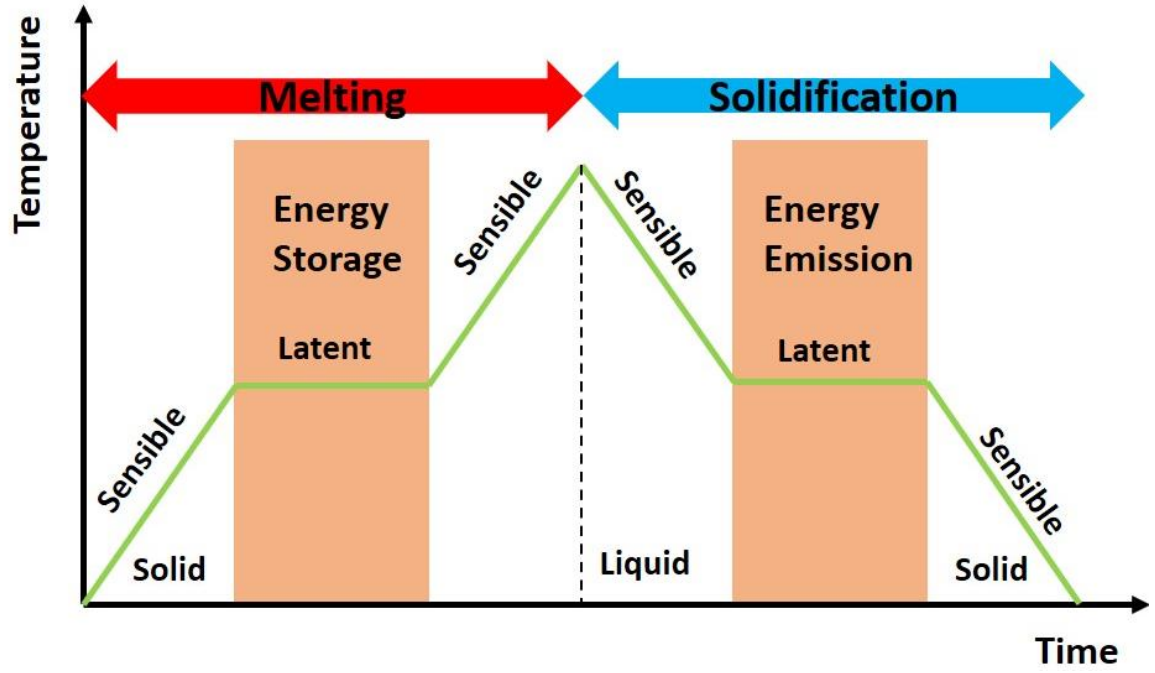


Figure 2.1: Schematic diagram of the energy storage process in the LHS system [18].

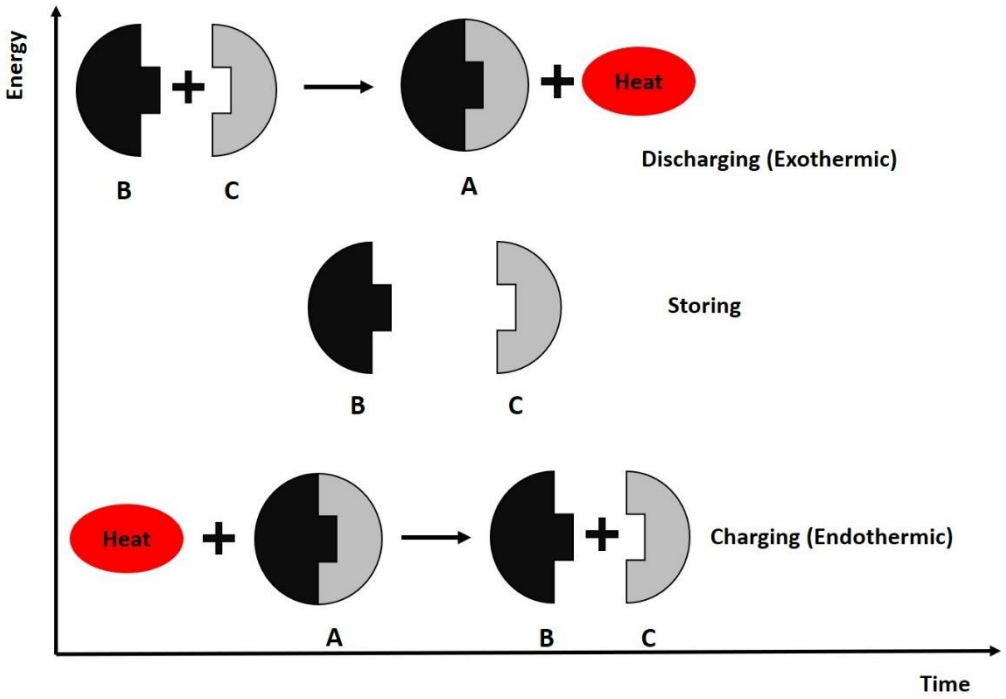


Figure 2.2: Schematic diagram of the energy storage process in the TCES system [19].

TCES is based on the utilisation of a reversible chemical reaction or a sorption process to store or release energy. The reaction or sorption heat, see Figure 2.2 [19], is absorbed to break molecular bonds during the system charging (endothermic) process and then released to reform new chemical bonds in the discharging (exothermic) process. The energy stored in a TCES unit can be calculated by:

$$Q_{thermochem} = a_r \cdot m \cdot \Delta h_r \tag{2.3}$$

where $Q_{thermochem}$ is the thermochemical heat stored (kJ), a_r is the extent of chemical reaction or sorption, m is the mass of the material (kg), and Δh_r is the enthalpy of the reaction.

Table 2.1 [19-21] gives some performance data and features of the TES technologies. The SHS technology has been in commercial applications for many years. It has a relatively low cost and a simple configuration. But it has the lowest energy storage density among these TES technologies for a given temperature range [20, 21]. The main feature of the LHS technology lies in its high energy

density compared to the SHS and charging/discharging of the latent heat at almost constant temperature. But the chemical and physical compatibility, and the stability of some PCMs are among crucial barriers for the use of the LHS technology [20, 21]. For the TCES technology, the negligible energy losses during storage process enables its energy storage efficiency higher than that of SHS and LHS technologies. The high energy storage density is another advantage of the TCES technology. However, the TCES systems are in the early technology development stage and are often complex and have a comparatively high cost [19-21]. Significant efforts are needed to bring the thermochemical technology to the marketplace [19-21].

Table 2.1: Some performance data and features of TES systems [19-21].

Performance data and features	Type pf TES		
	SHS	LHS	TCES
Energy density (kWh/t)	10-50 (low)	50-150 (moderate)	120-250 (high)
Energy storage efficiency (%)	50-90	75-90	75-100
Cost (€/kWh)	0.1-10	10-15	8-100
Storage time (h, d, m)	h/d	h/d/m	h/d/m
Lifetime	Long	Medium	Medium
Status	Available commercially	Available commercially	Rare commercially
Advantages	Low cost Simple system	Specific temperature Small volume required	High storage density Minor heat losses
Disadvantages	Heat losses Large volume	Material stability Low thermal conductivity	Complex system High cost

2.1.2 Criteria for TES material selection

To select a suitable material for a TES application, Table 2.2 lists some criteria which should be considered [22-24].

Table 2.2: Criteria for selecting TES materials [22-24].

Properties	Criteria
Thermal	➢ Appropriate phase transition temperature ➢ High phase transition enthalpy and high specific heat capacity ➢ High thermal conductivity ➢ Minimum supercooling behaviour
Physical	➢ High density ➢ Small volume change ➢ Low vapor pressure
Chemical	➢ Long-term chemical stability without degradation ➢ Non-corrosive, compatible with other materials ➢ Non-toxic, non-explosive, and non-flammable
Kinetic	➢ High nucleation and crystallisation rates to avoid supercooling issue ➢ Reproducible phase change (melting/solidification processes)
Economic	➢ Cost-effective ➢ Available and abundant ➢ Eco-friendly

2.1.3 Summary

In this section, three different TES technologies are explained. A comparison among these three technologies systems is made in terms of their performance data, advantages and disadvantages, as well as their application status. The criteria for the screening of TES materials are discussed. In the following section, the state of the art development of CTES materials will be discussed with more details.

2.2 Cryogenic thermal energy storage (CTES) materials

2.2.1 SHS materials

As briefly mentioned above, SHS systems have been widely used in various CTES applications. For CTES, many solid SHS materials have been studied for use at temperatures ranging from room temperature to around 77 K. These materials include quartzite rocks, pebbles, minerals, concrete, metals, polymers, and ceramics [9, 13-15, 25, 28, 29]. Smith [9] proposed the first design of a regenerator as the initial concept for the cryogenic temperature SHS applications. He suggested a 304 stainless steel matrix structure of solid rods in cross-inclined packing to make the regenerator. Araki et al. [25] developed a numerical simulation model to predict temperature variations of a cold storage unit with stainless steel pipes inserted in a concrete medium. However, the application of such SHS materials is usually achieved by designing a packed bed cold storage (PBCS) component due to their high thermal efficiency (around 85%) [26], flexible operating conditions, and inexpensive and straightforward system configurations [27], especially for the high-grade cold energy storage of the LAES system.

To increase the round-trip efficiency of the LAES system, a cellular pattern of PBCS was proposed by Morgan et al. [13], where individual packed beds can be arranged in parallel or series or isolated to store cold thermal energy, depending on the mass flow rate and the system load. Their simulation results showed that the round-trip efficiency of the LAES based on this multi-cell structure with quartzite gravel could be increased by 4.8% compared with a single-cell storage unit. The same authors [28] also reported that the quartzite gravel used in the cold energy recovery was thermally stable, and no dust or shattering was observed after approximately 100 thermal cycles from ambient temperature to cryogenic temperature. Huttermann and Span [14] described the PBCS device with a one-dimensional two-phase numerical model to evaluate the storage efficiency, η_{st}, using different SHS materials. The exergy efficiency of PBCS ($\eta_{ex} = 99\%$) and the time-averaged pressure drop ($\Delta p_a = 10\ kPa$) were introduced as boundary conditions in the modelling. Their results indicated that the polypropylene (PP) and high-density polyethylene (HDPE) achieved high storage efficiencies of 33.74% and 32.28%, respectively, and the quartz and sodium chloride reached medium efficiencies of 28.99% and 29.41%, respectively. Additionally, the storage efficiencies using metal materials, including aluminium oxide, aluminium 6061, zinc, and 304 stainless steels, were relatively low, ranging from 22.43% (aluminium oxide) to 21.13% (stainless steel 304). Sciacovelli et al. [15] found that the thermal properties of quartzite-based river shingle at cryogenic temperatures were significantly different from the ones at ambient temperatures. Their experimental results indicated that the measured specific heat capacity at cryogenic temperatures was around 20% lower than that at room temperature. However, the thermal conductivity at the cryogenic temperature increased by about 30% compared with that at the ambient temperature. Chai et al. [29] designed a PBCS test rig with granite pebbles medium to investigate the thermal behaviours of the packed bed at different pressures

(from 1 bar to 65 bar). The transient temperature distribution profiles of the packed bed revealed a typical thermocline behaviour at both low and high pressures. The granite pebbles showed good pressure resistance and strength within the operating temperature range of the device (77 K to ambient).

Table 2.3: Review on solid SHS materials for cryogenic energy storage applications [9, 13-15, 25, 28, 29].

Material	Operating temperature	Component	Research method	Reference
304 stainless steel	-188 to 20℃	Matrix	Numerical modelling	[9]
Concrete	-183 to 20℃	Cube	Numerical modelling	[25]
Quartzite gravel	-183 to 20℃	PBCS	Numerical modelling	[13]
Quartzite gravel	-190 to 20℃	PBCS	Experiment	[28]
PP	-150 to 30℃	PBCS	Numerical modelling	[14]
HDPE	-150 to 30℃	PBCS	Numerical modelling	[14]
Quartz	-150 to 30℃	PBCS	Numerical modelling	[14]
Sodium chloride	-150 to 30℃	PBCS	Numerical modelling	[14]
Aluminium Oxide	-150 to 30℃	PBCS	Numerical modelling	[14]
Aluminium 6061	-150 to 30℃	PBCS	Numerical modelling	[14]
Zinc	-150 to 30℃	PBCS	Numerical modelling	[14]
304 stainless steel	-150 to 30℃	PBCS	Numerical modelling	[14]
Shingle	-80 to 20℃	PBCS	Experiment	[15]
Pebble	-196 to 30℃	PBCS	Experiment	[29]

Table 2.3 summarizes the solid SHS materials for CTES, along with their working temperature, component configuration, and research method. However, the problem of large storage volume of such solid SHS materials has led to the use of liquid SHS materials.

Unlike solid materials, liquid SHS materials can be used as the heat transfer fluid (HTF) as well, which means that the system operating temperature must be between the boiling and freezing points of such materials. Laughlin [30] proposed the use of n-hexane as a storage fluid for pumped thermal energy storage. However, health and safety issues must be considered when using such hydrocarbons and their derivatives. Laughlin also pointed out that some shorter-chain alcohols, such as methanol, ethanol, propanol, propylene glycol, and their water solutions can be selected as liquid SHS materials. Li et al. [31] proposed a two-tank configuration with liquid SHS materials (propane and methanol) for cold energy recovery and storage. The use of propane and methanol for both transferring and storing thermal energy can extensively cover the required temperature range of the cold energy storage, simplify the design of the system as no additional heat exchangers are required, and control the cold energy storage process by adjusting the flow rate of liquid materials, which are extremely difficult to achieve using the packed bed with solid SHS materials. A comparison between liquid SHS materials-based multi-tank storage system and solid SHS materials-based packed bed storage system for CTES was performed by Hutterman et al. [32]. The multi-tank configuration employs propane and methanol as working fluids, and the packed bed system fills with solid storage materials. These two systems were integrated into a LAES cycle to investigate its exergy and round-trip efficiencies of the system. The results showed that the exergy losses of the packed bed system were significantly lower compared to the multi-tank system. Consequently, the round-trip efficiency of the LASE system can be increased to 60.48% based on the packed bed configuration. The main advantage of the multi-tank configuration is the steady and uncomplicated process. However, the packed bed is easily affected by unstable working conditions and gas hold-up effects during the LAES system charging and discharging processes.

In this section, solid and liquid SHS materials are reviewed based on their CTES applications. A packed bed with solid SHS materials is a commonly used configuration for cold recovery and storage. Novel liquid SHS materials can also be applied thanks to their dual role in energy storage and transfer. However, more suitable candidates for liquid SHS materials, especially materials with good thermal performance and cost-effectiveness at cryogenic temperatures, are worth exploring and developing in future research works.

2.2.2 LHS materials

2.2.2.1 PCM classification

LHS materials, also termed as phase change materials (PCMs), undergo a phase transition to store and release thermal energy. The phase transition can be in the following form: solid-solid, solid-gas, liquid-gas, and solid-liquid, and vice versa. Solid-gas and liquid-gas transitions can provide the highest latent heat of phase transition, but they are also accompanied by very large changes in volume and pressure, which are complex and less practicable [16]. The solid-solid PCMs store thermal energy by changing their crystallization structure from one lattice to another [33]. Although the solid-solid PCMs offer the advantages of small volume change and greater design flexibility, most of them have a relatively lower latent heat of phase transition compared with solid-liquid PCMs [34]. The thermal expansion coefficient of solid-liquid PCMs is generally low, with many less than 10% during the phase change process [35]. These make the solid-liquid PCMs to be attractive candidates for TES applications.

According to chemical compositions, sub-families of solid-liquid PCMs for CTES applications are respectively categorised as organic, inorganic, and eutectics; see Figure 2.3 [16, 22].

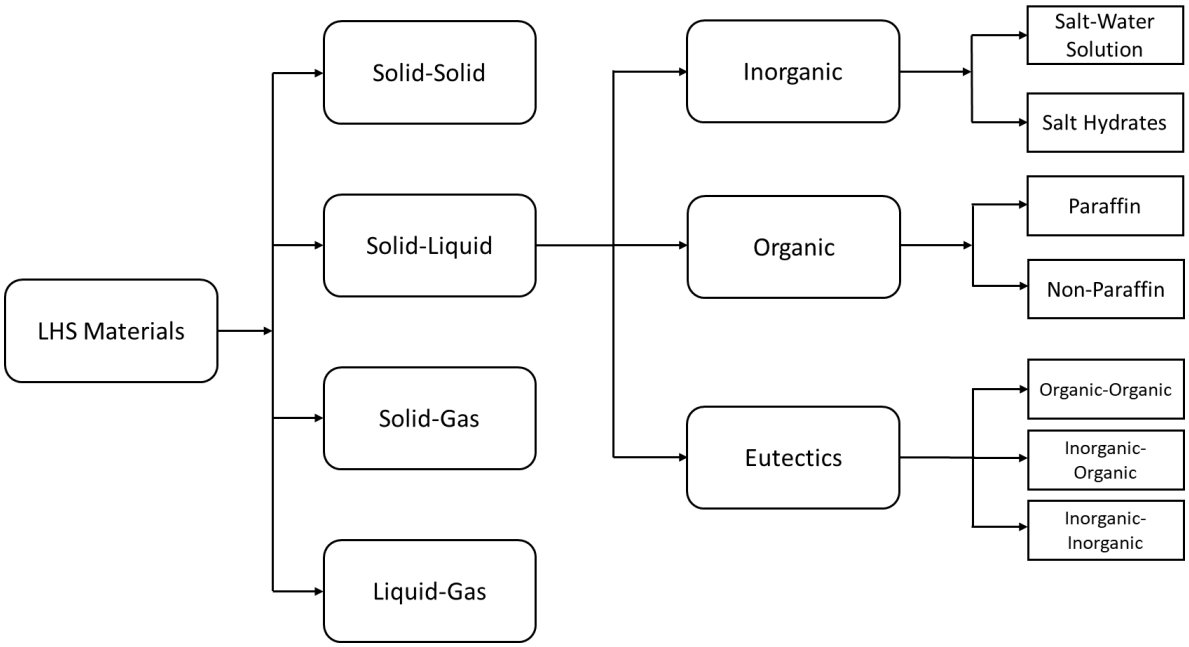


Figure 2.3: Classification of LHS materials for CTES applications [16, 22].

A comparison of the advantages and disadvantages of organic and inorganic PCMs was made by Zalba et al. [36]; see Table 2.4.

Table 2.4: Comparison of organic and inorganic PCMs for thermal energy storage [36].

	Organics	Inorganics
Advantages	Low or no supercooling	High latent heat
	Non-corrosive	High thermal conductivity
	Chemical and thermal stability	Cost-effective
Disadvantages	Low thermal conductivity	Supercooling
	Low latent heat	Corrosion
	Flammability	Phase separation

2.2.2.2 Inorganic PCMs

Inorganic materials can be further categorized as salt-water solution and salt hydrates. The salt-water solution is the most widely studied and applied as a PCM in CTES applications. Table 2.5 gives a list of salt-water solutions for the sub-zero temperature range is given in [37, 38]. Salt hydrates can be regarded as ionic compounds consisting of water molecules and inorganic salts and are denoted by the chemical formula $A_xB_y \cdot nH_2O$, where n refers to the number of water molecules and A_xB_y represents different types of inorganic salts, such as chlorides, carbonates, nitrates, sulphates, and phosphates [39]. Thermodynamically, the phase change process for salt hydrates implies that the hydrated salts desorb the crystallisation water and absorb heat during the heating process, and the inorganic salts recombine with the water to form hydrated salts and release heat during the cooling process [40]. However, most hydrated salts are not suitable for use in sub-zero temperatures due to their relatively high PCT [38]. In addition, some gases composed of inorganic non-metal elements can be used as solid-liquid PCMs for cryogenic applications theoretically, such as oxygen, nitrogen, hydrogen, neon, and helium [41]. Jisung et al. [42] tested the performance of a superconducting flywheel experimental apparatus that utilized solid nitrogen to store both the cold thermal energy and mechanical kinetic energy.

As mentioned above, the advantages of inorganic PCMs include high latent heat, high thermal conductivity, and low cost relative to organic PCMs. But these materials still face some issues, for instance, supercooling, phase separation, and poor compatibility with metals.

Table 2.5: Thermophysical properties of salt-water solutions (PCT up to -20^{O}C) [37, 38].

PCM	Composition (wt.% of Salt)	PCT (℃)	Latent heat (kJ/kg)	Reference
HCl/H_2O	24.8	-86	73.77 (kJ/mol)	[37]
$LiCl/H_2O$	24	-67	36.26 (kJ/mol)	[37]
$ZnCl_2/H_2O$	51	-62	116.84	[38]
$FeCl_3/H_2O$	33.1	-55	155.52	[38]
$CaCl_2/H_2O$	29.8	-55	164.93	[38]
$CaCl_2/H_2O$	30.5	-49.5	76.81 (kJ/mol)	[37]
$CuCl_2/H_2O$	36	-40	166.17	[38]
K_2CO_3/H_2O	39.6	-36.5	165.36	[38]
$MgCl_2/H_2O$	17.1	-33.6	221.88	[38]
$MgCl_2/H_2O$	21.01	-33.5	36.30 (kJ/mol)	[37]
$Al(NO_3)_3/H_2O$	30.5	-30.6	207.63	[38]
$Mg(NO_3)_2/H_2O$	34.6	-29	186.93	[38]
$Zn(NO_3)_2/H_2O$	39.4	-29	169.88	[38]
NH_4F/H_2O	32.3	-28.1	187.83	[38]
$NaBr/H_2O$	40.3	-28	175.69	[38]
KF/H2O	21.5	-21.6	227.13	[38]
$NaCl/H_2O$	22.4	-21.2	228.14	[38]

2.2.2.3 Organic PCMs

Organic PCMs can be further classified as paraffin and non-paraffin. As most commonly used organic PCMs, paraffins, also termed alkanes, consist of a pure hydrocarbon or a mixture of mostly straight-chain n-alkanes, CH_3-$(CH_2)_n$-CH_3. Several investigations by using high precision adiabatic calorimetry have been conducted to measure the thermal properties of linear n-alkanes. Parks et al.

[43] tested the specific heats and the heats of fusion of nine hydrocarbons (C_nH_{2n+2}) with n ranging from 16 to 27 over a temperature range between 78 and 300 K. Based on the low temperature calorimetric data of n-pentane, n-heptadecane, and n-octadecane, Messerly et al. [44] calculated the chemical thermodynamic properties of n-paraffins from C_5 to C_{18} at a selected temperature range between 10 and 300 K. According to these studies, the melting enthalpy (ΔH_{fus}) and the melting point (T_m) are related to the number of carbon atoms [45]. Typically, both the PCT and latent heat of alkanes increase with the carbon chain length [16]. Therefore, paraffins for CTES applications should have a short carbon chain. Typical paraffins are chemically stable, non-corrosive, and compatible with metals, and have little or no supercooling with no phase separation. In addition to these favourable characteristics, paraffins usually have a relatively low thermal conductivity and a low density. Moreover, they are moderately flammable and relatively expensive compared with inorganic PCMs [16, 37, 38].

Non-paraffin PCMs refer to compounds containing functional groups, such as alcohols, glycols, fatty acids, and esters [34]. Alcohol is an organic compound in which one or several hydrogen atoms are replaced by the hydroxyl functional group. Apart from salt-water solution-based PCMs, eutectic alcohol-water solutions have been widely studied for sub-zero applications, such as industrial refrigeration and supermarkets. [38]. According to the freezing point depression behaviour, Hägg [46] indicated that the freezing point of alcohol-water solutions could be suppressed by different concentrations of alcohols. The desirable freezing point for different cold energy storage requirements, therefore, can be achieved by selecting various types of inhibitors (alcohols) or changing their concentrations. Furthermore, Kumano et al. [47] investigated the relationship between the latent heat of different alcohol-water solutions and the degree of freezing point reduction. They found that the

decreasing tendency of latent heat depended on the concentration of alcohol. Although the addition of more alcohols can lower the freezing point, it also reduces the latent heat of PCMs.

Fatty acids constitute another significant category of non-paraffin PCMs, which can be expressed by the chemical formula $CH_3(CH_2)_{2n}COOH$. The most regularly used fatty acid can be divided into six groups: caprylic, capric, lauric, myristic, palmitic, and stearic [22]. Kenisarin [48] reviewed some low temperature fatty acid candidates with melting points within -7℃ to 75℃ and the latent heat between 45 and 210 kJ/kg. Since the primary sources of fatty acids are vegetable oils and animal fats, it is sustainable compared with other organic PCMs [45]. But the price of fatty acid materials is about three times higher than that of paraffins [49].

In addition, some alkanones also show a relatively low PCT, which can be obtained by an oxidation reaction to form the carbonyl functional group [38]. Table 2.6 [50] presents thermophysical properties of some alkanones containing carbon atoms from 3 to 7. They have excellent potential for sub-zero CTES applications owing to their low phase transition temperature and good latent heat. However, the flammability and toxicity issues need to be considered in the CTES application [38].

Table 2.6: Thermophysical properties of alkanones for CTES application (PCT up to -30℃) [50].

PCM	Formula	PCT (℃)	Latent heat (kJ/kg)	Liquid density (kg/m^3)
Acetone	C_3H_6O	-94.9	99.3	784
2-Butanone	C_4H_8O	-86.7	116.4	799
2-Pentanone	$C_5H_{10}O$	-76.8	123.4	809
2-Hexanone	$C_6H_{12}O$	-55.4	148.7	812

PCM	Formula	PCT (℃)	Latent heat (kJ/kg)	Liquid density (kg/m^3)
3-Hexanone	$C_6H_{12}O$	-55.4	134.5	815
3-Pentanone	$C_5H_{10}O$	-38.9	134.6	809
3-Heptanone	$C_6H_{12}O$	-37.2	153.5	818
2-Heptanone	$C_7H_{14}O$	-34.7	172.6	811
4-Heptanone	$C_7H_{14}O$	-32.9	141.5	817

2.2.2.4 Eutectics

A eutectic system is a mixture of two or more substances with a specific composition, which has the lowest melting temperature among all such mixtures formed by the same substances [41]. Sub-families of eutectics are grouped into organic-organic, organic-inorganic (alcohol-water solution), and inorganic-inorganic (salt-water solution) systems. In organic-organic eutectics category, the binary and ternary fatty acid eutectics have been investigated extensively as possible PCMs for various energy storage applications, such as building energy storage systems, air conditioning systems as well as solar photovoltaic systems [51]. Ke [51] and Sharma et al. [52] summarised previous studies on the binary and ternary fatty acid eutectics, with a melting temperature ranging from 20℃ to 50℃. However, it is hard to meet the temperature requirement of sub-zero TES applications. Zhang et al. [53] proposed a modelling method to predict the thermophysical properties of cryogenic eutectic PCMs composed of alkanes. Both hypothetical path for solid fugacity calculation and Soave-Redlich-Kwong (SRK)-UNIFAC model for liquid fugacity calculation were applied to evaluate the eutectic composition, eutectic temperature, and eutectic enthalpy of cryogenic composite PCMs. The

calculation deviation of these thermophysical properties was within 5% compared with the literature values. The study also suggested high-grade cold energy storage for the LNG gasification process by using binary n-pentane/n-hexane PCM, which has a eutectic temperature of 140.95 K, and a eutectic enthalpy of 118.2 kJ/kg. Therefore, eutectic PCMs composed of alkanes can be a possible candidate material for the cryogenic energy storage application.

2.2.2.5 Commercial PCMs

According to the thermophysical properties provided by different suppliers, several commercial PCMs are available nowadays, which are listed in Table 2.6 for the sub-zero temperature applications [54-57]. It is noticed that the lowest PCT of commercial PCMs is -114℃, and its thermal conductivity decreases sharply to about 0.2 W/m·K when the melting temperature is around -100℃. However, most of these materials are eutectic salt-water solutions, and few suitable organic candidates have been developed as PCMs commercially in the cryogenic field.

Table 2.7: Thermophysical properties of commercial PCMs for CTES application (PCT up to -30℃) [54-57]*.

Product	Supplier	PCT (℃)	Latent heat (kJ/kg)	Specific heat (kJ/ kg·K)	Thermal conductivity (W/ m·K)	Density (kg/m^3)
E-114	PCM products [54]	-114	107	2.39	0.17	782
E-90	PCM products [54]	-90	90	2.56	0.14	786
E-78	PCM products [54]	-78	115	1.96	0.14	880
E-75	PCM products [54]	-75	102	2.43	0.17	902
E-62	PCM products [54]	-62	180	4.01	0.58	1300

Product	Supplier	PCT (℃)	Latent heat (kJ/kg)	Specific heat (kJ/ kg·K)	Thermal conductivity (W/ m·K)	Density (kg/m^3)
E-60	PCM products [54]	-60	172	2.9	0.44	1280
SP-50	Rubitherm [55]	-50	190	2	0.6	1300
E-50	PCM products [54]	-49.8	218	3.28	0.56	1325
E-46	PCM products [54]	-46	240	3.05	0.54	1205
P-37	Puretemp [56]	-37	145	1.99	0.15	880
E-37	PCM products [54]	-36.5	213	3.15	0.54	1500
E-34	PCM products [54]	-33.6	240	3.05	0.54	1205
HS30N	Pluss [57]	-33	224	2.7	-	1425
E-32	PCM products [54]	-32	243	2.95	0.56	1290
SP-30	Rubitherm [55]	-30	250	2	0.6	1200
E-29	PCM products [54]	-29	222	3.69	0.64	1420
SP-29	Rubitherm [55]	-29	260	2	0.6	1200

* Some of these data have not been independently validated and are not necessarily all correct.

2.2.2.6 Summary

This section gives an up-to-date review of LHS materials for sub-zero applications; see also Figure 2.4 [37-57]. Most of the inorganic PCMs studied and developed in research laboratories, and commercial companies are eutectic salt-water solutions with phase transition temperatures below 0℃. Salt-water-based PCMs show good thermophysical properties in terms of latent heat and thermal conductivity. However, supercooling, phase separation, instability, and corrosiveness, are among challenges that need to be addressed for practical applications. For organic PCMs, paraffins have

benefits of chemically stable, non-corrosive, little or no supercooling, and no phase separation. But they have poor thermal conductivity and are flammable. In the non-paraffin group, alkanones exhibit a great potential for sub-zero applications thanks to their suitable low phase transition temperature and high latent heat. However, similar to alkanes, the flammability issue needs to be addressed or mitigated.

For a specific application, one of the most important criteria for PCM screening is their phase transition temperature. As mentioned above, alkanes with short carbon chains and their eutectic PCMs are appropriate candidates for CTES applications at cryogenic temperature range. In addition, it is also crucial to understand the thermophysical properties of PCMs within their operating temperature. Therefore, the characterization techniques and methods for PCM will be discussed in detail in the following section, especially in the low temperature range.

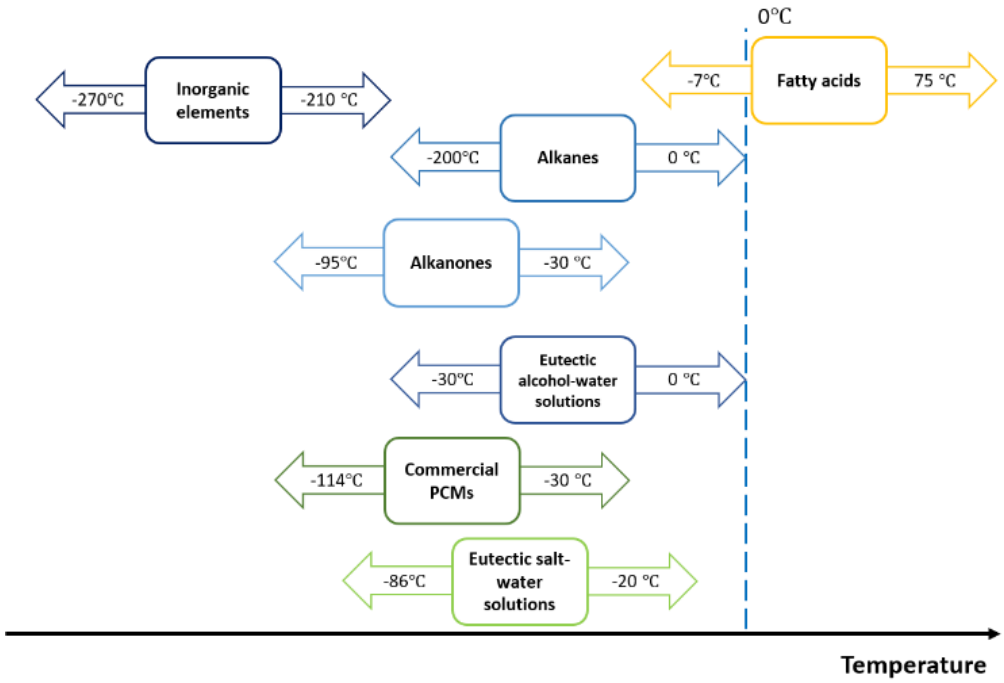


Figure 2.4: Solid-liquid materials being investigated and used as PCMs for sub-zero temperature applications [37-57].

2.3 PCMs characterisation techniques & methods

The performance of the PCM is usually achieved by a heat exchange unit, and one of the prerequisites for the design of an appropriate heat exchange device is to understand or determine the thermophysical properties of the PCM. The first set of significant properties that affect the thermal storage capacity are PCT (T_m), liquid and solid specific heat (C_p), and phase change enthalpy (H_m). The second set of properties include thermal conductivity (λ), density and viscosity at liquid state, which can play a vital role in the component design of the TES system particularly their effects on the charging/discharging kinetics of the system. Furthermore, safety considerations, such as flammability, should be carefully considered when using organic materials.

2.3.1 Thermal storage capacity determination

Among different thermal analysis (TA) techniques, differential scanning calorimetry (DSC) is one of the most powerful and versatile tools to determine the melting/solidification temperatures, the melting/solidification enthalpies, and the specific heat of a material over a wide temperature range [58]. Depending on the cooling method of DSC, the sample can be measured at various temperatures (e.g., -100℃ with a mechanical refrigeration cooling unit, or -196℃ when LN_2 is used as the coolant) [59]. In DSC measurement, the heat flow rate difference between a sample and a reference (with known thermal properties) is measured as a function of temperature while they are subjected to a controlled temperature program with constant heating and cooling rates [59]. As the specific heat and the phase change enthalpy are a function of temperature, the heating and cooling rates influence the measurement accuracy and the shape of the DSC curves. Castellon et al. [60] investigated the enthalpy-temperature relationship of organic PCM RT27 using a dynamic method, which has different

heating/cooling rates in the range of 0.2-10 K/min. Their study indicated that the melting enthalpy was lower than the solidification enthalpy under lower heating/cooling rates ($\leq$ 2K/min) and exceeds 10% permitted deviation. Kousksou et al. [61] reported that the specific heat of hexadecane decreased with increasing heating rate from 2 to 15 K/min.

The use of DSC should also consider the possible impact of the sample size and geometry on its thermal behaviour. Kinetic properties such as supercooling, crystal growth, and phase separation of materials may be affected by the sample size and geometry [62]. Typically, the sample weight in DSC experiments should be in the range of 5 to 20 mg. If the sample size is too large, an undesirable increase will occur in the thermal hysteresis and temperature gradient within the sample. On the other hand, a sample with a too small mass may reduce the sensitivity of the measurement [59]. Rathgeber et al. [63, 64] studied the effect of different sample amounts on the enthalpy [63] and supercooling [64] of commercial paraffin RT58. The sample masses used were 12.35 mg, 9.61 g, and 108 kg, respectively. The enthalpy-temperature plots were obtained to compare the enthalpy changes measured with different sample sizes upon the melting and solidification processes. Their results showed that the enthalpy change of RT58 was relatively low when the sample mass was 108 kg [63]. Regarding the influence of different sample sizes on supercooling behaviour, they found that the supercooling degree of paraffin RT58 was independent of the sample size. However, the other measured PCMs (Bischofite, D-mannitol, Hydroquinone) showed a common trend in terms of supercooling degree: the larger the measured sample size, the smaller the supercooling degree. It is therefore necessary to assess an application oriented PCM with different sizes to ensure correct data [64]. Kousksou et al. [61] investigated the influence of different sample geometries on the specific heat of a 10 mg hexadecane sample at a constant heating rate of 5 K/min. Their results showed that

the phase change peak of hexadecane in the $C_p(T)$-curve was shifted from 295 K to about 297 K, but the area under phase change peak remained constant at around 263 kJ/kg. A reasonable explanation was given as that during the melting process, the specific heat capacity varied with the temperature gradient inside the PCM, and the internal temperature gradient was caused by the change of sample geometry. Therefore, the sample geometry is a crucial factor in determining the thermal behaviour of PCMs in a DSC measurement.

These issues have led to the development of other methods for the analysis and determination of the thermal properties of PCMs. An example is the T-history method, which was originally proposed by Zhang et al. [65] in 1999. In terms of recording temperature versus time curves of the PCM, the PCT, heat of fusion, specific heat capacity, supercooling degree, and thermal conductivity of PCM samples are determined simultaneously. This method is shown in Figure 2.5 [65]. In a typical test, several glass tubes containing PCM samples and reference materials are heated in a water bath to/above the melting temperature of PCM ($T_0 > T_m$), and then they are suddenly exposed to the time-dependent ambient temperature (T_∞). The T-history (temperature versus time) curves of the PCM and the reference material are recorded during this cooling process, as illustrated in Figure 2.6. Figure 2.6 (a) shows the PCM with a supercooling degree $\Delta T_m = T_m - T_s$; Figure 2.6 (b) demonstrates the PCM without supercooling where the phase transition process is between $T_{m,1}$ and $T_{m,2}$; whereas Figure 2.6 (c) displays the water temperature as a reference T_r. To derive the specific heat of PCM for liquid ($C_{p,l}$) and solid phase ($C_{p,s}$) and the heat of fusion (H_m), the temperature distribution within the sample is assumed to be uniform, and the lumped capacitance method is applicable, which stands if the Biot number is less than 0.1. These are given in the following equations and are applied to PCM with supercooling.

$$C_{p,l} = \frac{m_w C_{p,w} + m_t C_{p,t}}{m_p} \frac{A_1}{A'_1} - \frac{m_t}{m_p} C_{p,t} \quad (2.4)$$

$$C_{p,s} = \frac{m_w C_{p,w} + m_t C_{p,t}}{m_p} \frac{A_3}{A'_2} - \frac{m_t}{m_p} C_{p,t} \quad (2.5)$$

$$H_m = \frac{m_w C_{p,w} + m_t C_{p,t}}{m_t} \frac{A_2}{A'_1} (T_0 - T_s) \quad (2.6)$$

where m_w, m_t, and m_p are the mass of the water, the tube and the PCM, A is the integral of the temperature gradient between the recorded temperature (T) and the ambient temperature (T_∞) at different time intervals, with $A_1 = \int_0^{t_1}(T - T_\infty)dT$, $A_2 = \int_{t_1}^{t_2}(T - T_\infty)dT$, $A_3 = \int_{t_2}^{t_3}(T - T_\infty)dT$, $A'_1 = \int_0^{t'_1}(T - T_\infty)dT$, and $A'_2 = \int_{t_1}^{t'_2}(T - T_\infty)dT$.

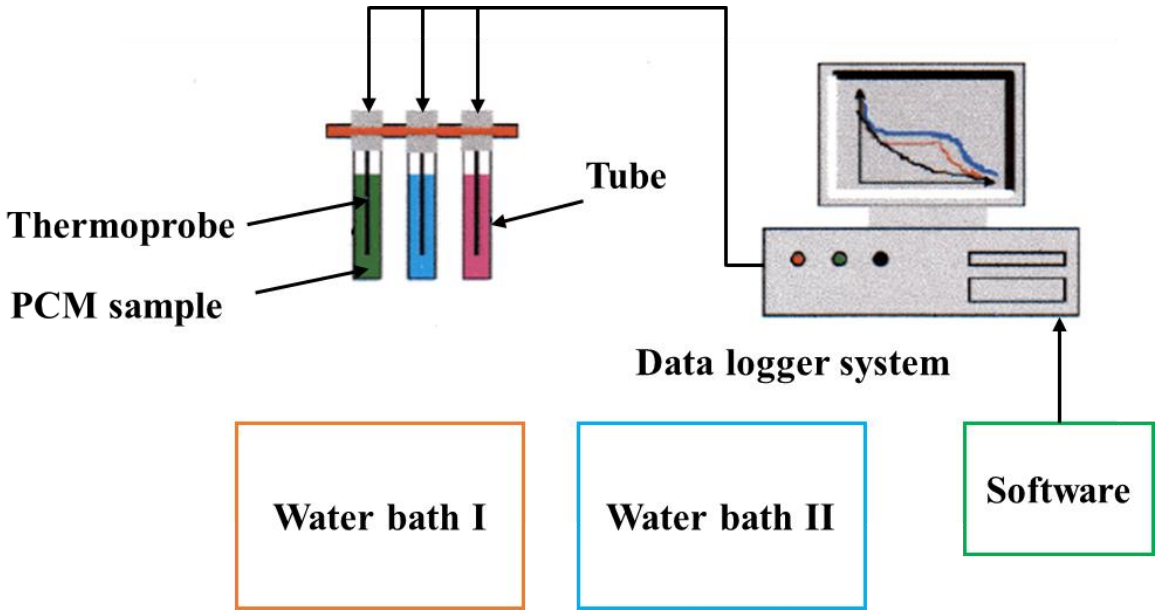


Figure 2.5: Schematic diagram of the T-history experimental rig [65].

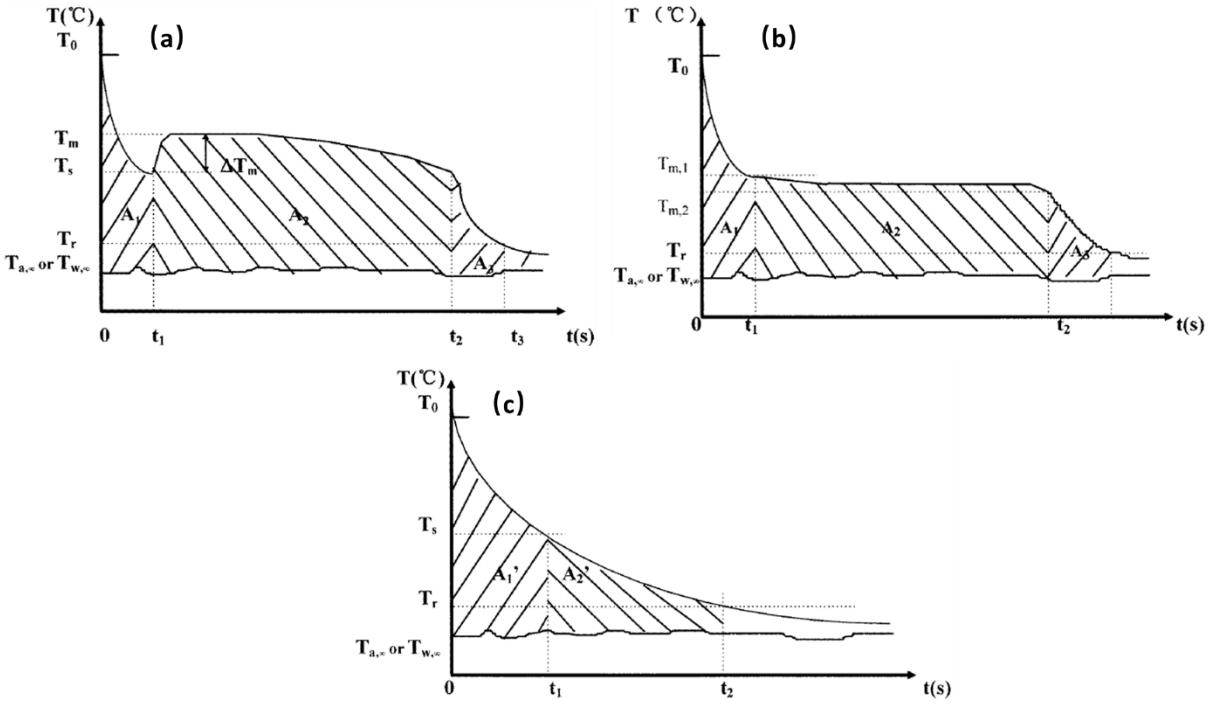


Figure 2.6: T-history curves: the PCM with supercooling (a), without supercooling (b), and the water (c) during the cooling process [65].

For PCM without supercooling, both liquid and solid specific heats are the same, and the phase transition enthalpy between the time interval t_1 and t_2 is given by:

$$H_m = \frac{m_w C_{p,w} + m_t C_{p,t}}{m_p} \frac{A_2}{A'_1} \left(T_0 - T_{m,1}\right) - \frac{m_t C_{p,t} \left(T_{m,1} - T_{m,2}\right)}{m_p} \tag{2.7}$$

To enhance the measurement accuracy of the T-history method, the research community has implemented many modifications to the experimental rig and the mathematical model. Compared with the original model, Lazaro et al. [66] performed a measurement in an insulated air enclosure chamber instead of exposing the heated tubes to the ambient in which the heat transfer coefficient from the environment to the PCM and reference can be considered as the same. They also indicated that a correct calibration of the temperature sensors was necessary for accurate results. They used Type K thermocouples, which were calibrated in a thermostatic bath using a calibrated Pt-100 as a reference

in their study. Before starting a measurement, the correctly calibrated thermocouples were checked by comparing the values when the sample, reference substance, and environment were in the thermal equilibrium. Peck et al. [67] proposed a horizontal setup to measure the low temperature PCM (distilled water, tetradecane, and PEG). This configuration could suppress the strength of the natural convection effect proportional to the vertical length of the test tube and reduce the deviation and temperature difference along the longitudinal direction of the test tube. In addition, a volume control tube was installed to avoid the influence of volume changes on the calculation of the heat transfer coefficient during the phase change process. Their results showed that the errors of distilled water and tetradecane were only 2.1% and 3.9%, respectively, compared with the reference values.

The original mathematical model and data evaluation have also been modified to increase the accuracy of the method. Since the exact point at which the phase transition process is completed is hard to confirm and highly hinges on the operator [68], Hong et al. [69] introduced an inflection point (point b in Figure 2.7 (a)) as the boundary between the phase change and the solid phase regions. As shown in Figure 2.7 (b), this point can be obtained by the first derivative of the T-history curve for PCM. They also suggested that the calculation of the phase change enthalpy should not include the sensible heat, which showed a difference up to 7% compared to the original method. Moreover, due to the volume change of the PCM, the heat transfer area of the test tube would change before and after the solidification process. Thus, the mean value of the areas was applied in this modification method. Marin et al. [70] proposed the use of a concept of enthalpy and its relationship with the temperature rather than using a concept of temperature changes over time. The original mathematical models, therefore, were improved by varying the temperature in a small interval of time, namely ΔT_i corresponding to time intervals $\Delta t_i = t_{i+1} - t_i$ and $\Delta t'_i = t'_{i+1} - t'_i$ for the PCM and the reference

substance, respectively. To obtain enthalpy-temperature curves, Equation 2.8 was rewritten with T_i being the average temperature of the interval:

$$\Delta H_p(T_i) = \frac{m_w C_{p,w}(T_i) + m_t C_{p,t}(T_i)}{m_p} \frac{A_i}{A'_i} \Delta T_i - \frac{m_t}{m_p} C_{p,t}(T_i) \Delta T_i \tag{2.8}$$

Also, the phase change enthalpy of PCM can be determined as the sum of the enthalpy intervals, assuming a constant value of $H_{p,0}$ as a reference:

$$H_p(T_i) = \sum_{i=1}^{N} \Delta H_{p,i} + H_{p,0} \tag{2.9}$$

In addition, the specific heat for both solid and liquid phases can be obtained by computing the slope of the curve at the selected temperature, as shown in the following Equation 2.10:

$$C_p = \frac{\partial H}{\partial T} \tag{2.10}$$

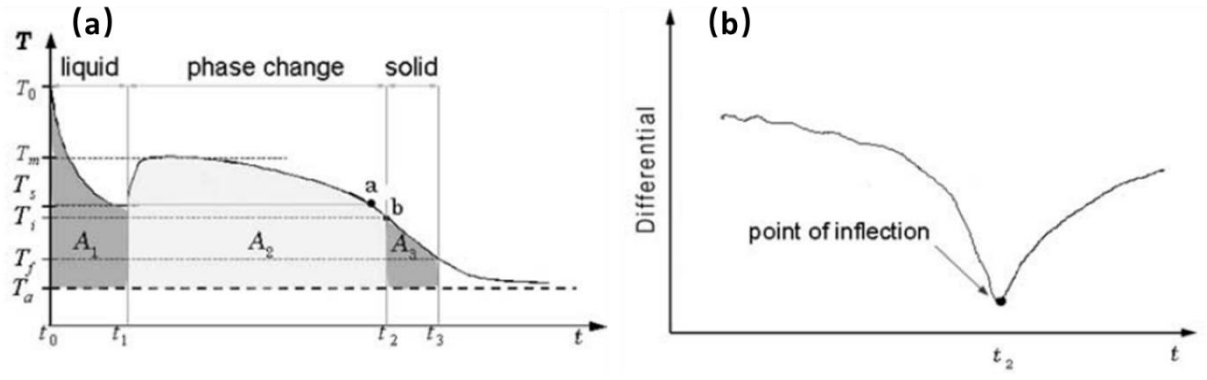


Figure 2.7: The modified mathematical model of the T-history method: (a) T-history curve with the inflection point b as the boundary; (b) the first derivative of the T-history curve [69].

The T-history method has some advantages for determining thermophysical properties of PCM compared with the commercially available thermal analysis techniques (DSC). For instance, it allows

large-sample analysis of various PCMs (inorganic, organic, and eutectic) so that more representative data can be measured for TES applications; the phase change process can be visually observed during the measurement, and the measuring temperature range and the cooling/heating rates are variable based on different samples [58]. Moreover, maintenance and equipment price are inexpensive, and the system configuration is simple [69]. However, the main drawback is the lack of common instrument configurations and standard data analysis processes, which may affect the accuracy of T-history measurement [58].

2.3.2 Thermal conductivity measurements

Thermal conductivity refers to the intrinsic physical ability of a material to transfer or conduct heat, and it represents the quantity of heat energy that flows through a unit cross-section area of a material pre-unit time when the temperature gradient is 1℃ [71]. The thermal conductivity of the material can be described following Fourier's law [72]:

$$Q = -\lambda A \frac{dT}{dx} \tag{2.11}$$

where Q is the heat flow rate of thermal conduction (W), λ is the thermal conductivity of the material (W/m·K), A is the cross-section area (m^2), and dT/dx is the temperature gradient of the test sample.

According to different measurement conditions, the thermal conductivity determination techniques can be classified as steady-state methods (heat flowmeter, guarded hot plate) and transient methods (transient hot wire/strip, laser flash apparatus, transient plane source, thermocouple method, etc.) [73]. The steady-state methods can determine the thermal conductivity directly by measuring the temperature ΔT under a steady-state heat flow Q through the sample. The transient techniques

measure thermal diffusivity by using heat sources that can be supplied either periodically or as a pulse [74]. Among these measurement methods, the testing temperature range of laser flash apparatus and transient hot wire/strip can reach sub-zero temperature, which are -120℃ to 2800℃, and -150℃ to 200℃, respectively [73]. These two techniques are suitable for measuring the thermal conductivity of low temperature PCMs, and hence are discussed further in the following.

2.3.2.1 Transient hot wire/strip method

The transient hot wire/strip method employs a hot wire/strip sensor that acts both as a linear heat source and a thermocouple (usually platinum or tantalum) during the thermal conductivity measurement. This linear heat source leads to the temperature rising of the sample over a known time interval, thereby determining the thermal conductivity of the sample. Equation 2.12 [75] is the mathematical representation of the thermal conductivity of the material based on the transient hot wire/strip method.

$$\lambda = \frac{q}{4\pi(T_2 - T_1)} \ln \frac{t_2}{t_1} \tag{2.12}$$

where λ is the thermal conductivity of the material (W/m·K), q is the heating power per unit length of the wire/strip (W/m), and Ti $(i = 1, 2)$ is the temperature of the wire/strip at corresponding time t_1 and t_2.

Currently, transient hot wire/strip instruments permit more than 1000 data acquiring within 1 ms up to 1 s (10s for solids) [74]. Moreover, it has been reported to be able to measure the thermal conductivity of gases, solids, and liquids with uncertainties below 1% [76]. Palacios et al. [73] reviewed various thermal conductivity measurement methods and found that the available instrument can work at

temperatures from -150℃ to 200℃, while the measuring range of the thermal conductivity can be from 0.001 to 500 W/m·K with different sensors. However, this method also has some limitations in terms of sample types and sample thickness. For instance, the specimen to be tested should be non-conductive material. Because the thermal conductivity is only tested in one direction, the results of irregular solids (e.g., sensible storage material), powders, heterogeneous are not accurate [73]. In addition, heat losses occur when the thickness of the sensor is equivalent to or greater than the thickness of the sample, such as thin films [76].

2.3.2.2 Laser flash apparatus

Laser flash apparatus (LFA) is a well-known technique that uses non-contact, non-destructive temperature sensing to measure the thermophysical properties (thermal diffusivity, specific heat, and thermal conductivity) of samples [77]. The working principle of the laser flash method is depicted in Figure 2.8 (a). During measurements, a laser pulse from a laser beam source uniformly heats up the front side of a planar-shaped sample, and an infrared detector monitors the time-dependent temperature change at the rear side of the sample [77]. The thermal diffusivity along the thickness direction of the sample can be expressed as a function of time by [78]:

$$\alpha = 0.1388 \times \frac{d^2}{t_{1/2}} \tag{2.13}$$

where α is the thermal diffusivity (m^2/s), d is the thickness of the sample (m), and $t_{1/2}$ is the time for the specimen to reach 50% of the maximum temperature, as shown in Figure 2.8 (b) [78].

The thermal conductivity (λ) can be obtained if the density (ρ) and the specific heat (C_p) of the sample are available by using the following Equation 2.14 [78]:

$$\lambda = \alpha \cdot \rho \cdot C_p \tag{2.14}$$

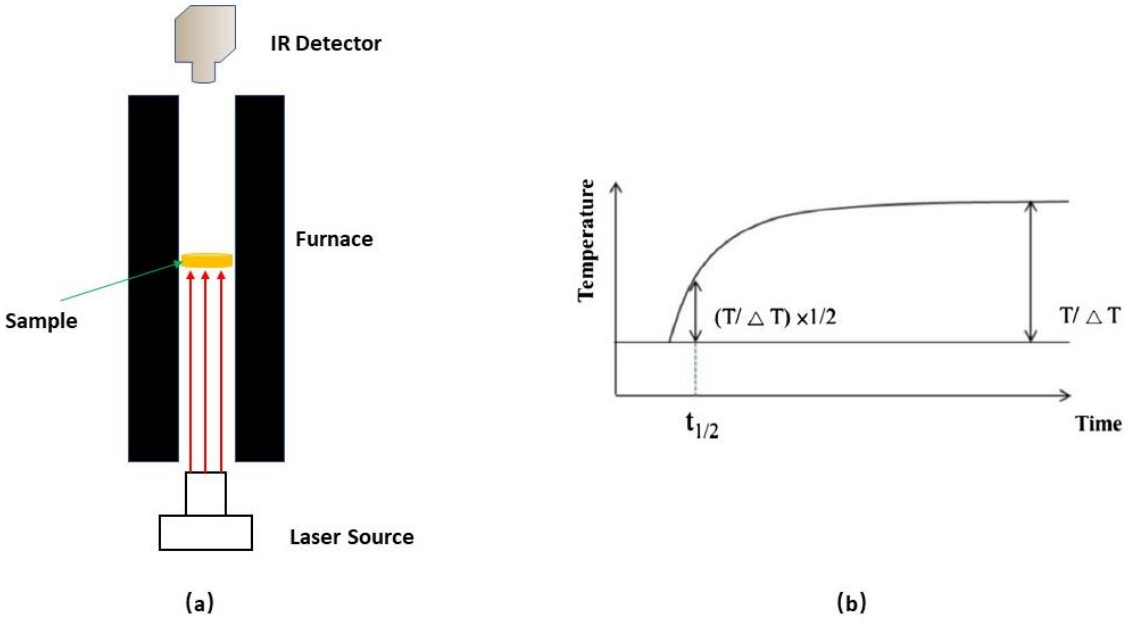


Figure 2.8: The principle and temperature rise curve of laser flash method [67, 68].

The laser flash technique is one of the commonly used techniques in the thermal conductivity measurement of solids and liquids. The commercially available instrument can conduct the measurement over a wide temperature range (-120℃ to 2800℃) with a high accuracy. Min et al. [77] claimed that the measurement uncertainty was less than 3%. The advantages of this method are: 1) measurement is fast, usually 1-2 s for solids; 2) only small samples are required, e.g., 6-12 mm in diameter with 1-4 mm thickness; 3) there are measurement standard for this, including ISO 220074 and ASTM E1461; 4) Because the measurement is carried out in a specific furnace, the test temperature, pressure, and atmosphere can be controlled [73]. However, there are also some factors that will increase the measurement uncertainty, including sample preparation and material properties. For instance, solid samples require a flat and smooth surface to obtain accurate and repeatable results [74], while liquid or powder samples need to maintain good contact between the sample and the

measurement area of the sample holder [73]. Moreover, specific heat and density of the sample should be known or measured from other experiments, which may generate large errors [74]. Also, the system is expensive, and the maintenance and operation costs are high. Additionally, the method is less suitable for thermal insulation or heterogeneous solid materials [73].

2.3.3 Flammability limits test

As aforementioned, one of the aspects of low temperature organic PCMs is their flammability, which is a potential fire hazard during storage, operation, transportation, and applications [79]. Generally, the flammable characteristic of a specific material is represented by flammability limits. These limits can be used to distinguish boundaries of the flammable mixture regions where the flame propagation occurs or does not occur [80]. There are two flammability limits for a hydrocarbon-air mixture: lower flammability limit (LFL) and upper flammability limit (UFL). The LFL is the minimum concentration (i.e., lean mixture) of hydrocarbon vapor or gas capable of propagating flame upon ignition at a given temperature and pressure, while the UFL is the maximum concentration (i.e., rich mixture) in the same scenario [81]. The LFL and UFL therefore define the flammable concentration range of a hydrocarbon-air mixture. Because flammability limits are affected by several factors, such as the geometry of the apparatus, the operating temperature and pressure, the strength of the ignition energy, and the oxygen concentration [82], the correct determination of flammability limits is important for the prevention of fires and explosions. Knowledge of flammability limits is mainly based on two methods: theoretical calculation and experimental measurement.

2.3.3.1 Theoretical calculation

Different theoretical methods are discussed to calculate flammability limits in the literature: the stoichiometric concentration [83], the combustion enthalpy [84], the vapor pressure [85], and the algebraic method [86]. In all these methods, the theoretical data of LFL fit the experimental values well; however, there are some differences between UFL values and experimental data [80].

Stoichiometric concentration. The LFL and the UFL for many hydrocarbon vapours are a function of the stoichiometric concentration (C_S) of the flammable mixture for complete combustion reaction in the air, as shown in the following equations [83]:

$$LFL = 0.55C_S \tag{2.15}$$

$$UFL = 3.5C_S \tag{2.16}$$

Combustion enthalpy. The LFL of combustibles in the air can be roughly estimated using the following Equation 2.17 [84]:

$$LFL = -\frac{4354}{\Delta H_{comb}} \tag{2.17}$$

where ΔH_{comb} is combustion enthalpy (kJ/mol), and LFL is given in volume percentage.

Vapor pressure. The LFL can be determined by using the pressure ratio of flammable substance and atmosphere [85]:

$$LFL = \frac{P_f}{P_0} \times 100 \tag{2.18}$$

where P_f is the vapor pressure of the flammable mixture at flashpoint, and P_0 is the standard

atmospheric pressure.

Algebraic method. Mathematically, the LFL can be expressed as [86]:

$$LFL = \frac{100}{1 + n_a} \tag{2.19}$$

where n_a is the number of moles of air per mole of combustible in the mixture at the LFL.

2.3.3.2 Experimental method

Experimental methods for measuring flammability limits of combustibles have been standardized by the combination of the following criteria: (a) visually inspect the flame propagation caused by a spark igniter among the flammable mixture in the transparent and closed vessel (visual criteria); (b) monitor the pressure change at the instant of ignition in the closed vessel (pressure criteria) [80].

Visual criterion. European standard EN 1839 defines two test methods (tube method and bomb method) to determine flammability limits of combustibles [87].

EN 1839 (T) offers one visual criterion: the flame detachment and propagation from the spark igniter are at least 100 mm.

American standard ASTM E-681 [88] provides two different visual criteria according to different vessel sizes:

• For the 5 L vessel, the flame spread upwards and outwards to a distance of at least 13 mm from the spark to the vessel wall (horizontal or vertical).

• For the 12 L vessel, the flame moves upwards and outwards from the spark igniter to the vessel wall

and forms an angle equal to or greater than 90° as measured from the ignition point to the vessel wall.

Pressure criterion. The ASTM E-2079 [89] and EN 1839 (B) standards are not for the flame propagation, but for pressure increase after ignition. The American standard recommends a pressure rise of 7% above the initial fixed pressure as the critical point condition, while the European standard suggests a 5% criterion. Takahashi et al. [90] reported that if the vessel size is large enough, the experimental results of flammability limits may be close to the values obtained in open space. Therefore, the minimum vessel volume recommended by EN 1839 (B) and ASTM E-2079 is 5 L and 4 L, respectively.

However, the fundamental difference between European and USA standards is the definition of flammability limits. According to the European standard [87], the flammability limit itself is not a part of the flammable range, and the flame cannot spread/propagate after being ignited. Instead, American standards [88, 89] define the flammability limit as the limit fuel concentration that permits the flame to propagate through the flammable mixture. From a safety consideration, Schroder et al. [91] suggested the use of the more conservative European standard with the final non-ignition concentration as flammability limits.

2.3.3.3 Fire retardants

To address the potential fire hazards of organic PCMs, fire retardants have been attempted to reduce the flammability of materials. According to the mode of action, fire retardants can be classified as either a chemical action type or physical action type [92]. The most commonly used chemical action type is known as a flame quencher, which may decompose to generate gases or char layers, thereby

interrupting the propagation of free radicals necessary for flame burning while increasing smoke, carbon monoxide, and other by-products of incomplete combustion [92, 93]. Materials such as halogenated alkanes (chlorinated paraffin) [94] and halogenated phosphate esters (TCEP, TCPP, TDCPP) [95] have been widely employed as fire retardants. These halogen-containing flame retardants, however, present some potential threats to the environment and human bodies, such as carcinogenicity, mutagenicity, corrosivity, and toxicity [96]. Consequently, halogen-free fire retardants are proposed as an alternative solution. Various environmentally friendly additives based on silicon materials, such as kaolin, clay, silsesquioxane, and silicon dioxide (SiO_2), have been extensively accepted as a new direction of flame retardant research [95, 97]. Huang et al. [98] performed an extensive study on the effects of incorporating different SiO_2 on flame retardancy of EVA/$Mg(OH)_2$ composites. The results showed that the fire performance index and ignition time had been increased, and the peak rate of heat release had been dramatically reduced.

While another type based on physical action is called heat absorber or hydrated filler, which decomposes endothermically to remove heat from the material and flame and creates a barrier layer to prevent oxygen from entering the flammable zone and hence mitigate the combustion [92, 93]. Some metal hydroxides have been used to enhance the flame retardancy of materials, among which are magnesium hydroxide and aluminium hydroxide [92, 95, 98-100].

2.3.4 Summary

In conclusion, the study of the thermophysical and, in some cases, chemical properties of the PCM is essential for designing a suitable TES device and further determining the thermal performance of the TES system. Correspondingly, thermal analysis of thermal storage capacity, thermal conductivity, and

flammability limits are reviewed for low temperature organic PCMs. A comparison between DSC and T-history methods illustrates that different sample amounts have a significant impact on thermal behaviours of PCM, especially on enthalpy and supercooling. Meanwhile, LFA and transient hot wire/strip methods are discussed to determine the thermal conductivity of storage materials because they can operate at a relatively low measurement temperature. Taking into account the flammable characteristics of organic PCMs, the determination of flammability limits is analysed in terms of the theoretical calculation and experiment verification. In addition, several fire retardants that can be potentially used for organic hydrocarbons are reviewed based on their mode of action.

2.4 CTES devices and applications

Successful utilisation of a TES material requires the use of devices or components for the provision of encapsulation for materials and container for HTF [101]. Therefore, in this section, different types of TES devices for CTES applications will be discussed, including both numerical and experimental studies.

2.4.1 Packed bed CTES device

As reviewed in Section 2.2.1, packed beds are one of the most commonly used TES technologies at cryogenic temperatures. Figure 2.9 illustrates a typical packed bed storage device consisting of an insulated tank, storage materials, a supported screen, and inlet and outlet pipelines [102]. The storage materials, also called packing elements, can be solid SHS materials [103] or PCMs contained in macro-encapsulation [41]. In the case of cold energy storage applications, a liquid or gas is used as a HTF to transport the energy from cold/heat source to the storage materials, which corresponds to the

charging/discharging process of the system. The advantage of the packed bed CTES is the simplicity in design and manufacture, low cost, and reliability over thermal changing and discharging cycles [27]. However, the disadvantages of the packed bed device are also clear, such as the large pressure loss on the HTF side, and the high void fraction leading to a lower energy storage density [41].

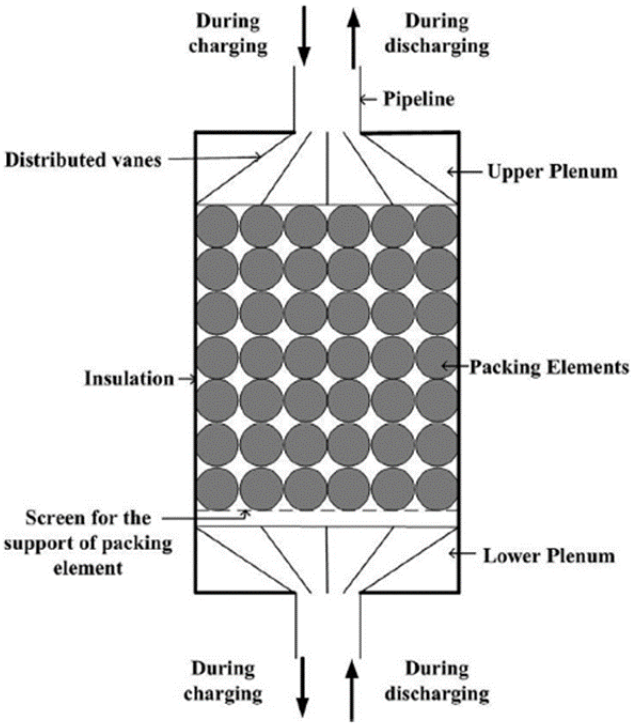


Figure 2.9: Schematic diagram of typical packed bed based CTES device [102].

2.4.1.1 Numerical models

Various numerical studies for the heat transfer analysis of packed bed devices have been reported in the literature. These numerical models can be divided into two groups: single phase models and two phase models.

In the single phase models, the solid and fluid phases are considered to be one phase, and their instantaneous temperatures are equivalent. As reported by Ismail and Stuginsky [104], this model is

applicable to storage materials with a high thermal conductivity and a high heat capacity in comparison to the working HTF. However, because of the limited thermal conductivity of commonly used PCMs, the use of this model is not prevalent when describing PCM packed bed devices.

Regarding the two phase models, heat transfers in the solid and the HTF are treated separately and the boundary between solid and fluid interfaces is linked by the Nusselt correlations [105]. These models have been used to represent the dynamic thermal behaviour of the packed bed, namely the Schumann's model [106], the concentric dispersion model, and the continuous solid phase model.

Schumann's model.

This two phase model assumes one-dimensional heat transfer and does not take into account heat conduction either in the HTF or in the solid phase. This methodology was one of the first attempts to numerically represent the behaviour of packed bed thermal storage devices. It adopts a lumped capacitance approach to solid particles and assumes that the convection coefficient is independent of time and space [106]. The major limitation of the Schumann's model is that it does not consider the thermal diffusion within solid particles, therefore no thermal gradients are considered in the sphere and only the convection drives the heat transfer process [105].

Concentric dispersion model.

This model treats a packed bed as an isotropic porous medium consisting of individual spherical particles and allows for the existence of thermal gradients within solid materials. In this model, the packed bed is divided into multiple elements in the axial direction, where fluid temperature is considered to be homogeneous. But the temperature gradient on the surface of the particles in only

due to the heat transfer between the HTF and the packed bed [107]. In addition, the calculation of heat loss to the environment can be implemented in this model [105].

Continuous solid phase model.

In this model, the solid is assumed to be a continuous medium, rather than a medium consisting of solid particles [107]. The heat conduction in the packed bed can occur in the axial direction (one-dimensional continuous solid phase model) or in the axial and radial directions (two-dimensional continuous solid phase model). Although the addition of the radial heat transfer intensely increases the computational cost of the model, it is the only model capable of capturing the thermal gradient in this direction, which is significant for systems with low mass flow rates that are affected by the heat losses from the environment or the uneven distribution of the inlet flow through the system [105].

Davenne et al. [108] performed a numerical analysis to compare the heat transfer behaviour of concrete based packed bed and a liquid thermocline as cold storage devices for an offshore wind driven pumped TES system, respectively. They used the one-dimensional single phase model with convection diffusion equations, including the speed of the thermocline and the effective diffusivity coefficient in the storage. Sciacovelli et al. [15] used a one-dimensional continuous solid phase model to estimate the performance of the packed bed cold storage as a component of the LAES system. Their results were compared with the experimental data obtained in a charging experiment with modular packed beds consisting of four U-shaped units filled with quartzite pebbles, as shown in Figure 2.10. Their simulation results correlated well with experimental results of measured temperatures at locations of 0.27, 1.7, and 3.13 m along the axis direction of the packed bed during the charging process.

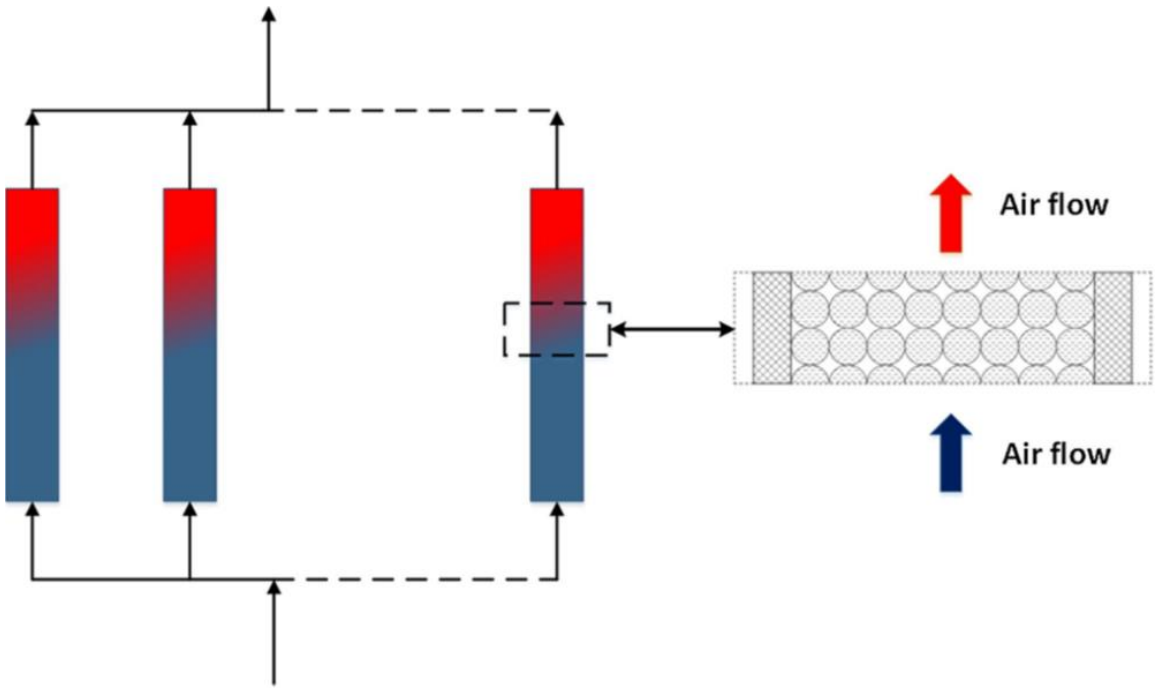


Figure 2.10: Schematic diagram of modular packed bed high-grade cold storage [15].

In addition, numerical studies have also been carried out on packed beds filled with PCM capsules for the storage of cold energy at temperatures below 0℃. Khor et al. [109] conducted a numerical investigation of a cascaded packed bed system comprising three different encapsulated PCMs with cascading phase transition temperatures (-49℃, -19.5℃ and 6.5℃, respectively) along with the packed bed, as shown in Figure 2.11. The concentric dispersion model with the enthalpy method was used to simulate the heat transfer and the phase change process generated in the PCM capsule along the radius of the capsule in a one-dimensional manner. Their simulation results provided a few performance graphs of the cascaded packed bed units and demonstrated that different storage capacities within each temperature region were determined by the quantity of PCMs and the various diameters of PCM particles.

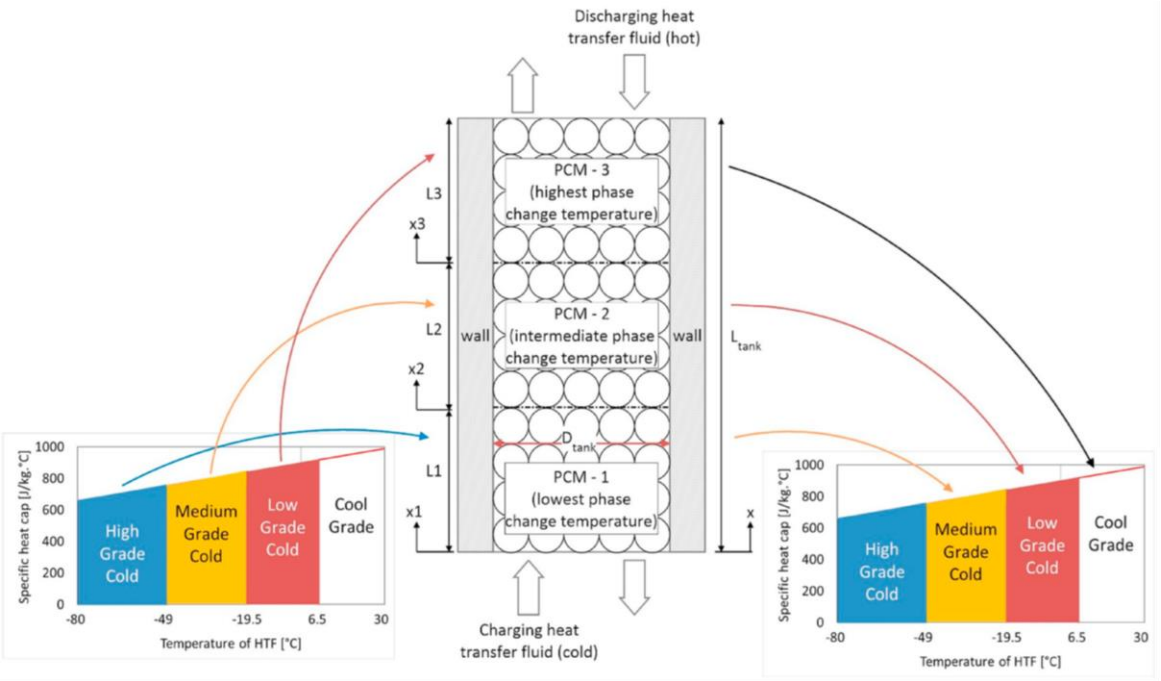


Figure 2.11: Schematic diagram of packed bed using cascaded PCMs as TES materials [109].

2.4.1.2 Experimental studies

As depicted in Figure 2.12, many physical phenomena govern the packed bed storage behaviour in terms of the heat transfer coefficients between HTF/solid and HTF/wall, the effective thermal conductivity, the temperature stratification (also known as a thermocline/thermal front), and the pressure loss of the bed [110]. The performance of the packed bed system will be affected by various design and operating factors, such as aspect ratio, particle size and shape, void fraction, and properties of both storage materials and HTF [102]. Therefore, those parameters need to be carefully considered during the designing procedure of the packed bed.

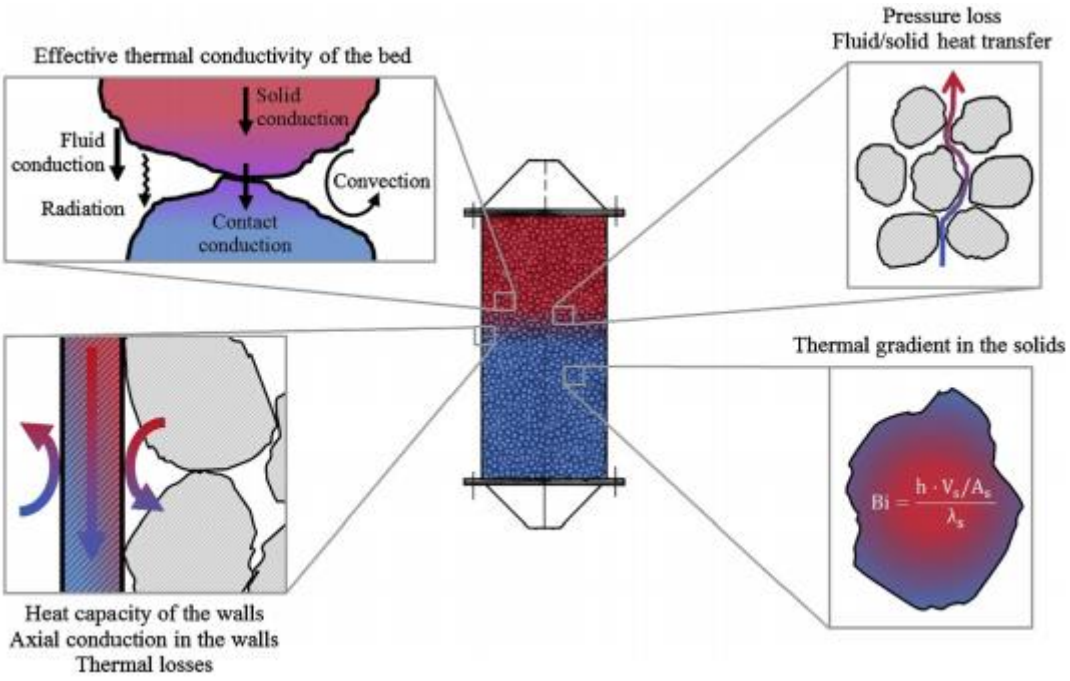


Figure 2.12: Schematic diagram of some physical phenomena involved in the packed bed storage system [110].

Colburn [111] studied heat transfer coefficients of air flowing through a packed bed filled with various sizes of granular materials, including porcelain balls, pebbles and zinc balls. It was found that the heat transfer coefficient was eight times higher than that of an empty tube, which depended primarily on the mass flow rate of the air and the ratio of the particle diameter to the tube diameter. Standish and Drinkwate [112] investigated the response of different shaped particles on the performance of the packed bed filled with glass balls, coke spheres, and ceramic rings with porosity between 0.41 and 0.59 and sphericity between 0.53 and 1.0. Air and water were used as the HTF, respectively. The study concluded that the pressure drop was strongly influenced by the pore spaces, and apart from the size of the storage material, its geometry also played an important role in the performance of the packed bed. Allen et al. [113] examined the effects of roughness, size distribution, packing arrangement and particle shape on pressure drop. In this study, three different packing arrangements were utilised, namely hexagonal closed, offset simple cubic and simple cubic with

various void fractions, where the simple cubic with a void fraction of 0.48 was found to have the minimum friction coefficient value. The friction coefficient increased with increasing roughness of the storage element, and the pressure drop performance of the packed bed was improved by two different sizes of storage elements. The packed beds with higher values of void fraction leads to a lesser pressure drop as well as a lower heat transfer. An optimum value of the void fraction, therefore, should be selected to obtain maximum heat transfer with minimum pressure loss [102].

The main benefit associated with the packed bed is thermal stratification, since it improves the efficiency of energy storge [104]. The physical significance of stratification was suggested by Phillips [114], and the results were presented in terms of a stratification coefficient, which was defined as the ratio of the actual useful energy gain to the energy gain at a uniform temperature. Figure 2.13 illustrates different levels of the temperature stratification within a packed bed device with the same stored heat: (a) highly stratified; (b) moderately stratified; (c) unstratified storage [115]. Ramana et al. [116] reported that the better stratification produced by a lower mass flow rate can improve the storage efficiency of the packed bed during the charging process. Lugolole et al. [117] demonstrated a comparison of the discharging performance of two packed beds with 10.5 mm and 31.9 mm granite rocks respectively at different flow rates. It was reported that the de-stratification is affected by the mass flow rate of the HTF and the equivalent diameter of the packing material. This study also observed an improvement in the stratification when the flow rate of HTF was reduced. Consequently, the thermal mixing between the flowing streams reduces as the flow rate decreases. Yang et al. [118] suggested that storage materials with a low thermal conductivity, complete charging of bed and adequate insulation of storage tank are some initiatives to maintain the stratification of the packed bed during the stationary period.

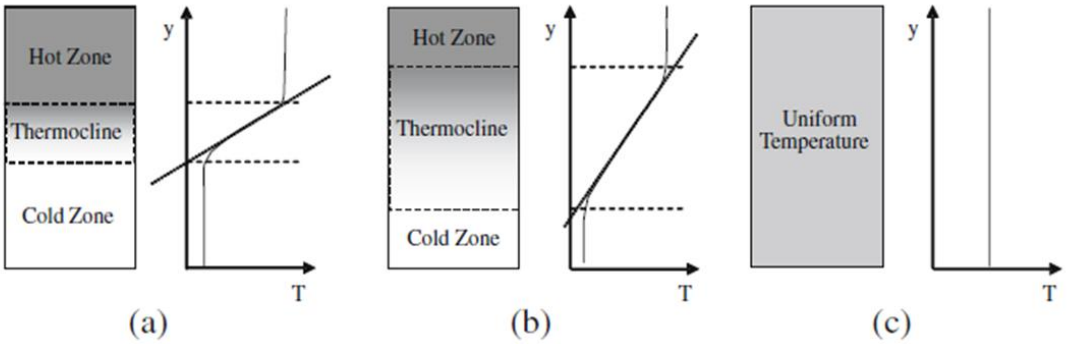


Figure 2.13: Schematic diagram of different degrees of stratification within a packed bed device with the same amount of stored thermal energy: (a) highly stratified; (b) moderately stratified; (c) unstratified storage [115].

Based on the reviewed studies, it is found that stratification is an essential feature for the effective utilisation of packed beds. It is affected by the internal wall material of the storage tank during the static condition. However, the axial heat conduction and the wall heat losses are the two dominant factors related to de-stratification in the packed bed storage system [102]. The stratification coefficient decreases with the increase of charging time, which is attributed to the increase of the temperature within the packed bed.

2.4.2 Shell-and-tube CTES device

The shell-and-tube based device is another commonly employed storage configuration in CTES applications; see Figure 2.14 for an illustration. From Figure 2.14, one can see that this storage unit operates according to the similar principle as a shell-and-tube heat exchanger, where the TES material fills the space between the shell and tube and the HTF flows through the tube. For systems using PCMs, heat is transferred to or from the PCMs through the tube walls. In addition, the melted PCM flows, leading to natural convection that enhances the overall heat transfer of the system. The heat transfer coefficient for a given HTF flow rate is highly determined by the number of tubes as well as

their diameter and length, and these parameters are also the most significant ones to be optimised via numerical simulations [41].

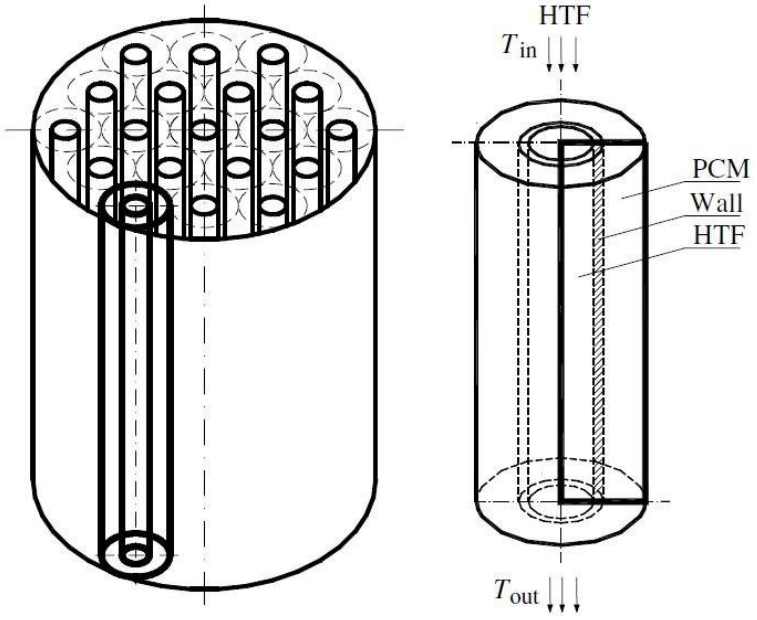


Figure 2.14: Schematic diagram of a shell and tube type CTES component.

Several studies on the shell-and-tube system have been conducted both numerically and experimentally. A shell-and-tube CTES designed for a low thrust cryogenic propulsion system was investigated numerically by Torras et al. [119] with a commercial software named TermoFluids. The numerical model was founded on the coupling of the three subroutines: 1) one-dimensional and transient resolution of the fluid flow inside the heat transfer tube; 2) two-dimensional and transient treatment of the heat conduction in solid tubes; 3) three-dimensional and transient resolution in the region occupied by the PCM. The simulation results were validated by an experimental cylindrical accumulator test facility using water as the PCM and operating in the temperature range of -195.0℃ to 7.74℃. Sang et al. [120] proposed a new efficient numerical approach to study the phase change processes of the full-scale vertical ice-on-coil type CTES [120]. In order to reduce the pressure drop,

the tubes were split into 8 channels, one of which consists of 92 tubes with a diameter of 12.75 mm. These copper tubes were arranged into a staggered matrix, and it was assumed that there was no thermal interaction between these tubes. The numerical model therefore was simplified to calculate the heat transfer of 92 hexagonal three-dimensional tubes by conveying the outlet conditions of one tube to the inlet conditions of the adjacent tube.

However, the heat transfer coefficient of a shell-and-tube system is limited due to limited heat transfer area. Enhanced heat transfer technologies are usually required, of which the use of finned tubes has been recommended as a simple and promising method [121]. Mosaffa et al. [122] numerically studied the solidification process of PCM in a shell-and-tube device with radial fins. The geometry of the device is shown in Figure 2.15. Calcium chloride hexahydrate ($CaCl_2 \cdot 6H_2O$) with a melting temperature of 29.7℃ was selected as the PCM and atmospheric air was chosen as the HTF to flow in the tube. The outer side was insulated to prevent heat loss. The effects of air velocity and inlet air temperature on the TES performance were investigated. Yamashita et al. [123] designed and experimented with a prototype finned tube CTES system to store and release the cold energy of liquefied natural gas (LNG) for the re-liquefaction of the boil-off gas (BOG). The vessel is made of stainless steel, and the fin tubes are made of aluminium. A 25 m^3 of n-pentane ($n\text{-}C_5H_{12}$) with a purity of 98.2%, whose freezing point is 143.55 K, is used as the PCM. The supports are used to stack the finned tubes, they can therefore be moved along the axial direction to release the thermal stress. During the charging process, the LNG flows through the tube to freeze the PCM outside the tube; during the discharging process, the PCM melts and converts the LNG/BOG two-phase flow into liquid LNG.

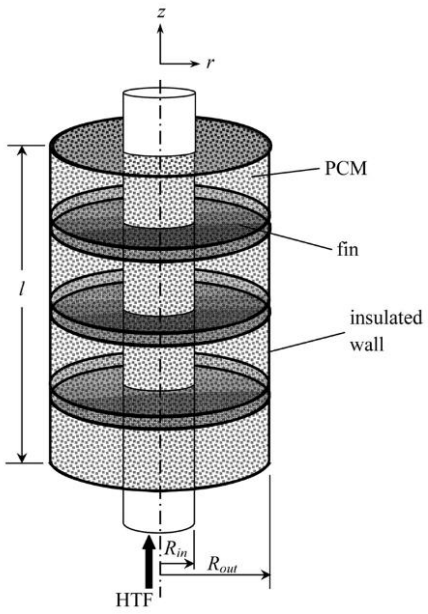


Figure 2.15: Schematic diagram of a shell and tube device with radial fins [122].

2.4.3 Applications of CTES technologies

CTES technologies in the sub-zero temperature ranges are already used or have the potential to be used in a wide range of applications where high-grade cold energy below 0℃ needs to be generated, utilised, and stored. For instance, refrigeration systems operating in the sub-zero temperature range, whether active or passive, are able to use CTES to improve efficiency, reduce energy consumption, and shift electrical loads. CTES also has a unique application in space exploration. Power storage systems that already employ CTES include LAES, PHES, and FES. The use of CTES in LAES has been commercially demonstrated, while PHES and FES equipped with CTES are in the prototype design stage. In addition, CTES can work with other energy systems for high-grade waste cold energy recovery to improve the performance of the entire system, such as the regasification process at LNG terminals.

2.4.3.1 Active refrigeration

Depending on whether the cold energy is generated in situ when it is required, refrigeration systems can be classified as active and passive refrigeration. In the active refrigeration system, the cold energy is actively generated by the refrigeration cycle. The use of PCM-based CTES in the active refrigeration system has been extensively studied [124-126]. In such applications, CTES units are usually located near/around the evaporator or between the refrigeration system and the refrigerated space. The temperature of the PCM should also be chosen carefully. A high PCT can lead to an increased coefficient of performance (COP) due to reduced compressor work and enhanced heat transfer from the evaporator, but also due to an increase in the air temperature inside the compartment [125].

In addition to domestic refrigerators, space exploration is another application where CTES has been used for active refrigeration. The NASA has designed and experimented with a CTES technology for space applications that employs PCM for the cooling and thermal management of temperature-sensitive sensors such as focal planes, optical components, reflectors, and telescopes, as shown in Figure 2.16 [127]. The PCM used in this application was 2-Methylpentane with 3% acetone, which has a PCT at -153℃. The results of ground and orbital experiments demonstrated that this technology significantly reduces the weight of the cooling system of the space infrared sensor by more than 100 times compared to its own weight, which is essential for a spacecraft since the weight reduction can lead to additional payload capacity or save millions of dollars in launch costs. The introduction of the CTES system compensated for the cooling load generated by the electrical and ambient heating during the operation of sensors, while the CTES unit also offered stricter temperature control as the

operating temperature can be maintained around the PCT. In addition, the CTES device can contribute to minimise vibrations of vibration-sensitive sensors by replacing refrigerators with moving mechanical components.

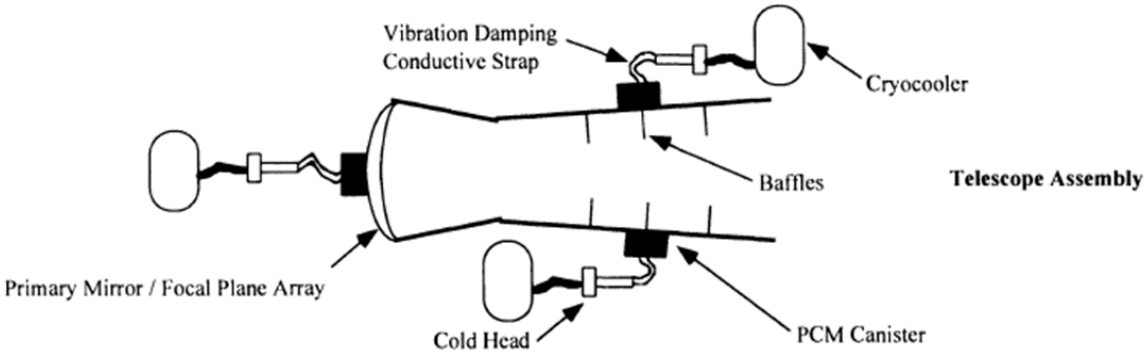


Figure 2.16: The use of CTES for cooling and thermal management of the space telescope assembly [127].

2.4.3.2 Electricity storage

Increasing the share of renewable energy, particularly solar and wind, in the energy mix is crucial for the future energy transition and climate mitigation. Power storage technologies can decouple the supply and demand of energy and address the intermittency of renewables, while supporting their integration into the grid. These technologies can also assist in securing grid balance and reducing peak load capacity [128]. Many concepts for power storage systems have been proposed or built so far, and CTES is a crucial part of some promising systems.

LAES is a technology that uses liquefied air as a storage medium (-196℃) to store and release energy [15, 128]. The working principle of a conventional LAES is shown in Figure 2.17 and comprises three major steps of operation [128]. Step 1 is the charging process, where excess (off-peak and cheap) electricity is used to liquefy the air. Step 2 is the storage process in which the liquefied air produced in Step 1 is placed in an insulated tank at nearly ambient pressure. Step 3 is the discharging process,

which recovers energy by pumping, reheating, and expanding in order to regenerate power during peak hours when demand for electricity is high and expensive. In the storage step, the heat from the air compression process in Step 1 and the high-grade cold energy during the reheating process in Step 3 can also be applied to increase the power output and decrease the energy consumption of the liquefaction process. In the first LAES pilot plant, a pack-bed CTES device was employed to store the cold energy being released during the discharging process of the LAES [28]. Sciacovelli et al. [15] proposed that the high-grade cold energy recovery is critical to achieve maximum performance in the LAES plant. This study indicated that both round-trip efficiency and liquid yield are greatly benefited by the increased cold recycle: an increase in cold recycle of 16% results in a 20% increase in the round-trip efficiency and a 30% improvement in the liquid yield.

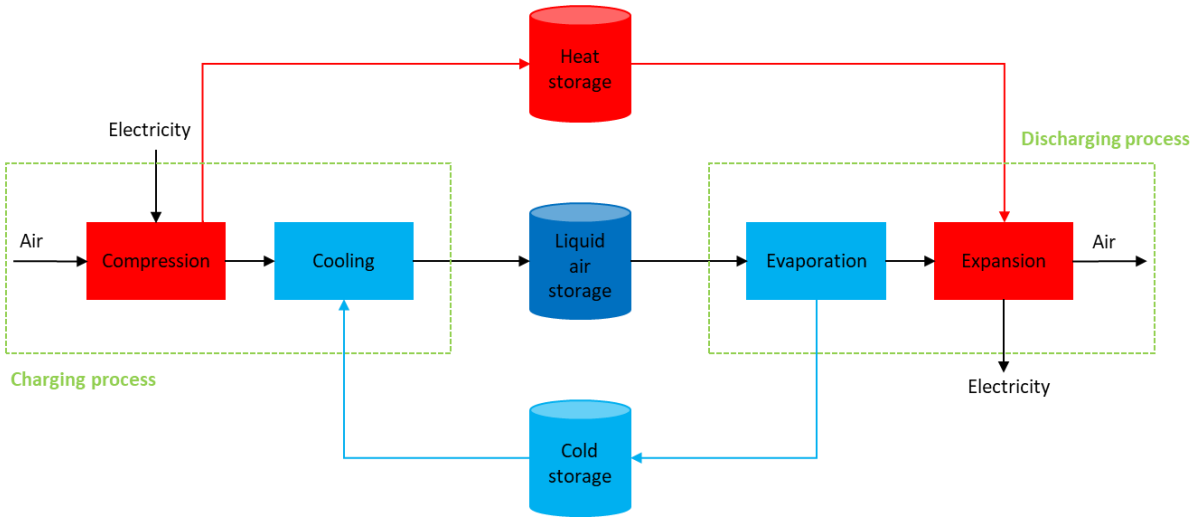


Figure 2.17: Schematic diagram of LAES technology [128].

2.4.3.3 High-grade waste cold energy recovery

Some energy processes operating in sub-zero temperature ranges, such as the regasification of LNG, produce high-grade cold energy that can be captured by CTES for subsequent reuse. CTES

implemented in association with such energy systems can improve the overall efficiency, reduce the energy consumption, and smooth out fluctuations in energy supply.

LNG plays an important role in the global energy structure of many countries globally, particularly in Europe and Asia [2]. Various systems have been proposed to recover the cold energy of the rapidly growing LNG, which is often wasted in the regasification process [129,130]. However, the daily and seasonal LNG demand at the terminal fluctuates due to changes in electricity and city gas demand, making it more difficult to utilise the cold energy directly. CTES can be used to smooth out fluctuations in cold energy supply and make effectively use of LNG cold energy [123]. Despite the enormous potential, the use of CTES for LNG cold recovery is rarely mentioned.

A BOG re-liquefaction facility with a CTES system has been installed at Senboku Terminal II of Osaka Gas [131-134]. Instead of compressing the BOG directly to high pressure, the system pressurises the BOG to 0.8 MPa and mixes it with the LNG stream. During the daytime operation, the LNG flow rate is high enough that the cold energy from the LNG is sufficient to re-liquefy the BOG at that pressure. The additional cold energy is stored in the CTES system, which contains a PCM that freezes at -130℃. During the night-time operation, the LNG flow rate is not adequate to re-liquefy the BOG in the LNG/BOG two-phase flow and the CTES releases cold energy for the re-liquefaction of the BOG. In an analysis carried out by Ito et al. [134], the use of a CTES system resulted in a 30-60% reduction in the compression power compared to the traditional method of compressing the BOG for re-liquefaction. In addition to the BOG re-liquefication, He et al. [129] proposed the concept of using PCM to store cold energy from LNG and subsequently use it for other purposes. As shown in Figure 2.18, PCM can be used for distribution for cooling purposes, while air or carbon dioxide is suitable

for power generation. More systems using CTES to recover cold energy from LNG are worth investigating.

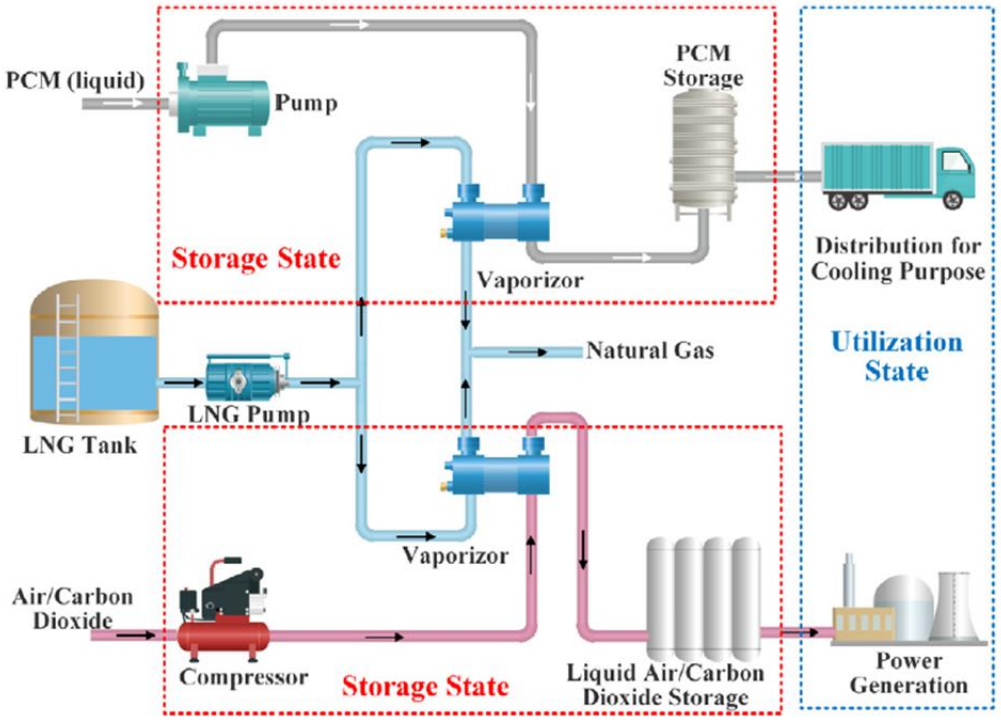


Figure 2.18: Cold energy storage system for LNG cold energy utilisation [129].

2.5 Summary

As an important category of energy storage technologies, TES has gained significant attention in recent years. Depending on the energy storage medium used, TES technologies can be subdivided into sensible heat storage (SHS), latent heat storage (LHS), and thermochemical energy storage (TCES).

For CTES applications, SHS and LHS materials are reviewed according to their operating temperatures, and CTES based devices are also reviewed. The packed bed system with solid SHS materials is a commonly used method for cold energy storage. Although there are suggestions to use liquid SHS materials as both energy storage medium and HTF, more suitable candidates still need to

be validated experimentally. Besides, different types of sub-zero LHS materials, including inorganic PCMs, organic PCMs, eutectic PCMs and commercial PCMs, are discussed according to their advantages and disadvantages. Existing PCM studies have been mainly focused on properties and mechanisms in the ambient or sub-zero temperature ranges, few studies have been conducted on the deep cryogenic temperature range, e.g., below -100℃. Under the condition that only the phase transition temperature is considered, the appropriate cryogenic PCMs can be alkanes containing shorter carbon chains and their eutectic mixtures. This study is therefore focused on screening suitable CTES candidates for the deep cryogenic temperature range, and on characterising and optimising their thermal performance (See Chapter 4).

The development of CTES materials usually involves two important steps for a given application. The first step is to understand the thermophysical properties of the material at its working temperature range. Correspondingly, several thermal analysis techniques and methods are compared for the PCMs. Considering the flammable characteristics of organic PCMs, the determination of flammability limits is analysed both theoretically and experimentally. The second step is to design a suitable CTES device or component based on the thermophysical properties of the material. Two commonly used CTES devices are reviewed, namely the packed bed for SHS materials and the shell-and-tube for PCMs. Besides, some applications of CTES technologies are also briefly reviewed for different sub-zero temperature ranges, including active refrigeration, electricity storage and high-grade waste cold energy recovery. This work aims to develop a high-grade cold energy storage technology and a system for the application of CTES materials, which will be discussed in Chapter 5 and Chapter 6.

CHAPTER 3

MATERIALS AND METHODOLOGIES

This chapter explains the methodology used in this study including both experimental and theoretical aspects. Section 3.1 provides information on the chemicals used and material preparation procedures. Section 3.2 presents the thermophysical characterisation techniques as well as associated instruments. Section 3.3 explains the details of mathematical models, analysis principles and parameters.

3.1 Materials

3.1.1 SHS materials

The basic description and supplier information of the SHS materials studied in this work are listed in Table 3.1. The Dorset gold and Brittany bronze gravels are natural quartzites that are mainly composed of silica (~99.08%) and alumina (~0.274%), and the average diameter of these materials is around 2-5 mm. Borosilicate glass beads (containing ~81% SiO_2 and ~13% B_2O_3) with a diameter of 2.9-3.5 mm were purchased from Sigmund Lindner.

Table 3.1: Basic information of SHS materials.

Material	Ingredient	Size (mm)	Supplier
Dorset gold	Quartzite	2-5	Long Rake Spar Ltd
Brittany bronze	Quartzite	2-5	Long Rake Spar Ltd
Glass bead	Borosilicate	2.9-3.5	Sigmund Lindner GmbH

3.1.2 Chemicals

Table 3.2 presents the chemicals used in the experiments and measurements, particularly organic PCMs and additives. More information associated with the cryogenic PCM screening will be detailed in Chapter 4. The additives used in this study are thermal conductivity enhancer, thickeners and fire retardants. The expanded graphite powder (EG) with an average particle size of the 20 μm was used as the thermal conductivity enhancer. Two thickeners were compared: 1) fumed silica after-treated with dimethyldichlorosilane (hydrophobic SiO_2 with an average particle size of 16 nm); 2) styrene-ethylene-butylene-styrene (SEBS). In addition, the fumed hydrophobic SiO_2 was also investigated as

a fire retardant to compare its effectiveness with tris (2-chloroethyl) phosphate (TCEP) in reducing the flammability of selected PCMs.

Table 3.2: Basic information of chemicals used in this study.

	Material	Purity (%)	Formula	CAS Number	Supplier
Organic PCMs	1-Hexene	98	C_6H_{12}	592-41-6	Alfa Aesar
	2-Methylbutane	99	C_5H_{12}	78-78-4	Sigma-Aldrich
	3-Methylpentane	99	C_6H_{14}	96-14-0	Alfa Aesar
Additives	Expanded graphite powder	97	-	-	SGL Carbon
	SEBS	-	-	-	SINOPEI
	Fumed silica	99.8	SiO_2	11297-52-5	Evonik
	TCEP	97	$C_6H_{12}Cl_3O_4P$	115-96-8	Sigma-Aldrich

3.1.3 Preparation of modified PCM

The procedure for preparation of the modified PCM is shown in Figure 3.1. Firstly, the EG was weighted and homogenously mixed into the 1-Hexene solution at ambient temperature. The thickening agent was then added slowly while stirring gently with a glass stick to avoid the formation of large agglomerates in the solution. The last step was to place the beaker in the ultrasonic bath for 15 to 20 minutes, and the dispersion of the solution was observed at all times. Simultaneously, the temperature of the ultrasonic bath was controlled at 20℃ to prevent evaporation of PCM at high temperatures.

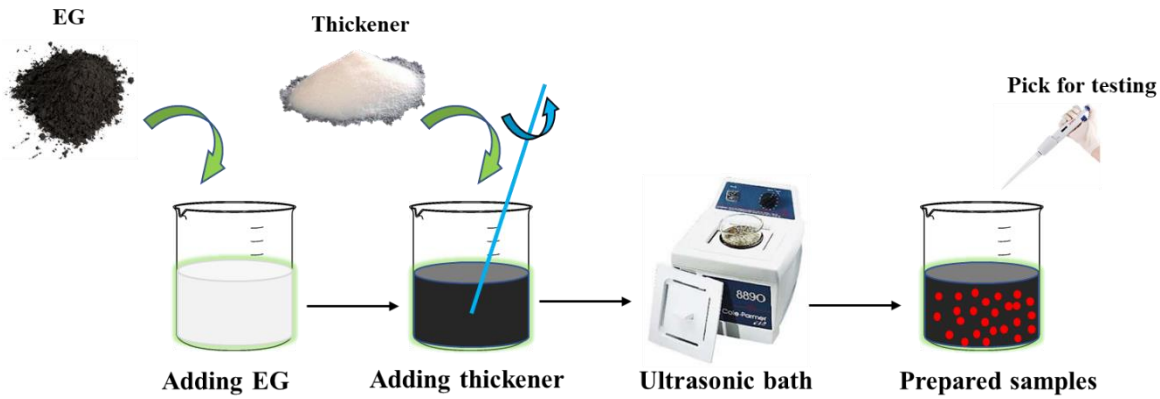


Figure 3.1: The preparation procedure of modified PCM.

3.2 Characterisation techniques

To characterise and analyse thermophysical properties of CTES materials, various techniques were used in this study. Each experiment was performed multiple times to minimize bias errors. The following section describes the detailed experimental operating procedures and operating conditions of the instruments.

3.2.1 Differential scanning calorimetry (DSC)

DSC is a widely used thermal analytical method to determine the thermophysical properties, including phase transition temperature, enthalpy, and specific heat capacity. The principle of this technique is that when a sample undergoes a phase transition, such as liquid to solid, the amount of heat flux that maintains the sample at a pre-set temperature can differ from that for a reference sample. The temperatures of both the sample and reference (see Figure 3.2 (b)) are controlled practically to the same value throughout the entire measurement. The energy absorbed or released by the sample will present as an endothermic peak or exothermic peak, corresponding to the melting or solidification of the sample during the measurement process, respectively, as shown in Figure 3.2 (e). The phase change enthalpy of the melting process, also known as heat of fusion, is considered as the latent heat

of the sample by integrating the melting peak. In addition, for pure or eutectic substances where the phase change curve only shows a single symmetry peak, the onset temperature is more representative of their phase transition temperature than the peak temperature. This is because the peak value varies with the heating rate of the measurement procedure or the measured sample weight, but the intersection of the tangents to the peak, referred to as the onset temperature, is maintained unchanged [135]. Therefore, the onset temperature is served as the phase transition temperature of the sample in this study.

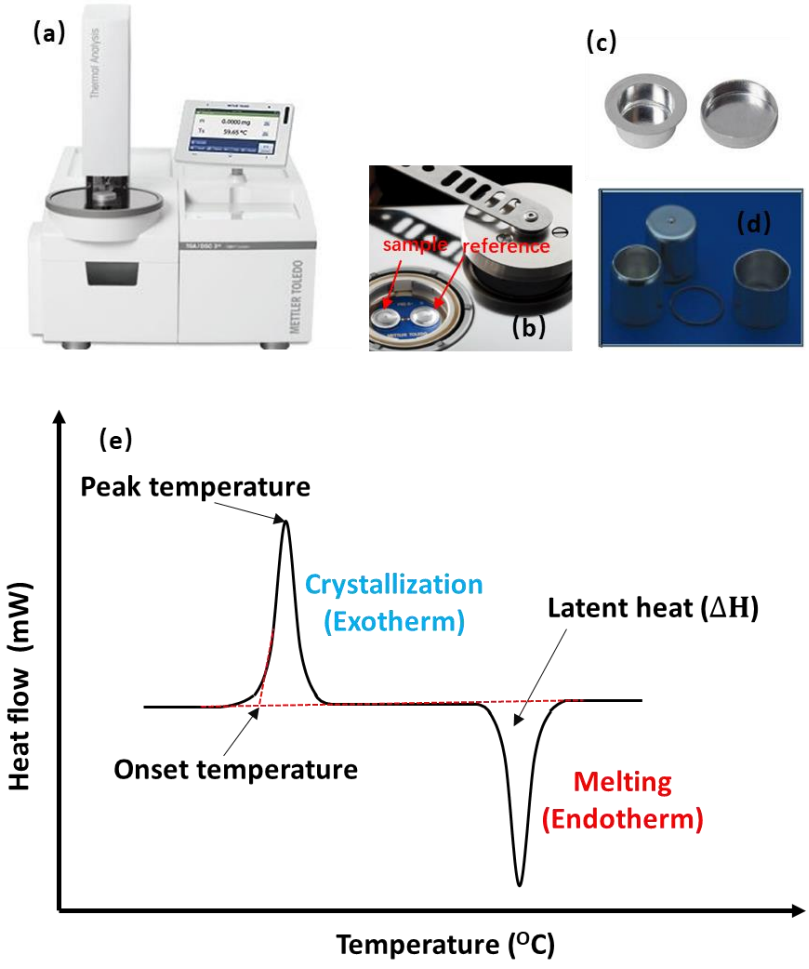


Figure 3.2: (a): Mettler Toledo DSC3+ instrument; (b): Furnace inside of the DSC instrument that contains both sample and reference; (c): 100 μL aluminium crucible; (d) 120 μL stainless steel medium-pressure crucibles; (e) A typical DSC curve of phase transition process.

In this study, the DSC was used to obtain the specific heat capacity of SHS materials and the phase transition temperature and enthalpy of cryogenic LHS candidates.

3.2.1.1 Specific heat capacity

The Mettler Toledo DSC was used in this work to determine the specific heat capacity of SHS materials with sapphire as a standard (standard DIN 51007). This method needs to perform blank, sapphire, and sample measurements under identical procedures and experimental conditions. By comparing with the known $C_{p,s}$ of the sapphire standard, the $C_{p,m}$ of the sample can be calculated by the following equation:

$$C_{p,m} = \frac{Q_m \cdot m_s}{Q_s \cdot m_m} \cdot C_{p,s} \tag{3.1}$$

where Q_m and Q_s are respectively the heat flux of the sample and sapphire, and m_m and m_s are the mass of the sample and sapphire, respectively.

The specific heat capacity measured in this work was performed at a constant pressure with a cooling rate of 5 ℃/min. The system was cooled from 20℃ to -40℃ and then the temperature was held at -40℃ for 10 minutes to stabilize the system. Afterwards, the same rate was applied to heat up the system back to the initial temperature. Since the shape of the SHS material is irregular, the measurement used a 100 μL aluminium crucible to load the sample with a mass of approximately 40 mg; see Figure 3.2 (c). Each sample was measured three times under the same test procedure to obtain the average specific heat value.

3.2.1.2 Phase transition temperature and enthalpy

The Mettler Toledo DSC was also employed to measure the phase transition temperature and enthalpy of LHS materials. The operating temperature range of this instrument can reach -170℃ by coupling with a LN_2 cooling device. The system was started cooling from -110℃ to -165℃ with the rate of 1 ℃/min, and from -130℃ to -170℃ with the rate of 0.5 ℃/min, respectively. Then the temperature was held at -165℃/-170℃ for 30 minutes for system stabilisation. Following this, the same rate was applied to heat up the system back to the initial temperature. Because the light hydrocarbons are easy to volatilize at room temperature, the 120 μL stainless steel medium-pressure crucibles were used to hold the PCM sample with a mass of approximately 30 mg, which has a Viton O-ring to prevent the sample from evaporating; see Figure 3.2 (d).

3.2.2 Temperature-history measurement

In order to eliminate the effect of the size and geometry of the test sample on its thermal properties, the temperature-history (T-history) measurement method with the bulk material was performed to obtain more reliable thermal performance data, which are close to practical applications. Figure 3.3 (a) shows the major components of a T-history measurement device, including computer, data logger, thermocouple, and sample holder. Figure 3.3 (b) shows the experimental setup for the T-history measurement. The cylindrical sample holder is composed of three concentric cylinders with different diameters. As a support structure for the test rig, the inner and outer walls of the outer cylinder are attached with thermal insulation materials to isolate the direct contact between the sample holder and the environment, thereby minimising heat leakage. The lowest isothermal temperature for the cooling process is -196℃ provided by LN_2 placing in the middle cylinder, and this chamber is also used for

heat exchange between the frozen sample and the environment during the heating process. The liquid PCM sample is placed inside the inner cylinder with a volume of 100-150 mL. The inner cylinder lid can be tightened to avoid sample evaporation during the measurement process.

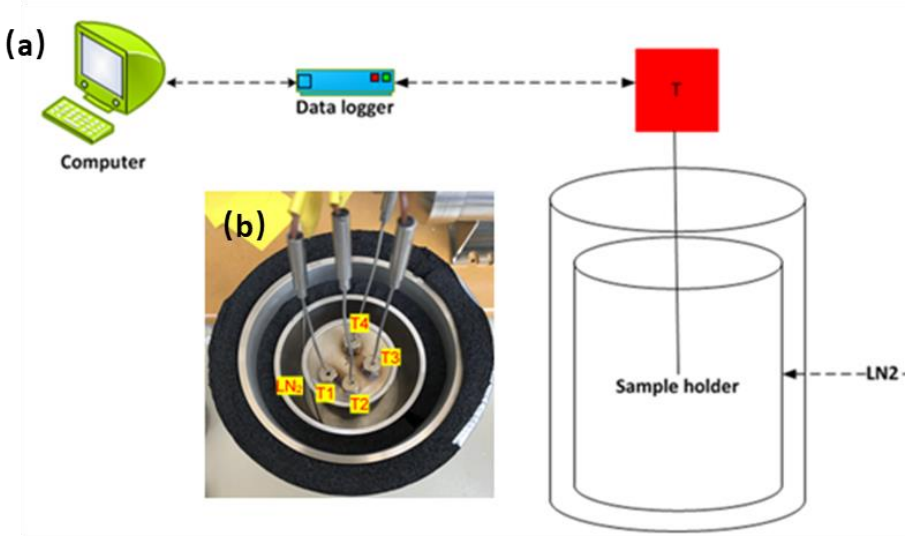


Figure 3.3:(a) Schematic diagram of the test rig configuration for T-history measurement; (b): The setup of the T-history experiment (LN_2 will be held in the middle layer. Thermocouples T_1-T_4 were placed at the same level but at different positions to the centre of the sample cylinder).

In addition, four compression glands are welded onto the surface of the lid to fix the Type T thermocouples, which are labelled as T_1, T_2, T_3, and T_4, respectively, and have an accuracy of $\pm$0.5℃. These thermocouples are located at different distances from the inner wall of the inner cylinder, which are 0.5 cm, 1 cm, 1.5 cm, and 2 cm, respectively, but the depth of their immersion into the sample remains the same. Besides, T_0 is placed in the middle cylinder to record the temperature of LN_2 (cooling process) or the ambient temperature around the inner cylinder as the measurement reference temperature (heating process). During the test, the temperature changes of the sample are recorded by a data logger every 5 s, and the T-history profile of the sample is displayed on the PC for in-situ monitoring purpose.

3.2.3 Thermal conductivity

3.2.3.1 Laser flash apparatus (LFA)

The thermal conductivity measurements of the SHS materials were carried out by using a NETZSCH LFA 427 system; see Figure 3.4. The measurement program initiated from 20℃, and three individual laser shots were conducted for each temperature to improve accuracy until the system temperature approached -40℃. The solid SHS samples were stacked in the Pt/Rh holder with a diameter of 12.7 mm and a thickness of 0.505 mm. At the same time, the graphite coating for both the front and rear surfaces of the sample holder was required to achieve uniform heat entry and departure in the sample preparation step. By using Equations (2.13) and (2.14) as discussed in the literature review, the thermal diffusivity and conductivity can be obtained by using the Proteus® software, which also provides comprehensive correction models to increase the accuracy of the results obtained.

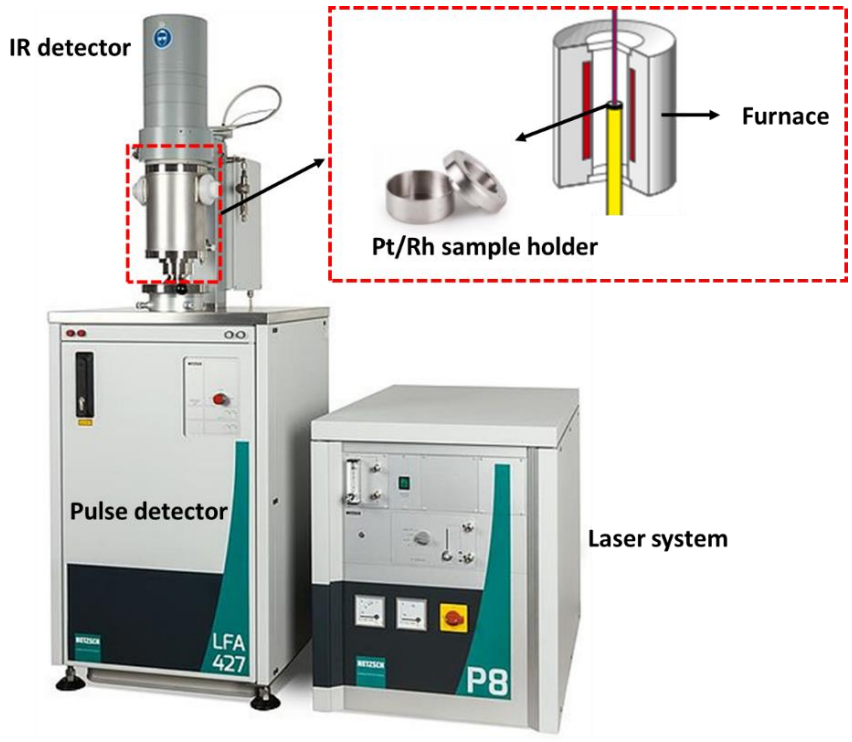


Figure 3.4: Schematic diagram of NETZSCH LFA 427 instrument with Pt/Rh sample holder.

3.2.3.2 Transient hot bridge (THB)

A Transient Hot Bridge (THB)-500 instrument (see Figure 3.5 (a)) was used for the thermal conductivity measurements of PCMs. Such a device is based on the transient strip method, as shown in Figure 3.5 (b), which uses a strip-shaped conductor that serves as a heat source and a temperature sensor. During the measurements, the THB sensor emits a constant heat flow, which causes the temperature to rise over time, providing the heat transfer characteristics of the sample.

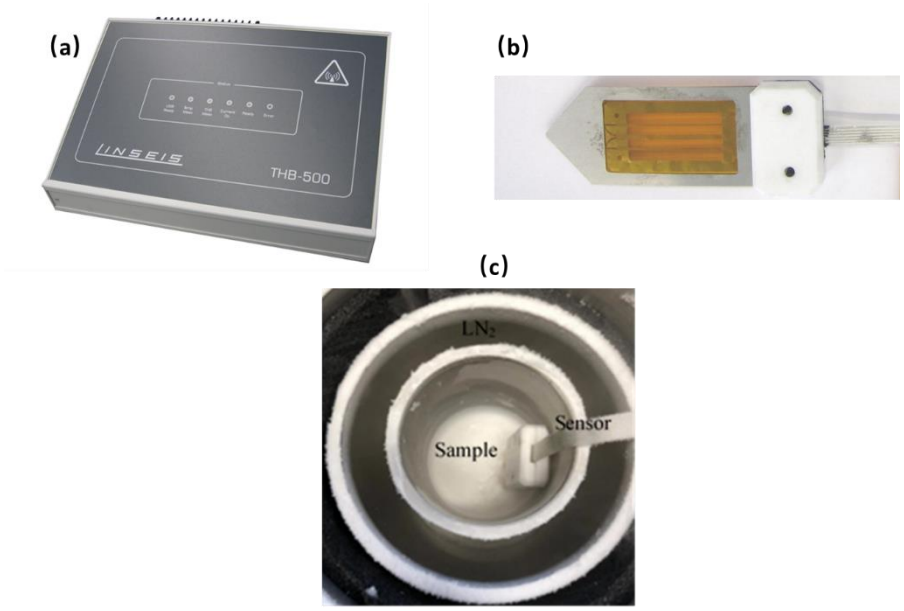


Figure 3.5: (a) Linseis THB-500 instrument; (b) low temperature THB sensor; (c) schematic diagram of the thermal conductivity measurement procedure (The sample was placed into the inner cylinder of the sample holder, and the measurement circuit of the sensor was entirely submerged by the sample. The outer cylinder is filled with LN_2 to cool down the sample).

Three steps were included in a typical experimental procedure; see Figure 3.5 (c). Firstly, a 100 mL liquid PCM sample was loaded into the inner cylinder and the position of the THB sensor was adjusted so that its measuring circuit can be completely submerged by the sample. LN_2 was then introduced into the middle cylinder of the test rig to cool the sample down to below its phase

transition temperature. The measurement began once the sample was fully frozen. The data of both thermal diffusivity and thermal conductivity corresponding to the change of temperature were recorded continuously during the sample melting process. Three tests for each sample were carried out to obtain repeatable results.

In order to reduce the uncertainty of the THB sensor caused by the significant change of the sample temperature in a short time, the raw data were processed to remove unreasonable measurement points by following some temperature and heat transfer assumptions:

(1) The ambient temperature remains constant at 25℃ during all measurements, which is broadly correct in our lab.
(2) The influence of natural convection is not considered within materials on the result, and the temperature of the sample varies uniformly during the heating process.
(3) The main factor affecting the heat transfer between the frozen sample and the ambient is the temperature difference between the PCM and the environment, and other factors are neglected here.

3.2.4 Infrared microscopy (IR)

Infrared microscopy (IR) is a non-destructive technique that allows materials with covalent bonds to be identified by infrared spectrum. When the frequency of the infrared spectrum is the same as vibrational frequency of the bond, it can be detected due to the absorption of the infrared spectrum. According to the spectra obtained by scanning the entire wavelength range, the sample can be determined from the database as each material has its own specific spectra. In this work, the infrared microscopy (Bruker, LUMOS) allows observation by scanning the surface of the sample with a high

spatial resolution. It can perform point, line, or map scans on the surface.

There is a sample stage which can be used to position the sample and can be adjusted to focus on the surface. The detector must be cleaned before each test as there may be previous sample contamination on the detector. A low pressure was applied when the detector is in contact with the sample. A blank measurement was conducted to remove noise from background. In this work, each spectrum was scanned 64 times to obtain an average value.

3.2.5 Volume expansion coefficient

A 10 mL graduated cylinder with an accuracy of ± 0.2 mL was used to determine the volume expansion coefficient of the low temperature organic candidates during the phase change from liquid to solid. The graduated cylinder with a liquid sample was immerged in the LN_2 bath to induce the phase transition of the material. The reduction in the sample volume between the liquid and solid phase was then recorded. Thus, the volume expansion coefficient (volume %) can be expressed as:

$$\partial = \frac{V_r}{V_i} \times 100 \tag{3.2}$$

where, V_i is the initial volume of the PCM in the liquid phase; and V_r stands for the volume change of the PCM that undergoes the liquid to the solid phase transition.

3.2.6 Thermal cycling performance

The thermal cycling test was conducted to understand the performance of materials after a long-term continuous operation and to determine whether these repeated thermal cycles would lead to degradation or phase separation of materials. The measurement has two steps: 1) Thermal cycling

experiments based on the small test rig for T-history measurements; 2) DSC measurements of the cycled sample as a function of cycling times. In one cycle, the material should first be completely frozen by LN_2 and then heated to the end of the phase transition at the ambient temperature. After every 25 cycles, a small quantity of material was taken out to perform the DSC measurement. The DSC measurement procedure used a cooling/heating rate of 0.5 ℃/min and a temperature range of -130℃ to -170℃. By comparing the DSC results before and after the thermal cycling tests, the thermal stability of materials was analysed, and the feasibility of the long-term operation was evaluated.

3.2.7 Flammability limits (FLs)

An OZM FRTA-I instrument was used to determine both the lower flammability limit (LFL) and upper flammability limit (UFL of the target PCMs); see Figure 3.6 for a photograph of the device. It operates on high voltage electrical ignition (15 kV/30 mA), allowing the operator to observe the flame propagation phenomenon through the viewing glass door. It consists of a spherical glass pressure test vessel of 5 L internal volume placed inside a stainless steel oven. The test vessel is equipped with a temperature sensor and a pressure transducer to monitor respectively the gas temperature and pressure. There are two touch panels on the front of the oven. One is for the control and display of the temperature value inside the oven, and the other serves to display the atmospheric pressure and the pressure inside the vessel and to control and configure the ignition device. The speed of the egg-shaped magnetic stirrer can be adjusted from 400 to 1200 rpm.



Figure 3.6: OZM FRTA-I instrument: 1. 5 L test vessel; 2. Magnetic stirrer; 3. Magnetic stirrer speed control button; 4. Temperature control panel; 5. High voltage key-switch; 6. Operation control panel; 7. Testing assemblies.

As reviewed from the literature, different criteria have been proposed to evaluate FLs of various materials [87-89]. In general, an accurate FL value would attain by adopting the concept of both visual criteria and pressure criteria. As stated in the European standard EN 1839 [87], visual and pressure criteria are used to determine whether a PCM is flammable:

a) Flame detachment: an upward movement of the detached flame from the spark igniter is at least 100 mm.

b) Pressure increase: the final pressure in the test vessel is 5% above the initial value.

According to the experimental results, the lower and upper concentration limits of flammability (volume %) can be calculated by using the following equations:

$$LFL = \frac{(L_V)(d)(T)}{(MW)(P)} \times \frac{(V_0)(P_0)}{(V)(T_0)} \times 100 \tag{3.3}$$

$$L_V = \frac{1}{2}(L_1 + L_2) \tag{3.4}$$

$$UFL = \frac{(U_V)(d)(T)}{(MW)(P)} \times \frac{(V_0)(P_0)}{(V)(T_0)} \times 100 \tag{3.5}$$

$$U_V = \frac{1}{2}(U_1 + U_2) \tag{3.6}$$

where L_1 is the minimum sample quantity (cm^3) that gives flame propagation, and L_2 is the minimum sample quantity that does not incur flame propagation; U_1 is the maximum sample quantity in which flame propagation can occur, and U_2 is the maximum sample quantity in which no flame propagation occurs; d and MW are the sample density (g/cm^3) and molecular weight (g/mol), respectively; and T and P stand for the test temperature (K) and pressure (kPa), respectively. The rest parameters are constants: the volume of test vessel (V) = 5 L, the standard molar volume (V_0) = 22.4 L, the standard temperature (T_0) = 273 K, and the standard pressure (P_0) = 101.3 kPa.

3.3 Mathematical modelling of LHCS tank

A one-dimensional transient tube model with cylindrical fins was developed to investigate the effect of different parameters including fin length, thickness, gap, and material on the heat transfer between the HTF and the PCM in the LHCS tank in the MATLAB environment.

3.3.1 Geometric model

Figure 3.7 shows the geometric model of the tube with cylindrical shape fins. The heat transfer involves several steps: from cylindrical fins to the PCM, from tube wall to the PCM and within the tube. Heat transfer rate through the cylindrical fins (q_f) has been intensively studied [136-138]. It can

be expressed in terms of the known heat transfer coefficient (h_{PCM}) of the external PCM and its temperature (T_∞); see Equation 3.7 below:

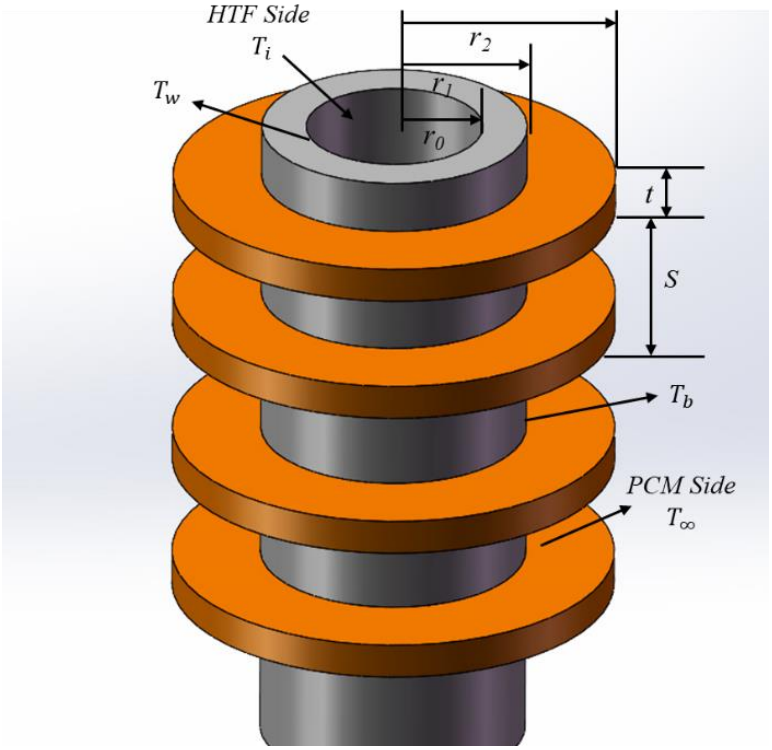


Figure 3.7: Schematic diagram of the geometric model of the tube with cylindrical shape fins.

$$q_f = h_{PCM} A_t \left[1 - \frac{NA_f}{A_t}\left(1 - \eta_f\right)\right](T_b - T_\infty) \tag{3.7}$$

where N is the number of fins; A_t is the total surface area; A_f is the surface area of one fin; and η_f is the fin efficiency which can be calculated using the following Equation 3.8 to 3.12:

$$\eta_f = C\frac{K_1(mr_1).I_1(mr_{2c}) - I_1(mr_1).K_1(mr_{2c})}{I_0(mr_1).K_1(mr_{2c}) + K_0(mr_1).I_1(mr_{2c})} \tag{3.8}$$

$$C = \frac{2r_1/m}{r_{2c}^2 - r_1^2} \tag{3.9}$$

$$m = \sqrt{\frac{2h}{kt}} \tag{3.10}$$

$$A_f = 2\pi(r_{2c}^2 - r_1^2) \tag{3.11}$$

$$r_{2c} = r_2 + \frac{t}{2} \tag{3.12}$$

where I_0 and K_0 are modified, zero-order Bessel functions of the first and second kinds, respectively; and I_1 and K_1 are modified, first order Bessel functions of the first and second kinds, respectively, which can be calculated using Table A.1 in the Appendix; k and t are respectively the thermal conductivity and thickness of the fins; and r_1 and r_2 are the base and tip radiuses of the fins, respectively.

Since the one-dimensional model only considers the heat transfer from the fins to the surrounding PCM, it ignores the heat transfer in areas without fins. The heat transfer rate from the inner fluid to the inner tube surface (q_i) and the heat transfer rate from the inner surface to the outer surface (q_w) can be calculated by the following Equations 3.13 and 3.14, respectively:

$$q_i = 2\pi r_0 L h_{TP}(T_i - T_w) \tag{3.13}$$

$$q_w = \frac{2\pi kL}{ln\left(\frac{r_2}{r_1}\right)}(T_w - T_b) \tag{3.14}$$

where h_{TP} is two-phase flow heat transfer coefficient during boiling/condensation of LN_2; L and k are respectively the tube length and thermal conductivity; r_0 is the inner radius of the tube; T_w is the temperature of the inner tube surface; and T_b is the temperature of the outer tube surface. The energy balance of the heat transfer between the HTF and the PCM through all parts (from the fluid to the tube inner surface, from inner surface to the outer surface and from the outer surface to the fin) is considered to be equal, giving the following equilibrium Equations:

$$q_f = q_i \tag{3.15}$$

$$q_f = q_w \tag{3.16}$$

Therefore, the heat transfer coefficient at boiling/condensation of LN_2 needs to be calculated to obtain the effect of the geometric model on the heat transfer rate in order to determine the appropriate configuration of the LHCS tank.

3.3.2 Boiling heat transfer coefficient

There are several approaches to calculate the boiling flow heat transfer coefficient such as Shah [139, 140], Chen [141], Kandlikar [142] and other correlations [143-146]. Among these correlations, the Chen correlation works fairly well with both horizontal and vertical tubes, but its accuracy is significantly less than the Shah and the Kandlikar correlations. For LN_2, it can be seen that the Shah correlation is in good agreement with the measured data, while the Kandlikar correlation is over-predicted [146, 147]. Therefore, the Shah correlation was used in this model, and the boiling flow heat transfer coefficient can be calculated as follows:

$$h_{TP} = F_o h_{LO} \tag{3.17}$$

where h_{LO} is the liquid only heat transfer coefficient and can be calculated using Equation 3.18; F_o is the enhancement factor due to the two-phase flow and is calculated using Equation 3.19.

$$h_{LO} = 0.023 Re^{0.8} Pr^{0.4} \frac{k_l}{d} \tag{3.18}$$

$$F_o = F_{cb}(1 - x) \tag{3.19}$$

where x is the vapour quality; and F_{cb} is the convection boiling factor. For pure convection boiling that occurs at high vapour qualities, and low boiling numbers, the convection boiling factor defined as:

$$F_{cb} = 1.8\, Co^{-0.8} \quad for \quad Co < 1.0 \tag{3.20}$$

$$F_{cb} = 1 + 0.8\, Exp[1 - (Co)^{0.5}] \quad for \quad Co > 1.0 \tag{3.21}$$

where Co is the convection number and can be defined as:

$$Co = K_{FR}\left(\frac{1-x}{x}\right)^{0.8}\left(\frac{\rho_g}{\rho_l}\right)^{0.5} \tag{3.22}$$

The Froude number (Fr_L) is given in Equation 3.23 to determine whether stratification effects due to gravity are important. $Fr_L > 0.04$ indicates that stratification effects are negligible and inertial forces are dominant compared with gravitational forces.

$$Fr_L = \frac{G^2}{g\rho_l^2 d} \tag{3.23}$$

where G is the mass flux, ρ_l is the liquid phase density of LN_2 and d is the inner diameter of the tube. A correction factor (K_{FR}) is used for low Froude number ($Fr_L < 0.04$) and expressed as:

$$\begin{cases} K_{FR} = (25Fr_L)^{-0.3} & Fr_L < 0.04 \\ K_{FR} = 1 & Fr_L > 0.04 \end{cases} \tag{3.24}$$

3.3.3 Condensation heat transfer coefficient

To validate the effect of the geometric model derived from the LN_2 boiling process on the N_2 condensation, particularly in terms of the condensation flow heat transfer coefficient and the condensation rate, the N_2 condensation model was proposed based on different flow regimes of the two-phase flow in a vertical tube, as illustrated in Figure 3.8 [148]. In this condensation model, mainly annular, slug and bubble flows are considered. The study of two-phase condensing flows in a vertical tube has produced different methods to predict the condensation heat transfer coefficient, including the use or development of semi-empirical correlations [149-153]. However, these methods have only been validated for specific flow configurations and relatively narrow ranges of operating

conditions.

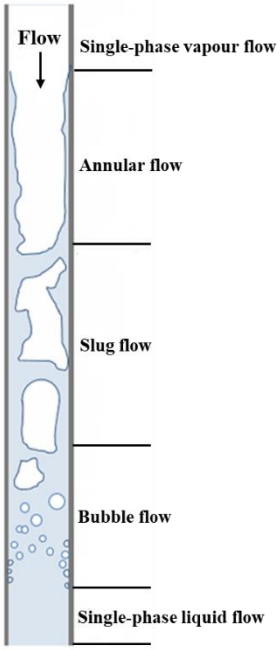


Figure 3.8: Two-phase flow regimes in a vertical tube [148].

This model adopted two correlations proposed by Kim [154], one for predominantly annular flow, and the second for slug and bubble flows, which show excellent predictive capability in a consolidated database consisting of 4045 condensation points, with an overall mean absolute error of 16% [149, 155, 156]. The condensation flow heat transfer coefficient for annular flow ($\hbar_{ann}$) can be calculated as follows:

$$\hbar_{ann} = 0.048 Re_l^{0.69} Pr_l^{0.34} \frac{\emptyset_g}{X_{tt}} \frac{k_l}{D_h} \qquad for \;\; We^* > 7X_{tt}^{0.2} \tag{3.25}$$

where D_h is the hydraulic diameter and is equal to the inner diameter of the tube (d); Pr_l is the Prandtl number, which can be expressed by Equation 3.26; Re is the Reynolds number defined according to different vapour qualities (x) as shown in Equations 3.27 to 3.29; $\emptyset_g$ and X_{tt} are the two-phase pressure drop multiplier [157] and the Lockhart–Martinelli parameter [158], denoted by Equations

3.30 and 3.31.

$$Pr_l = \frac{Cp_l \mu_l}{k_l} \tag{3.26}$$

where Cp_l, μ_l, and k_l are the specific heat capacity, dynamic viscosity and thermal conductivity of LN_2 at the corresponding operating pressure of the system, respectively. The Re_l, Re_g and Re_{lo} are defined by:

$$Re_l = \frac{G(1-x)D_h}{\mu_l} \qquad for\ 0 < Re_l < 79202 \tag{3.27}$$

$$Re_g = \frac{GxD_h}{\mu_g} \qquad for\ 0 < Re_g < 247740 \tag{3.28}$$

$$Re_{lo} = \frac{GD_h}{\mu_l} \qquad for\ 276 < Re_{lo} < 89798 \tag{3.29}$$

where Re_l is the saturated liquid Reynolds number, Re_g is the saturated vapour Reynolds number and Re_{lo} is the liquid only Reynolds number.

$$\emptyset_g^2 = 1 + CX + X^2 \tag{3.30}$$

$$X_{tt} = \left(\frac{\mu_l}{\mu_g}\right)^{0.1} \left(\frac{1-x}{x}\right)^{0.9} \left(\frac{\rho_g}{\rho_l}\right)^{0.5} \tag{3.31}$$

$$X = \sqrt{\frac{(dp/dz)_l}{(dp/dz)_g}} \tag{3.32}$$

$$-\left(\frac{dp}{dz}\right)_l = \frac{2f_l v_l G^2 (1-x)^2}{D_h} \ and\ -\left(\frac{dp}{dz}\right)_g = \frac{2f_g v_g G^2 x^2}{D_h} \tag{3.33}$$

where v_l,and v_g denote the kinematic viscosity of the liquid and the vapour at the corresponding working pressure, respectively; the friction factor f is determined based on the Reynolds number which corresponds to the actual flow rate. For instance, the liquid phase f_l can be given by:

$$f_l = 16Re_l^{-1} \qquad for\ Re_l < 2000$$

$$f_l = 0.079Re_l^{-0.25} \qquad for\ 2000 \leq f_l < 20000 \tag{3.34}$$

$$f_l = 0.046Re_l^{-0.2} \qquad for\ f_l \geq 20000$$

Similarly, the coefficient C in the two-phase pressure drop multiplier is derived from the following different Reynolds numbers:

$$C = \begin{cases} 3.9E-2Re_{lo}^{0.03}Su_{go}^{0.1}\left(\frac{\rho_l}{\rho_g}\right)^{0.35} & Re_l \geq 2000 \quad Re_g \geq 2000 \\ 8.7E-4Re_{lo}^{0.17}Su_{go}^{0.5}\left(\frac{\rho_l}{\rho_g}\right)^{0.14} & Re_l \geq 2000 \quad Re_g < 2000 \\ 1.5E-3Re_{lo}^{0.59}Su_{go}^{0.19}\left(\frac{\rho_l}{\rho_g}\right)^{0.36} & Re_l < 2000 \quad Re_g \geq 2000 \\ 3.5E-5Re_{lo}^{0.44}Su_{go}^{0.5}\left(\frac{\rho_l}{\rho_g}\right)^{0.48} & Re_l < 2000 \quad Re_g < 2000 \end{cases} \tag{3.35}$$

where ρ_l and ρ_g refer to the density of the vapour and the liquid at the corresponding working pressure, respectively; Su_{go} is the vapour only Suratman number, which can be calculated using Equation 3.33:

$$Su_{go} = \frac{\rho_g \sigma D_h}{\mu_g^2} \tag{3.36}$$

where σ is the surface tension and μ_g is the dynamic viscosity of the vapour.

The modified Weber number (We^*) is used to determine different condensation regimes [152, 159], it can be represented as follows:

$$We^* = 2.45\frac{Re_g^{0.64}}{Su_{go}^{0.3}(1+1.09X_{tt}^{0.039})^{0.4}} \qquad for\ Re_l \leq 1250 \tag{3.37}$$

$$We^* = 0.85\frac{Re_g^{0.79}X_{tt}^{0.157}}{Su_{go}^{0.3}(1+1.09X_{tt}^{0.039})^{0.4}}\left[\left(\frac{\mu_g}{\mu_l}\right)^2\left(\frac{\rho_l}{\rho_g}\right)\right]^{0.084} \qquad for\ Re_l > 1250 \tag{3.38}$$

For slug and bubble flows, the condensation flow heat transfer coefficient ($\acute{h}_{non-ann}$) can be written as follows:

$$\acute{h}_{non-ann} = \left[\left(0.048Re_l^{0.69}Pr_l^{0.34}\frac{\emptyset_g}{X_{tt}}\right)^2 + \left(3.2\times10^{-7}Re_l^{-0.38}Su_{go}^{1.39}\right)^2\right]^{0.5}\frac{k_l}{D_h} \tag{3.39}$$

$$for\ We^* < 7X_{tt}^{0.2}$$

According to the Equation 3.13, the condensation rate ($\dot{m}$) therefore can be calculated using Equation 3.40:

$$\dot{m} = \frac{q_i}{h_{LN2}} \tag{3.40}$$

where h_{LN2} is the latent heat of the LN_2 at corresponding operating pressure of the system.

3.3.4 Boundary conditions

The boundary conditions are different for different processes. During the system charging process (LN_2 boiling process), the temperature of the LN_2 at 8.5 barg is -170.19℃. The operating pressure of the discharging process (N_2 condensation process) is 17 barg, and the corresponding saturation temperature of the LN_2 is -159.5℃. The detailed thermophysical properties of LN_2 are listed in Table 3.3 [50].

Table 3.3: The thermophysical properties of LN_2 at different operating pressures [50].

Pressure (barg)	PCT (℃)	ρ (kg/m^3)	λ (W/m·K)	C_P (kJ/kg·K)	μ (Pa·s)	σ (N/m)
		Liquid/Gas				
8.5	-170.19	670.94/39.184	0.095/0.012	2.4/1.62	$6.9\times10^{-5}/7.7\times10^{-6}$	0.0035
17	-159.5	591.16/79.674	0.075/0.016	3.07/2.51	$4.9\times10^{-5}/9.2\times10^{-6}$	0.0016

The phase transition temperature of 2-Methylbutane is -160.15℃, and the thermal conductivities of 2-Methylbutane at liquid and solid phases are 0.195 W/m·K and 0.191 W/m·K, respectively. In addition, different tube and fin materials are investigated, and their thermal conductivities at around -170.19℃ are stainless steel-304 9 W/m·K [160], aluminium-6061 100 W/m·K [161] and pure copper 500 W/m·K [160].

CHAPTER 4

RESULTS AND DISCUSSION: CTES MATERIAL SCREENING AND CHARACTERISATION

This chapter presents the screening procedure and results of the thermophysical properties characterization of CTES materials, including the SHS material and the phase change material. In Section 4.1, different SHS materials are compared and screened according to their specific heat and thermal conductivity. Section 4.2 discusses the screening procedure for the cryogenic PCMs, where the results of the thermophysical properties of selected PCM candidates are also presented. Section 4.3 presents the experimental results for the feasibility study of the selected cryogenic PCM.

4.1 Sensible heat storage (SHS) materials

The physical shape and size of SHS candidates are displayed in Figure 4.1 (a), (b), and (c), respectively. It can be seen that the surface of the glass beads is smooth, and their shape and size are regularly distributed. The Dorset gold and Brittany bronze gravels have irregular shapes with a wide range of sizes, and their surfaces are comparatively rough.

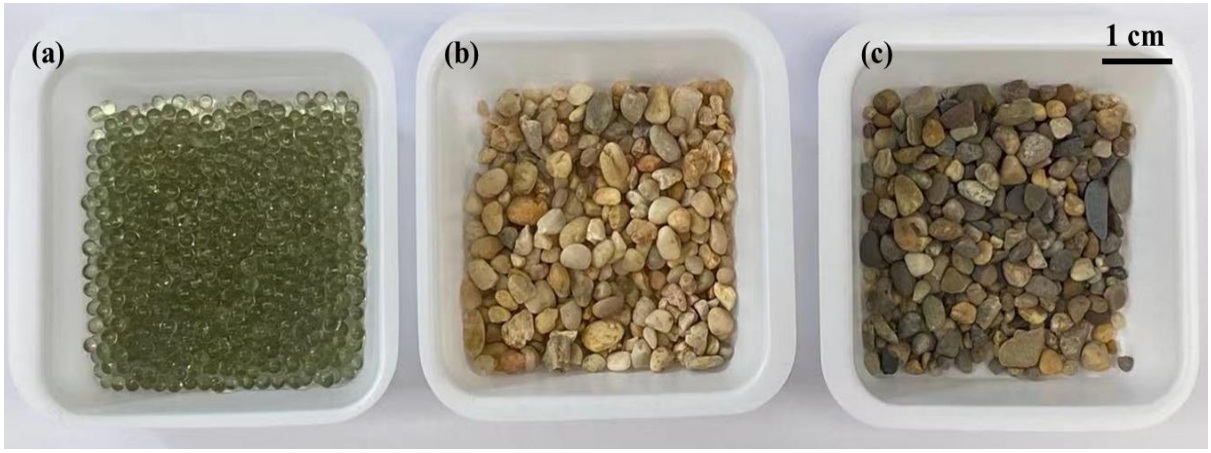


Figure 4.1:Physical surface morphology (shape and size) of SHS materials: (a) glass bead; (b) Dorset gold gravel; (c) Brittany bronze gravel.

4.1.1 Specific heat capacity

The specific heat determines the energy storage capacity of the SHS device within a defined temperature range, which was measured and used as an indicator for choosing the suitable SHS candidate. The average specific heat values of the SHS materials at different temperatures are shown in Figure 4.2. One can see that in all measurements the average values increase with the temperature, and this tendency gradually slows down when the test temperature approaches the ambient temperature, which is consistent with other studies of SHS materials [15]. Temperature variations have a significant effect on the specific heat values of the glass bead, the Dorset gold gravel and

Brittany bronze gravel, decreasing by ~21.7%, ~13.08% and ~20.9% separately at -40℃ compared to that at the room temperature. In addition, the glass bead has the highest specific heat among the three samples. Considering that the reduction in the size of solid particles in a defined volume heat exchanger can lead to an increase in the quantity of their packing, thereby enhancing the heat transfer area between the solid particles and the HTF [107], the smallest size of glass beads was selected as the SHS material. However, the specific heat value of glass bead at the cryogenic temperature range cannot be obtained by the DSC instrument due to its measurement limitations. Thus, the 3rd order polynomial fitting function ($R^2 = 0.9993$) is used to fit the data as shown in Figure 4.2 and the fitted expression is used to estimate the specific heat of glass beads within the cryogenic temperature range:

$$C'_P = -1.1e^{-6} \times T^3 - 4.4e^{-5} \times T^2 + 0.00338 \times T + 0.787 \quad (4.1)$$

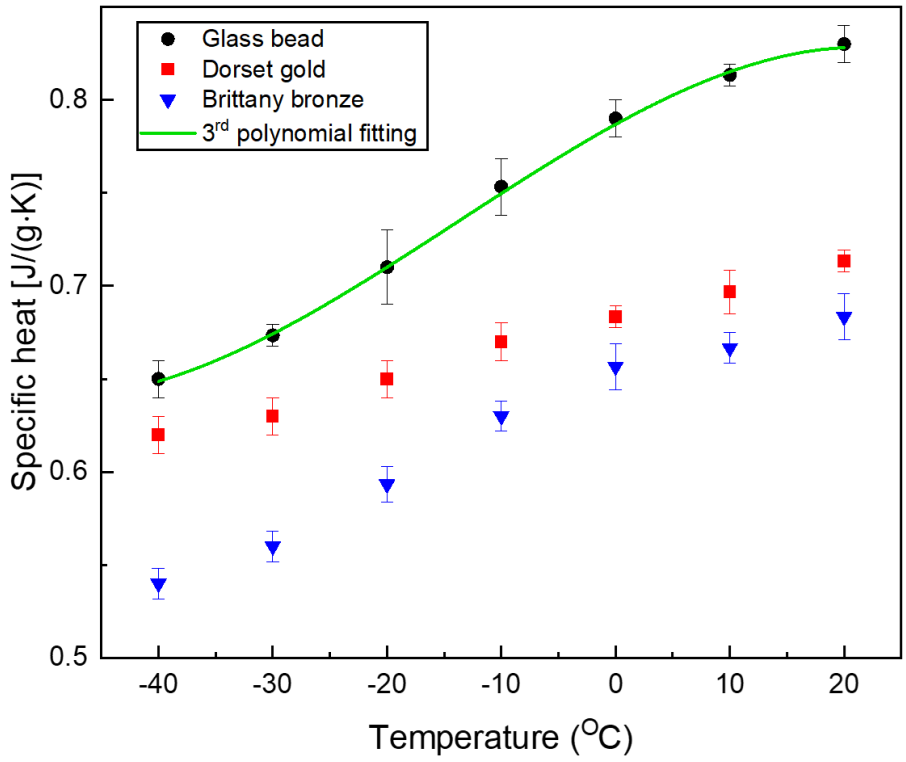


Figure 4.2:The average specific heat values of glass bead, Dorset gold gravel, and Brittany bronze gravel at different temperatures were determined by DSC (with a cooling/heating rate of 5 ℃/min, in the temperature range of -40℃ to 20℃).

4.1.2 Thermal conductivity

The average thermal conductivities of glass bead over the range of -40℃ to 20℃ are shown in Figure 4.3. It can be seen that the thermal conductivity of the material decreases with decreasing temperature, which agrees with the theory that the thermal conductivity of glassy materials decreases sharply with decreasing temperature [162-165]. Besides, Figure 4.3 also shows a comparison between the measured data of borosilicate glass and the reference value [166]. One can see that there is a good agreement at the test temperatures above 0℃. The deviations (~0.05 W/m·K) from the reference data occur in the low temperature range, which are relatively small. Hence, the thermal conductivity of borosilicate glass beads at cryogenic temperatures is estimated by using the data from the literature.

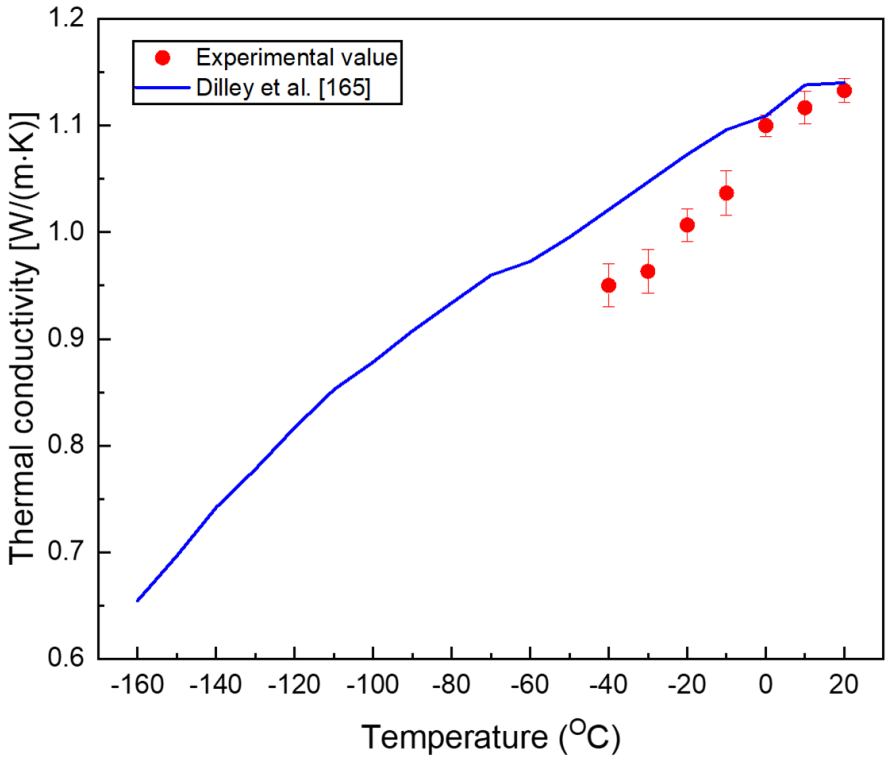


Figure 4.3:The average thermal conductivities of glass bead at different temperatures were measured by LFA (with a cooling/heating rate of 5 ℃/min, in the temperature range of -40℃ to 20℃).

4.2 Latent heat storage (LHS) materials

4.2.1 Cryogenic PCM screening

For cryogenic applications, the desirable phase transition temperature range is from -140℃ to -160℃. Following the selection criteria reviewed in Section 2.2.2.3, hydrocarbons with a few carbon atoms (C_5 and C_6) are suitable for cryogenic energy storage applications because of the applicable PCT and the adequate energy storage density. Hence potential PCM candidates were selected from the above-mentioned material type and the temperature range. Table 4.1 lists some thermophysical properties [50] and prices of cryogenic PCM candidates.

Table 4.1: Desirable PCM candidates and their thermophysical properties for the cryogenic application [50].

Cryogenic PCM Candidates						
Candidates	**Name**	**Formula**	**Boiling point (℃)**	**Melting point (℃)**	**Heat of fusion(kJ/kg)**	**Price (£/kg)**
1	2-Methylpentane	C_6H_{14}	60.25	-153.55	72.74	12.51
2	2-Methylbutane	C_5H_{12}	27.85	-159.78	71.46	1.47
3	3-Methylpentane	C_6H_{14}	63.25	-162.85	61.62	4.78
4	1-Pentene	C_5H_{10}	31.65	-165.13	84.70	3.31
5	1-Hexene	C_6H_{12}	62.47	-139.76	111.06	1.66

Generally, these candidates can be classified as alkanes and unsaturated olefins, and the phase transition temperatures of these candidates are from -140℃ to -165℃, which match the temperature

requirements for the cryogenic energy storage applications. Most characterisation instruments have a temperature measurement limitation of around -150℃ to -160℃, which makes it challenging to determine the thermophysical properties of candidate 4. Although 1-Pentene has the lowest PCT and highest latent heat among these candidates, it was not studied in the current work due to difficulties in the thermal characterisation. In addition, considering of large-scale system testing and further applications, a suitable PCM candidate should be commercially available and abundant. Limited by their complicated production process, the commercially available 2-Methylpentane is reagent grade, and its relatively high price is not suitable for large-scale applications.

Of the remaining candidates, 2-Methylbutane and 3-Methylpentane have excellent potential for cryogenic applications due to their suitable phase transition temperatures. However, 2-Methylbutane is a highly volatile substance at ambient temperature, which requires that experiments are prepared and operated at as low environmental temperatures as possible. 3-Methylpentane is a more expensive candidate, but it has a lower phase transition temperature and a higher boiling temperature in comparison to 2-Methylbutane. Therefore, 3-Methylpentane was selected as an alternative LHS material in this study. Besides, 1-Hexene was also studied and compared as a reference material for control experiments, which assisted in understanding and estimating some thermophysical properties of 2-Methylbutane and 3-Methylpentane that cannot be reliably measured by our available equipment.

4.2.2 Phase transition temperature and enthalpy

The energy storage density of PCM is closely related to its enthalpy and PCT. In order to obtain accurate phase transition temperatures and enthalpies of these PCM candidates, DSC and the T-history measurements were performed, respectively.

4.2.2.1 DSC measurements

Firstly, 1-Hexene was tested because it is less volatile and possesses a relatively higher melting point than other potential candidates. It is, therefore, easy to be implemented in the initial stage of cryogenic material study. Two different cooling rates were applied in the DSC measurements to study the crystallisation behaviour of the material (see Figure 4.4 and Figure 4.5), the measurement results are summarised in Table 4.2.

Table 4.2: The phase transition temperature and heat of fusion of 1-Hexene under different measurement conditions.

Cooling rate (℃/min)	Onset T_f (℃)	Peak T_f (℃)	Onset T_m (℃)	Peak T_m (℃)	Heat of fusion (kJ/kg)
1	-165	-164.99	-138.83	-137.7	156.39
0.5	-159.51	-158.89	-140.36	-139.46	158.07

Figure 4.4 shows the DSC curve of 1-Hexene (28.7 mg) over a temperature range between -110℃ and -165℃ with a cooling/heating rate of 1 ℃/min. One can see a small exothermic peak appears near the end of the cooling process. The instrument can automatically adjust the heat flux supply when the set temperature program enters a new measure segment, such as from a cooling process to an isothermal process. Hence, the small exothermic peak induced by the heat flux change in the measurement chamber at around -165℃ could trigger the crystallisation event of 1-Hexene. During the 30 minutes isothermal stage, a distinct crystallisation peak is observed at this time. The 1-Hexene sample was then heated to -110℃ at a heating rate of 1 ℃/min. The endothermic peak represents the melting process of the material from solid to liquid phase transition with an onset temperature of -138.8℃.

The phase change enthalpy of 1-Hexene is 156.39 kJ/kg by integrating the melting peak. This is approximately 40.8% greater than the value reported by McCullough et al [167] in 1957. In their study, a copper calorimeter was applied to test 55 mL material under sealed conditions. Their data showed a large distribution of values, which was attributed to the incomplete crystallisation of the sample in the calorimeter. The use of the DCS instrument with a smaller sample size will avoid this issue. Therefore, the measured enthalpy of 1-Hexene is considered to be reasonably accurate.

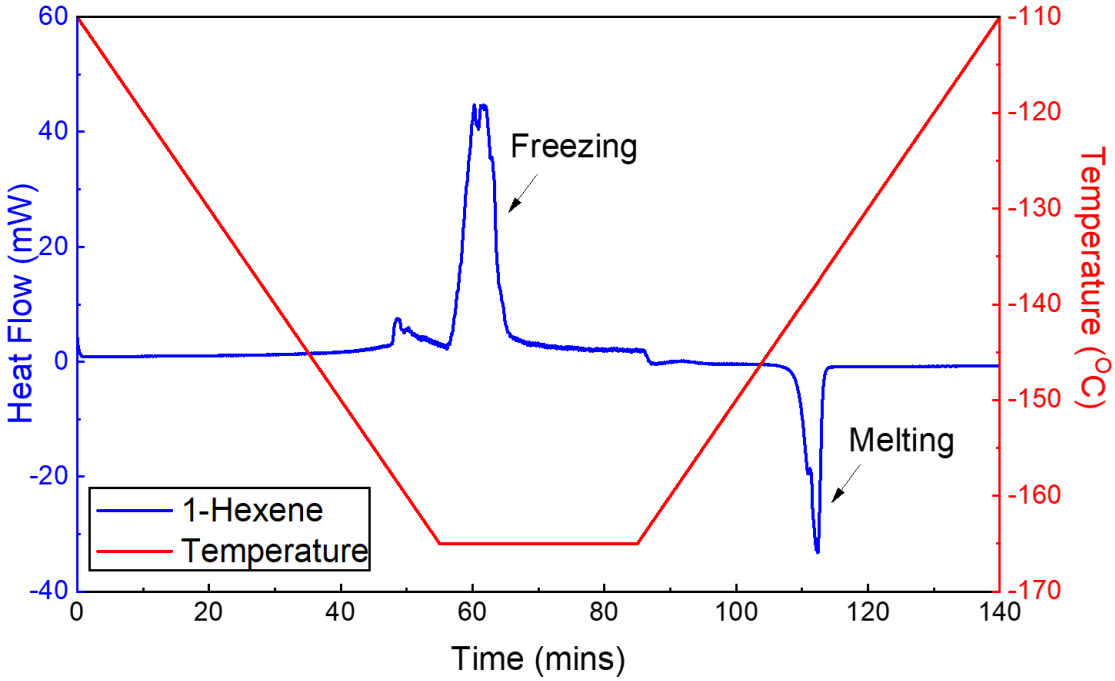


Figure 4.4: DSC measurement curve of 1-Hexene with a cooling/heating rate of 1 ℃/min, in the temperature range of -110℃ to -165℃.

To decrease or eliminate the impact of heat flux change on crystallisation, both the cooling and heating rates were fixed at 0.5 ℃/min. Meanwhile, based on the previous result, the temperature range of the cooling process was also enlarged, aiming to obtain better results. The experiment was repeated in the new temperature range of -130℃ to -170℃.

Figure 4.5 shows the DSC measurement curve of 1-Hexene after using the revised procedure. It can

be seen that as the system temperature continues to rise, an explicit sharp crystallisation peak is obtained near -159℃, and a melting peak is also observed at -140℃. The onset temperature difference between crystallisation and melting is the supercooling degree of 1-Hexene under the current experimental condition, which is 19.15 ℃. The phase change enthalpy obtained with the new procedure has not changed, which is 158.07 kJ/kg, giving a confirmation of the higher latent heat obtained under the previous measurement procedure. Typically, the crystallisation of the sample will occur during the cooling process. However, the crystallisation of 1-Hexene during the heating process indicates that the induction time of its nucleation is comparatively long under the current experimental conditions. One possible reason for this phenomenon is that the supercooling degree of PCM is affected by sample size. To understand this, a larger volume of 1-Hexene is used in the subsequent T-history measurements.

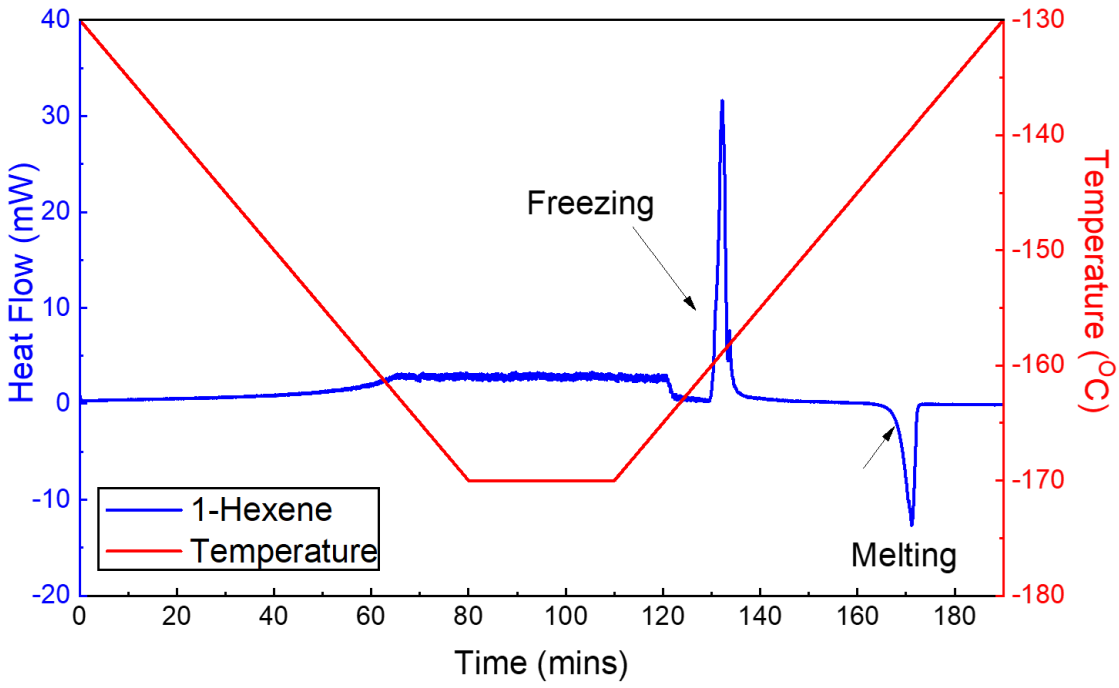


Figure 4.5: DSC measurement curve of 1-Hexene with a cooling/heating rate of 0.5 ℃/min, in the temperature range of -130℃ to -170℃.

The same program was applied to measure the second candidate, 2-Methylbutane. Its melting point is around -159℃, lower than 1-Hexene. According to the result illustrated in Figure 4.6, 2-Methylbutane did not undergo any phase transition during the measurement process. As stated in Section 3.2.1.2, the lowest measurement temperature of the characterization instrument is -170℃, and the theoretical crystallisation temperature of 2-Methylbutane is -160℃. Therefore, one possible reason is that the supercooling degree of 2-Methylbutane is greater than 10 ℃ under the applied measurement conditions. The instrument is not capable of providing the low temperature required to trigger the material nucleation. Consequently, no crystallisation or melting peaks were observed in the DSC curve. Considering a set of experimental results reported by Edelstein [168], who used acetone as a nucleation agent to mix 2-Methylpentane with a volume ratio of 3% to 10% (v/v) to suppress the supercooling behaviour, experiments, therefore, were carried out with different volume ratios of 2-Methylbutane mixed with acetone. However, the DSC measurements (see example of 2-Methylbutane + 5% Acetone in Figure 4.6) did not show significant improvement in the reduction of supercooling degree. As a result, the use of acetone could not mitigate the supercooling issue probably due to the different base materials. The T-history method was used subsequently to compare and evaluate the phase transition of 1-Hexene and 2-Methylbutane under identical experimental conditions.

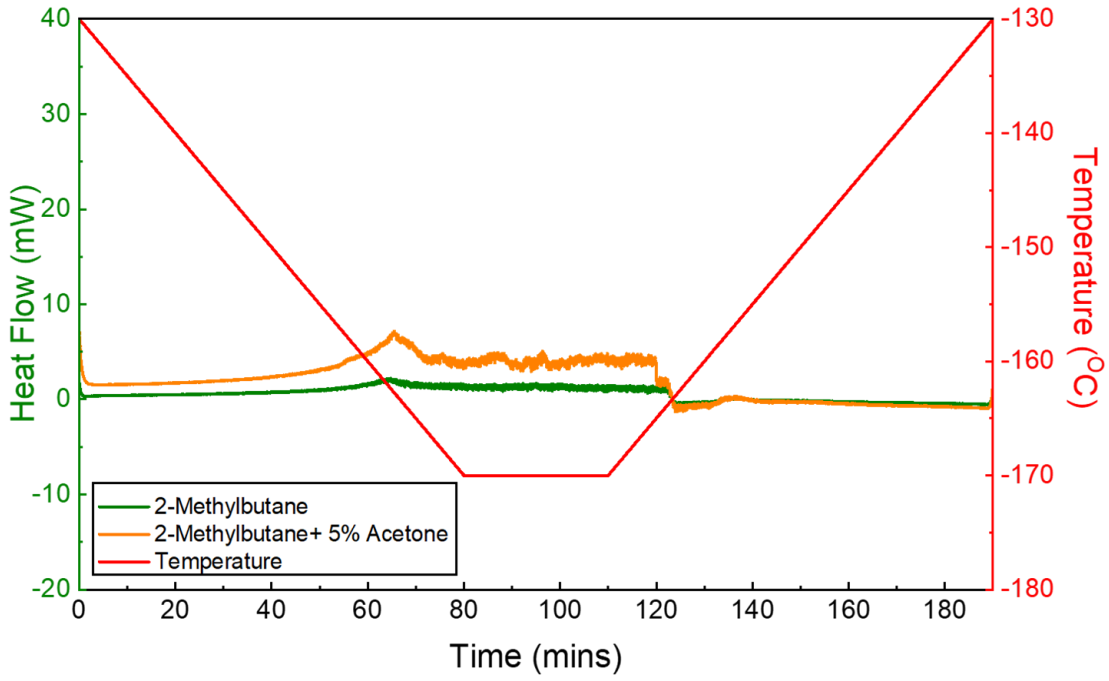


Figure 4.6: DSC measurement curves of 2-Methylbutane and its mixture with 5% (v/v) acetone with a cooling/heating rate of 0.5℃/min, in the temperature range of -130℃ to -170℃.

4.2.2.2 Temperature-history measurement

Figure 4.7 illustrates the result of the T-history measurement of 1-Hexene. The positions of T_0 to T_4 are as described in Section 3.2.2, where T_0 is placed in the middle cylinder, and the distances from T_1 to T_4 to the inner wall of the inner cylinder are 0.5 cm, 1 cm, 1.5 cm, and 2 cm, respectively. The upper diagram of Figure 4.7 represents the crystallisation process of 1-Hexene. It can be seen that the temperature of the material starts dropping immediately after the introduction of LN_2 and exceeds the solidification point (-139℃) directly. As the temperature difference between 1-Hexene and LN_2 gradually decreasing, the cooling curve is slowly approaching flat, but no obvious platform is generated around -139℃. This change in the slope of the cooling curve can be considered as an indication of 1-Hexene crystallisation. However, when the LN_2 level in the middle layer slowly declines, the sample temperature continuously drops for a while, then rebounds back by

approximately 16℃ and stabilizes at -144℃ to form a small plateau lasting about 2 minutes, see the green line in Figure 4.7. This temperature fluctuation is mainly caused by the exothermic crystallisation event of l-Hexene. Hence, after the completion of crystallisation, the temperature commences to decrease and finally approaches the temperature of LN_2.

The lower diagram of Figure 4.7 displays the melting process of 1-Hexene, which was measured straight after the crystallisation process. One can see that when the remaining LN_2 is entirely evaporated, the reference temperature (T_0) gradually increases due to the temperature difference with the surroundings, and the reduction in temperature difference does not have a significant effect on the variation rate of the reference temperature throughout the melting process, which implies a relatively uniform heat exchange between the environment and the T-history system. The PCM begins to melt at around -140℃ and remains at this temperature for approximately 28 minutes. As the phase transition of the material ends (after approximately 2520 seconds), the sensible heat of the material is released, and the PCM temperatures at different positions (T_1, T_2, T_3, and T_4) progressively overlap with each other. The temperatures of the reference and the PCM increase at an almost similar rate, which further validates that the entire system is evenly heated by the environment.

Figure 4.7 also indicates that the supercooling degree is approximately 12℃ under the current experimental conditions of solidification and melting. It is approximately 40% lower compared to the DSC results. The evaluation of the supercooling degree of 1-Hexene obtained by different measurement methods supports that the supercooling degree is affected by the amount of the test sample as mentioned earlier. Besides, the cooling rate and the container roughness could also play a role in the supercooling reduction.

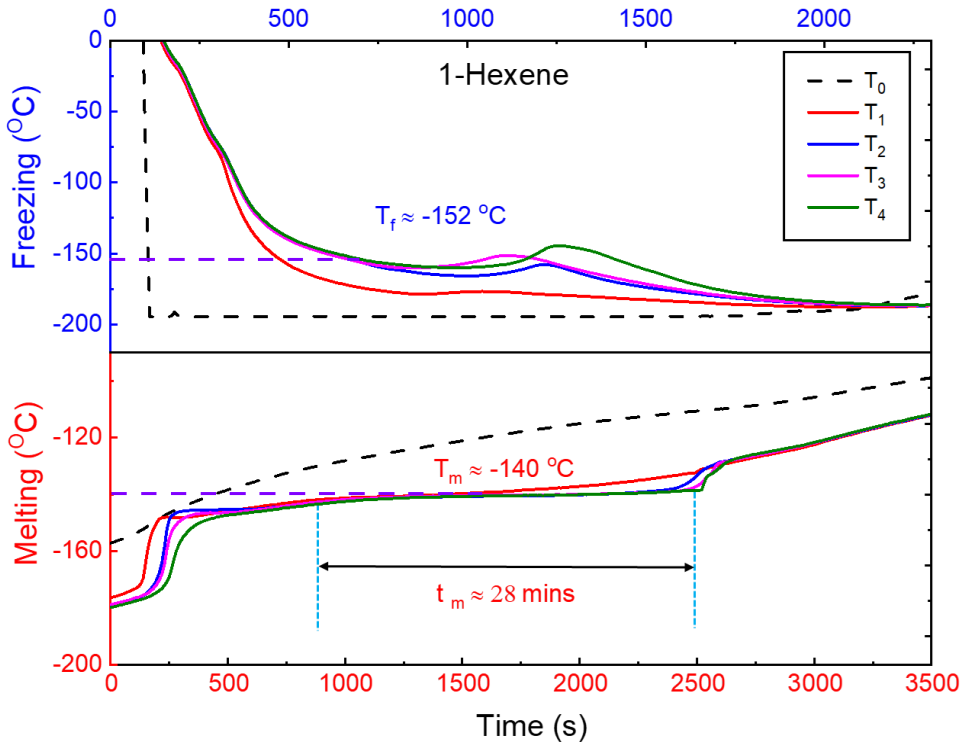


Figure 4.7: T-history measurement profile of 1-Hexene PCM, the upper diagram illustrates the freezing process, and the lower one shows the melting process of 1-Hexene.

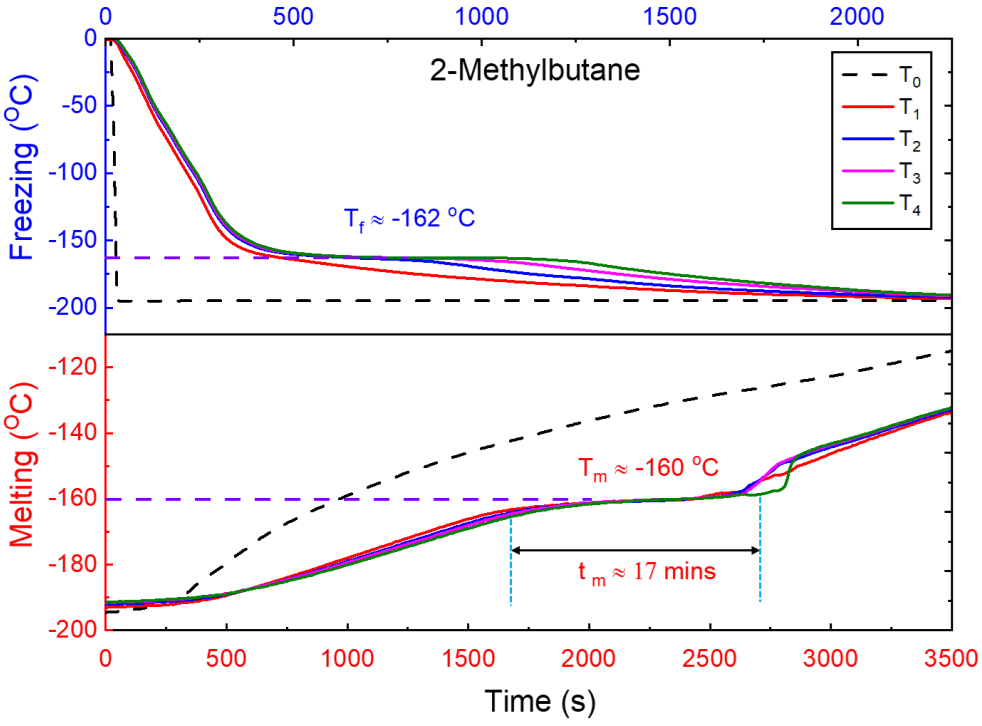


Figure 4.8: T-history measurement profile of 2-Methylbutane PCM, the upper diagram illustrates the freezing process, and the lower one shows the melting process of 2-Methylbutane.

Figure 4.8 shows the T-history measurement profile of 2-Methylbutane under the identical experimental conditions as for 1-Hexene, i.e., the measurements were both performed at an ambient temperature of 25℃ and the thermocouples were in the same position. Similarly, the upper diagram represents the crystallisation process of 2-Methylbutane. It can be found that during the solidification, a more obvious platform appears at around -162℃ compared to that of 1-Hexene. This is due to the fact that the temperature difference between the LN_2 boiling point and the phase transition temperature of 2-Methylbutane (~36℃) is much higher than that of 1-Hexene (~56℃). The heat released by the crystallisation of the material at lower temperatures is more likely to compensate for the heat absorbed by the LN_2 evaporation, thus forming a stable plateau. However, the length of the platform corresponding to each position of the sample is different. This is correlated with the heat transfer of the sample at different positions. For instance, the material at position T_1 firstly undergoes a phase transition from liquid to solid because the heat transfer near the cylinder wall is earlier than elsewhere. Thus, the cooling curve at this position shows a fluctuating downward trend. While thermocouple T_4 is placed close to the middle of the cylinder, the heat transfer to this point is mainly contributed by heat conduction within the material, which is relevant to the thermal conductivity of the material itself. Therefore, the crystallisation occurs slightly later at the position T_4, and the length of the platform is longer than other positions.

The lower graph of Figure 4.8 shows the melting process of 2-Methylbutane, which has a platform at -160℃ and lasts for approximately 17 minutes. The supercooling degree of 2-Methylbutane is only 2℃ under the current measurement conditions. In general, the supercooling degree of the organic material is influenced by different factors, for instance, the cooling/heating rate, the surface roughness of the test containers, the amount of PCM tested, etc [169]. The results from the DSC and T-history

measurements indicate that the sample amount has a significant impact on the supercooling degree. Certainly, the T-history method is more realistic as it is closer to practical applications.

Since the enthalpy of 1-Hexene, $\Delta h_{1-Hexene}$, has already been measured and analysed accurately via DSC experiments, the enthalpy of 2-Methylbutane, $\Delta h_{2-Methylbutane}$, is therefore estimated by comparing the under-curve area of the melting process of 1-Hexene and 2-Methylbutane with the following equation:

$$\Delta h_{2-Methylbutane} = \frac{S_T'}{S_T} \times \Delta h_{1-Hexene} \tag{4.2}$$

where S_T and S_T' are respectively measured under the same conditions during the melting process; see Figure 4.9. They can be obtained by integrating the melting curve over the corresponding melting time period. The area ratio of 2-Methylbutane to 1-Hexene is found to be 0.47, and the heat of fusion of 2-Methylbutane is therefore estimated to be 74.29 kJ/kg. The measurement uncertainty using the T-history method is around 3.9% compared to the results obtained by adiabatic calorimetric system [170]. The measurement errors are mainly from: 1) part of the sensible heat of the material is included in the area calculation; 2) this area comparison method is based on the assumption of negligible influence of the temperature difference on the natural convection between the T-history system and the air. The second reason is considered acceptable as the average temperature difference between the phase transition temperatures of both materials with respect to their reference temperatures (see black dash line in Figure 4.9) is not as large as expected, which is 22.5℃ for 1-Hexene and 25.1℃ for 2-Methylbutane.

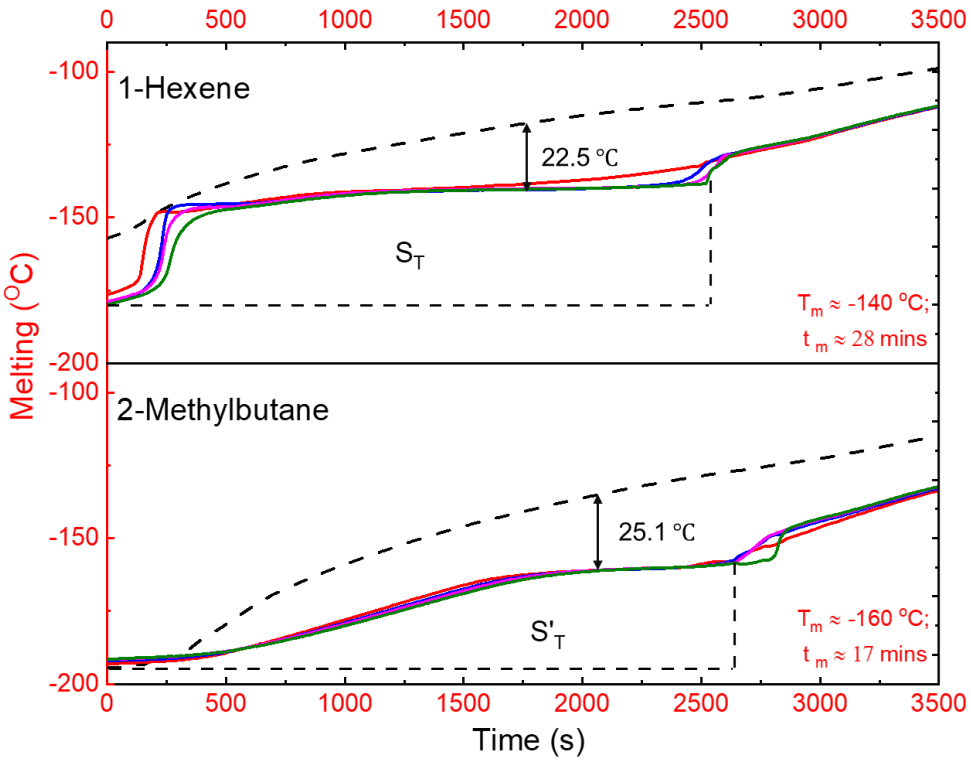


Figure 4.9: The comparison of the T-history melting curves of 1-Hexene and 2-Methylbutane under the identical experimental conditions.

4.2.3 Thermal conductivity

The thermal conductivity of PCM affects its thermal storage and release rate, which is critical for the design of heat exchange component and the evaluation of the charging/discharging kinetics of the overall system and hence its energy storage efficiency. As described in Section 3.2.3.2, measurements were performed using the THB method to determine the thermal conductivity of the samples during the dynamic melting process, and the results were categorised as the solid and liquid states according to the different phase transition temperatures of the samples.

Figure 4.10 (a) and (b) show the thermal conductivity results of 1-Hexene in the solid and liquid states. The measurement is regarded on the solid phase state if the temperature ranges from -190℃ to -145℃; where the liquid phase state occurs from -135℃ to -25℃. The 3rd order polynomial fitting curves are

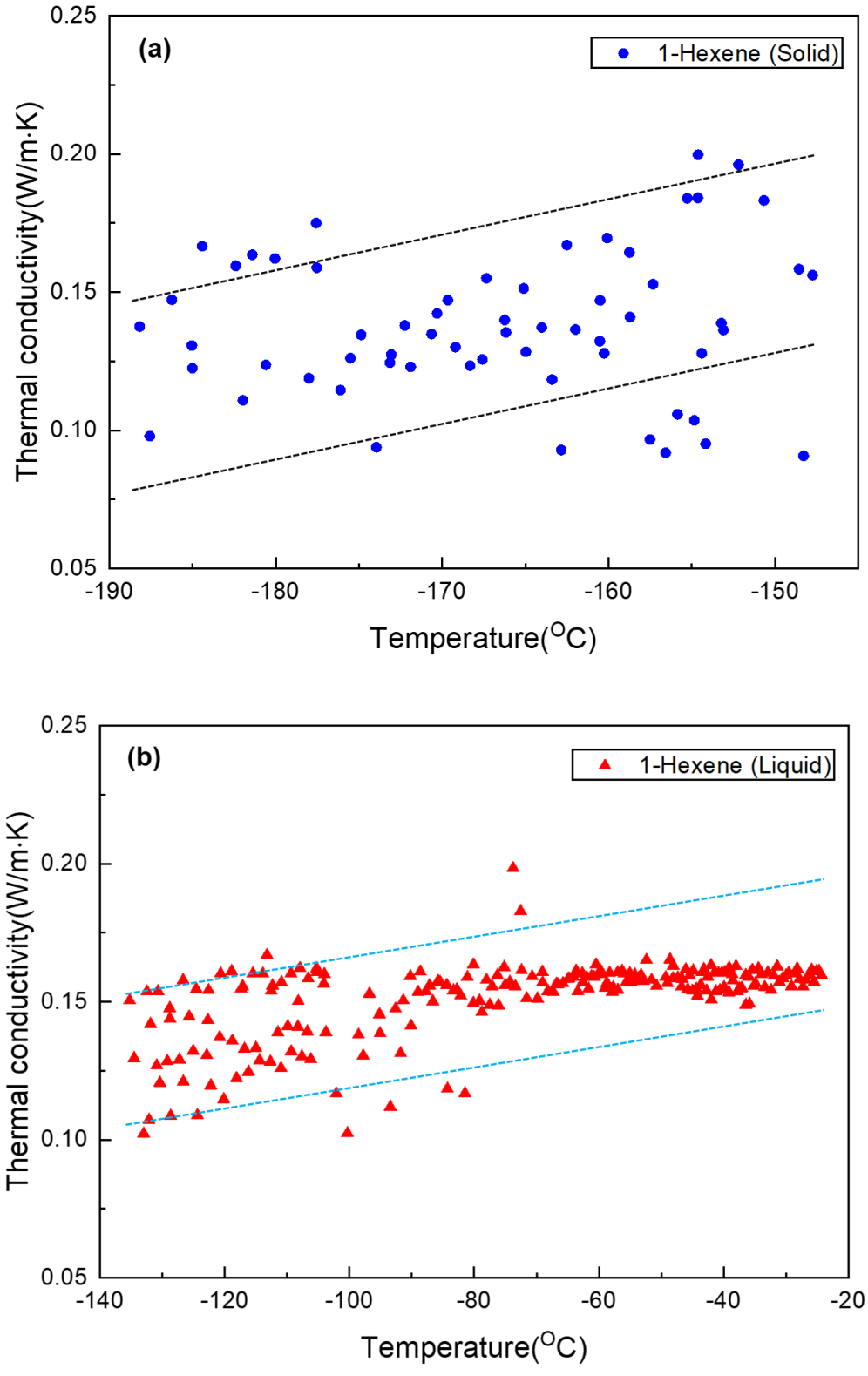


Figure 4.10: (a) Thermal conductivity measurement results for the solid state of 1-Hexene from -190℃ to -145℃; (b) Thermal conductivity measurement results for the liquid state of 1-Hexene from -135℃ to -25℃.

used to characterise data dispersion with variation in temperature for both states. It can be seen that the data in the solid state is more dispersed, which is likely to be attributed to the intense heat transfer between the environment and the sample due to the large temperature difference. This dispersion trend also appears in the initial liquid state. However, as the temperature difference between the sample and the environment gradually decreases, the measured data are evenly distributed around the fitted curve when the sample temperature is greater than -80℃. In order to minimise the effect of scattered data on the accuracy of the results, the data within dashed lines in Figure 4.10 (a) and (b) are averaged as the thermal conductivities of 1-Hexene in the solid and liquid states, see Table 4.3. One can see that the thermal conductivities of 1-Hexene in the solid and liquid states are both lower than 0.2 W/m·K, and the average thermal conductivities of the solid and liquid phases are 0.139 and 0.151 W/m·K, respectively.

Figure 4.11 (a) and (b) present the thermal conductivity results of 2-Methylbutane in the solid and liquid states. The temperature range is adjusted based on the phase transition temperature of 2-Methylbutane, ranging from -190℃ to -175℃ for the solid state and -155℃ to -35℃ for the liquid state. It can be seen in Figure 4.11 (a) and (b) that the thermal conductivity of 2-Methylbutane is lower than 0.3 W/m·K, and the average thermal conductivities in both solid and liquid states are close, 0.195 W/m·K and 0.191 W/m·K, respectively. The dispersion of 2-Methylbutane data is relatively large compared to that of 1-Hexene, and the distributions of these data are comparatively scattered in both solid and liquid states. This is likely to be related to the lower phase transition temperature of 2-Methylbutane. The significant temperature difference with the surrounding environment is likely to affect the stability of the heat flow signal of the measuring sensor, leading to the fluctuation. However, the data are more centralized again when the sample temperature approaches -80℃.

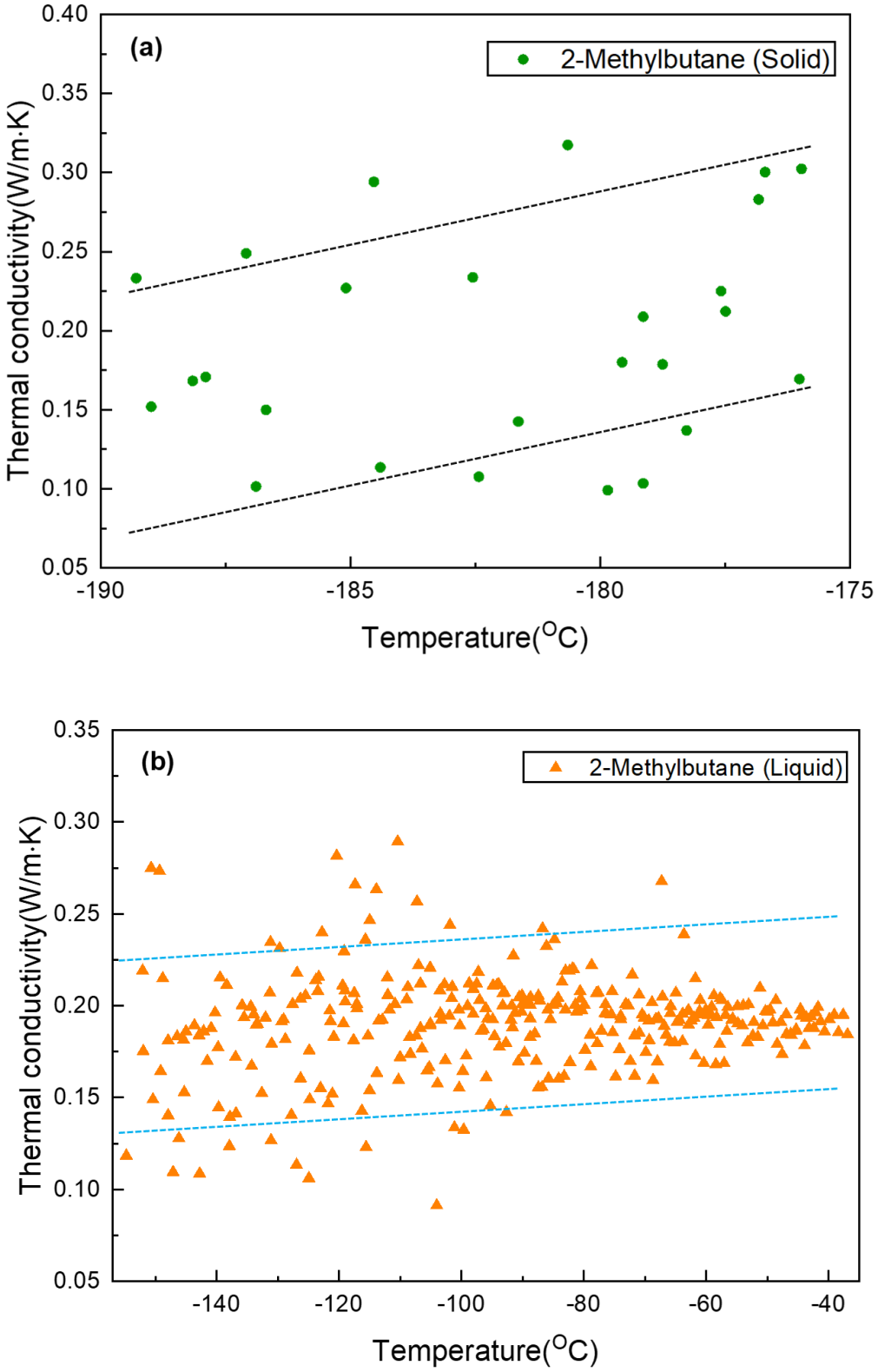


Figure 4.11: (a) Thermal conductivity measurement results for the solid state of 2-Methylbutane from -190℃ to -175℃; (b) Thermal conductivity measurement results for the liquid state of 2-Methylbutane from -155℃ to -35℃.

Table 4.3: Thermal conductivity measurement results of 1-Hexene and 2-Methylbutane in both solid and liquid phases.

	Sample	Solid phase (W/m·K)	Liquid phase (W/m·K)
Average value	1-Hexene	0.139±0.003	0.151±0.001
	2-Methylbutane	0.195±0.013	0.191±0.002

There are very limited experimental data available in the literature that can be used to validate the thermal conductivity of liquid organic compounds obtained at temperatures investigated in this work, especially for the solid state data. Missenard and Pachaiyappan proposed an estimation method to obtain the thermal conductivity of the liquid state of organic compounds as a function of the temperature [171]. The correlation equation can be written as:

$$\log_{10} \lambda_{liq} = A + B\left[1 - \frac{T}{C}\right]^{\frac{2}{7}} \tag{4.3}$$

where λ_{liq} is the thermal conductivity of a liquid organic compound (W/m·K), A, B, and C represent regression coefficients of the compound, and T is the prevailing temperature (K).

In terms of coefficients for Equation 4.3, namely the values of A, B, and C, the thermal conductivities of 1-Hexene and 2-Methylbutane at the corresponding temperatures are calculated and shown graphically in Figure 4.12. The results indicate that the thermal conductivities of 1-Hexene and 2-Methylbutane are lower than 0.18 W/m·K, which are very close to the experimental results. Besides, it was observed that both materials became viscous or glassy as the temperature decreased. As reported by Edelstein [168], this is because that the low thermal energy levels present at cryogenic temperatures, which weakens the molecular mobility of materials and makes them exhibit a low

thermal conductivity.

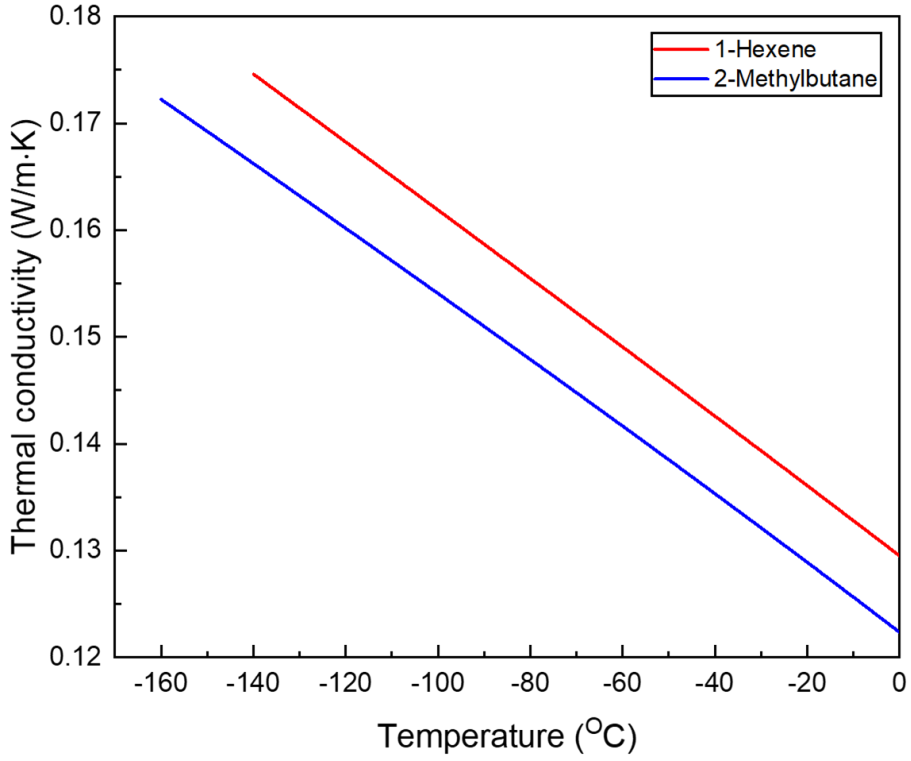


Figure 4.12: Thermal conductivity estimations of 1-Hexene and 2-Methylbutane based on modified Missenard and Pachaiyappan methods [171].

4.2.3.1 Thermal conductivity enhancement

The lower thermal conductivity of the PCMs can, to some extent, lead to longer thermal storage and release times, leading to slow charging/discharging kinetics [172]. Therefore, modification of 1-Hexene was carried out to address the low thermal conductivity issue. Different methods and thermal conductivity enhancement additives have been used to enhance the thermal conductivity of PCMs, including the inclusion of metal foams/fins, ceramics and carbon-based/metal-based particles [173-176]. Carbon-based particles are widely used as the thermal conductivity enhancer because of their low density, better stability and dispersion in PCM compared to metal-based particles. In this study,

the expanded graphite (EG) with an average particle size of 20 μm was used to mix with pure 1-Hexene for the thermal conductivity enhancement. Figure 4.13 (a) shows the use of EG to formulate the composite PCM sample. EG particles are seen to settle to the bottom of the container as soon as it is added into the 1-Hexene solution. The use of thickener was therefore studied. Two thickeners, SiO_2 and styrene-ethylene-butylene-styrene (SEBS), were used. The amount of thickener added to the PCM should be as small as possible in order to minimise the reduction in the PCM enthalpy while achieving a good EG dispersion effect. 1-Hexene mixtures containing 1 wt.%, 2 wt.%, 3 wt.%, 4 wt.% and 6 wt.% of each of the thickeners were mixed with 0.5 wt.% of EG (all concentrations were with respect to the total amount of 1-Hexene). As shown in see Figure 4.13 (b) and (c), no significant graphite agglomeration or sedimentation were observed when the addition of SiO_2 was 3 wt.% and higher, and the addition of SEBS was 2 wt.% and higher, after placing these samples in a refrigerator at -45℃ for 48 hours. It indicates that 3 wt.% SiO_2 and 2 wt.% SEBS are sufficient to disperse 0.5 wt.% of EG in the 1-Hexene solution, and there is no necessary to increase the proportion of thickeners. Therefore, the optimum dispersion of 0.5 wt.% EG in 1-Hexene solution can be achieved with 3 wt.% SiO_2 and 2 wt.% SEBS, respectively.



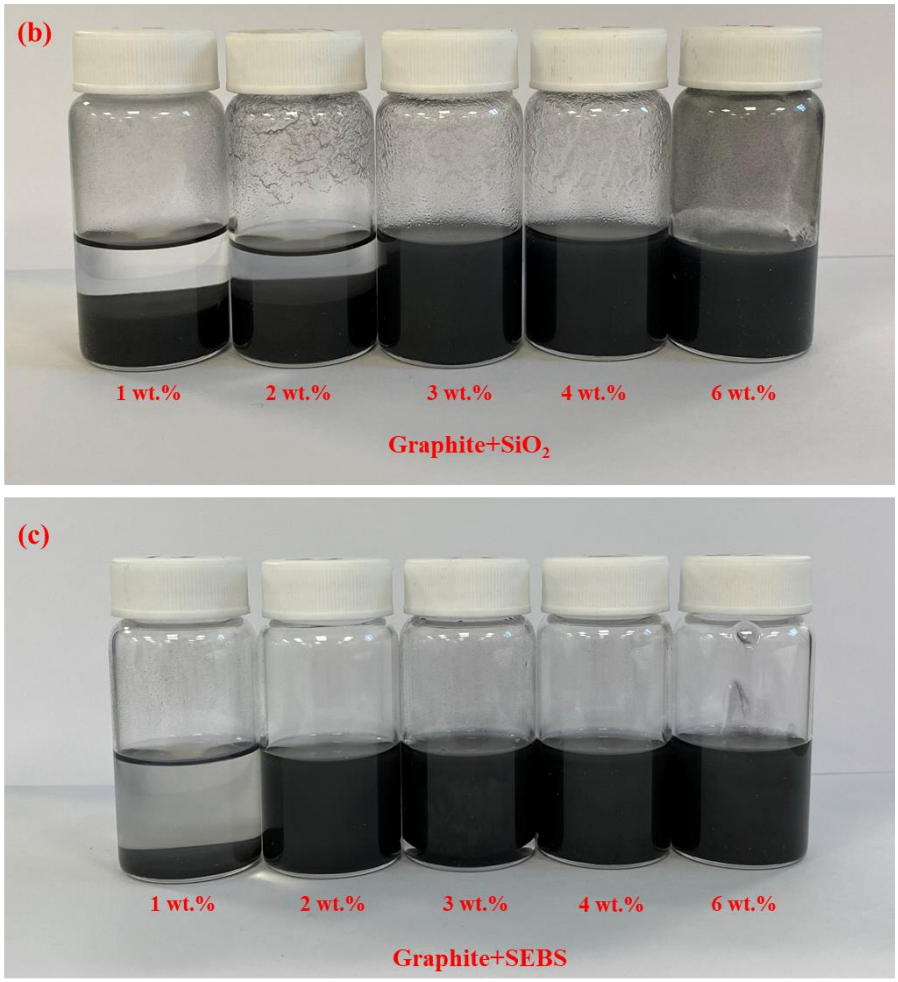


Figure 4.13: (a) 1-Hexene with 0.5 wt.% EG mixture; (b) the stability of composite 1-Hexene solutions containing 1 wt.%, 2 wt.%, 3 wt.%, 4 wt.%, 6 wt.% SiO_2 and 0.5 wt.% EG respectively after being stored in a freezer at -45℃ for 48 hours; (c) the stability of composite 1-Hexene solutions containing 1 wt.%, 2 wt.%, 3 wt.%, 4 wt.%, 6 wt.% SEBS and 0.5 wt.% EG respectively after being stored in a freezer at -45℃ for 48 hours.

4.2.3.2 Thermal conductivity measurements of 1-Hexene with additives

The composite 1-Hexene mixtures were prepared based on the two optimum ratios (Figure 4.13 (b) and (c)) and measured for their thermal conductivity by using the THB instrument. Figure 4.14 (a) and (b) and Figure 4.15 (a) and (b) show the measured thermal conductivity results for the two formulated 1-Hexene composites in the solid and liquid states, respectively.

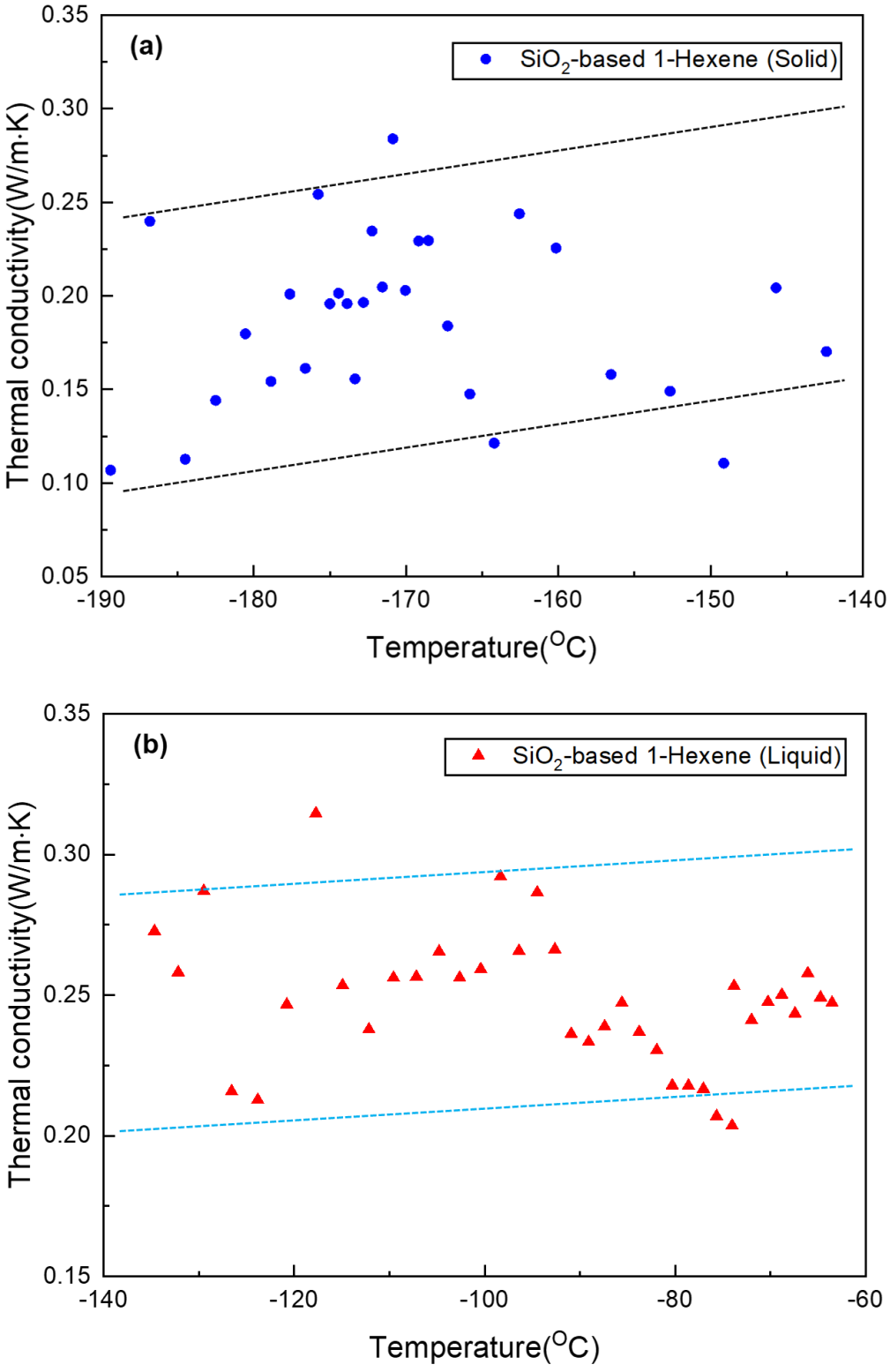


Figure 4.14: Thermal conductivity measurement results of modified 1-Hexene with 3 wt.% SiO_2 and 0.5 wt.% graphite: (a) solid state from -190℃ to -140℃; (b) liquid state from -140℃ to -60℃.

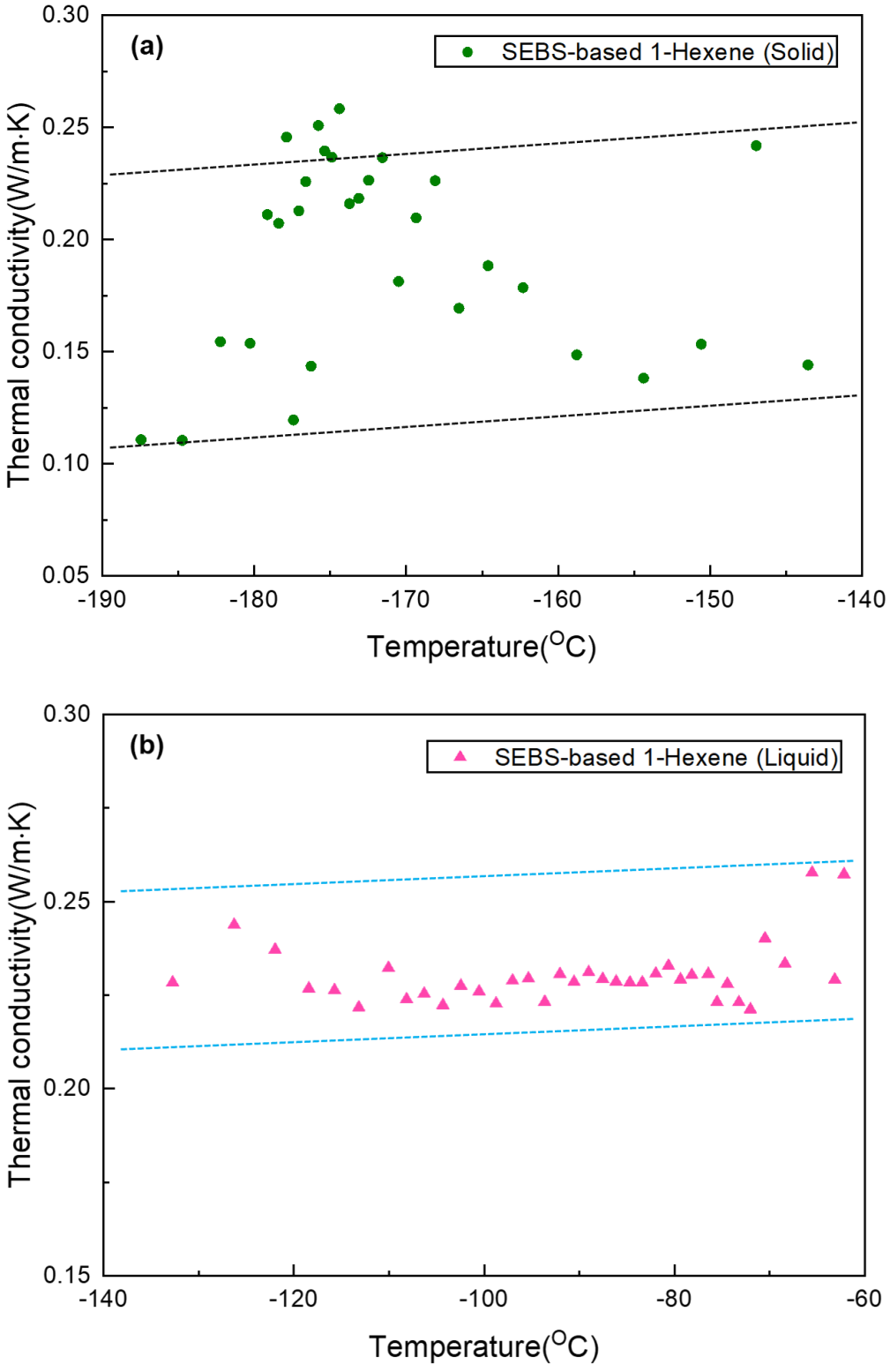


Figure 4.15: Thermal conductivity measurement results of modified 1-Hexene with 2 wt.% SEBS and 0.5 wt.% graphite: (a) solid state from -190℃ to -140℃; (b) liquid state from -140℃ to -60℃.

It can be seen from Figure 4.14 (a) and (b) Figure 4.15 (a) and (b) that the solid and liquid thermal conductivities of two optimally modified 1-Hexene mixtures are improved compared to the pure material. For the solid state, the thermal conductivities of SiO_2-based and SEBS based 1-Hexene mixtures are enhanced by 34.5% and 38.1% to 0.187 W/m·K and 0.192 W/m·K, respectively. However, partial aggregation of SiO_2 in the 1-Hexene solution was observed during the melting process of the SiO_2-based 1-Hexene mixture, leading to a reduction in the dispersion of EG. As a result, the measured data of the SiO_2-based 1-Hexene fluctuate considerably in the testing temperature range compared to the SEBS-based 1-Hexene. Furthermore, this fluctuation also leads to a higher thermal conductivity of SiO_2-based 1-Hexene than that of SEBS-based 1-Hexene in the liquid state, despite the fact that the same amount of EG is added to both composites. The introduction of 0.5 wt.% EG results in a 64.2% and 52.3% improvement in the liquid thermal conductivity of two optimally modified 1-Hexene mixtures compared to the pure 1-Hexene, reaching 0.248 W/m·K and 0.230 W/m·K, respectively.

Table 4.4: Thermal conductivity measurement results of modified 1-Hexene in liquid phases.

	Sample	Solid phase (W/m·K)	Liquid phase (W/m·K)	Increment (%)
Average value	1-Hexene with SiO_2	0.187±0.008	0.248±0.004	34.5 (S)/64.2 (L)
	1-Hexene with SEBS	0.192±0.008	0.230±0.001	38.1 (S)/52.3 (L)

4.2.3.3 Impact of thermal conductivity enhancers on thermal properties of 1-Hexene

To understand potential effect of material modification on the enthalpy and phase transition temperature of the PCMs, DSC measurements were carried out on both composites with a cooling/heating rate of 0.5 ℃/min. Figure 4.16 and Figure 4.17 show the DSC curves for the SiO_2-based 1-Hexene (Composite 1) and SEBS-based 1-Hexene (Composite 2), respectively. The measurement results are also summarised in Table 4.5.

Table 4.5: The phase transition temperature and heat of fusion of modified 1-Hexene.

Composite	Onset T_f (℃)	Peak T_f (℃)	Onset T_m (℃)	Peak T_m (℃)	Heat of fusion (kJ/kg)
Composite 1	-151.56	-152.15	-140.59	-138.59	157.27
Composite 2	-154.41	-155.40	-141.10	-140.00	155.75
Pure	-159.51	-158.89	-140.36	-139.46	158.07

It can be found that both composites obtain distinct sharp crystallisation peaks during cooling, which means that the time required for crystallisation becomes shorter than that for the pure substance. Besides, their freezing onset temperatures increase from -159.51℃ to -151.56℃ and -154.41℃, respectively. As reported by Lu and Tassou [177], during the charging process, if the HTF temperature is reduced by 1℃, there is a corresponding 3% reduction in the coefficient of performance (COP) of the system. These results imply a potential increase in the charging performance of the PCM by reducing the temperature conditions of the HTF, and hence improving the COP of the system. This variation in the crystallisation of composite PCMs is mainly attributable to the addition of extra particles, which is likely to have accelerated the formation of the crystalline

nucleus and the crystal growth.

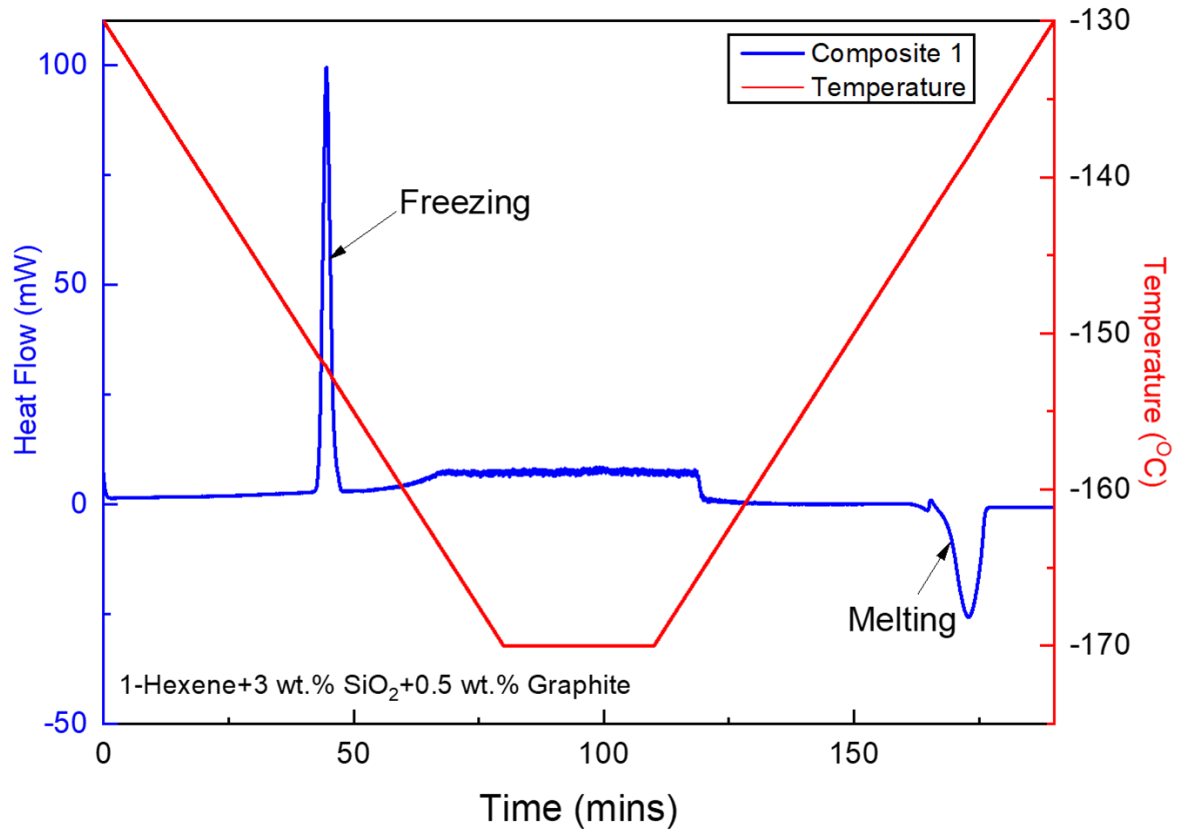


Figure 4.16: DSC measurement curve of Composite 1 (1-Hexene containing 3 wt.% SiO_2 and 0.5 wt.% EG) with a cooling/heating rate of 0.5℃/min, in the temperature range of -130℃ to -170℃.

Moreover, the enthalpy of the modified materials does not change significantly, decreasing by only 0.51% for Composite 1 and 1.47% for Composite 2. Although the enthalpy change of the Composite 2 is expected, the appearance of a splitting peak is observed during the melting process; see Figure 4.17. Possible reasons for this phenomenon are: 1) some 1-Hexene is chemically bonded to the added materials thus changing its original melting point; 2) there is a hysteresis in the melting of the material due to the colloid formed when SEBS is dissolved in 1-Hexene.

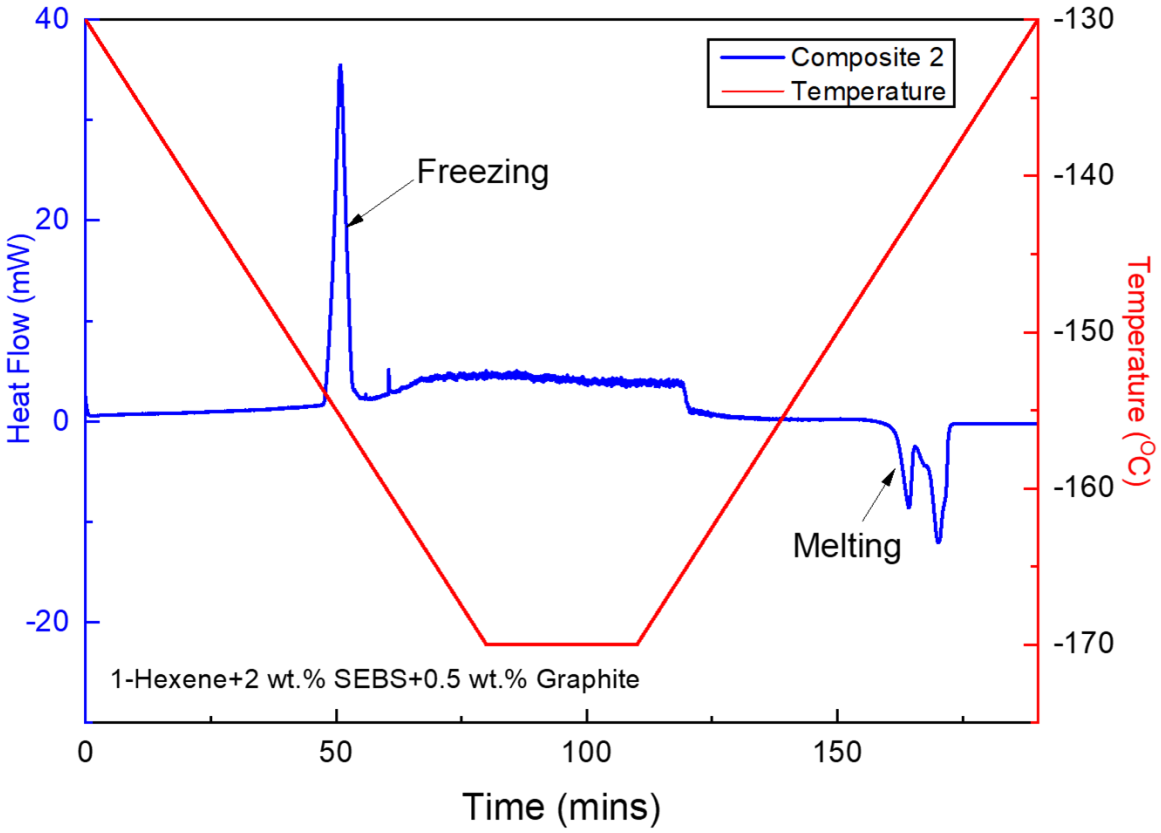


Figure 4.17: DSC measurement curve of Composite 2 (1-Hexene containing 2 wt.% SEBS and 0.5 wt.% EG) with a cooling/heating rate of 0.5℃/min, in the temperature range of -130℃ to -170℃.

Therefore, chemical compatibility between additives of the Composite 2 was studied by IR spectroscopy. Figure 4.18 shows the IR spectra of the pure material and the composite 1-Hexene. It can be seen that the graphite spectrum does not have any characteristic peak, as it does not have any functional groups. 1-Hexene displays the spectrum for the groups of $C_{SP^2} - H$ stretching (3150-3000 cm^{-1}), $C_{SP^3} - H$ stretching (3000-2850 cm^{-1}), and the $C = C$ stretching (1650 cm^{-1}), in agreement with data reported in the literature [178]. The IR spectrum of SEBS shows the characteristic peaks at 2919, 2850, 1454 and 1376 cm^{-1} for the CH_3 stretching, CH_2 stretching, CH_2 and CH_3 bending and CH_3 wagging, which are identical to the literature data [179-181]. After the mixing of SEBS, EG and 1-Hexene, the IR spectra of the composite 1-Hexene show no new peaks generated and no shifts,

indicating no chemical reaction among 1-Hexene, SEBS and EG, and the mixing of the composite 1-Hexene solution being a physical process. In other words, the splitting peak that appear in the DSC measurement is not caused by new substances generated during the mixing process. Therefore, the colloid formed when SEBS is dissolved in 1-Hexene is likely to be the reason for the appearance of the splitting peak.

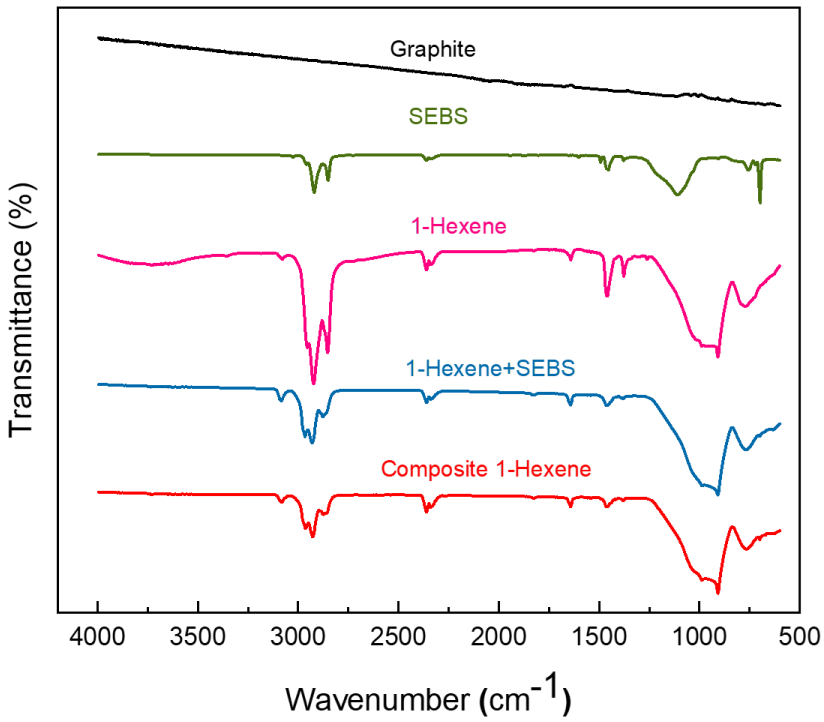


Figure 4.18: Infrared spectra of different additives in SEBS-based composite 1-Hexene.

In summary, both formulations exhibit improvements in terms of the thermal conductivity and the crystallisation behaviour without a significant enthalpy reduction. However, the SiO_2-based 1-Hexene shows a poor stability, the partial aggregation of SiO_2 leads to a reduction in EG dispersion. The formulation of 1-Hexene with 2 wt.% SEBS and 0.5 wt.% EG not only increases the thermal conductivity but also reduces the time required for crystallisation.

4.2.4 Thermal cycling stability

The commercialisation of LHS systems often requires the repeated thermal charging and discharging of the PCM without excessive changes in its thermophysical properties [182]. To give a preliminary assessment, 100 thermal cycling tests were carried out and compared with the uncycled material. 1-Hexene was selected to perform the thermal cycling test because of its relative non-volatility and easiness of its phase transition process to be determined by DSC measurements.

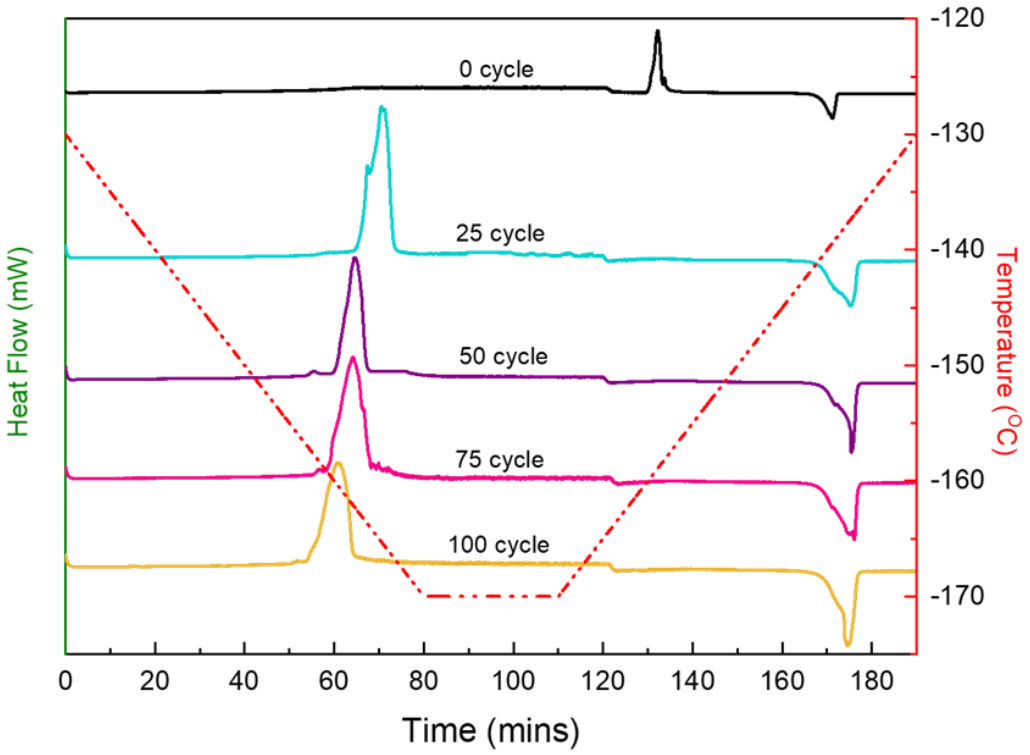


Figure 4.19: DSC measurement curves of 1-Hexene after 25, 50, 75, and 100 thermal cycles with a cooling/heating rate of 0.5 ℃/min, in the temperature range of -130℃ to -170℃.

Figure 4.19 displays the DSC curves of 1-Hexene that has undergone different numbers of thermal cycling. One can see that the crystallisation peak shifts from the ramp-up phase to the ramp-down phase of the measurement procedure after 25 cycles and continues to move towards higher temperatures as the number of cycles increases. The measured onset freezing temperatures of 1-

Hexene are listed in Table 4.6, which shows an increasing trend from -163.11℃ to -156.68℃, indicating that the cycling of the material can reduce the time required for solidification to some extent. This has a considerable impact on the application of PCM, as the less charging time implies the less cold energy requirements and faster system response. Different from the changes in crystallisation caused by the modification of 1-Hexene, the changes in the crystallisation behaviour of the material after multiple charging and discharging are likely attributed to the crystalline memory effect. Such an effect is manifested in "morphological" and "kinetic" memory in a particular crystal state [183]. In general, the recrystallised structure bears some resemblance to the molecular clusters that retained their crystallographic arrangements prior to melting, particularly with regard to the position of the nuclei and the relative orientation of crystallites [183, 184]. These aggregated molecular clusters can act as predetermined nucleation sites allowing recrystallisation to occur rapidly, which can greatly improve the overall crystallisation rate during the subsequent cooling process [183-186]. As a result, the crystallisation required time for 1-Hexene after thermal cycling is significantly reduced.

The onset melting temperatures of 1-Hexene varies in the range of $\pm$0.5℃, which is within the measurement uncertainty of the instrument. The thermal cycling test has almost no effect on the melting behaviour of the material. In terms of the latent heat, it can be found that the phase change enthalpy decreases slightly with increasing thermal cycling time. The enthalpy variation of 3.16% after 100 times of thermal cycling is acceptable for long-term stability.

Table 4.6: The phase transition temperatures and heat of fusion values of 1-Hexene under 25, 50, 75, and 100 thermal cycles.

Measured Data						
Cycles	Onset T_f (℃)	Peak T_f (℃)	Onset T_m (℃)	Peak T_m (℃)	Heat of fusion (kJ/kg)	Variation (%)
0	-159.51	-158.89	-140.36	-139.46	158.07	-
25	-163.11	-165.22	-139.21	-137.45	157.83	0.15
50	-160.75	-162.3	-139.59	-137.4	157.15	0.58
75	-159.47	-162.1	-139.75	-137.05	153.79	2.7
100	-156.68	-160.37	-139.28	-137.84	153.08	3.16

4.2.5 Volume expansion

In the liquid-solid phase transition of the PCM, the volume expansion is crucial to the design of the heat exchanger. This is because the volume change affects the internal arrangement of the heat exchanger, especially the determination of the effective heat transfer area. For instance, if the volume expansion of the material is not considered during the phase transition process, there will be a mismatch between the required heat exchange area and the practical design. In addition, it is essential to understand the volume expansion of PCM for the material encapsulation in actual applications. The reserved space according to the volume expansion of PCM can avoid leakage issues during the heating and cooling cycles. Consequently, the volume expansion measurements of 1-Hexene and 2-Methylbutane were performed in this study.

The graduated cylinders containing 10 mL 1-Hexene and 2-Methylbutane were simultaneously immersed in the LN_2 bath to trigger their liquid-solid phase transition. As shown in Figure 4.20, the

solid volumes of 1-Hexene and 2-Methylbutane are 7.9 mL and 8 mL, respectively. Therefore, the volume expansion coefficient for both candidates are estimated to be 21% and 20%, respectively, by using Equation 3.2.

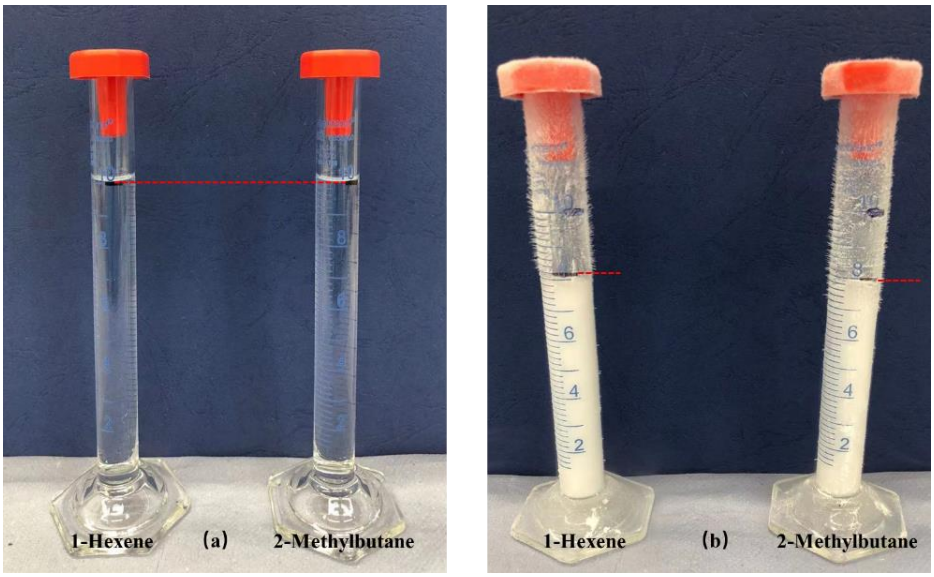


Figure 4.20: Thermal expansion determination of 1-Hexene and 2-Methylbutane: (a) PCM in liquid phase under room temperature (25℃); (b) PCM in the solid phase.

4.2.6 Flammability Limits (FLs)

As reviewed in Chapter 2, the flammability is one of the apparent disadvantages of organic PCMs, which may create some fire risks in their applications. Although this property was not used as the primary criterion for the material selection, it is related to the maximum quantity of PCM loading for an acceptable fire risk, thus bears an importance in practical applications. In this section, the flammability of the selected organic PCMs was determined by FRTA-I instrument at ambient temperature and atmospheric pressure.

As described in Section 3.2.7, the UFL and LFL of samples were determined based on both visual and pressure criteria. The results of flammability tests based on the visual standard show that the different

ignition colours of PCM-air mixtures are related to the amount of PCM added and irrelevant to the substance itself. Therefore, only 1-Hexene is discussed here as an illustration of the test results. Figure 4.21 (a) shows time sequence photographs of flame propagation after ignition of a mixture containing 0.35 mL of 1-Hexene and air. It can be clearly seen that the light blue flame propagates upwards from the spark igniter to the top of the test vessel, and then extends to the vessel wall and travels downwards. As the PCM addition was gradually decreased to the value corresponding to the lower non-flammable point (0.32 mL), the brightness of the flame and the intensity of the explosion sound diminished accordingly. As shown in Figure 4.21 (b), the flame propagation of the mixture containing 0.32 mL of 1-Hexene and air does not meet the distance of 100 mm required in the visual standard [87]. Therefore, this PCM addition can be regarded as the minimum sample quantity that does not induce flame propagation. In the case of 1.5 mL of 1-Hexene and air mixture, the colour of the flame changes from a light blue at low PCM amounts to a bright orange; see Figure 4.22 (a) and (b). However, the flame propagation pattern does not change significantly, but the noise of the explosion is not as intense as that at the low PCM volumes. In addition, carbon residues from the explosion can be observed deposited on the surface of the test vessel.

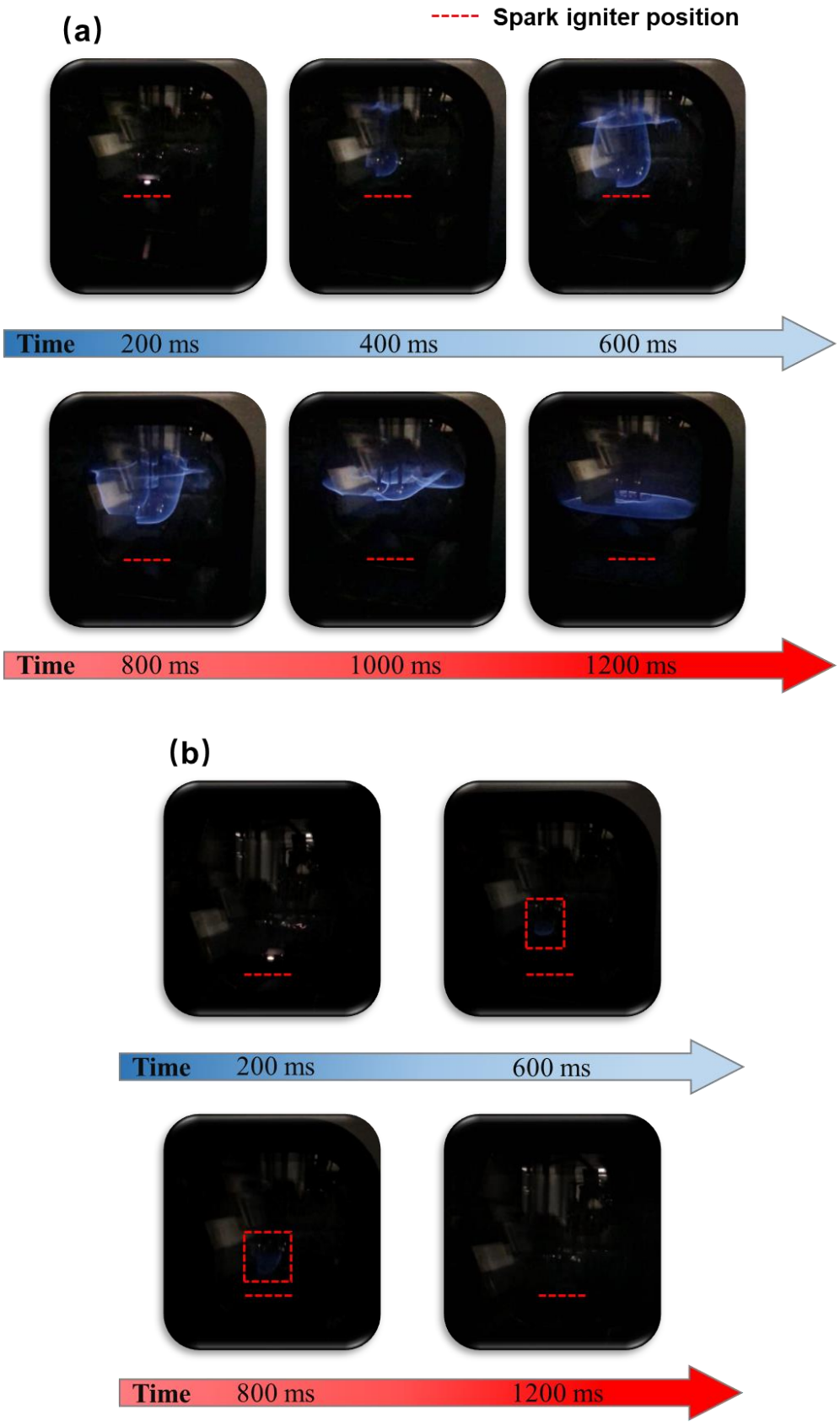


Figure 4.21: Time series photographs of flame propagation after ignition of a mixture: (a) containing 0.35 mL of 1-Hexene and air at 25℃; (b) containing 0.32 mL of 1-Hexene and air at 25℃.

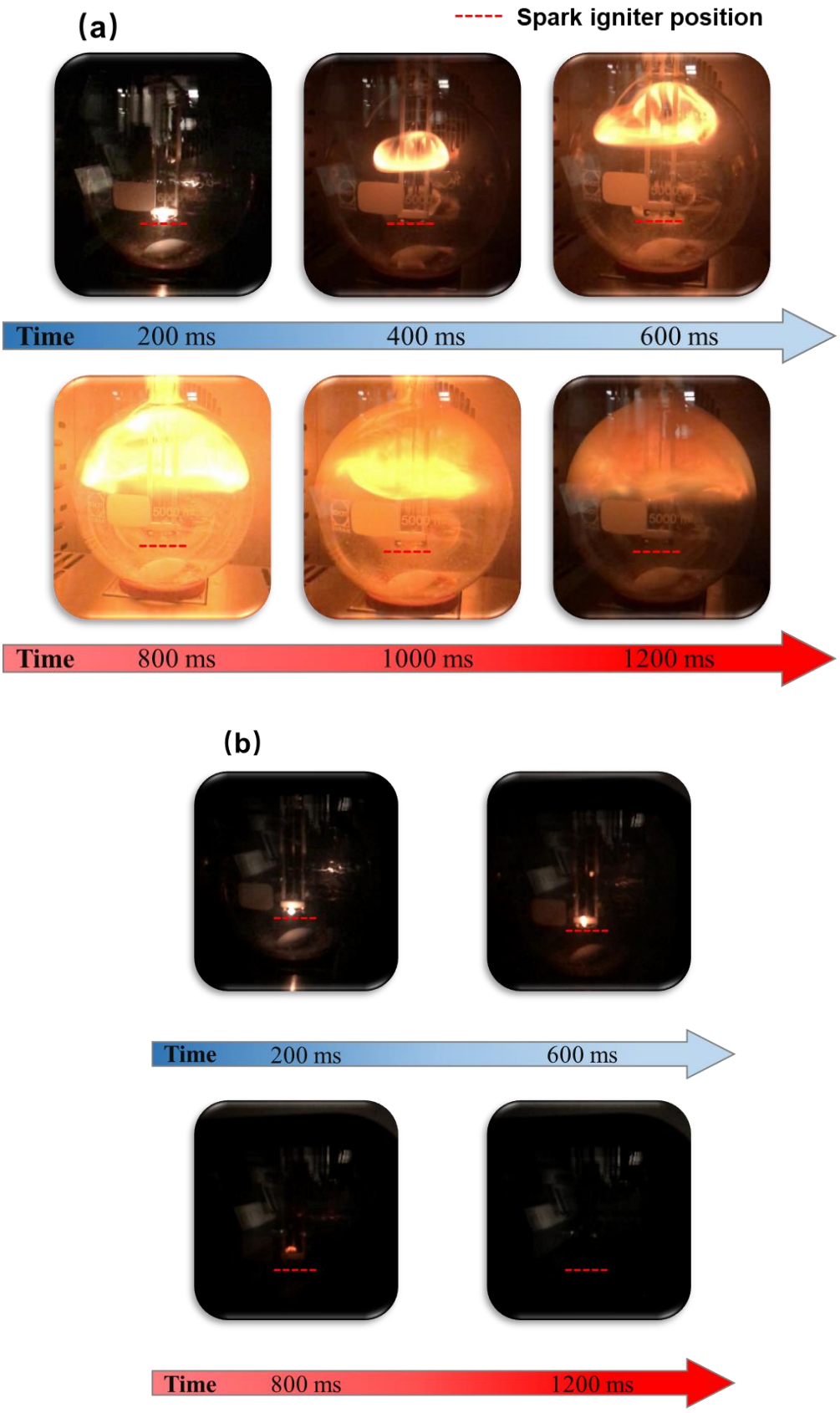


Figure 4.22: Time series photographs of flame propagation after ignition of a mixture: (a) containing 1.5 mL of 1-Hexene and air at 25℃; (b) containing 2.2 mL of 1-Hexene and air at 25℃.

The test was conducted in a step-by-step manner to determine the flammability limit of the sample by monitoring pressure changes at the instant of ignition in the closed vessel caused by different sample injection quantities. For instance, as shown in Figure 4.23, 0.35 mL and 1.5 mL of 1-Hexene are injected into the test vessel causing a detonation, while their pressures reach a maximum value and then decreased rapidly. It indicates that the injection volume to approach the UFL and LFL of the sample must be greater than 1.5 mL and less than 0.35 mL, respectively. In the case of 0.34 mL, although the duration of maintenance at maximum pressure is longer than the scenario at 0.35 mL, there is a time delay from 500 ms (0.35 mL) to 780 ms (0.34 mL) in terms of reaching the maximum pressure. As the sample amount is further reduced to 0.33 mL, this time delay appeared much later, at approximately 1150 ms. It means that the burning intensity of 1-Hexene is progressively reduced as the amount of sample introduced decreases and eventually approaches its LFL (0.32 mL). The UFL of 1-Hexene was determined in a similar manner. However, during the determination of the UFL, the pressure gradually declines with increasing sample addition, and no plateau period is observed; see Figure 4.23.

Table 4.7: Pressure changes in the test vessel after ignition of the mixtures of 1-Hexene and air.

	UFL of 1-Hexene				**LFL of 1-Hexene**			
	1.5 mL	**2 mL**	**2.15 mL**	**2.2 mL**	**0.35 mL**	**0.34 mL**	**0.33mL**	**0.32 mL**
Initial Pressure (kPa)	101.30	100.95	100.72	100.79	98.28	98.34	101.10	101.35
Final Pressure (kPa)	181.96	132.72	107.10	101.46	130.87	216.99	249.89	101.61
Increasing %	79.62	31.47	6.33	0.66	33.16	120.65	147.17	0.26

Furthermore, the same conclusion can be drawn when correlating the sample injection volume with the visual observations. When 0.34 mL of 1-Hexene was introduced, only a flame was seen in the vessel without spreading explosion sound. As the injection volume was reduced to 0.32 mL, no flame propagation occurred in the vessel. The pressure changes in the test vessel accompanied by ignition of mixtures consisting of different amounts of 1-Hexene and air are listed in Table 4.7. Based on the pressure criteria, the pressure increase in the vessel after ignition of the mixture is 0.26% and 0.66% for the addition of 0.32 mL and 2.2 mL PCM respectively, which is less than 5% increase above the initial value [87]. Hence the mixture at these two points is non-flammable. Subsequently, by using Equations 3.3 to 3.6, the flammable concentration range of 1-Hexene is calculated to be 1.191%-8.042%.

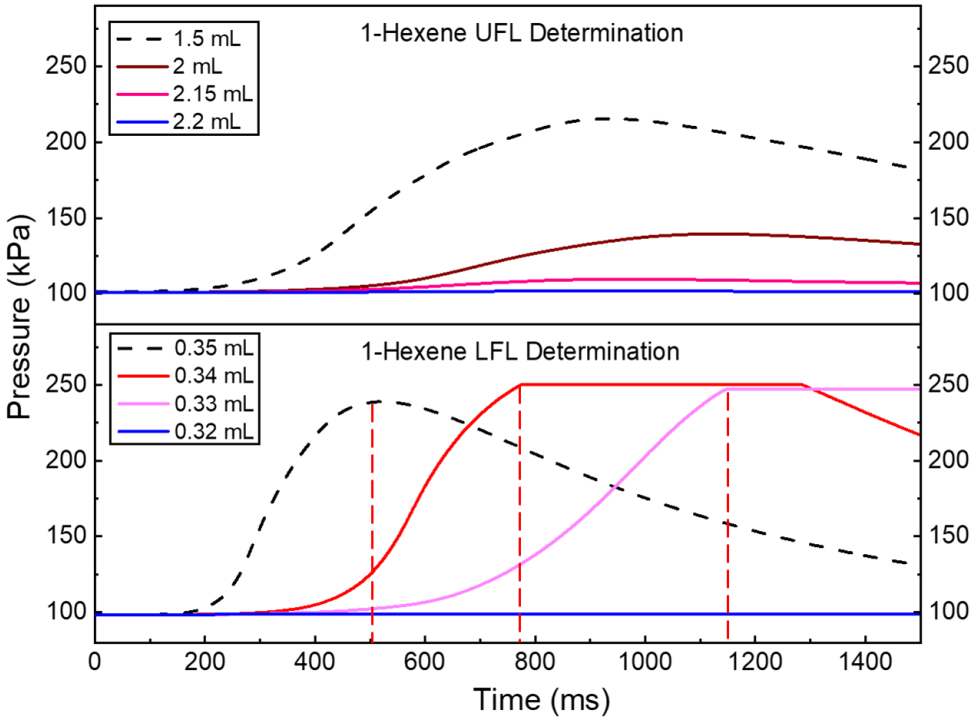


Figure 4.23: Pressure change curves in the test vessel after ignition of mixtures consisting of different volumes of 1-Hexene and air.

Similarly, both visual and pressure criteria are also used in determining the UFL and LFL of 2-

Methylbutane. In the presence of 0.34 mL and 1.9 mL PCM, the pressure increase in the vessel after ignition of the mixture is 0.19% and 2.80% respectively. The flammable concentration range of 2-Methylbutane is therefore 1.362%-7.158%.

Table 4.8: Pressure changes in the test vessel after ignition of the mixtures of 2-Methylbutane and air.

	UFL of 2-Methylbutane		**LFL of 2-Methylbutane**	
	1.8 mL	**1.9 mL**	**0.35 mL**	**0.34 mL**
Initial Pressure (kPa)	101.72	102.08	100.94	100.96
Final Pressure (kPa)	123.64	104.94	249.89	101.15
Increasing %	21.55	2.80	147.56	0.19

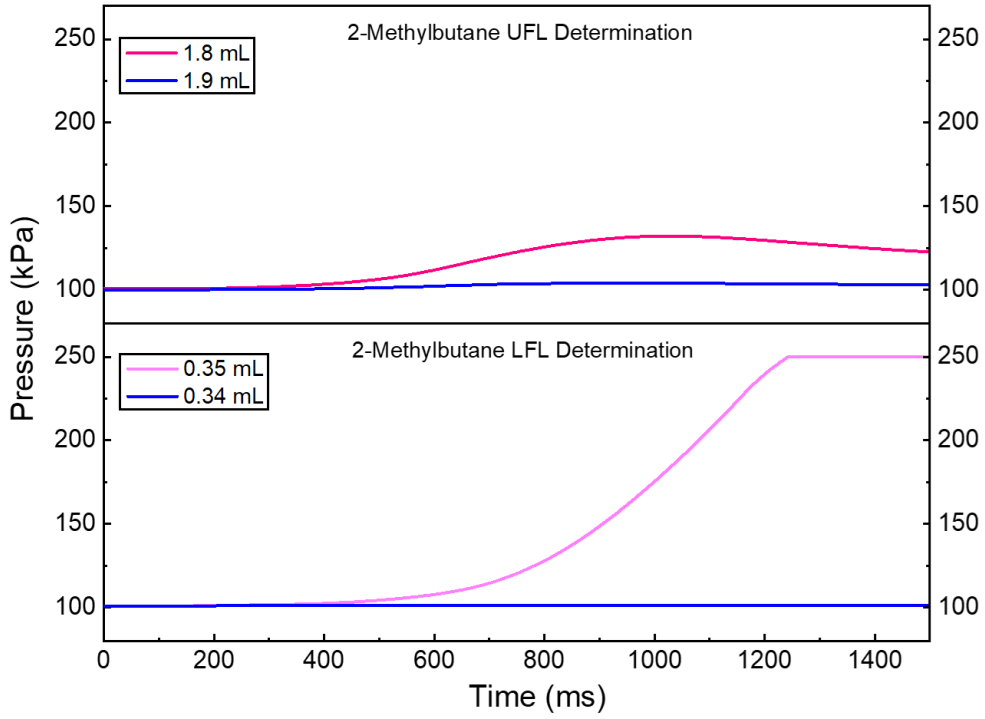


Figure 4.24: Pressure change curves in the test vessel after ignition of mixtures consisting of different volumes of 2-Methylbutane and air.

In order to mitigate the fire risk that may result from the application of these PCMs, a feasibility study was carried out on the impact of fire retardants on the flammable limits of PCM. Two different types of fire retardants were used in this work: 1) organic halogenated phosphate esters, TCEP; 2) inorganic nanoscale (with an average particle size of 16 nm) fumed hydrophobic SiO_2. Since the plateau period formed by the pressure variations and the time delay phenomenon were not observed during the UFL determination, it is hard to evaluate the effect of flame retardants on the UFL of materials. Only the LFL of modified PCMs, therefore, was tested in this study. In addition, the amount of pure PCM that provided an intense combustion on both visual and pressure criteria was selected to verify the effectiveness of fire retardants, where 1-Hexene was 0.34 mL and 0.35 mL, 2-Methylbutane was 0.35 mL and 0.36 mL.

The upper diagram of Figure 4.25 compares the pressure variations between the 0.34 mL of pure substance and the same volume of 1-Hexene mixed with different proportions of flame retardants. It can be found that the addition of SiO_2 generally results in a delay in the formation of a platform for pressure changes, and this effect becomes more pronounced as the amount of the SiO_2 added is increased from 2% to 5% (v/v) with an increase in time delay from 710 ms to 1210 ms. Although the flame retardancy exhibited by 5% TCEP is superior to that of SiO_2 at 1-Hexene volume of 0.34 mL, it exhibits an earlier time delay on the pressure change platform (~640 ms) than that of SiO_2 (~795 ms) when the sample volume is raised to 0.35 mL. This is likely to be attributed to the poor solubility of TCEP in 1-Hexene, whereas SiO_2 is comparatively easy to disperse in solution.

Figure 4.26 shows time sequence photographs of flame propagation after ignition of the mixture, which includes 0.35 mL of 1-Hexene modified by 5% SiO_2 and air. Compared with the pure material

(see Figure 4.21 (a)), the SiO_2 has a significant effect on reducing the flammability of the same volume of 1-Hexene. The light blue flame only propagates upwards from the spark igniter to the top of the test vessel, and then does not extend to the vessel wall.

According to the pressure variations listed in Table 4.9, the addition of 5% TCEP increases the LFL of 1-Hexene from 1.191% to 1.265%. For 2-Mehtylbutane, the addition of 5% either TCEP or SiO_2 results in an improvement in the low non-flammable point from 0.34 mL to 0.35 mL; see Figure 4.27. The improved flammability of 2-Methylbutane ranges from 1.401% to 7.158%. Considering its compatibility and environmental benefits, SiO_2 is regarded as a more suitable candidate for mitigating the flammability of the PCMs.

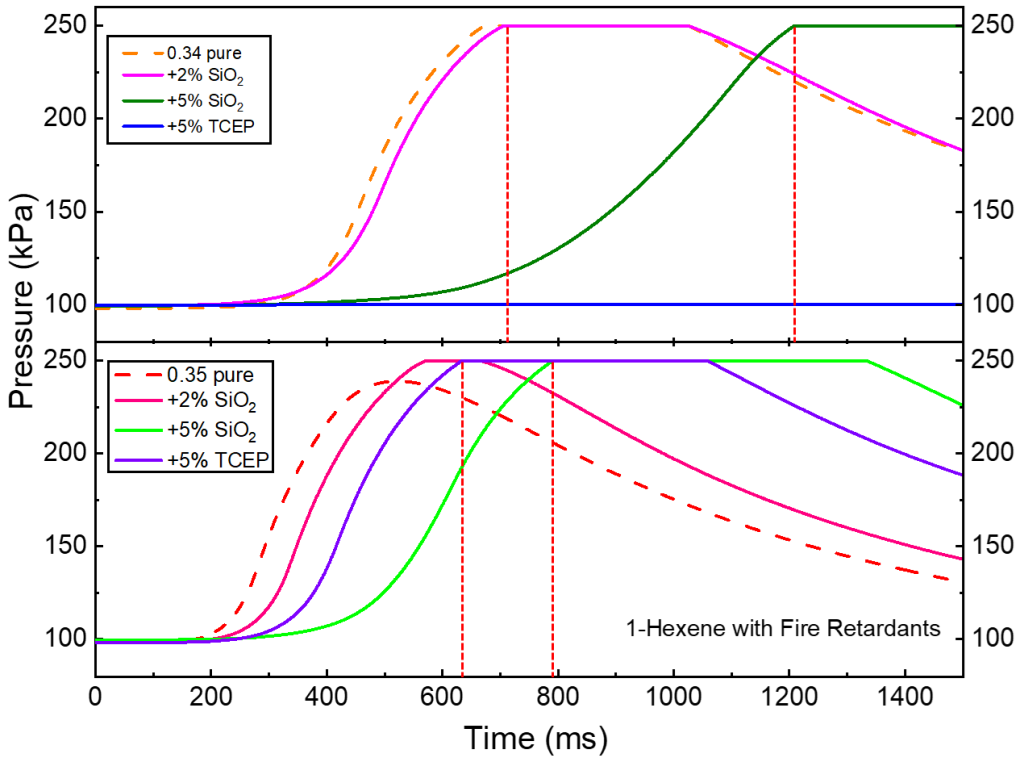


Figure 4.25: Pressure change curves in the test vessel after ignition of mixtures containing 1-Hexene modified with different fire retardants and air.

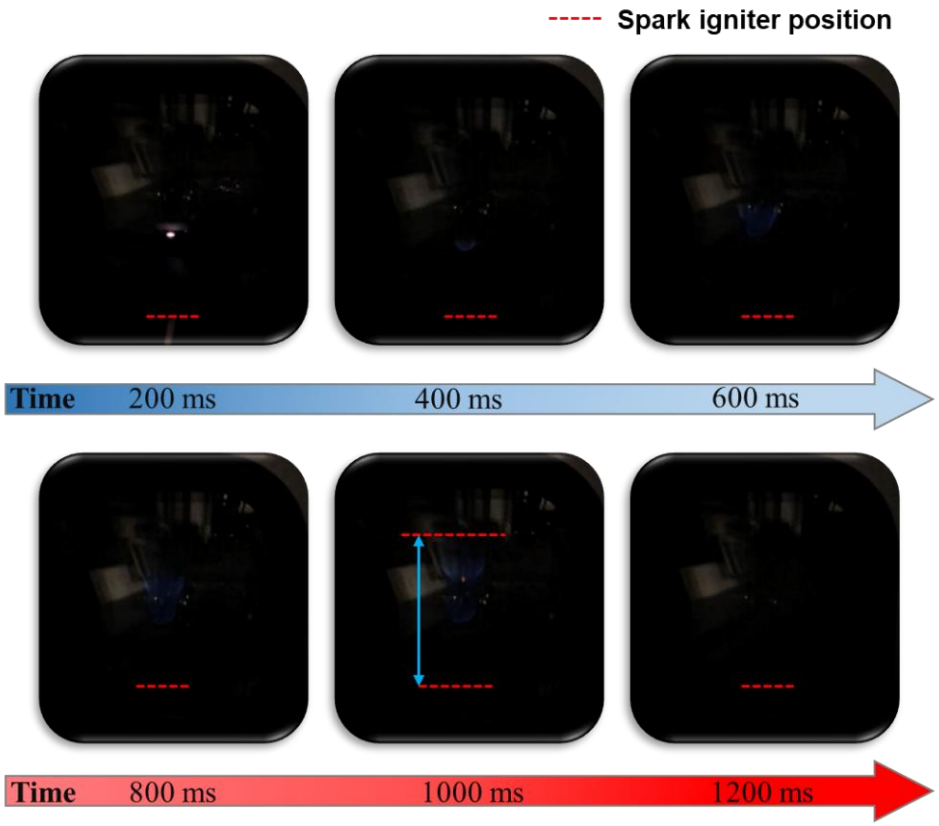


Figure 4.26: Time series photographs of flame propagation after ignition of a mixture containing 0.35 mL of 1-Hexene modified by 5% (v/v) SiO_2 and air at 25℃.

Table 4.9: Pressure changes in the test vessel after ignition of the mixtures of PCMs modified with different fire retardants and air.

	LFL of 1-Hexene				**LFL of 2-Methylbutane**			
	0.35 mL		**0.34 mL**		**0.36 mL**		**0.35 mL**	
	5% TCEP	**5% SiO_2**	**5% TCEP**	**5% SiO_2**	**5% TCEP**	**5% SiO_2**	**5% TCEP**	**5% SiO_2**
Initial Pressure (kPa)	98.2	99.73	99.59	99.33	100.8	101.11	100.96	100.67
Final Pressure (kPa)	188.42	226.17	99.89	249.89	249.89	242.92	100.98	100.81
Increasing %	91.87	126.78	0.30	151.57	147.91	140.25	0.02	0.14

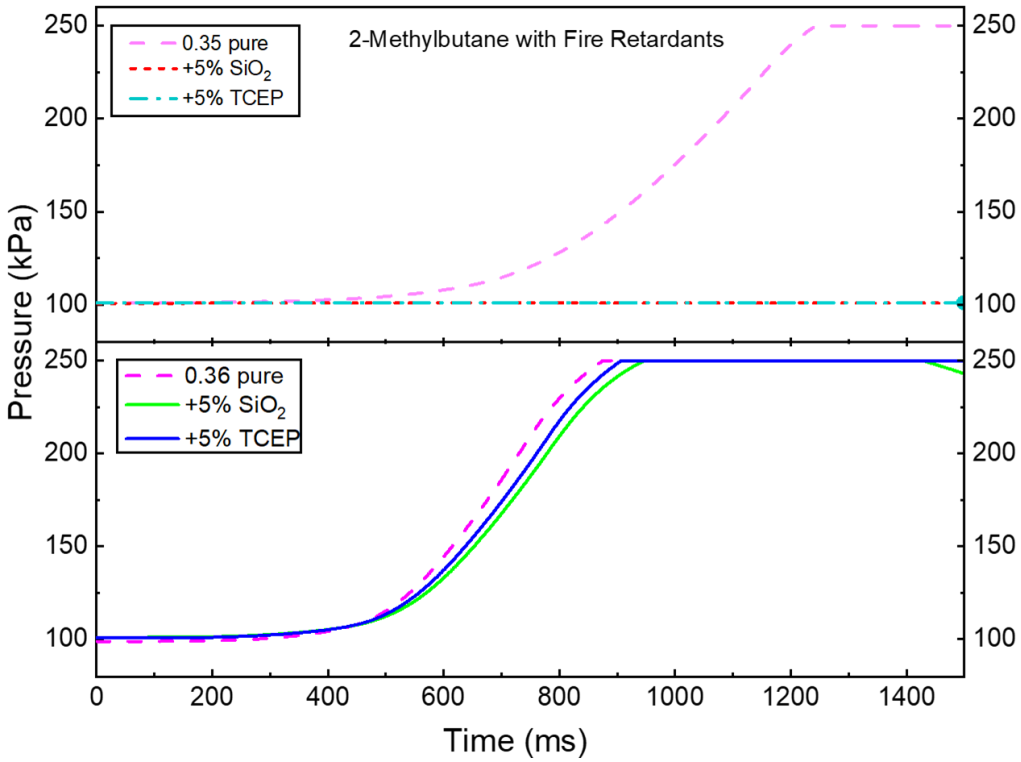


Figure 4.27: Pressure change curves in the test vessel after ignition of mixtures containing 2-Methylbutane modified with different fire retardants and air.

4.3 Alternative cryogenic latent heat storage (LHS) material

As discussed in PCM screening section, 3-Methylpentane was investigated as an alternative to LHS material. The thermophysical properties of 3-Methylpentane were therefore also determined according to the same experimental methods as used for 2-Methylbutane.

4.3.1 Phase transition temperature and enthalpy

Figure 4.28 shows the T-history measurement profile of 3-Methylpentane under the identical experimental conditions as for 1-Hexene and 2-Mehthylbutane.

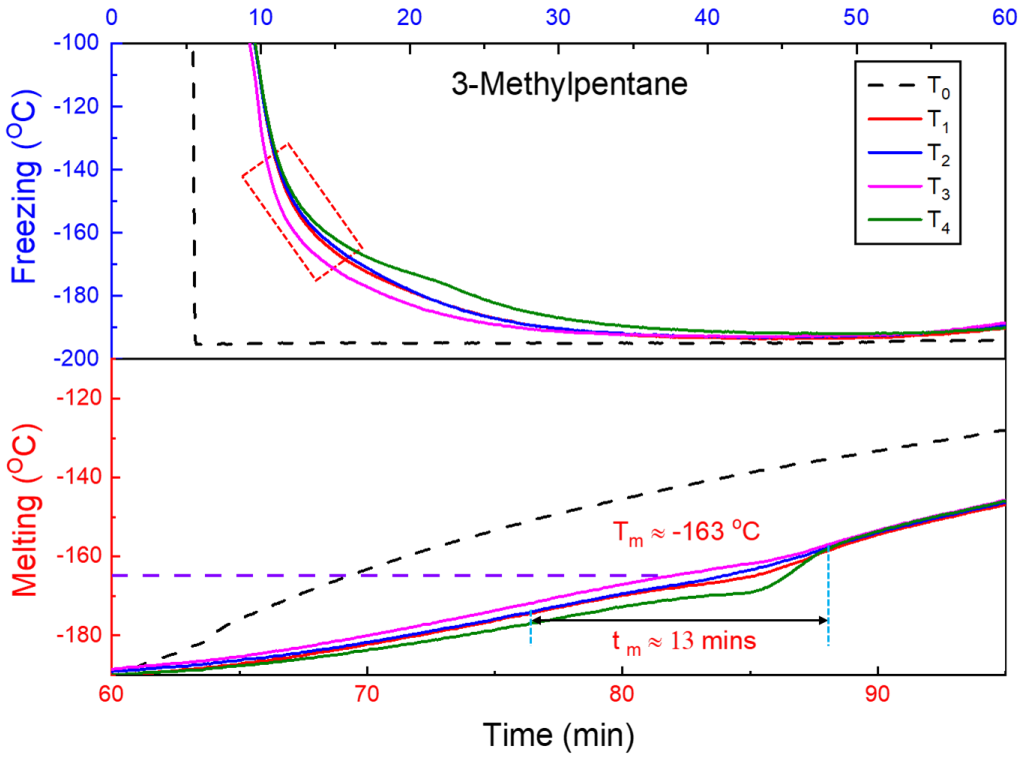


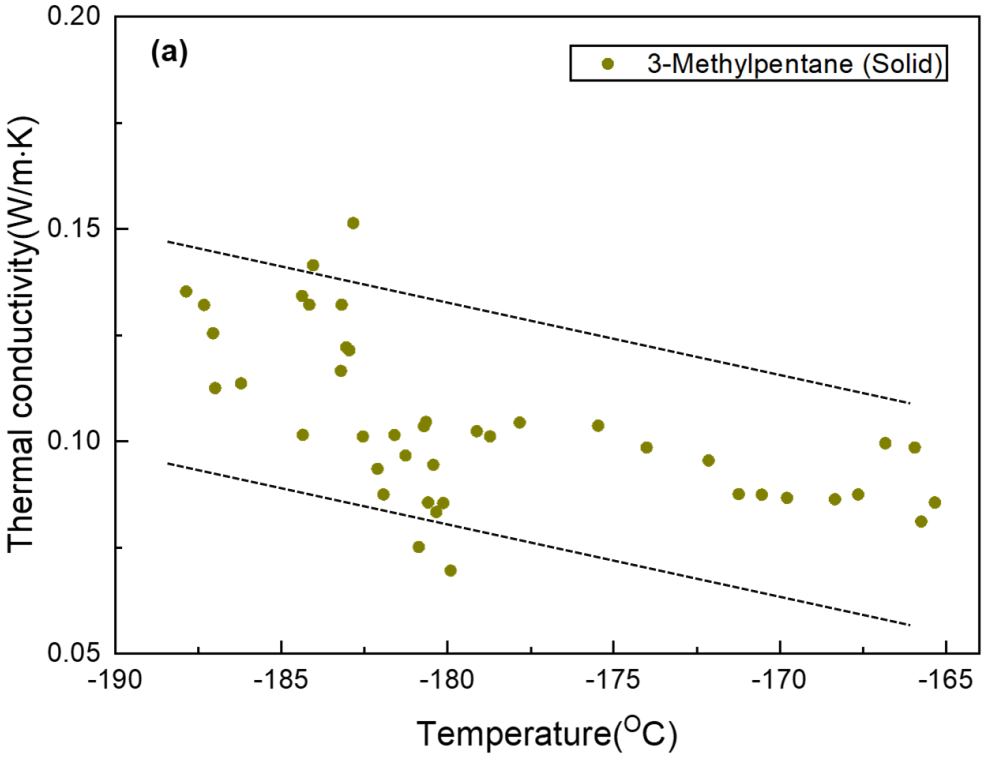
Figure 4.28: T-history measurement profile of 3-Methylpentane PCM, the upper diagram illustrates the cooling process, and the lower one shows the melting process of 3-Methylpentane.

It can be observed during the freezing process that the slope of the sample temperature curve starts to decrease at around -163℃, which indicates the onset of sample solidification. The slop drops rapidly

again as the temperature exceeds -170℃, the temperature of the solid 3-Methylpentane is attempting to reach equilibrium with the LN_2. However, no temperature platform is seen during the solidification of the sample. The lower diagram of Figure 4.28 displays the melting behaviour of 3-Methylpentane, which has a relatively short temperature plateau compared to 2-Methylbutane, lasting only about 13 minutes. Based on the under-curve area of the melting process of 1-Hexene and 3-Methylpentane, the enthalpy of 3-Methylpentane is estimated to be 60.84 kJ/kg, which is in agreement with literature data [50].

4.3.2 Thermal conductivity

Figure 4.29 (a) and (b) present the thermal conductivity results of 3-Methylpentane in the solid and liquid states, respectively. The measurement temperature ranges were -190℃ to -165℃ for the solid phase and -160℃ to -60℃ for the liquid phase.



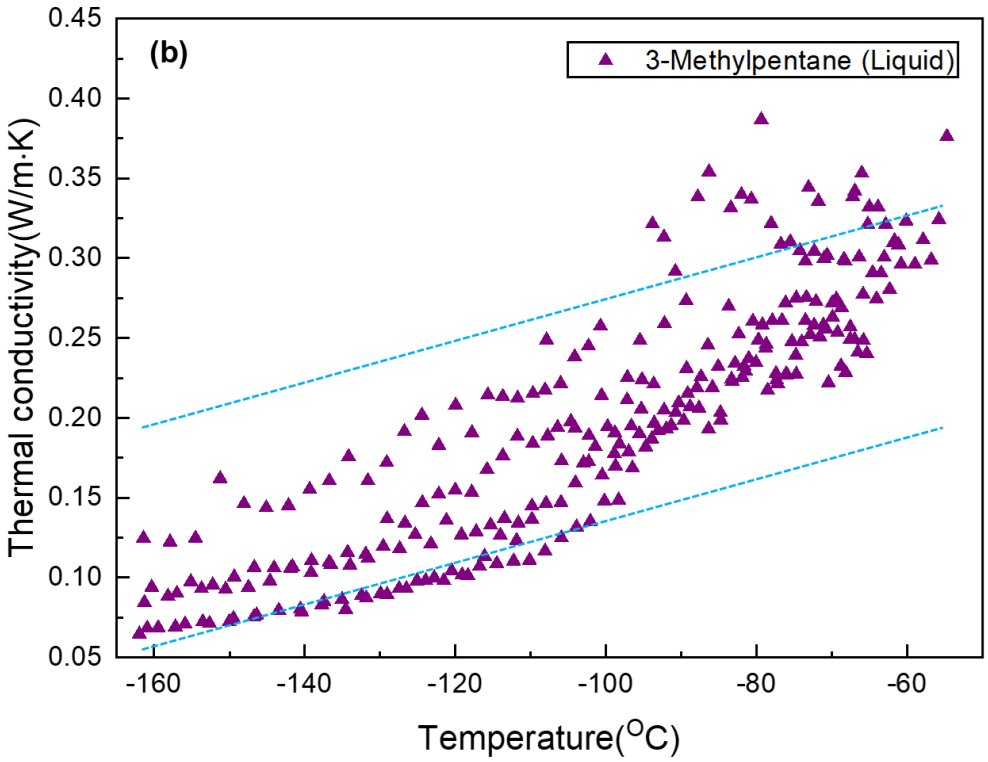


Figure 4.29: (a) Thermal conductivity measurement results of 3-Methylpentane solid phase from -190℃ to -165℃; (b) Thermal conductivity measurement results of 3-Methylpentane liquid phase from -160℃ to -60℃.

It can be seen from Figure 4.29 (a) and (b) that the thermal conductivity of 3-Methylpentane in the solid state is much lower than that in the liquid state, and the average thermal conductivities of the solid and liquid states are 0.104 W/m·K and 0.20 W/m·K, respectively. Compared with 1-Hexene and 2-Methylbutane, the solid state data are less accurate as it has the lowest phase transition temperature among these PCMs. When the test temperature approaches -100℃, the data appear to fluctuate less with thermal conductivity rising above 0.2 W/m·K.

Table 4.10: Thermal conductivity measurement results of 3-Methylpentane in both solid and liquid phases.

	Sample	Solid phase (W/m·K)	Liquid phase (W/m·K)
Average value	3-Methylpentane	0.104±0.003	0.20±0.005

4.3.3 Flammability Limits (FLs)

The same step-by-step method was used to determine the flammability limit of 3-Methylbutane. Figure 4.30 depicts the pressure change in the vessel along the ignition test of 3-Methylpentane and air mixture. It can be found that the UFL and LFL of 3-Methylpentane can be obtained by incrementally increasing the amount of material from 2.0 mL or by gradually decreasing the amount of material from 0.36 mL, respectively.

The pressure changes in the test vessel accompanied by ignition of mixtures with different amounts of 3-Methylpentane and air are listed in Table 4.11. Based on the pressure criteria, the pressure increase in the vessel after ignition of the mixture is 0.26% and 0.66% for the addition of 0.35 mL and 2.1 mL PCM, respectively, which is less than 5% increase over the initial pressure. The flammable concentration range of 3-Methylpentane is therefore 1.254%-7.299%.

Table 4.11: Pressure change in the test vessel after ignition of the mixtures of 3-Methylpentane and air.

	UFL of 3-Methylpentane		**LFL of 3-Methylpentane**	
	2.0 mL	**2.1 mL**	**0.36 mL**	**0.35 mL**
Initial Pressure (kPa)	100.67	100.59	100.31	100.27
Final Pressure (kPa)	108.17	103.42	117.84	100.29
Increasing %	7.45	2.81	17.47	0.02

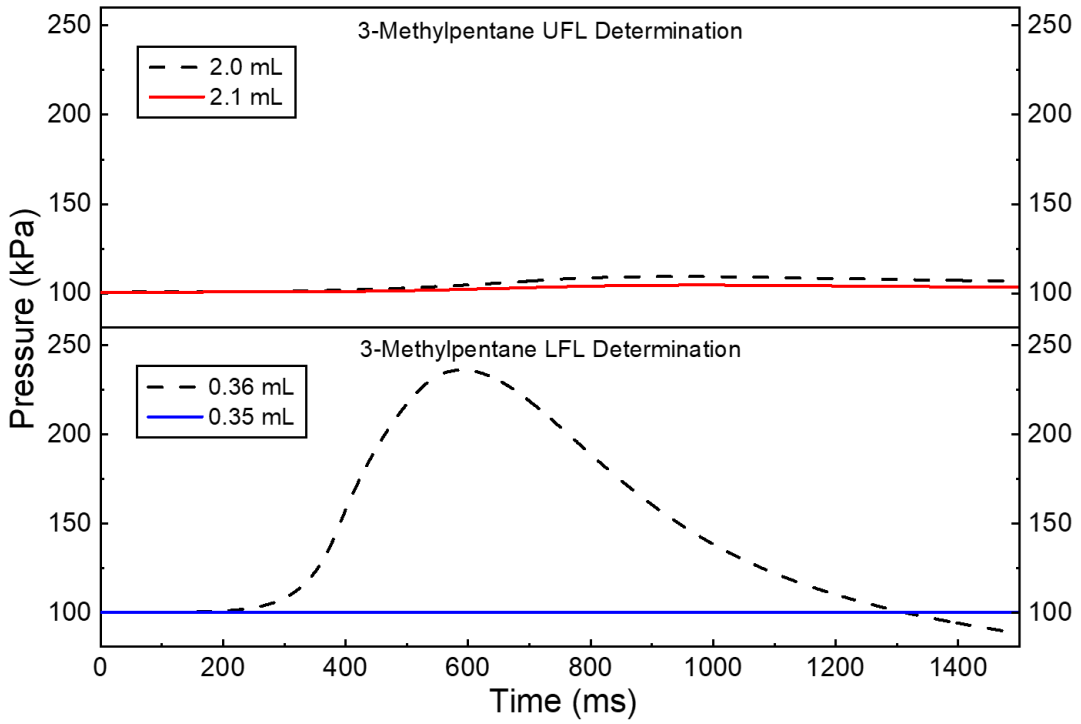


Figure 4.30: Pressure change curves in the test vessel after ignition of mixtures consisting of different volumes of 3-Methylpentane and air.

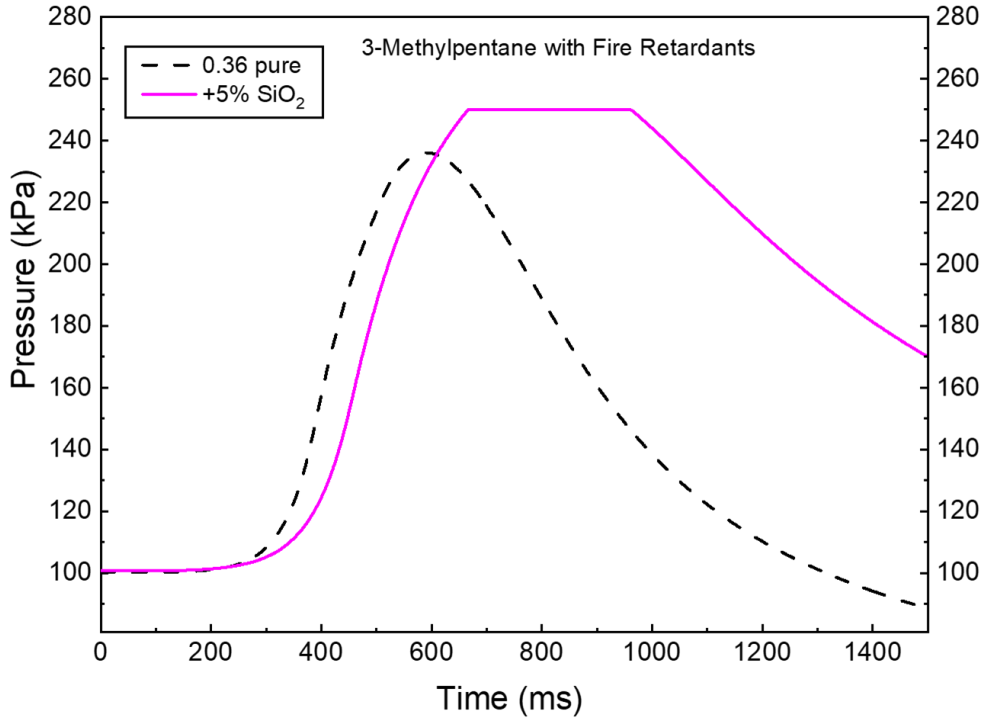


Figure 4.31: Pressure change curves in the test vessel after ignition of mixtures containing different modified 3-Methylpentane and air.

The fire retardants were also added to investigate the impact of fire retardant on the flammability behaviours. Figure 4.31 shows the pressure changes between the pure substance and the 3-Methylpentane mixed with 5% (v/v) of SiO_2. It can be seen that the time required for the vessel to reach maximum pressure is delayed backwards, and this pressure is maintained for a short while before falling, which demonstrates a clear flame retardancy. Therefore, the SiO_2 fire retardant is also suitable for mitigating the flammable behaviour of 3-Methylpentane.

4.3.4 Volume expansion

3-Methylpentane was cooled in the LN_2 bath until it underwent a phase transition. As shown in Figure 4.32, the solid volume of 3-Methylpentane is 7.95 mL. The volume expansion coefficient, therefore, is 20.5%. It can be found that the difference in volume expansion between 2-Methylbutane and 3-Methylpentane is very small, which can eliminate the influence of material variations on equipment design, and indirectly extend the range of applications for the identical heat exchange device.

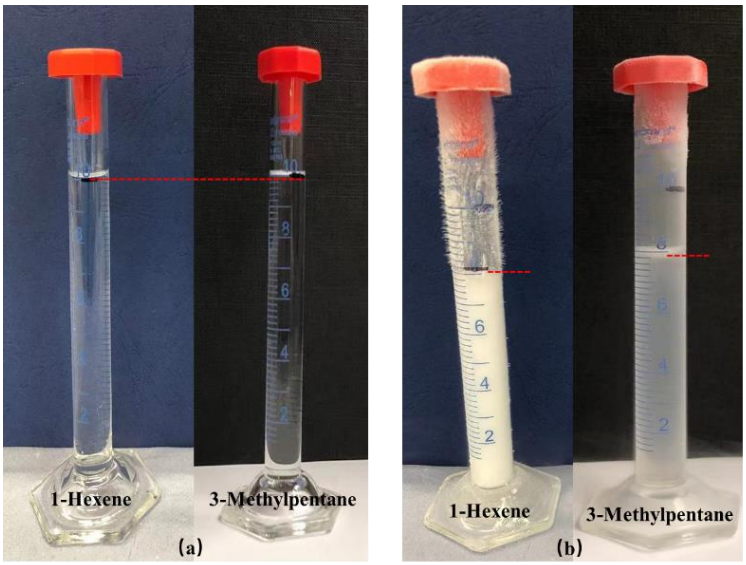


Figure 4.32: Thermal expansion determination of 1-Hexene and 3-Methylpentane: (a) PCM in liquid phase under room temperature (25℃); (b) PCM in the solid phase.

4.4 Summary

This chapter studies thermophysical properties of CTES materials for cryogenic applications. The Borosilicate glass bead was selected as a suitable SHS material due to its relatively high specific heat capacity and thermal conductivity among candidates. It is found that the temperature reduction leads to a decrease in the specific heat of materials. The data measured by DSC are fitted using a 3rd order polynomial fitting function and the fitted expression can be used to estimate the specific heat of glass beads within cryogenic temperature range. The small deviations between measured and literature values (~0.05 W/m·K) allow the thermal conductivity of the glass beads at cryogenic temperatures to be estimated from the literature.

Thermophysical properties of LHS materials are studies including energy storage density, thermal conductivity, thermal stability, volume expansion and flammability. The phase transition behaviour of sample 1-Hexene was characterised at different cooling/heating rates, the results indicate that there is a serious supercooling issue. Similarly, due to the supercooling issue, the phase transition of 2-Methylbutane results was not observed in the same DSC measurements. The T-history method, therefore, was employed for both 1-Hexene and 2-Methylbutane under the same experimental conditions. The melting enthalpy of 2-Methylbutane is obtained by comparing and calculating the under-curve arear of the melting process of 1-Hexene and 2-Methylbutane, which is estimated to be around 74.29 kJ/kg. Besides, the supercooling degree of 1-Hexene (12℃) is approximately 40% lower than the DSC results. For 2-Methylbutane, it is only 2℃. The results from the DSC and T-history measurements demonstrate that the sample volume has a significant influence on the supercooling degree. Of course, the T-history method is more realistic as it is closer to practical applications.

The thermal conductivities of PCMs in the solid and liquid states were investigated during dynamic melting process. In order to address the low thermal conductivity problem, the expanded graphite (EG) was applied as a thermal conductivity enhancer. Two different thickeners were also blended into the 1-Hexene solution to improve the stability of the EG dispersion. Both SiO_2-based (3 wt.%) and SEBS-based (2 wt.%) composites with 0.5 wt.% EG enhance the thermal conductivity of solid state by 34.5% and 38.1% compared with the pure substance, respectively. The introduction of 0.5 wt.% EG leads to an increase in the liquid thermal conductivity of both optimally modified 1-Hexene mixtures by 64.2% and 52.3%, achieving 0.248 W/m·K and 0.230 W/m·K, respectively. Besides, the time required for crystallisation of the composite PCMs is reduced due to the addition of extra particles. Although the SEBS-based composite shows a splitting peak during the melting process in the subsequent DSC measurements, its dispersion performance of the EG is superior to that of SiO_2-based composite at cryogenic temperatures. The IR spectra indicates that the mixing of 1-Hexene, EG and SEBE is a physical process. The colloid produced by the dissolution of SEBS is likely to be responsible for the appearance of the splitting melting peak. Therefore, the homogenous mixing of the composite PCM is essential in practical applications.

The long-term stability of 1-Hexene was performed by 100 complete charging and discharging thermal cycles. It shows an acceptable variation (3.16%) in the latent heat after 100 thermal cycles. Besides, the volume expansion coefficients from solid to liquid phase are 21% and 20% for 1-Hexene and 2-Methylbutane, respectively.

The flammability of pure PCMs and PCMs modified with two different fire retardants (SiO_2 and TCEP) was investigated at ambient temperature. The results demonstrate that the addition of both fire

retardants can inhibit the burning intensity of PCM. However, the flame retardancy exhibited by 5% (v/v) TCEP decreases compared with that of SiO_2 as the amount of 1-Hexene is increased. This could be due to a better dispersion of SiO_2 in 1-Hexene than in TCEP. In addition, the flame retardancy of SiO_2 is proportional to its adding amount. SiO_2 is regarded as a more suitable candidate for mitigating the flammability of the PCMs due to its compatibility and environmental advantages.

Moreover, the measured thermophysical properties of 3-Methylpentane indicate that it can be a good alternative LHS material at cryogenic applications.

CHAPTER 5

LAB TEST RIG: DESCRIPTIONS, COMPONENTS AND DESIGN

This chapter concerns with an integrated laboratory-scale cryogenic energy storage system using the CTES materials investigated and discussed in Chapter 4. In Section 5.1, the system configuration of the laboratory test rig is described. Section 5.2 explains the design of CTES components, including the LHS and SHS units, respectively. Finally, Section 5.3 introduces the auxiliary components of the test rig.

5.1 System configuration

Based on the thermal properties of CTES materials obtained in Chapter 4, an experimental system was proposed and designed to store and utilise high-grade cold energy through the integrated use of latent and sensible TES materials. The 2-Methylbutane was selected as the LHS candidate with a phase transition temperature of -160℃, and the borosilicate glass bead was chosen as the SHS material with a diameter of 2.9-3.5 mm. As shown in Figure 5.1, the system consists of two main processes corresponding to the storage and utilisation of the cold energy, which are: a) system charging process; b) system discharging process.

5.1.1 System charging process

In the system charging process, the CTES materials are cooled down from ambient temperature to cryogenic temperature as a cold energy storage process. The high-grade cold energy stored in LHS materials mainly includes two categories: 1) sensible cold energy stored by the PCM at temperatures outside the phase transition temperature; 2) latent cold energy at the phase transition temperature, i.e., the phase change enthalpy of PCM. For the SHS materials, only the sensible cold energy is stored during the system charging process. The liquid nitrogen (LN_2) is selected as the system cooling source because it is easily available and relatively safe for laboratory level experiments compared to liquid oxygen. Since the temperature difference between the PCM and the boiling point of LN_2 at the atmospheric pressure (-195.8℃) is relatively large. The pressurized LN_2 with a higher boiling point, therefore, is used to avoid the PCM being overcooled. Besides, the LN_2 first flows through the latent heat cold storage (LHCS) tank and exchanges heat with the internal PCM, see Figure 5.1, and then the evaporated cryogenic nitrogen gas (N_2) is passed into the sensible heat cold storage (SHCS) tank to

reduce the temperature of the glass beads. Therefore, two materials should reach different cryogenic temperatures at the end of the charging process. In the system downstream, the use of a gas heating system that heats up the N_2 to ambient temperature before it is removed from the system ensures that the exhaust gas is warm and safe. The degree of the system charging depends on the phase transition process of the PCM, which can be evaluated by recording the internal PCM temperature profile of the LHCS tank. Once the PCM is completely frozen and the glass beads are simultaneously cooled to a cryogenic temperature, the LN_2 supply is stopped as the end of the system charging process.

5.1.2 System discharging process

The main purpose of the system discharging process is to perform a feasibility study of the N_2 liquefaction/condensation by applying the stored high-grade cold energy. To achieve this purpose, the system operating pressure should be sufficiently high to lower the saturation temperature of LN_2, so that it can exceed the temperature of the stored cold energy in the system charging process and thus allow N_2 liquefaction/condensation to occur. The specific system operating pressure will be provided in Chapter 6, where the experimental results of the discharging process are discussed. As shown by the red line in Figure 5.1, the system discharging experiment starts from the N_2 cylinder, and ends with the gas heating system. Firstly, the pure high pressure N_2 is precooled to a cryogenic temperature in the SHCS tank. The precooled N_2 is then transferred to the LHCS tank where its temperature difference from the frozen PCM enables further heat exchange and temperature decrease to occur. Similar to the system charging experiments, the cooled N_2 fluid is heated by flowing into the gas heating system before being discharged from the system. After the cold energy provided by the PCM melting is gradually exhausted, the N_2 supply will be disconnected to complete the system discharging process.

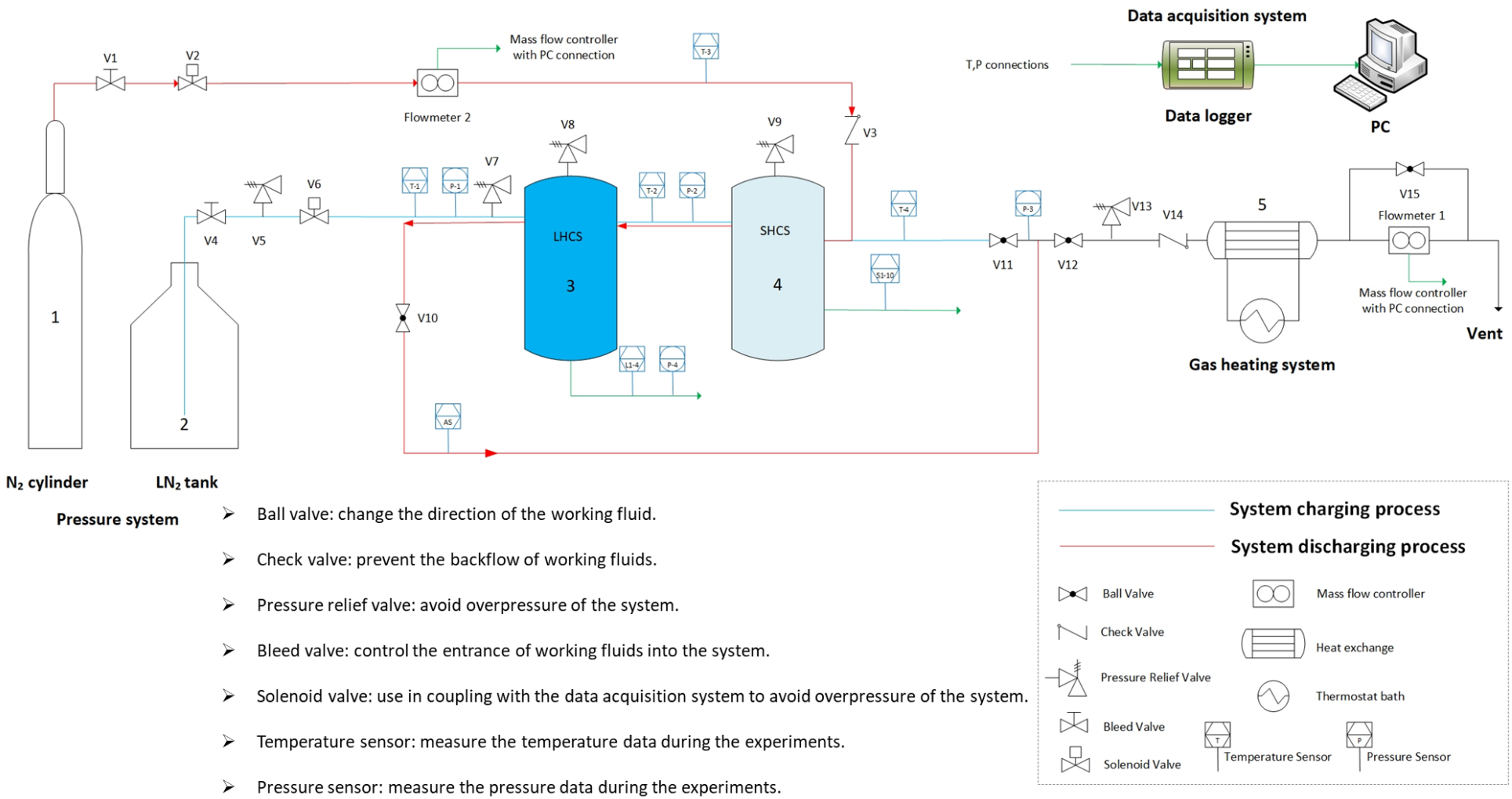


Figure 5.1: The flow chart of the experimental system to store and utilise high-grade cold energy through the application of CTES materials.

5.2 CTES components

In this lab-scale cryogenic energy storage test rig, CTES materials are packed into the LHCS and SHCS tanks to achieve high-grade cold energy storage and utilisation. During the system charging and discharging processes, phase transitions of the PCM and the HTF are involved in the LHCS tank. The one-dimensional transient tube model with cylindrical fins was proposed for the design of the LHCS tank. The SHCS tank employs the typical packed bed pattern to implement direct heat exchange between the glass beads and the HTF.

5.2.1 Numerical simulation of the LHCS tank

The design considerations for the LHCS tank are discussed in terms of fin length, fin thickness, fin gap, and tube material, respectively, according to the simulation results of the one-dimensional transient tube model with cylindrical fins as described in Section 3.3. Firstly, the model investigates the effect of inner tube diameter and mass flow rate on both heat transfer coefficients during LN_2 boiling/condensation. The effect of fin thickness and gap is then investigated under the defined flow rate and inner tube diameter constraints. Finally, the effect of different tube materials on boiling and condensation heat transfer rates is compared, respectively.

5.2.1.1 Effect of inner tube diameter and mass flow rate on heat transfer coefficient

Figure 5.2 (a) shows the correlation between the boiling heat transfer coefficient and the proportion of vapour in the two-phase flow, where the LN_2 flow rate is kept constant and only the inner tube diameter is varied. It can be found that the boiling heat transfer coefficient increases with increasing vapour quality for different inner tube diameters, and then begins to decrease when the vapour quality

is 0.7. This is due to the variation in the vapour quality which affects the two-phase flow enhancement factor (F_o) and thus changes the boiling heat transfer coefficient, as described in Section 3.3.3. Besides, it is inversely proportional to the inner tube diameter. This model also considers the effect of different mass flow rates of LN_2 on the boiling heat transfer coefficient when the inner tube diameter is kept at 4 mm; see Figure 5.2 (b). For different cases, the coefficient reaches a maximum value at the vapour quality of 0.6, and then gradually decreases. Furthermore, it is proportional to the mass flow rate of LN_2. Since the design of the LHCS tank should allow for a certain design margin, the following investigations of boiling process will therefore be based on the inner tube diameter of 4 mm, the LN_2 flow rate of 1.5 g/s and the vapour quality of 0.9.

Although the variation patterns of the condensation heat transfer coefficient are similar to those of the boiling process when varying the inner tube diameter and the N_2 mass flow rate, their changes with the vapour quality are relatively complicated; see Figure 5.3 (a) and (b). This is due to different flow regimes that are discussed in Section 3.3.3. Figure 5.4 displays the determination of the flow pattern based on the ratio of We^* to $7X_{tt}^{0.2}$. The upper part of the black dashed line is the annular flow region, and the bottom part is the slug and bubble flows region. The condensation heat transfer coefficient in the annular flow region is higher than the slug and bubble flows region, which is in agreement with the data reported by Kim and Mudawar [155]. For most cases, the change in the flow pattern form the slug and bubble flows to the annular flow corresponds to the vapour quality of 0.3. Therefore, the following investigations of condensation process will be based on the inner tube diameter of 4 mm, the LN_2 flow rate of 1 g/s and the vapour quality of 0.3.

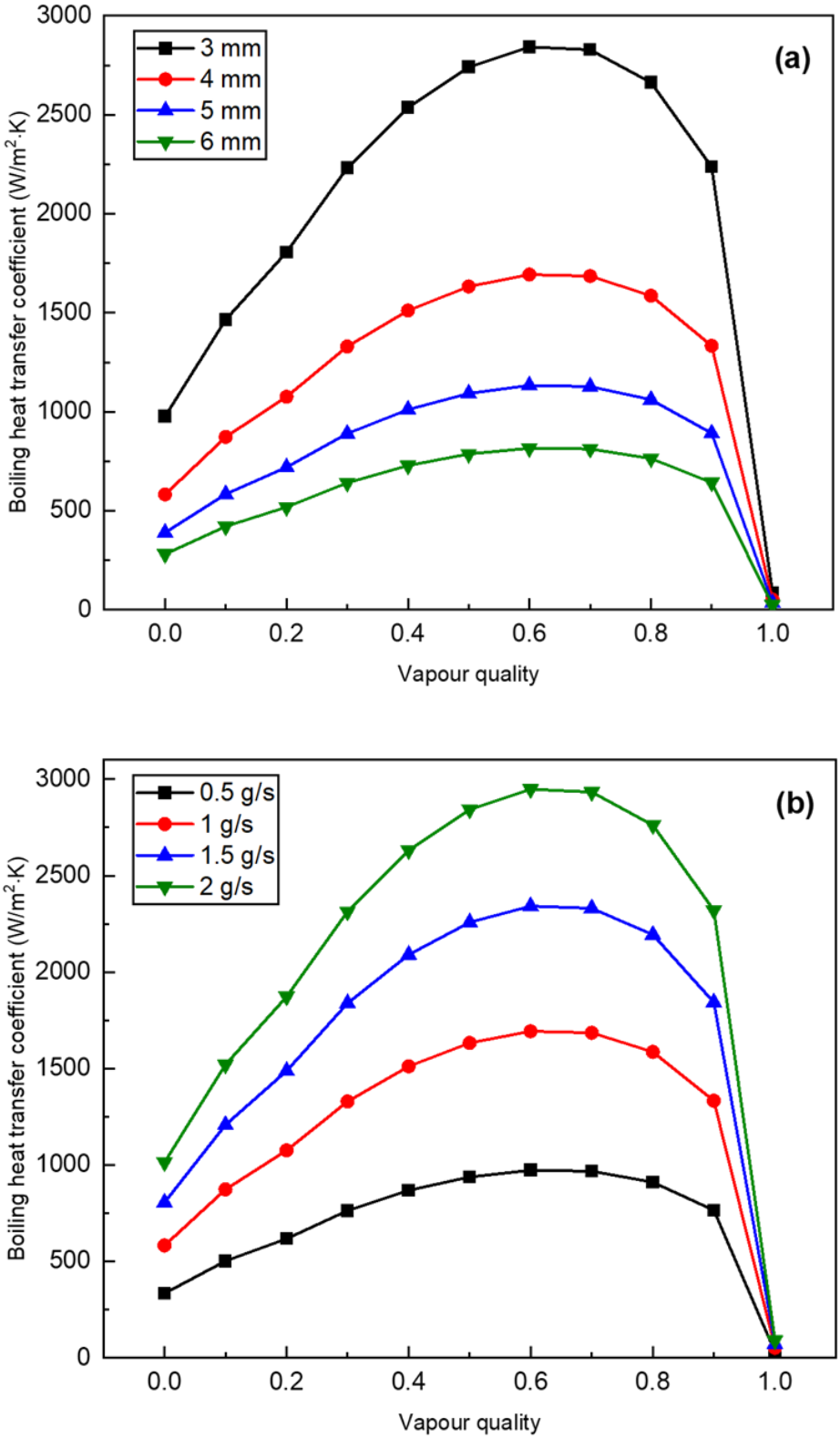


Figure 5.2: (a) The effect of inner tube diameter on the boiling heat transfer coefficient when the mass flow rate of LN_2 is maintained at 1 g/s; (b) The effect of mass flow rate of LN_2 on the boiling heat transfer coefficient when the inner tube diameter is maintained at 4 mm.

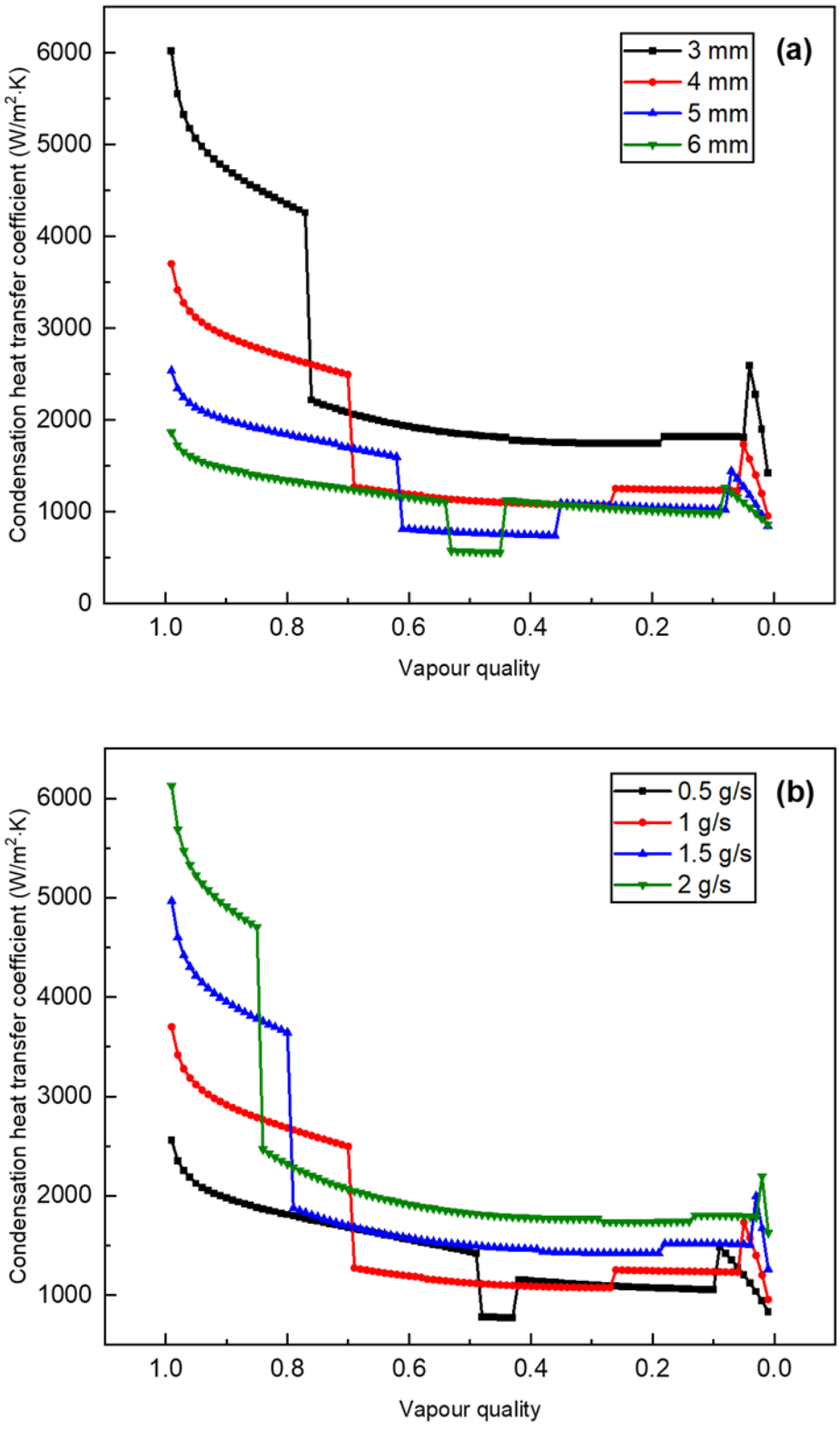


Figure 5.3: (a) The effect of inner tube diameter on the condensation heat transfer coefficient when the mass flow rate of LN_2 is maintained at 1 g/s; (b) The effect of mass flow rate of LN_2 on the condensation heat transfer coefficient when the inner tube diameter is maintained at 4 mm.

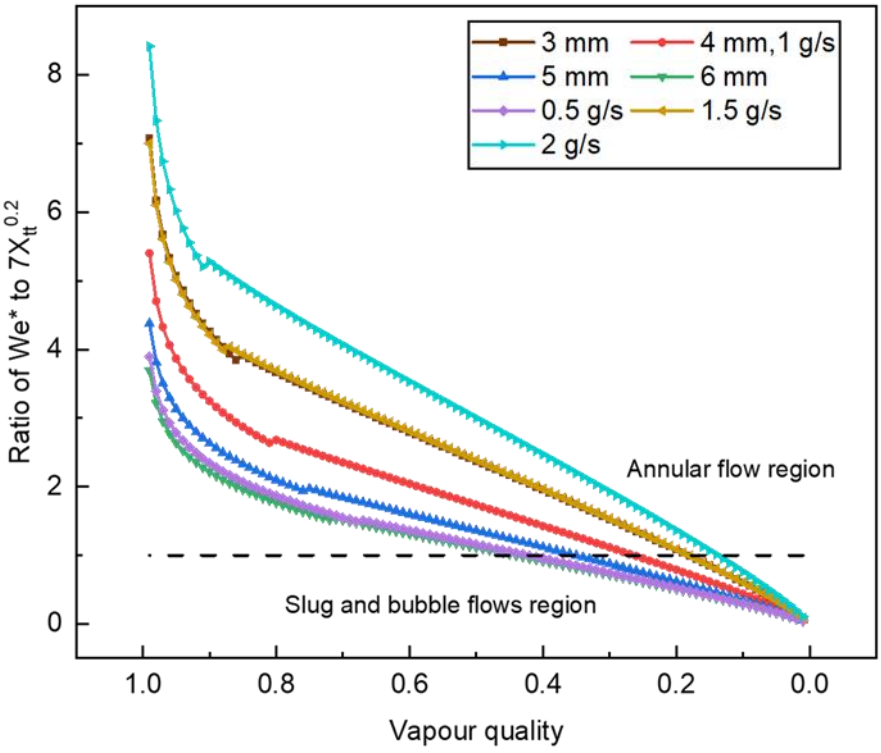


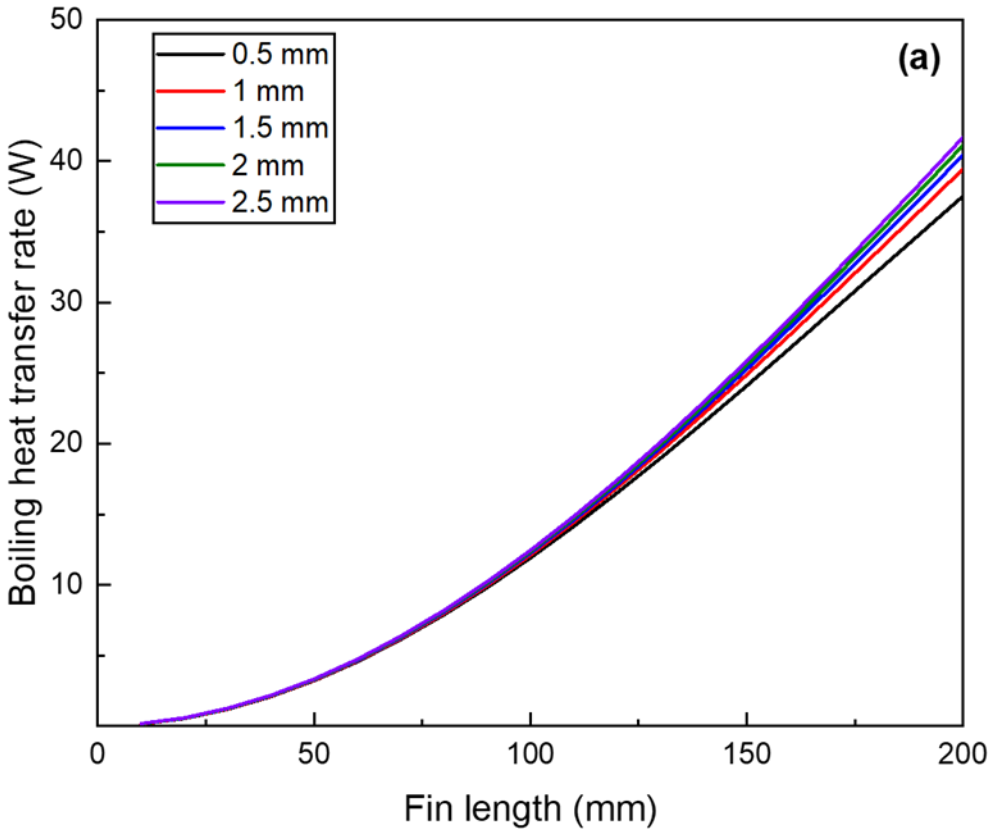
Figure 5.4: The flow pattern determination based on the ratio of We^* to $7X_{tt}^{0.2}$ in the condensation process ($We^*/7X_{tt}^{0.2} < 1$, Slug and bubble flows region; $We^*/7X_{tt}^{0.2} > 1$, Annular flow region).

5.2.1.2 Effect of fin thickness and gap on heat transfer rate

Figure 5.5 (a) shows the correlation between the boiling heat transfer rate and the fin length, maintaining the fin gap constant and only varying the fin thickness. It can be observed that the boiling heat transfer rate presents a nearly exponential growth with the increase in fin length in all cases. The maximum heat transfer rates at a fin length of 200 mm are improved as the fin thickness increases. However, this improvement is less apparent when the fins are thicker than 1.5 mm. The effect of different fin gaps on the boiling heat transfer rate is positively correlated when the fin thickness is kept at 4 mm; see Figure 5.5 (b). This means that a larger gap is more beneficial for heat transfer from the fins to the surrounding PCMs. Since the maximum heat transfer rates obtained with fin gaps of 10 mm and 20 mm are not significantly different at the fin length of 200 mm, and considering the

restricted dimensions of the LHCS tank, the fin gap is therefore maintained at 10 mm.

Similarly, the effect of different fin thicknesses and gaps on the condensation heat transfer rates are shown in Figure 5.6 (a) and (b), respectively. It can be seen that the variations in the condensation heat transfer rate with fin thickness and gap are identical to the boiling process. The obtained fin thickness and gap are therefore also applicable to the condensation process. However, the maximum heat transfer rate is far less than that of the boiling process, which is approximately 15 W. This is due to the given temperature difference between the PCM and the working fluid in the simulation. During the boiling process (system charging), the temperature difference between the LN_2 at 8.5 barg and the PCM was set at 30℃. But this value was reduced to 10℃ during the condensation process (system discharging), which meant that the inlet N_2 exceeded its saturation temperature at the corresponding pressure and was in an overheated state.



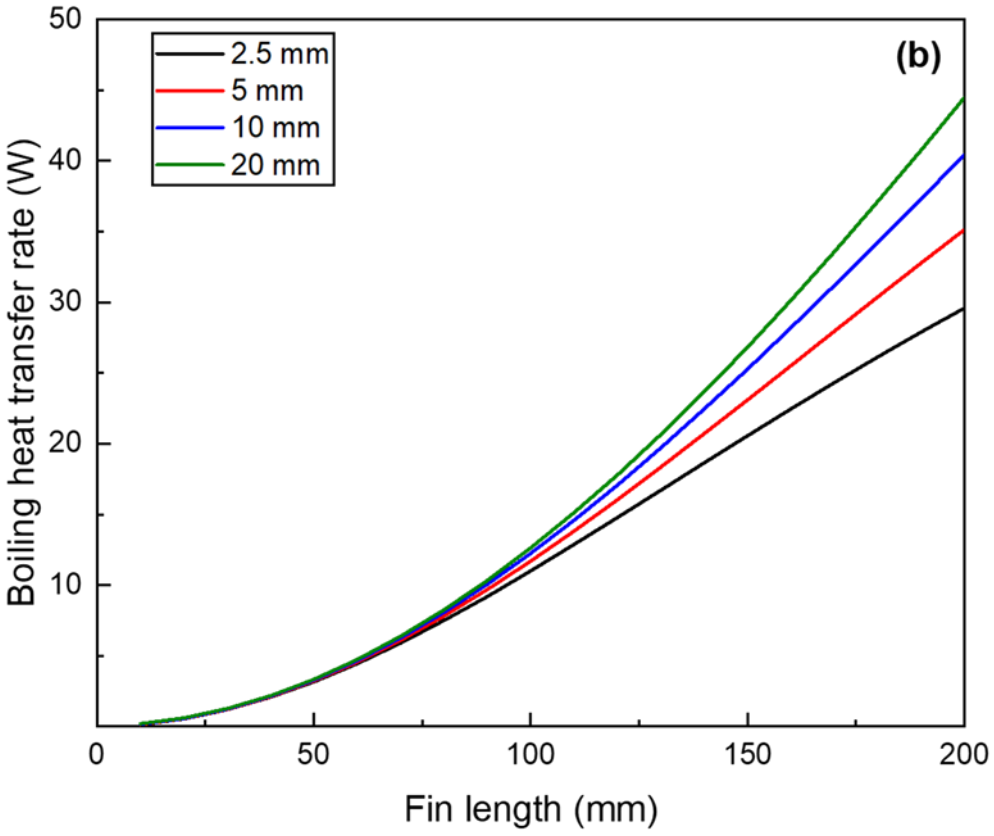


Figure 5.5: (a) The effect of fin thickness on the boiling heat transfer rate when the fin gap is fixed at 10 mm; (b) The effect of fin gap on the boiling heat transfer rate when the fin thickness is fixed at 1.5 mm.

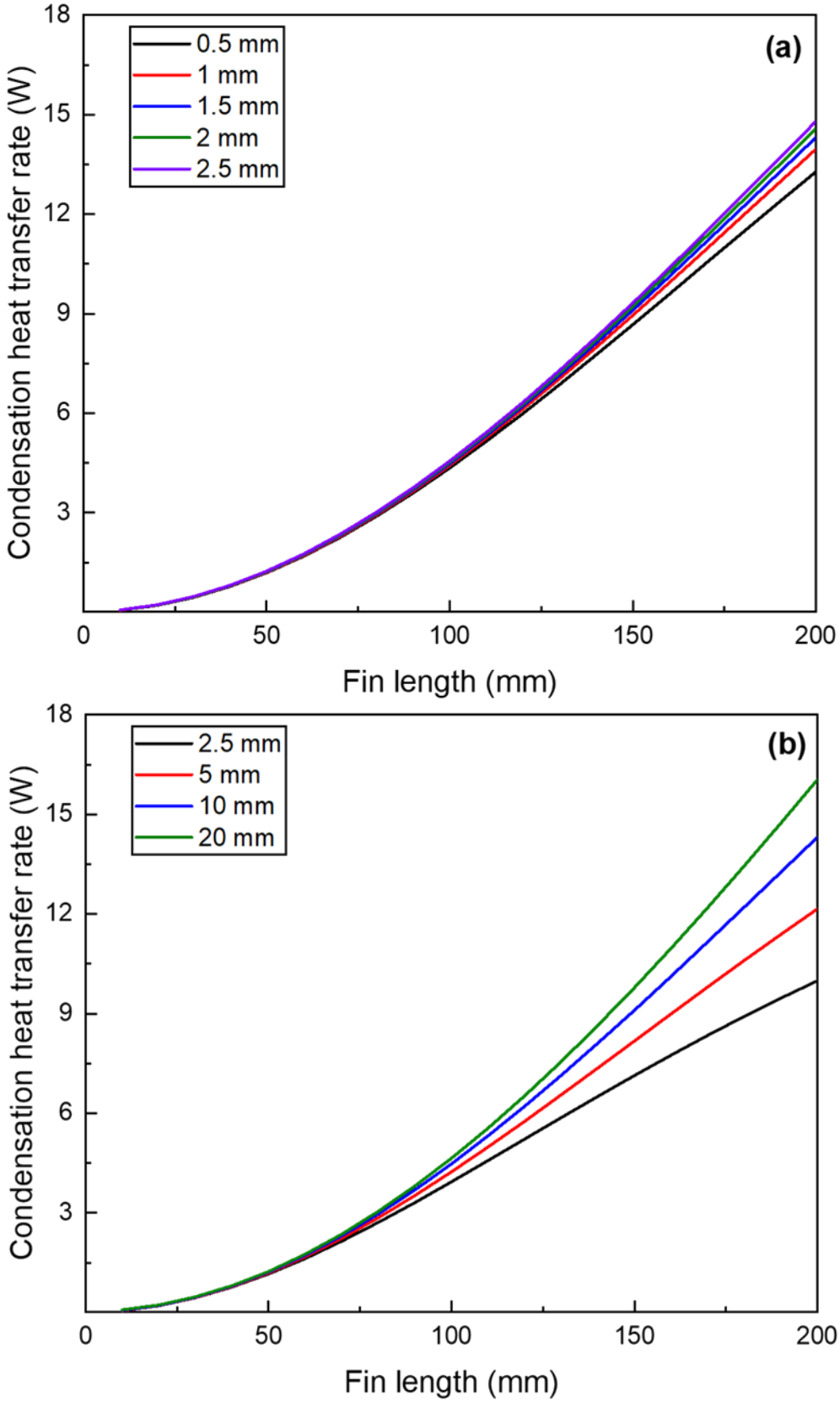
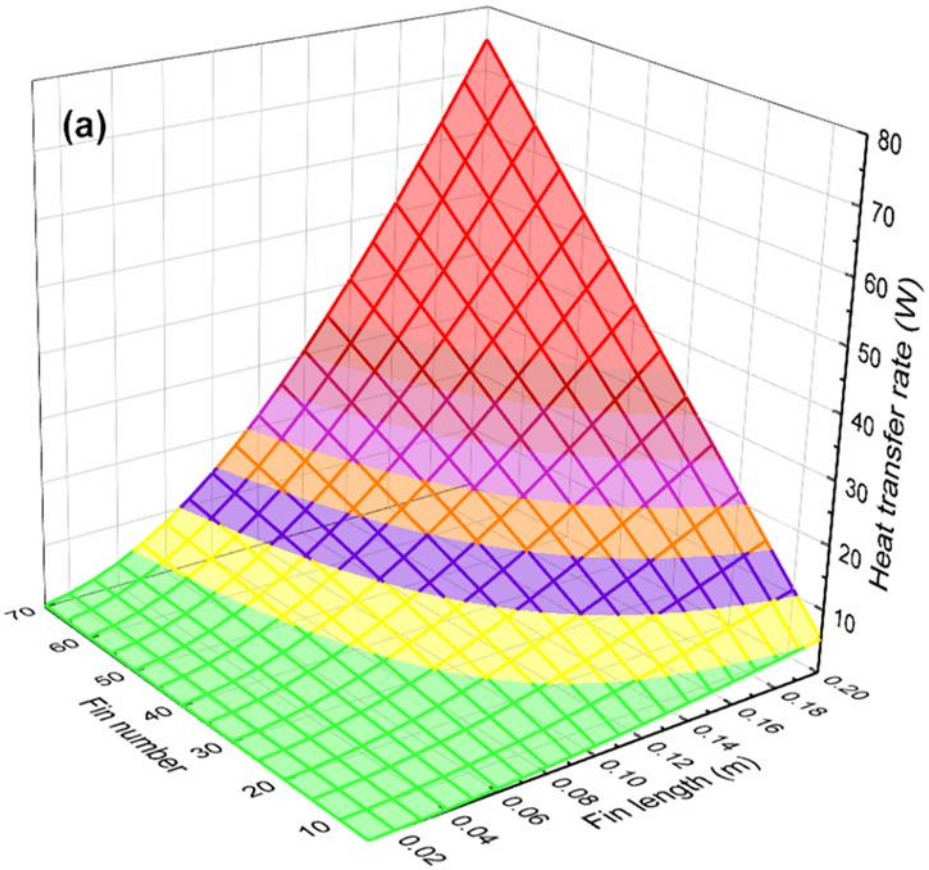


Figure 5.6: (a) The effect of fin thickness on the condensation heat transfer rate when the fin gap is kept at 10 mm; (b) The effect of fin gap on the condensation heat transfer rate when then fin thickness is kept at 1.5 mm.

5.2.1.3 Effect of different tube materials on heat transfer rate

For the boiling process, the obtained maximum heat transfer rates for different tube materials were the 73.02 W (stainless steel-304), 74.65 W (aluminium-6061) and 74.79 W (pure copper, see Figure 5.7 (a)), respectively. It can be found that the different tube materials have a negligible effect on the heat transfer rate. This model uses copper as the fin material, the tube material is also adopted copper due to material compatibility and welding intensity considerations. The overall condensation heat transfer rates corresponding to different fin numbers and fin lengths are shown in Figure 5.7 (b) for copper as the tube material. When the fin number is fixed at 10 (see red dashed line in Figure 5.7 (b)), the heat transfer rate varies from 0.044 W to 10.68 W, as the fin length increases from 0.01 m to 0.2 m, indicating that the fin length should be as long as possible. Therefore, this parameter is selected to be 0.2 m.



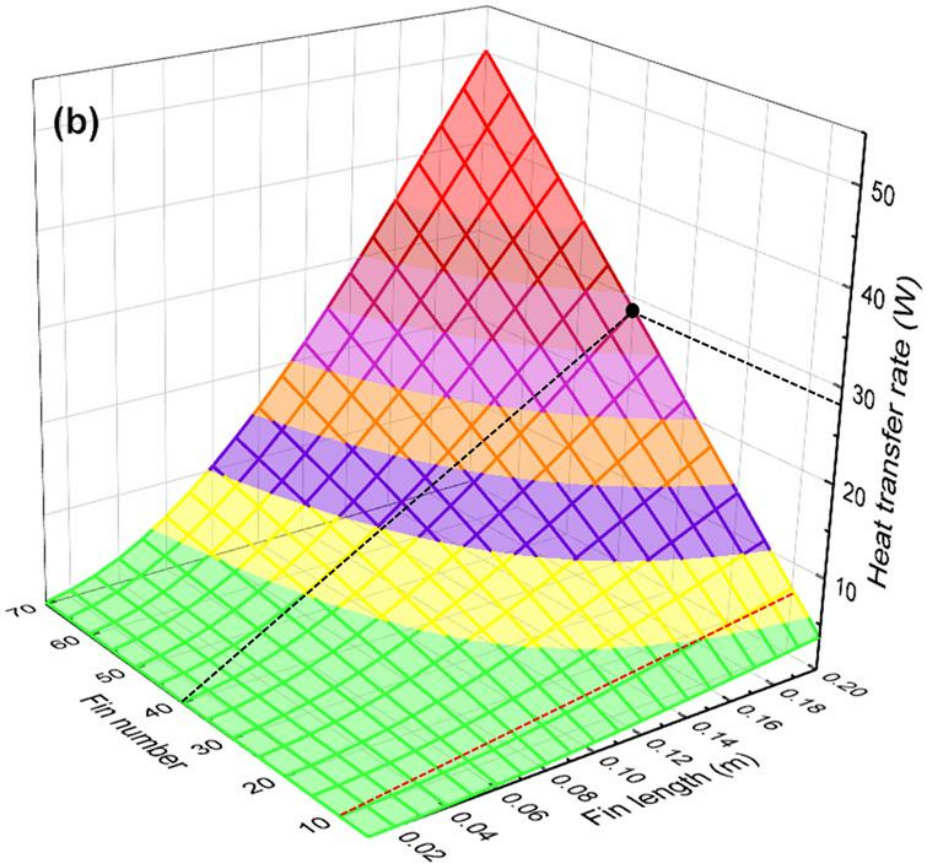


Figure 5.7: (a) The boiling heat transfer rate when the tube material is pure copper; (b) The condensation heat transfer rate when the tube material is pure copper.

Figure 5.7 (b) shows the correlation between the condensation heat transfer rate and the fin length and the fin number. The fin number can be determined using Equation 3.40 based on the known latent heat of fusion of the LN_2 at the corresponding pressure and the design required condensation rate. For instance, the black point in Figure 5.7 (b) is the required heat transfer rate for the LN_2 condensation rate of 0.5 g/s at 17 barg. The corresponding number of fins at this point is approximately 40. However, the actual required fin number may be less than the obtained value, as the above design parameters are selected based on relatively rigorous heat transfer conditions, and the temperature difference between the inlet N_2 and the PCM is highly dependent on the temperature of the glass beads after the cooling process.

5.2.2 Design of the LHCS tank

The detailed design of the LHCS tank adopts a layout in which the internal PCM vessel is contained by an external cylinder, as shown in Figure 5.8 (a). There are two main types of ports on the top surface of the external cylinder: 1) inlet and outlet of the working fluid via Ports A, B and C (see below); 2) safety port (bursting disc). Depending on the experimental process, the LHCS tank also has different inlets and outlets. Ports A and B are applied as inlet and outlet during the system charging process, respectively, while during the system discharging process, Port B becomes the inlet for the N_2 that has been pre-cooled by the SHCS unit, the outlet is made up of a 3 mm aspiration tube (AS) embedded in Port C. The other side of the aspiration tube is placed at the bottom of the U-shaped tube. The bottom Port D of the external cylinder is fitted with a thermocouple feedthrough, which allows the thermocouple to extend through the internal tube to the PCM vessel. The other side of Port D is connected to the other two ports: 1) Port E is used to install a pressure relief valve to avoid the overpressure scenario of the PCM vessel; 2) Port F is used to connect a pressure transducer to measure the internal pressure variation of the PCM vessel.

The flange section of the PCM vessel consists of three layers, as shown in Figure 5.8 (b). The top layer is used to weld the PCM vessel to the external cylinder via the inlet and outlet pipes. The chamber formed by the top and middle layers together is linked with both ends of the U-shaped tube. The working fluid entering the LHCS tank reaches this chamber first and then continues to flow into the U-shaped tube. The bottom layer is used to seal the PCM to prevent it from evaporating. In addition, a lateral movement inhibitor located at the bottom is applied to ensure that the PCM vessel can be fixed vertically within the external cylinder; see red dashed line in Figure 5.8 (a).

The practical dimensions of the LHCS tank are shown in Figure 5.8 (c). Based on the simulation results of the inner tube diameter on the heat transfer coefficient, the actual U-shaped tube is made of 0.25 inches outer diameter copper tube with a wall thickness of 1 mm. The mass flow rate of the working fluid in practical experiments is guided by the conclusion that the heat transfer coefficient is proportional to itself in both boiling and condensation processes. The simulation results also indicate that the fin thickness, fig gap and fin length are positively correlated with the heat transfer rate, which means a better heat transfer performance can be achieved as these parameters are increased. The fin thickness, fig gap and fin length are therefore set at 1.5 mm, 11.5 mm and 198 mm, respectively, based on the designed 0.5 g/s condensation rate of LN_2 at 17 barg and the overall dimensional restrictions of the LHCS tank design. In addition, it can be found that different tube materials have a negligible effect on the heat transfer rate. Thus, as with the fin material, copper is selected as the tube material. A fin stack consisting of 37 fins is strung on the outer surface of the U-shaped tube by welding, see Figure 5.8 (c), which is less than the required number of fins as discussed in Section 5.2.1.3. This is because the volume expansion of the PCM can result in some upper fins being not used appropriately. Furthermore, the fin groove with a length of 140 mm and a width of 20 mm is chiseled out in the middle of the fin to facilitate the installation of thermocouples; see Figure 5.8 (b).

Based on these detailed dimensions, the maximum PCM filling volume of the vessel can be obtained by subtracting the U-shaped tube volume (0.08 L) and the fin stack volume (1.7 L), which is around 16.5 L. Following the principle that the solid 2-Methylbutane should contain as many fins as possible to achieve a high heat transfer efficiency and its volume expansion during the phase transition is 20%, the actual amount of liquid 2-Methylbutane used to match the 37 fins was 15 L, which is less than the maximum PCM filling volume. The remaining volume of the LHCS tank was filled with air. The

pressure change within the LHCS tank due to the liquid-solid phase change of the PCM is therefore based on the atmospheric pressure.

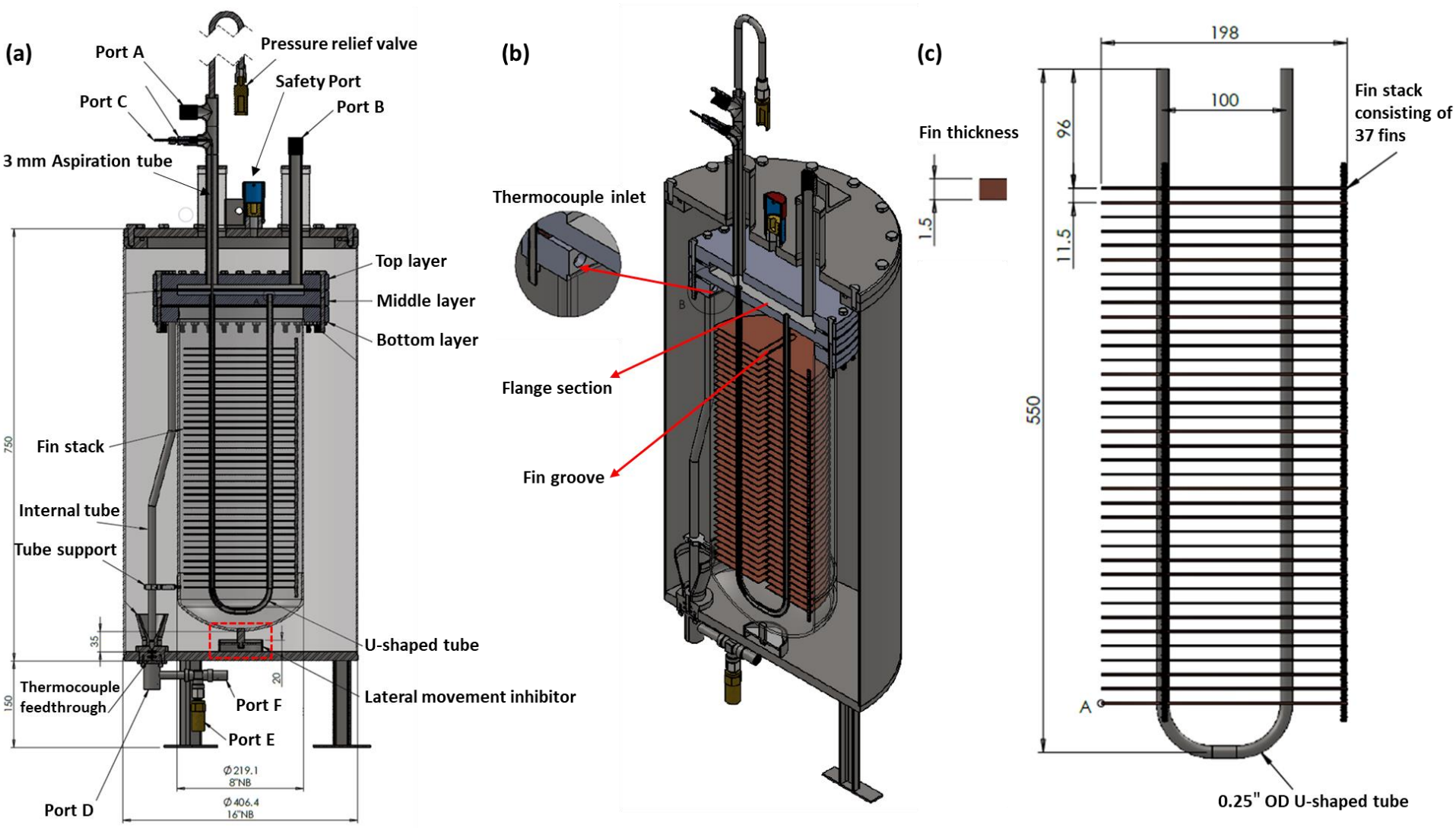


Figure 5.8: The detailed design layout of the LHCS tank (a: front view, b: three-dimensional vertical section, c: geometric dimensions of the fin stack, unit: mm).

5.2.3 Design of the SHCS tank

The detailed design of the SHCS tank also uses a layout where the internal vessels are loaded by an external cylinder, as shown in the Figure 5.9 (a) and (c), the internal vessels are fixed to the bottom flange of the external cylinder using the inlet and outlet pipeline as welded points. On the top flange surface of the external cylinder, there is a bursting disc, also known as a pressure safety disc, covered with a blue-red rubber sleeve to prevent safety problems caused by overpressurisation of the vessel during the system charging and discharging processes. This safety port is also used to connect a vacuum pump in order to create a vacuum condition among the SHCS tank prior to the experiment, which acts a thermal insulation layer to minimize the dissipation of cold energy. In addition, two thermocouple feedthroughs are arranged to connect the internal thermocouples by penetrating the vacuum chamber. Figure 5.9 (b) shows a top view of the distribution of these cylinders, which are arranged in series. As a result, the gas will flow sequentially in these cylinders to exchange heat with the glass beads. During the system charging experiment, the heat transfer between the evaporated cryogenic N_2 and the glass beads initially occurs in cylinder 1, which is therefore the coldest side at the end of the charging process. On the contrary, the ambient temperature N_2 is introduced to the SHCS tank from the cylinder 7, which is the warmest side. Figure 5.9 (a) and (b) also show the geometric dimensions of the tandem vessels from front and top views. For each cylinder, the diameter is 88.9 mm, and the height is 602 mm. Excluding the rounded upper and lower lids (51 mm), the effective material filling height is 500 mm. Therefore, the total volume that can be filled with the glass beads is 21.7 L. In practical, 30.97 kg of glass beads were filled to the internal cylinders of the SHCS tank, which corresponds to a volume of approximately 13.9 L. Thus, the overall porosity of the SHCS tank is ~0.36.

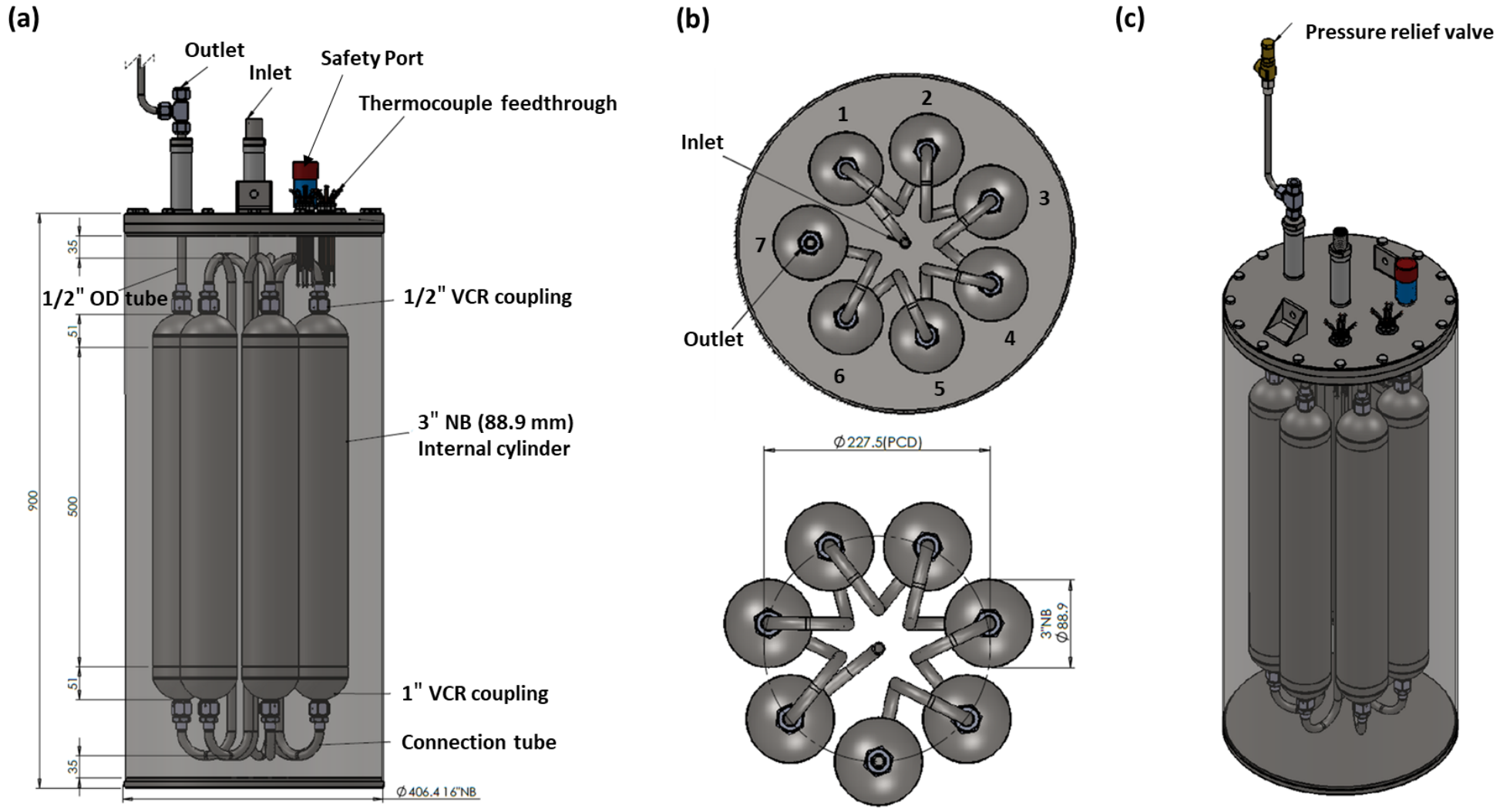


Figure 5.9: The detailed design layout of the SHCS tank (a: front view, b: top view, c: three-dimensional view, unit: mm).

5.3 Auxiliary components

Figure 5.10 shows a photography of the experimental system, which consists of the following sub-systems: the CTES system (including LHCS tank and SHCS tank), the data acquisition system, the pressure system, and the gas heating system.

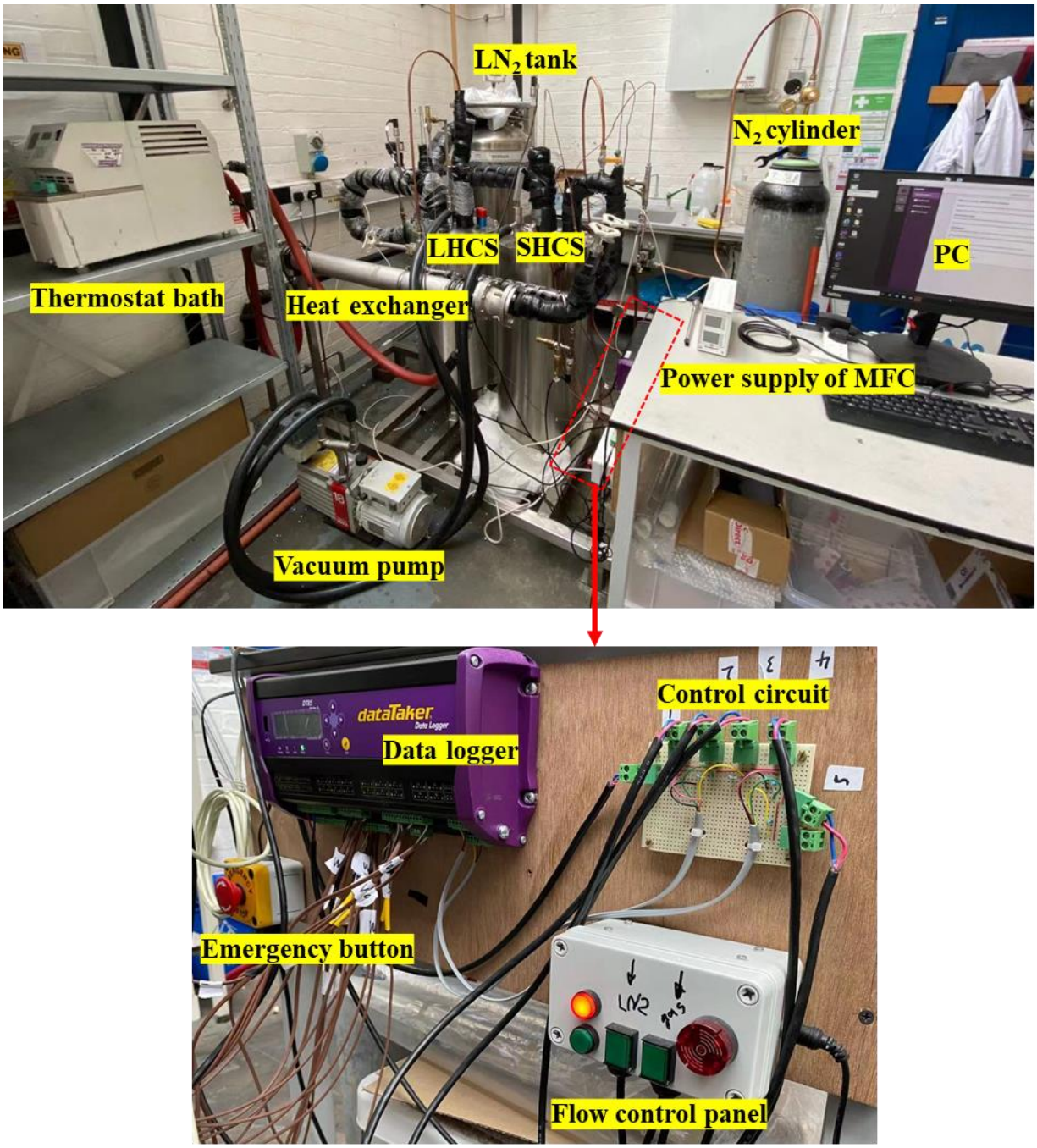


Figure 5.10: The physical view of the experimental system.

5.3.1 Data acquisition system

The data acquisition system is composed of the temperature and pressures sensors, the mass flow controllers (MFCs) and the data logger; see Figure 5.10. Thermocouples are connected to the data logger directly, while the signal of the pressure transducer is converted by the control circuit and then connected to the data logger. The mass flow rate of the system is controlled and recorded by the computer software. The data to be collected and monitored during both experimental processes are the mass flow rates of working fluids (LN_2 and N_2), the temperature profiles of main components and pipelines, and the pressure variations in the system.

5.3.1.1 Temperature measurements

Table 5.1 lists thermocouple configuration and parameters used to monitor temperature profiles of main components and pipelines. The mineral insulated type T thermocouples with a diameter of 3 mm are located at different positions in the system pipeline: the inlet of the LHCS tank (T_1), the inlet of the SHCS tank (T_2 for charging process, T_3 for discharging process) and the outlet of the SHCS tank (T_4), respectively; see Figure 5.1. The temperature data measured by thermocouples in different positions vary depending on the experimental procedure. For instance, T_2 indicates the inlet temperature of the SHCS tank during the charging process, while during the discharging process it provides the outlet temperature of the SHCS tank.

The mineral insulated type T thermocouples with a diameter of 1 mm are utilised in the LHCS tank. Due to the limited space available for thermocouples to pass through, thermocouples are arranged only at the geometric center of the LHCS tank (L_1) and at the same distance away from the U-shaped tube, but at different depths (L_2-L_4).

Table 5.1: Basic configuration and parameters on the thermocouples used for system temperature measurement.

Thermocouple configuration and parameters					
Number	**Type**	**Diameter (mm)**	**Quantity**	**Accuracy**	**Location**
1	Mineral insulated type T	3	4	±0.5℃	Pipeline
2	Mineral insulated type T	1	5	±0.5℃	LHCS tank
3	Washer type T	3.5	10	±0.5℃	SHCS tank

To determine the exact location of these thermocouples within the fin stack, a two-dimensional coordinate axis is established using the radial edge of the last fin on the bottom as the origin (O), see Figure 5.11 (a) and (b). The coordinate values (X, Y), therefore, are 100, 200 for L_1, 170, 300 for L_2, 170, 200 for L_3 and 170, 80 for L_4, respectively (mm). Besides, another thermocouple (AS) is attached to the outer wall of the aspiration tube and placed at the bottom of the U-shaped tube. It is primarily used to determine the state of the working fluid at the bottom from the temperature data during the experiment.

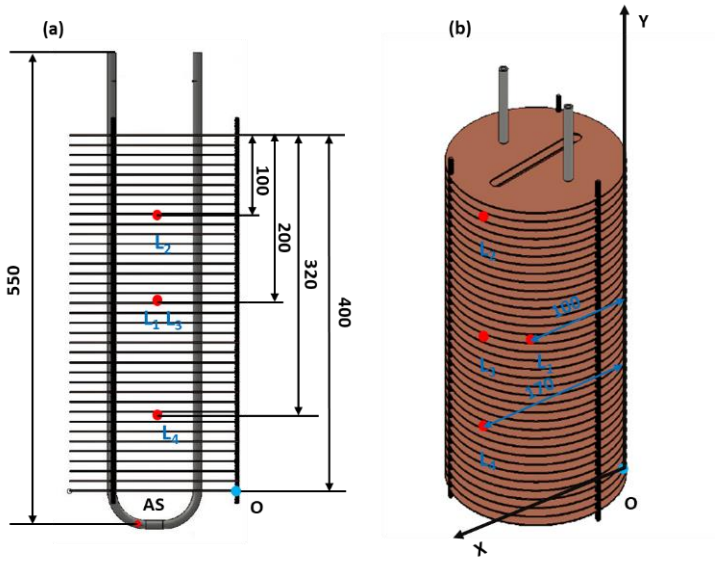


Figure 5.11: The distribution of thermocouples in the LHCS tank (a: cross section; b: three-dimensional view, unit: mm).

Different from the LHCS tank, the temperature profiles of the glass beads cannot be measured directly because the restricted space between each cylinder makes it difficult to install a feed-through device that allows thermocouples to be inserted inside the cylinder. Since the space between the internal and external cylinders of the SHCS tank is maintained under vacuum conditions during the experimental operation, only the inlet/outlet wall temperature of each cylinder and the cylinder surface temperature are measured in this context. As a result, the surface-attached washer type T thermocouples with a diameter 3.5 mm are used in different sites within the SHCS tank, as shown in its distribution Figure 5.12. The inlet/outlet wall temperature of each cylinder is measured by seven thermocouples mounted on the outer wall of the pipe by bolt connection, namely S_1, S_2, S_3, S_4, S_8, S_9, and S_{10}. Same representation as pipeline temperature, the inlet wall temperature corresponds to the system charging process, while the outlet wall temperature, in contrast, is the system discharging process. Thermocouples S_5, S_6 and S_7 are attached vertically to the outer surface of the fourth cylinder at a distance of 125 mm, 250 mm and 375 mm from the bottom, respectively.

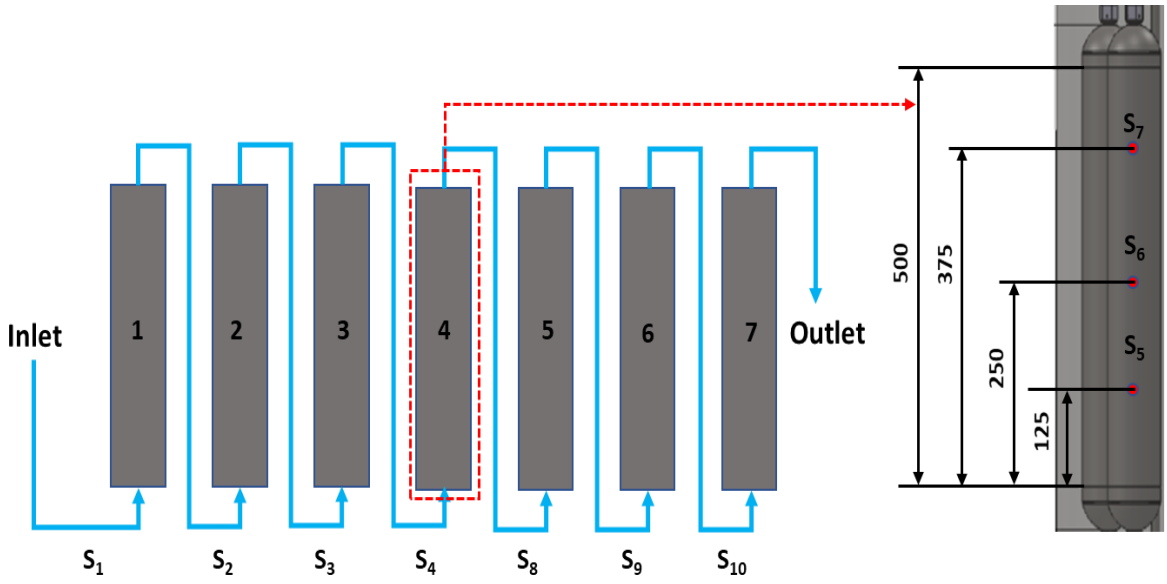


Figure 5.12: The distribution of thermocouples in the SHCS tank (unit: mm).

5.3.1.2 Thermocouple calibration

Thermocouples for temperature measurements were calibrated at six defined temperatures: -195.8℃, -30℃, -20℃, -10℃, 0℃, and 25℃. The defined reference temperatures were provided by the atmospheric pressure LN_2 bath and the temperature-controlled thermostat bath. The starting temperature was 25℃ and gradually decreased to -195.8℃. Thermocouples collected 5 minutes of data at each defined temperature. The calibration curves were then obtained by fitting a 2nd order polynomial to the average of these thermocouple readouts and the defined temperatures. Figure 5.13 shows an example of the fitted curves for one thermocouple at different locations in the system, and the R^2 values for these curves are all greater than 0.99.

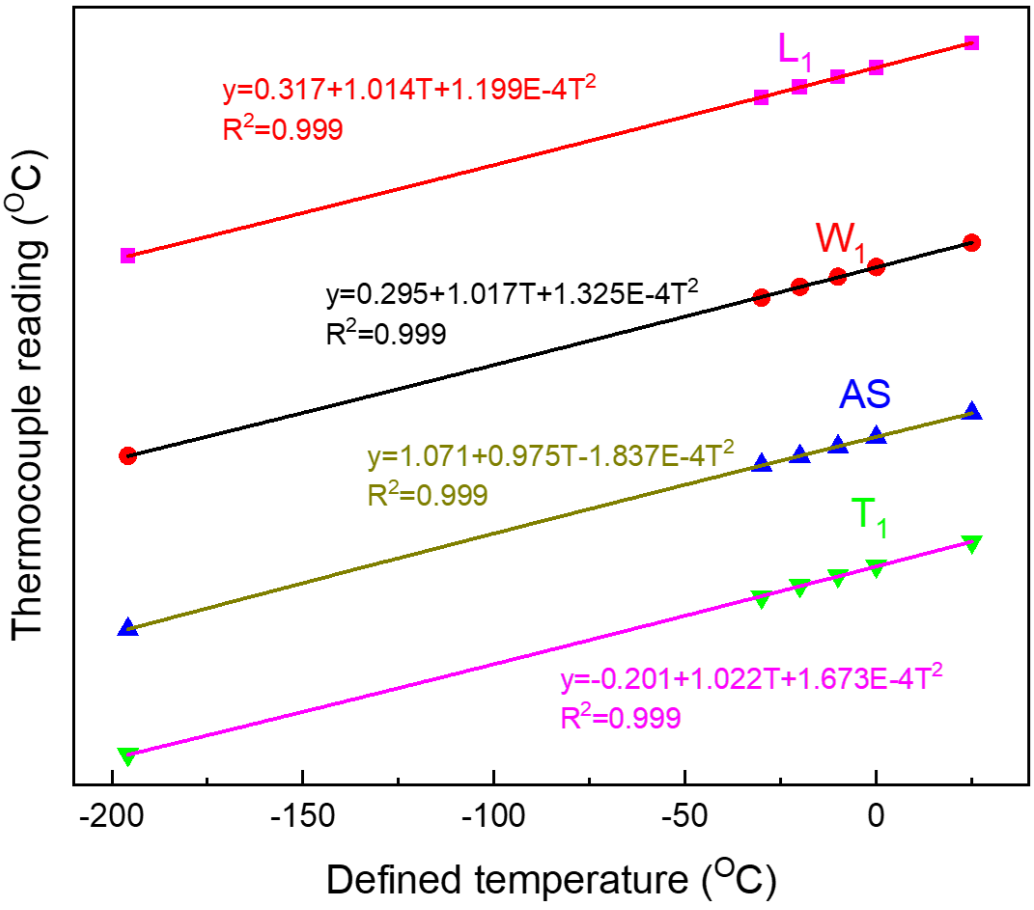


Figure 5.13: Calibration curves of thermocouples at different positions of the system.

5.3.1.3 Pressure measurements

As shown in Figure 5.1, pressure transducers with two measuring ranges are installed at different positions of the system to monitor pressure changes during the experiment. In the system pipeline, pressure transducers with a measuring range of up to 25 bar are located at the inlet of the LHCS tank (P_1), the inlet of the SHCS tank (P_2) and the outlet of the SHCS tank (P_3), respectively. In addition, the pressure transducer P_4 is directly connected to the PCM vessel inside of the LHCS tank in order to record pressure changes in the container caused by volume changes of the PCM during the system charging and discharging processes. Since its internal pressure gradually decreased from the atmospheric pressure as the PCM was cooled down, the vacuum pressure transducer, therefore, was applied in which has a relatively low mearing range of -1 to 0 bar. For both mearing ranges pressure transducers, the calibration work has been performed by the supplier to provide an accuracy of $\pm$0.5% of the full scale reading.

5.3.1.4 Mass flow rate control and measurements

Because the working fluid of this test rig undergoes phase transitions during both charging and discharging processes, the mass flow rate is used as a parameter to control and monitor throughout the experiment. There are two MFCs installed in different locations on the system: 1) MFC 1 is located at the downstream of the system, which is to record the mass of LN_2 heated by the heating system in both charging and discharging processes; 2) MFC 2 is connected to the system discharging pipeline to monitor the mass of N_2 flowing into the system. Both MFCs have been calibrated by the supplier at a calibration temperature of 20℃ and a pressure range of 10-25 barg, which can provide an accuracy of $\pm$0.5% of the reading.

5.3.1.5 Uncertainty analysis

The overall uncertainty of the experimental results (∂R) is affected by the devices used to measure various parameters (δX_n), it can be expressed by Equation 5.1 [187]:

$$\delta R = \sqrt{\sum_{n-1}^{N} \left(\frac{\partial R}{\partial X_n}\right)^2 (\delta X_n)^2} \tag{5.1}$$

The uncertainties come from two aspects: systematic/fixed errors and random errors, which can cause the results to deviate from the true values [188]. The first category refers to the lack of measurement accuracy due to inappropriate calibration, installation errors and user errors in the measurement process. These errors can be eliminated by proper calibration and correct installation of the equipment. The random errors are due to the effect of measurement fluctuations on the accuracy of results.

Based on calibration certificate reports issued by suppliers, the full-scale measurement deviations of MFCs, thermocouples and pressure transducers are 0.105%, 0.147%,0.131%, respectively. Therefore, under the conditions of this study, the overall uncertainty calculated for the charging process is 4.27% and for the discharging process is 5.12%, which can achieve a 95% confidence level [187].

5.3.2 Pressure system

The pressure source of the system is provided by a pressurized LN_2 vessel (charging process) and a N_2 cylinder (discharging process); see Figure 5.10. Figure 5.14 exhibits a general arrangement of the LN_2 vessel from top and front views, respectively. The operating pressure of the LN_2 vessel can be adjusted from 7 to 23 barg by using in combination with the pressure building regulator, the pressure building valve and the internal pressure build coil. During the system charging experiment, the

operating pressure was set to 13 barg and 8.5 barg to create a temperature difference of 5℃ and 10℃ between the saturation temperature of the LN_2 and the phase transition temperature of the PCM, respectively. However, the pressure of the LN_2 supplied by the vessel will decease as the level inside the tank decreases, which will also result in a lower saturation temperature of LN_2. This is due to the increasing amount of LN_2 that needs to be evaporated to maintain the pre-set operating pressure. As a result, there is a possibility of excessive cooling of the CTES materials used in the system during the system charging process. The specific effects will be discussed based on the results of the charging experiments. In addition, the reading of the level indicator is used to calculate the total LN_2 consumption during the system charging process.

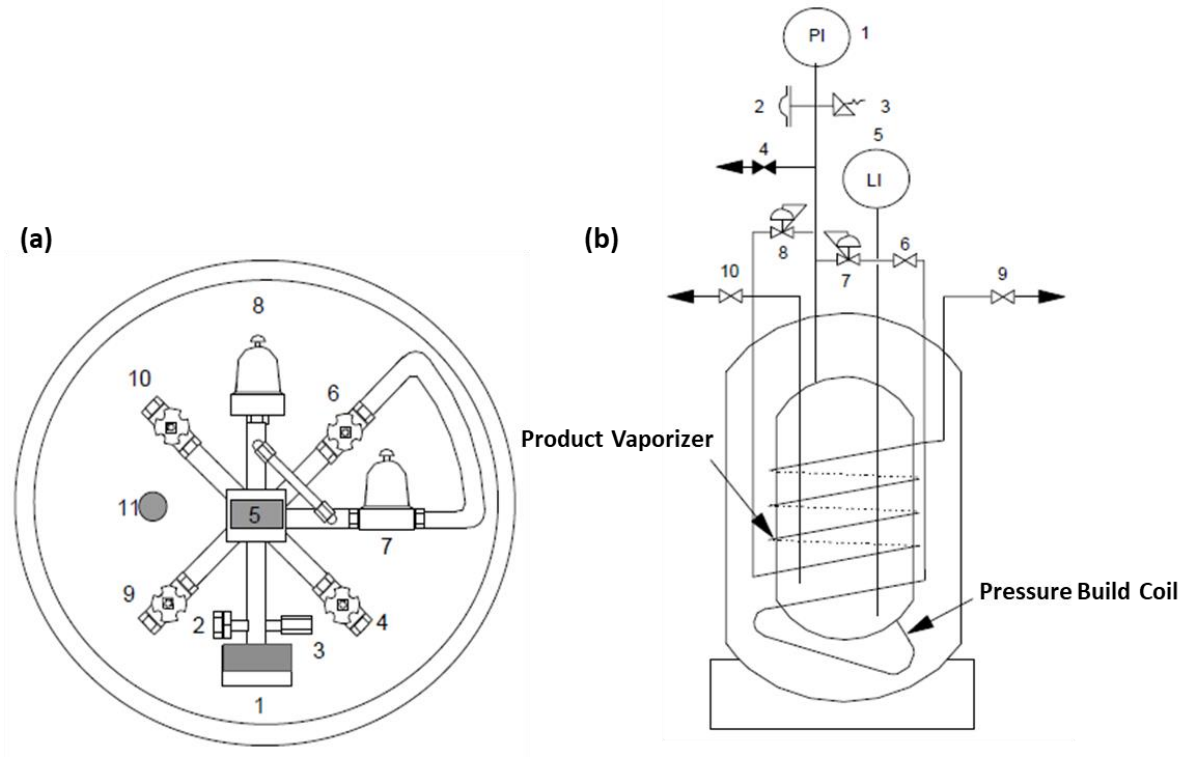


Figure 5.14: (a) Top view; (b) Front view including 1: Pressure gauge; 2: Bursting disc inner vessel; 3: Relief valve; 4: Vent valve; 5: Level indicator; 6: Pressure building valve; 7: Pressure building regulator; 8: Economizer regulator; 9: Gas use valve; 10: Liquid valve; 11: Bursting disc outer vessel.

For the system discharging process, the operating pressure is obtained by adjusting the pressure regulator of the N_2 cylinder. The pressurized N_2 is then introduced to the system at room temperature. The discharging process occurs at different pressures, more details will be given in the Chapter 6.

5.3.3 Gas heating system

To ensure that the gas exhausted from the system is at room temperature, a gas heating system is connected at the downstream of the system, which consists of a water-based heat exchanger and a thermostat bath; see Figure 5.10. Figure 5.15 shows the dimensions of the water-based shell and tube heat exchanger with a from front view (Figure 5.15 (a)) and a cross section view (Figure 5.15 (b)). The cold N_2 flows into the heat exchanger on the tube side, and the hot water fills the shell side to take the cold energy from the N_2. The thermostat bath is set to an operating temperature of 40℃ to provide sufficient heat.

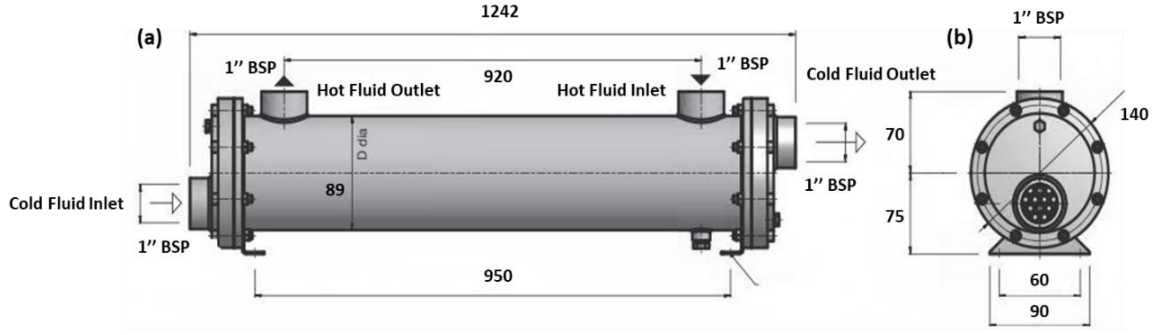


Figure 5.15: Schematic diagram and dimensions of the water-based heat exchanger (a: front view, b: cross section view, unit: mm).

5.4 Summary

An integrated laboratory-scale cryogenic energy storage system is set up based on the studied CTES materials in this chapter. Section 5.1 introduces the system configuration through the charging and discharging processes.

Section 5.2 explains the design of the CTES components of the test rig. Since the LHCS tank is the critical component of this test rig, the mathematical modelling has been performed to investigate the effect of different parameters including fin length, fin thickness, fin gap, and materials on the heat transfer between the HTF and the PCM in the LHCS tank, thereby providing guidelines for its design. Although the heat transfer coefficients for boiling and condensation vary in different patterns with the proportion of vapour in the two-phase flow, the inner tube diameter and the mass flow rate are positively related to these coefficients. The simulation results also indicate that the heat transfer rate is significantly influenced by fin thickness, fin gap, fin length and number of fins. However, the influence of different tube materials on the heat transfer rate is negligible.

In addition, the detailed descriptions of the data acquisition system, the pressure system, and the gas heating system are presented in Section 5.3.

CHAPTER 6

RESULTS AND DISCUSSION: TEST RIG EXPERIMENTAL RESULTS

This chapter discusses the experimental results of the test rig under different experimental conditions. Section 6.1 compares the system charging performance under different working pressures. Section 6.2 discusses the experimental results of N_2 condensation processes under the static and dynamic discharging processes, respectively. In Section 6.3, the system condensation capacity is evaluated during the dynamic discharging process under different working pressures.

6.1 System charging process

In the system charging process, LN_2 fluids at different pressures were applied as a cold source for cooling both SHCS and LHCS tanks. Table 6.1 lists some basic information on LN_2 for working pressures of 13 and 8.5 barg, respectively.

Table 6.1: Basic information on LN_2 during system charging process.

Pressure (barg)	Density (kg/m^3)	Boiling point (℃)	Usage amount (L)	Flow rate (g/s)
13	636.77	-165.19	110	3
8.5	670.94	-170.19	110	2

6.1.1 Charging process at a working pressure of 13 barg

The initial charging pressure in the experiment was set at 13 barg to obtain a temperature difference of 5℃ between the boiling point of LN_2 and the PCT of 2-Methylbutane. The charging process took approximately 6.5 hours, cooling the LHCS tank from -125℃ to -160℃ and the SHCS tank from -80℃ to -160℃ with a constant mass flow rate of 3 g/s. This process consumed around 110 L of LN_2 in total.

Figure 6.1 and Figure 6.2 show the temperature change of the LHCS and the SHCS tanks at different measurement positions during the charging process, respectively. In the initial stage of the cooling process, the temperature of the PCM remains almost constant. This is due to the cold energy of the LN_2 being used to cold down the system pipelines and the internal parts of the LHCS tank (U-shaped tube and fins) from ambient to cryogenic temperatures. Therefore, temperature changes in the PCM

require time to be observed. After around 1 hour of the charging process, the PCM temperature shows a significant downward trend. Simultaneously, the inlet temperatures of each cylinder in the SHCS tank have reached a lower temperature level, indicating that the glass beads have been excessively cooled. Therefore, the extended spindle needle valve (V10) was opened after one hour of the charging process to change the path of LN_2 through the system to avoid overcooling of the SHCS tank, while continuing to cool the PCM. However, this operation inevitable caused the waste of cold energy from LN_2, so the mass flow rate was reduced to 1.5 g/s. The fluctuations due to this operation are that the PCM temperature is not falling rapidly, showing a steady trend. Whereas, the bottom U-shaped tube temperature (AS) gradually increases, as indicated by the red dashed line in Figure 6.1. This is because the warmer N_2 inside the SHCS tank flows into the U-shaped tube due to the change in charging path. With the system thermal equilibrium being re-established, the AS temperature returns to approximately -165℃, while the PCM temperature begins to decrease further, eventually forming a platform near its phase transition temperature of -160℃.

For the SHCS tank, the overall temperatures decrease dramatically before changing the charging path; see Figure 6.2. This could be due to the poor vacuum condition between the internal and external cylinders, thus resulting in a sharp change in the overall temperatures of the SHCS tank. This assumption is also corroborated by the frost on the outer cylinder wall as observed during the practical experiment. Such poor vacuum condition may lead to inaccurate temperature measurements of the glass beads. After changing the charging path, the inlet temperature of the SHCS tank T_2 (see Figure 6.4) gradually increases, causing the glass beads to be heated. The coolant path was therefore changed to continue cooling the SHCS tank after around 5 hours of the charging process.

The change in coolant path during system charging process can also lead to the system pressure to increase up to 14 barg and then decrease down to 13 barg; see Figure 6.3. Since the system pressure and the saturation temperature of LN_2 are positively correlated, and the AS temperature approaches the saturation temperature of LN_2 when the system is at steady state. Therefore, the fluctuations in the system pressure can also be monitored by variations in the AS temperature. In Figure 6.4, the inlet temperature of the LHCS tank T_1 displays an unreasonable reading at the beginning of the charging process, even higher than T_2. This is because the pipeline thermocouple was not installed against the inner wall of the pipe, but was placed in the centre of the pipe. The mass flow rate used in the charging process did not allow the LN_2 to completely fill the pipe, so T_1 was actually measuring the temperature of cold N_2.

Apparently, such working pressure (13 barg) and LN_2 flow rate (3 g/s) are not an appropriate operating condition of the system charging process. Because these operating conditions can cause the SHS material to be excessively cooled, and this issue is due to the fact that 2-Methylbutane has a lower thermal conductivity than glass beads and requires a longer time to fully charge. Although changing the heat exchange path of the LN_2 can achieve the expected system charging process, it can also lead to severe system fluctuations and significantly reduce the utilisation of cold energy. Hence, the working conditions of the system need to be optimised to obtain improved cooling performance. According to the existing test rig configuration, a feasible solution to weaken the impact of this non-synchronous heat transfer between the PCM and the glass beads on the system cooling performance is to reduce the working pressure and the LN_2 flow rate. Because the lower working pressure can offer a greater heat transfer gradient between coolant and materials. In addition, the lower LN_2 flow rate means that the heat transfer time is increased, and thus more cold energy can be stored.

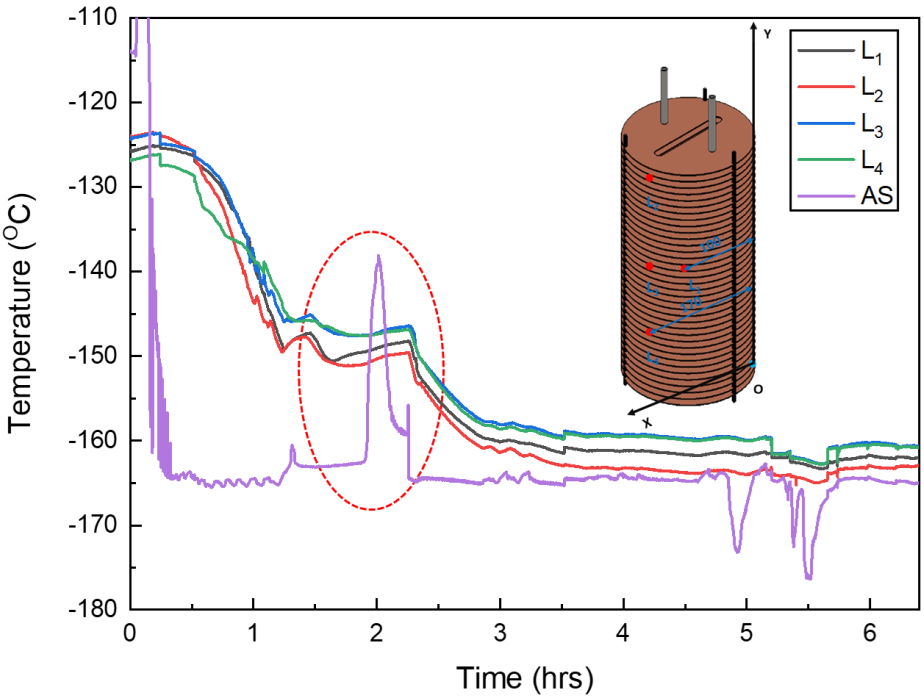


Figure 6.1: Temperature variation curves of the LHCS tank during the charging process at a system pressure of 13 barg (The distribution of thermocouples is illustrated in the legend).

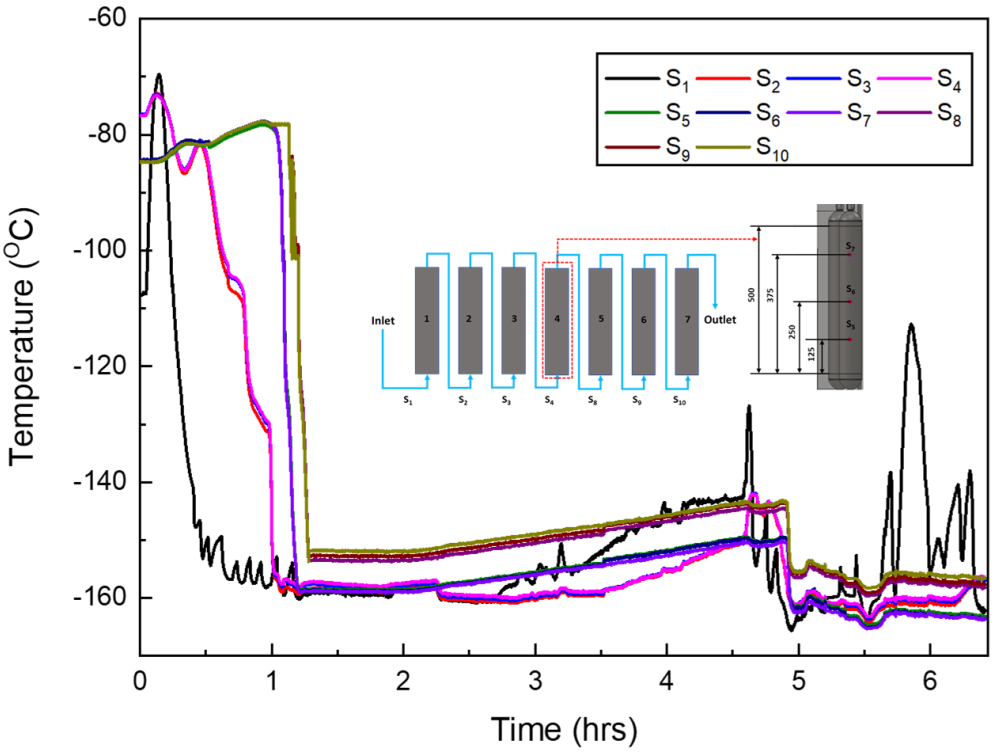


Figure 6.2: Temperature profiles of the SHCS tank during the charging process at a system pressure of 13 barg (The distribution of thermocouples is illustrated in the legend).

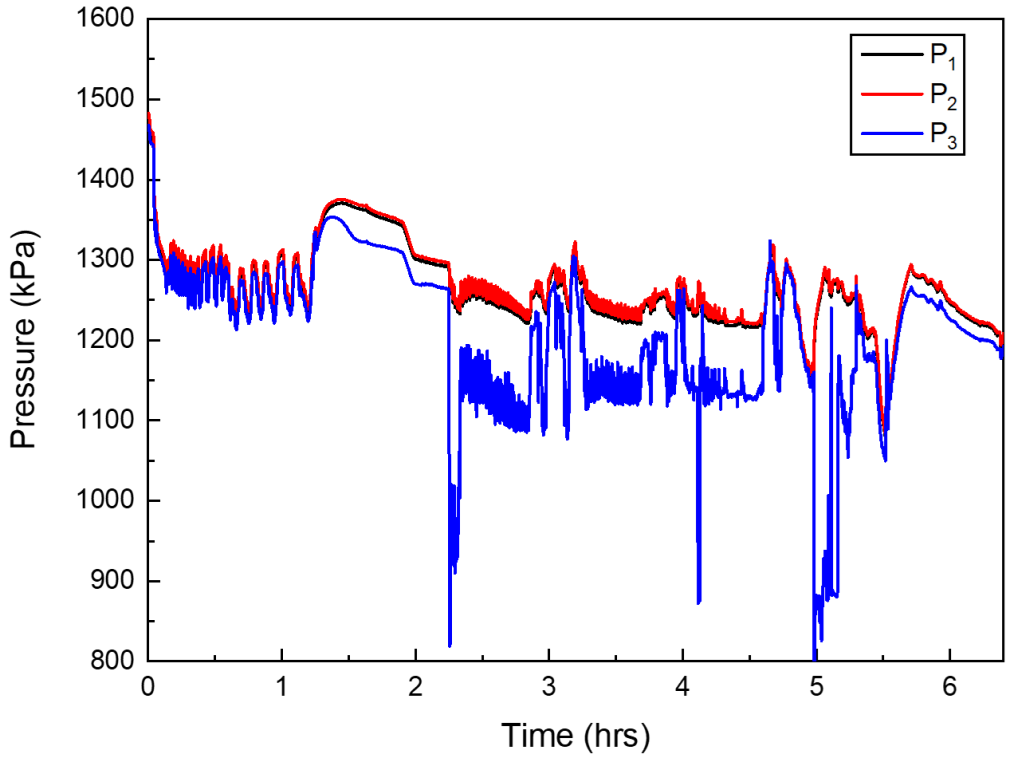


Figure 6.3: Pressure fluctuations during the system charging process at 13 barg .

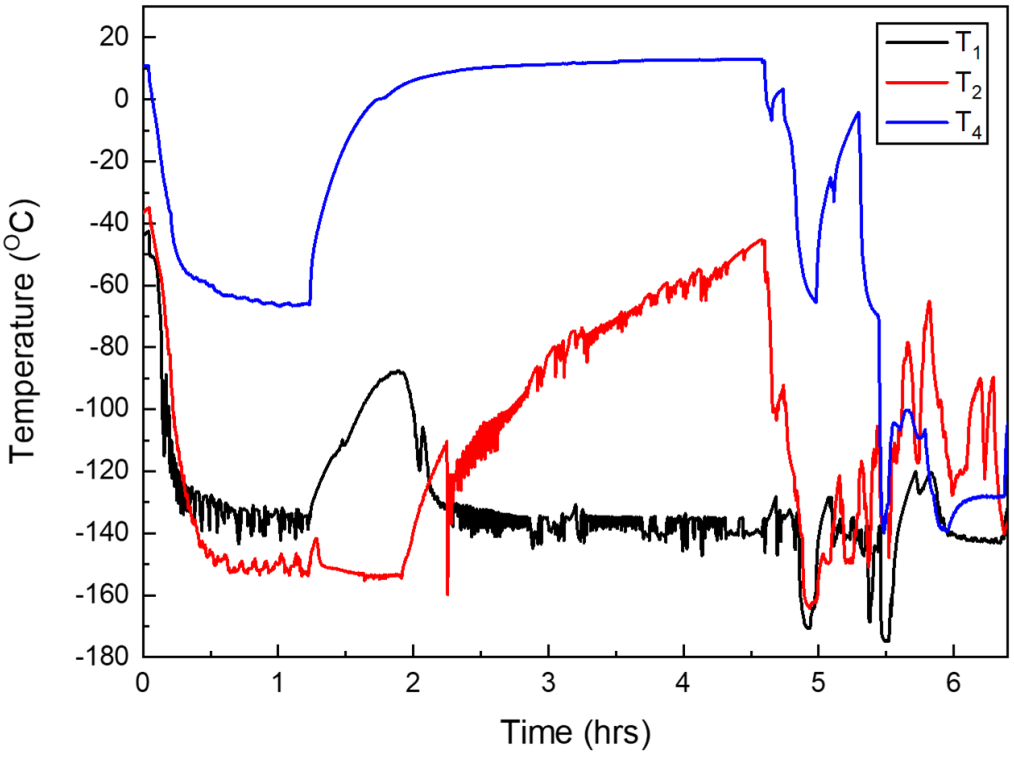


Figure 6.4: Pipeline temperature fluctuations during the charging process at a system pressure of 13 barg.

6.1.2 Charging process at a working pressure of 8.5 barg

In order to study the effect of the working pressure and the LN_2 flow rate on the system cooling performance, the working pressure of the charging experiment was set to 8.5 barg to obtain a temperature difference of 10℃ between the boiling point of LN_2 and the PCT of 2-Methylbutane, and the LN_2 flow rate was reduced to 2 g/s. In addition, the amount of LN_2 used was consistent with the initial charging experiment, which cooled down the LHCS tank from -95℃ to -165℃ and the SHCS tank from -10℃ to -150℃ within 10 hours, respectively.

The PCM within the LHCS undergoes two stages during the charging process at 8.5 barg, including the cooling stage and the phase transition stage; see Figure 6.5. At the initial cooling process ($t < 2\ hrs$), the relatively small temperature variations in the LHCS tank are accompanied by sharp fluctuations in the AS temperature. The cooling stage starts when the AS temperature reaches -170℃, and the PCM temperature gradually decreases to the phase transition point with a cooling rate of 14℃/hr. The PCM enters the phase transition stage after around 5 hours of cooling, and it exhibits a supercooling issue under the current cooling conditions, which is around 2.5℃. Although different amounts of 2-Methylbutane are used, the supercooling degree is similar to the T-history measured data obtained in Chapter 4. The entire phase change process of the PCM takes approximately 2 hours. The different change trend among four thermocouples (L_1-L_4) is caused by their distribution pattern. For instance, PCM at position L_2 (top of the LHCS tank) first undergoes the phase transition process, because LN_2 first flows through the top of the U-shaped tube, the heat transfer is faster than other locations. Thermocouples L_3 and L_4 are placed near the bottom of the U-shaped tube, the heat transfer to this position, therefore, is relatively slower. After the phase change of the material is finished, its

overall temperature continues to be cooled down to reach the saturation temperature of the LN_2. This part of the sensible heat will also be used during the system discharging process.

The inlet temperature profiles for each cylinder in the SHCS tank are close to the lowest temperature (around -150℃) after 6 hours of cooling, which is 10℃ higher than the minimum temperature obtained during the 13 barg charging process; see Figure 6.6. However, the inlet temperatures of the first four tanks (S_1 to S_4) exhibit a decreasing trend after 9 hours of the charging process, corresponding to the end of the phase change process of the PCM in the LHCS tank, which indicates that the lower cold energy has entered the SHCS tank at this time, thus allowing the inner glass beads to be overcooled. This process can also be demonstrated by the inlet (T_2) and outlet (T_4) temperatures of the SHCS tank in Figure 6.8. Initially, the cold energy is greatly absorbed by the glass beads within the first 2 hours of the charging process due to the large temperature difference between the material and the cold N_2. The inlet temperature T_2 is then maintained almost constant until the completion of the phase change of the PCM. The glass beads are thus excessively cooled with the lower grade cold energy entering the SHCS tank. For the outlet temperature T_4, it starts to decline rapidly after 2 hours of the cooling process and approaches a steady state within 6 hours. However, T_4 is relatively higher than the last inlet temperature of the cylinder (S_{10}) in the SHCS tank by approximately 10℃ at the end of the cooling process due to the heat soak between the pipeline and the environment.

Furthermore, since this process does not change the path of LN_2 flowing through the system, a more stable system pressure fluctuation is obtained compared with the cooling process at 13 barg, and the system pressure presents a slight downward trend as the LN_2 is gradually consumed during the cooling process; see Figure 6.7. The average pressure drops (difference between P_2 and P_3) of the

SHCS tank is around 10 kPa, which indicates that the main pressure drop of the system is not serious during the system cooling process.

Compared with the charging process at 13 barg, the charging process at 8.5 barg not only reduces the system fluctuations considerably, but also avoids the excessive cooling of the glass beads to a certain extent. Firstly, the temperature difference provided by the charging process at 8.5 barg can effectively address the non-synchronous heat transfer between the PCM and the glass beads, thus improving the utilisation of cold energy. Secondly, although the reduced mass flow rate of LN_2 increases the time required for the system charging process, it provides a more stable heat exchange, which enables a more accurate measurement of the data.

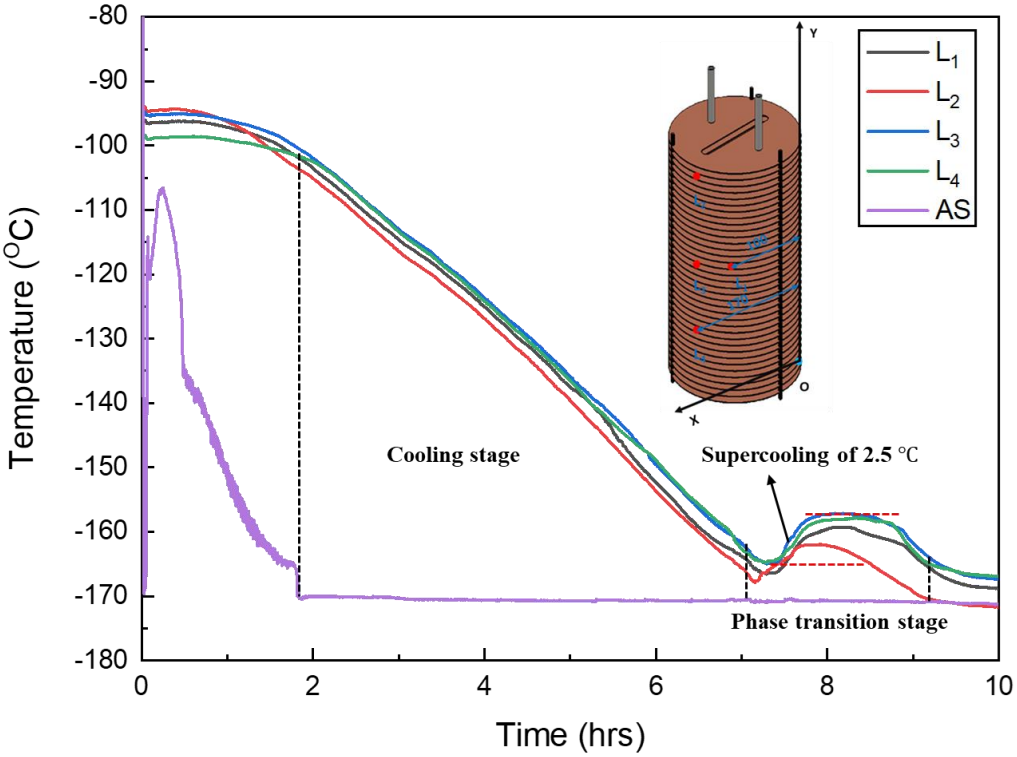


Figure 6.5: Temperature variation curves of the LHCS tank during the charging process at a system pressure of 8.5 barg (The distribution of thermocouples is illustrated in the legend).

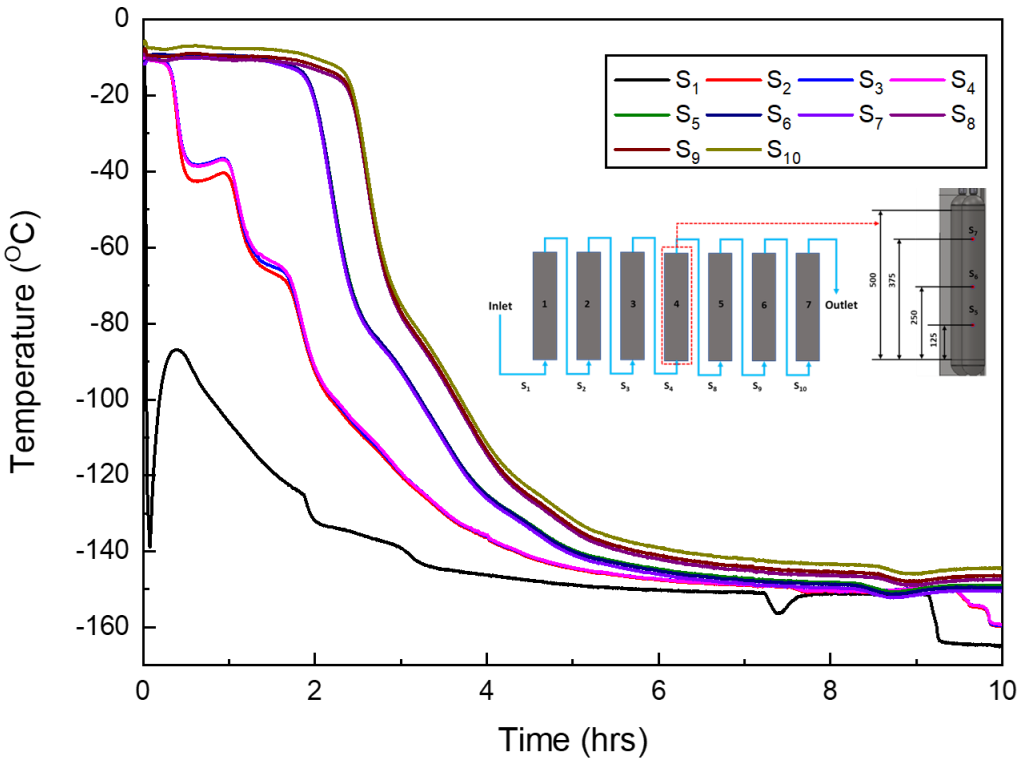


Figure 6.6: Temperature profiles of the SHCS tank during the charging process at a system pressure of 8.5 barg (The distribution of thermocouples is illustrated in the legend).

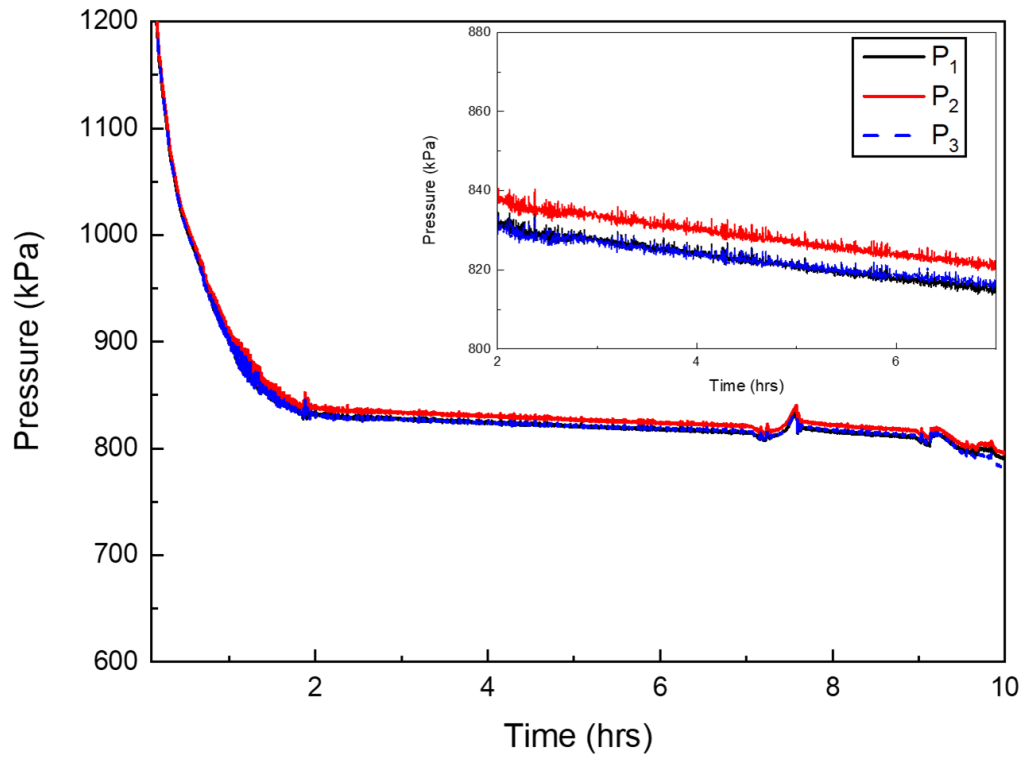


Figure 6.7: Pressure fluctuations during the system charging process at 8.5 barg.

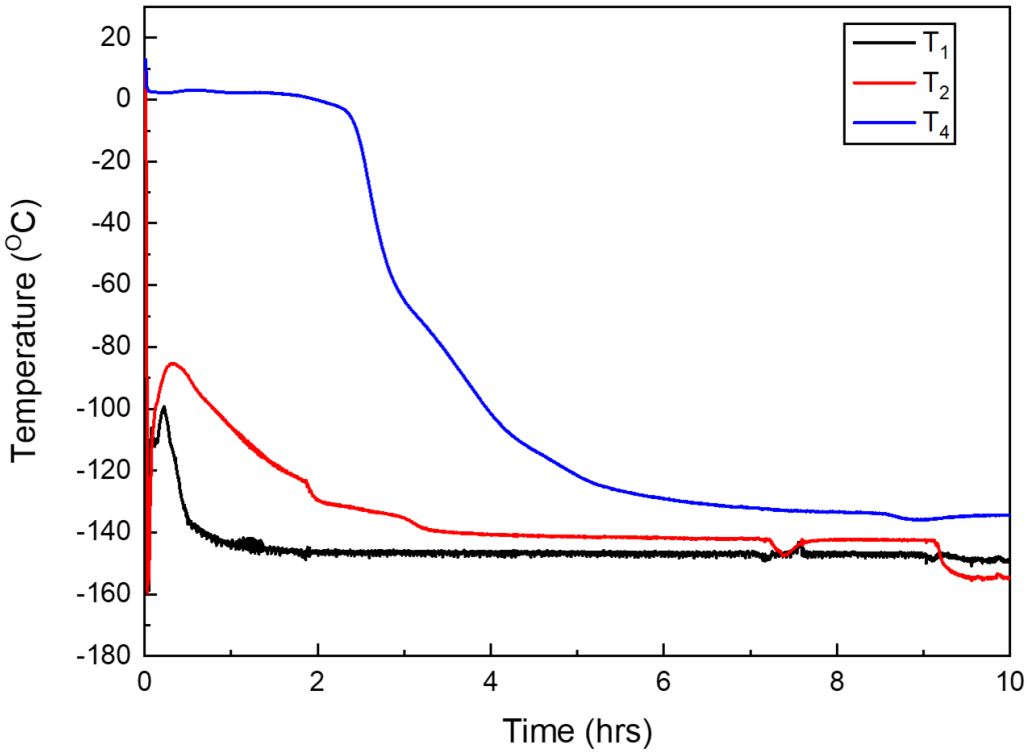


Figure 6.8: Pipeline temperature fluctuations during the charging process at a system pressure of 8.5 barg.

6.2 System discharging process

The system discharging process utilizes the stored high-grade cold energy to liquefy high pressure N_2, which has a saturation temperature higher than the phase transition temperature of the PCM. The discharging experiments were implemented under static and dynamic conditions, respectively. Besides, as the preparation step of the discharging process, the remaining LN_2 from the charging process had been rejected completely by reducing the system pressure.

6.2.1 Static discharging process

Initially, the downstream bypass valve (V15) and the mass flow controller (MFC1) were closed to create a sealed condition for the discharging process, and the pressure regulator of the N_2 cylinder was set at 19.5 barg as the pressure source.

Generally, the method to determine the condensation of N_2 is to compare the saturation temperature of LN_2 (under the real-time pressure of the system) with the real-time AS temperature while maintaining the system pressure constant. There are three scenarios; 1) $T_{AS} < T_{saturation}$; 2) $T_{AS} \approx T_{saturation}$; 3) $T_{AS} > T_{saturation}$. In the first scenario, the cold N_2 is liquefied at this system pressure and is in a supercooled state. The second scenario is that the condensed N_2 can be gas, liquid, or gas-liquid mixture. In the third scenario, the low temperature N_2 cannot be liquefied under this pressure.

As shown in Figure 6.9 (a), the system pressure starts to increase from 12 barg and reaches 19.5 barg after 10 minutes. Then, the system pressure remains at 19.5 barg in the interval of 10 to 20 minutes to induce the condensation of N_2. During this period of time, the AS temperature is observed lower than the saturation temperature dash line of LN_2 at 19.5 bar; see Figure 6.9 (b). It indicates that the condensed N_2 accumulated at the bottom of the U-shaped tube is a sub-cooled liquid phase at this working pressure. The AS temperature gradually increases and approaches the saturation temperature of LN_2 with the natural convection inside the U-shaped tube. In addition, the experiment also applied the method of reducing the system pressure to further prove whether LN_2 can be generated. The bypass valve (V15) was opened to reduce the system pressure to 15 barg after around 28 minutes of the discharging process. As shown in Figure 6.9 (b), the AS temperature has a rapid decrease from the saturation temperature to -162℃, which is due to the endothermic evaporation of the generated LN_2 under the reduced system pressure.

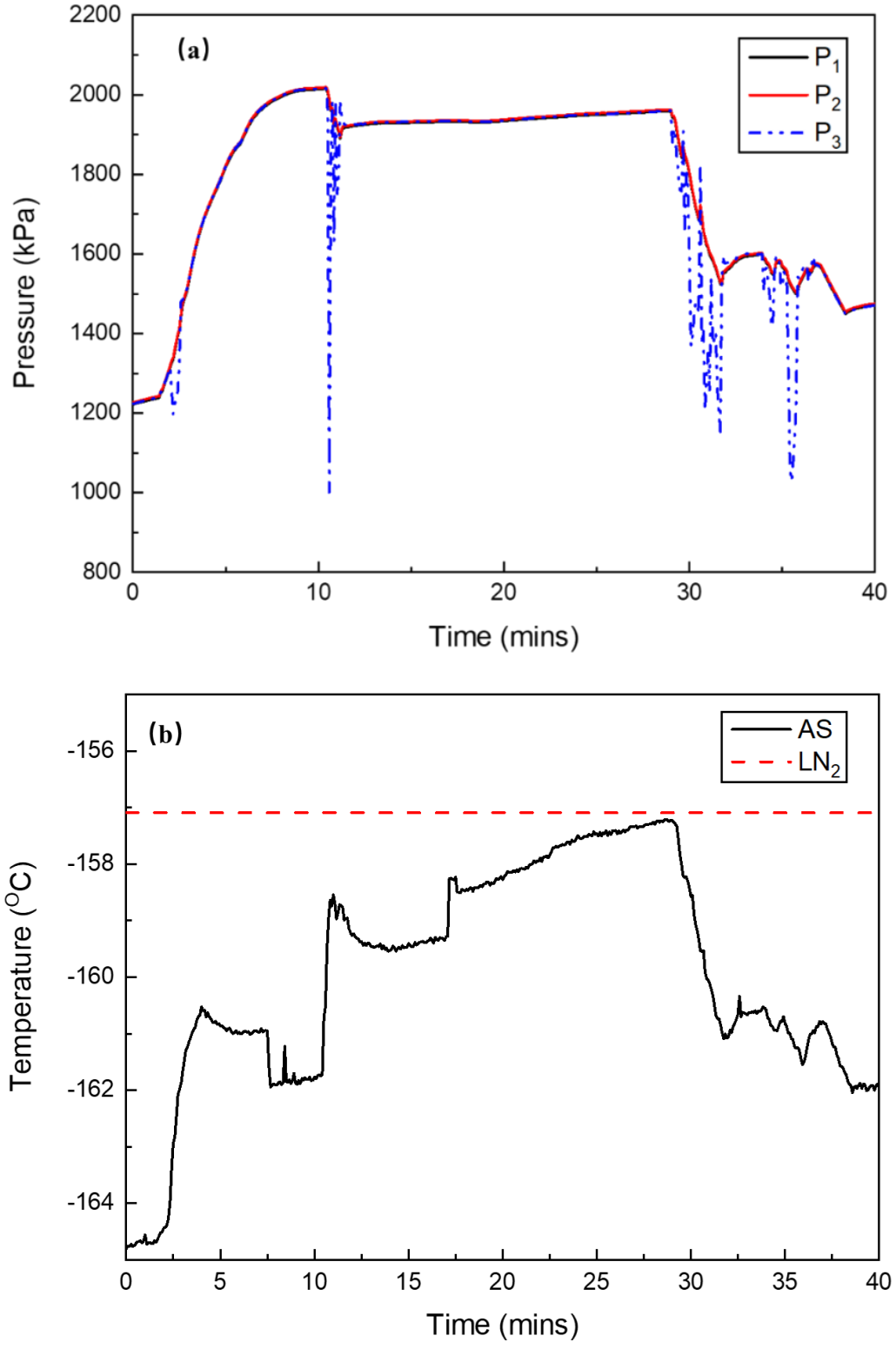


Figure 6.9: (a) System pressure variation curves during the static liquefaction process of N_2 at a working pressure of 19.5 barg; (b) Temperature profile of the AS during the static liquefaction process of N_2 at a working pressure of 19.5 barg.

However, this static experiment can only qualitatively analyse the condensation process of N_2. In order to quantitatively analyse the N_2 condensation rate during the system discharging process, the flow rate parameter is introduced to evaluate the condensation process, and the above mentioned three scenarios can be modified as 1) $T_{AS} < T_{saturation}$, $\dot{m}_{discharging} \cong \dot{m}_{N_2}$; 2) $T_{AS} \approx T_{saturation}, \dot{m}_{discharging} \geq \dot{m}_{N_2}$; 3) $T_{AS} > T_{saturation}, \dot{m}_{discharging} > \dot{m}_{N_2}$. In the first scenario, the same mass flow rate of N_2 flowing into and out of the system maintains the system pressure constant, and the real-time AS temperature is lower than the saturation temperature of LN_2. It indicates that the cold N_2 is liquefied at this constant pressure and has a supercooled state. Therefore, the system condensation rate of N_2 is approximately equal to the current mass flow rate of the discharging process. In contrast, if the AS temperature is higher than the saturation temperature, it indicates that the corresponding mass flow rate is too large to liquefy N_2. The second scenario is a more complicated one, which can be divided into three sub-cases: 1) the cryogenic N_2 is in a gas state, which means the condensation rate is smaller than the mass flow rate; 2) the cold N_2 is completely converted to the saturated LN_2, the condensation rate of N_2, therefore, is the same as the downstream mass flow rate; 3) N_2 is only partially liquified in this case, and its gas-liquid composition is unknown, which indicates that the actual condensation rate is lower than the mass flow rate of the discharging process.

6.2.2 Dynamic discharging process

In order to further verify the three scenarios proposed, the downstream MFC1 was opened set to 0.31 g/s to change the N_2 condensation process from static to dynamic. The AS temperature and the MCF1 readings corresponding to the real-time pressure of the system were monitored during the entire condensation process.

As shown in Figure 6.10 (a), the system pressure increases from 12 barg to 19 barg and reaches dynamic equilibrium after 5 minutes. Correspondingly, the AS temperature also gradually increases and tends to be stabilized at -158℃, which is slightly lower (around 0.5℃ difference) than the saturation temperature of LN_2 under the system pressure at 19 barg. At this time, the state of the system is consistent with the first scenario mentioned above. Because the cold energy provided by the PCM in the initial stage of the discharging process is greater than that required for N_2 liquefaction, the generated LN_2 is in a supercooled state. As the same operation conducted in the static experiment, the system pressure was reduced to 16 barg to monitor the AS temperature change and exhaust the generated LN_2 after 10 minutes. The result is that a sharp temperate decline peak caused by the endothermic evaporation can be obtained during the process of system pressure drop. Therefore, under the condition that the system pressure remains constant at 19 barg, the LN_2 can be produced at a condensation rate of 0.31 g/s.

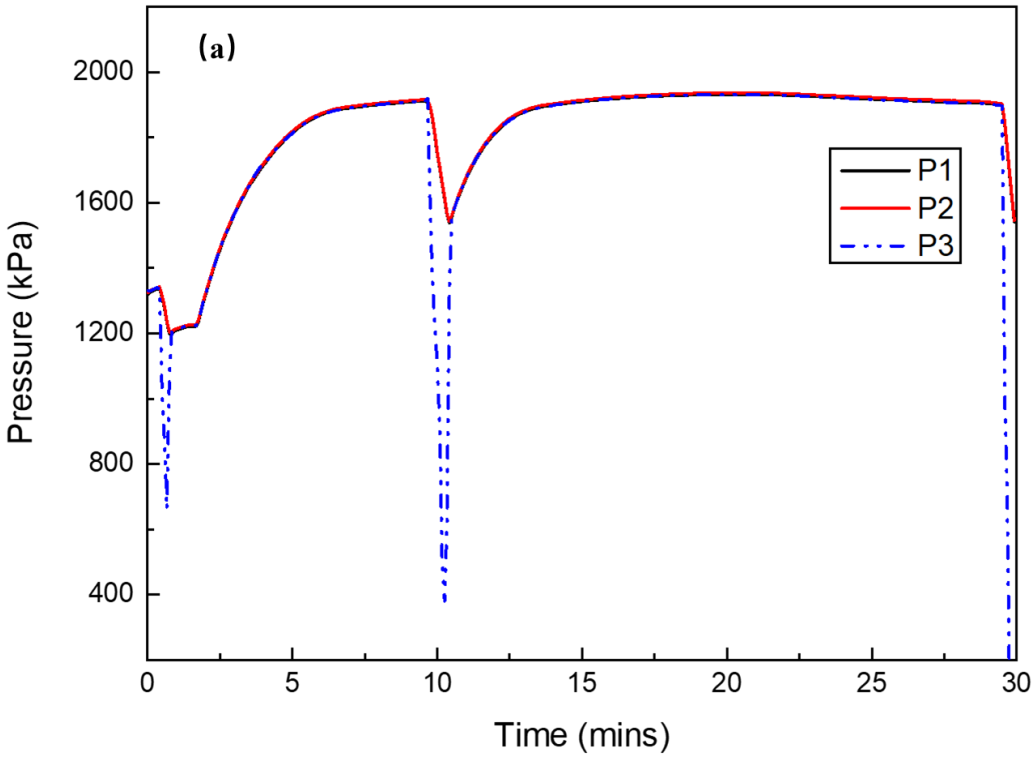
However, as the system pressure returns to 19 barg again, the AS temperature rises first, and then stabilized at the saturation temperature of the LN_2. In this scenario, since the AS temperature is close to the saturation temperature of LN_2 after the system pressure is rebalanced, it is difficult to determine whether the N_2 inside the U-shaped tube is in a gas-liquid phase or a single phase. Thus, the MFC1 reading cannot reflect the actual condensation rate of the system, which should be smaller than the measurement value of the MFC1.

Figure 6.10 (b) also presents the temperature change profile of the PCM during the dynamic discharging process at 19 barg. One can see that the temperature between different parts of the PCM is not uniform. The average overall temperature difference between the middle part (L_1) and the

bottom part (L_3 and L_4) is around 2℃, while the top part (L_2) has the lowest temperature, which is -163℃. This indicates that the heat exchange between the N_2 and the PCM is mainly concentrated at the bottom of the U-shaped tube due to its relatively larger heat transfer area compared with the top side. Other reasons for the temperature difference inside the PCM are likely to be: 1) the influence of the U-shaped tube configuration on the heat transfer, including the geometry, size and distribution; 2) the relatively lower thermal conductivity of the PCM. As described in Chapter 5, the diameter of the U-shaped tube is comparatively smaller than the inner LHCS tank, and the cold N_2 enters the LHCS tank from both sides of the U-shaped tube at the same time. Therefore, the heat exchange between the N_2 through the tube wall and the PCM may be uneven, resulting in different melting rates of the PCM at different positions. While the lower thermal conductivity of the PCM means that the heat transfer ability among the material is poor, which can easily lead to temperature difference. It also illustrates that the cold energy generated during its phase transition cannot be conducted to the U-shaped tube wall timely, the temperature difference between the tube wall and the cold N_2, therefore, cannot remain stable and will change to a certain degree over time, thereby affecting the N_2 liquefaction process.

In addition, it can also be seen in Figure 6.10 (b) that the temperatures of the PCM at different locations show a rapidly upward trend for the first 15 minutes, and then gradually stabilizes at different temperatures. The initial part can be considered as the sensible cold period of the PCM, which is quickly consumed. The following part is the phase transition period of the PCM, which has a stable temperature plateau. However, for the reasons discussed above, the PCT of the material are not equal at different positions. For instant, the bottom part L_3 and L_4 gradually increases and finally stabilizes at around -157℃, which is higher than the saturation temperature of LN_2. The phase

transition temperatures of the middle part L_1 and the top part L_2 are around -159℃ and -162℃ separately. This difference in phase transition temperature of the PCM caused by multiple factors has a great impact on the condensation efficiency of the system. Although it is possible to increase the discharging working pressure to obtain a new temperature difference that can liquefy N_2, it has exceeded the maximum pressure of the system design. Thus, the experimental time of the N_2 condensation process is usually shorter than the system charging process, which is around 30 to 35 minutes.



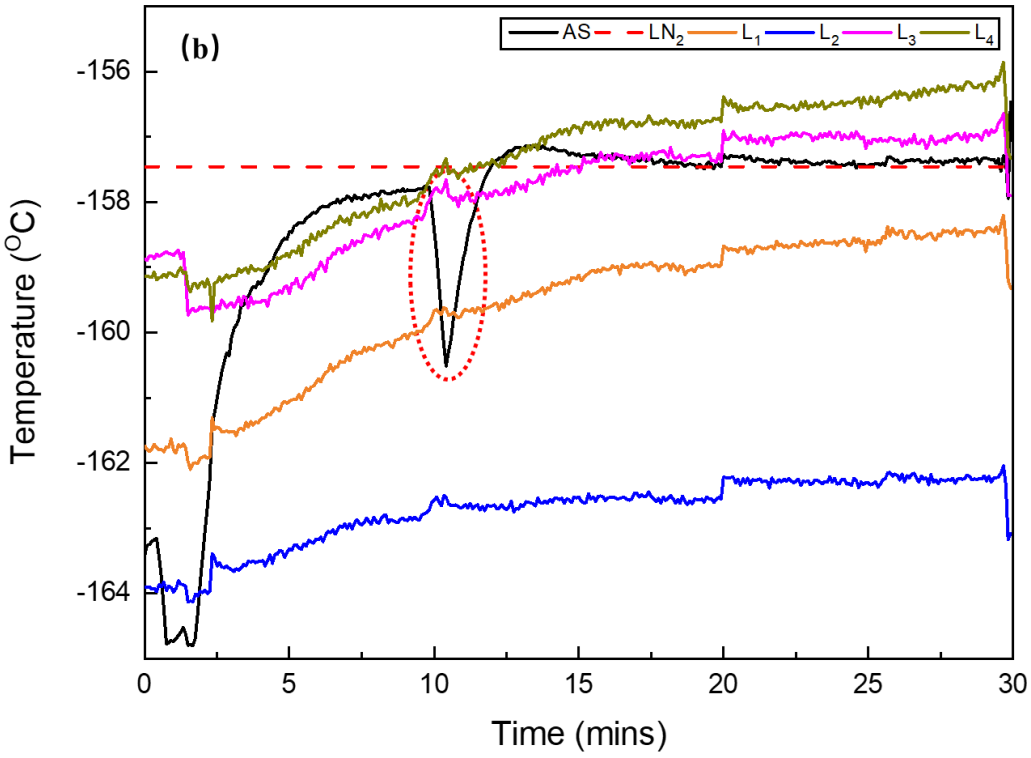


Figure 6.10: (a) System pressure variation curves during the dynamic liquefaction process of N_2 at a working pressure of 19 barg; (b) Temperature profiles of the AS and the PCM during the dynamic liquefaction process of N_2 at a working pressure of 19 barg.

6.3 Evaluation of the system condensation capacity

To further determine the system condensation capacity of N_2, the test rig discharging experiment was repeated based on the conclusion mentioned above. The system was fully charged by using LN_2 at 8.5 barg working pressure. Since the temperature difference between the PCM and the working fluid is 10℃. The experiments, therefore, were classified as the sensible cold period and the latent cold period according to the temperature of the 2-Methylbutane. However, the LN_2 pressure provided by the LN_2 tank gradually decreases as the cooling process progresses, which leads to the final temperature of some parts of the PCM (L_1 and L_2) being lower than -170℃ after the cooling process is completed, as shown in Figure 6.11.

6.3.1 System condensation rate of N_2 in the subcooled period of the PCM

Figure 6.11 presents some main parameters using sensible heat of the PCM during the system condensation process. One can see that the system pressure remains at 16.5 barg after 7 minutes, and the corresponding saturation temperature of the LN_2 is -160.02℃. At the same time, the AS temperature quickly increases in the process of the system pressure build-up, and then gradually stabilizes at around -161℃, which is lower than the current saturation temperature of the LN_2. Therefore, under the condition that the system pressure remains constant at 16.5 barg, the LN_2 can be produced at a condensation rate of 1 g/s in the subcooled period of the PCM. The effective time of N_2 liquefaction ($T_{AS} < T_{saturation}$) is denoted by the black dotted circle in Figure 6.11, which is around 18 minutes. The total amount of N_2 liquefied at a system pressure of 16.5 barg is 1.08 kg during the sensible cold period of the PCM. Subsequently, the AS temperature gradually increases and eventually approaches the saturation temperature of the LN_2 in the last 5 minutes of the condensation process.

The temperature change trend of the PCM is also shown in Figure 6.11. It can be seen that the overall temperature of the PCM does not change significantly during the first 8 minutes of increasing system pressure. When the system pressure stabilizes at 16.5 barg, the PCM temperature starts to be heated by the flowing N_2.

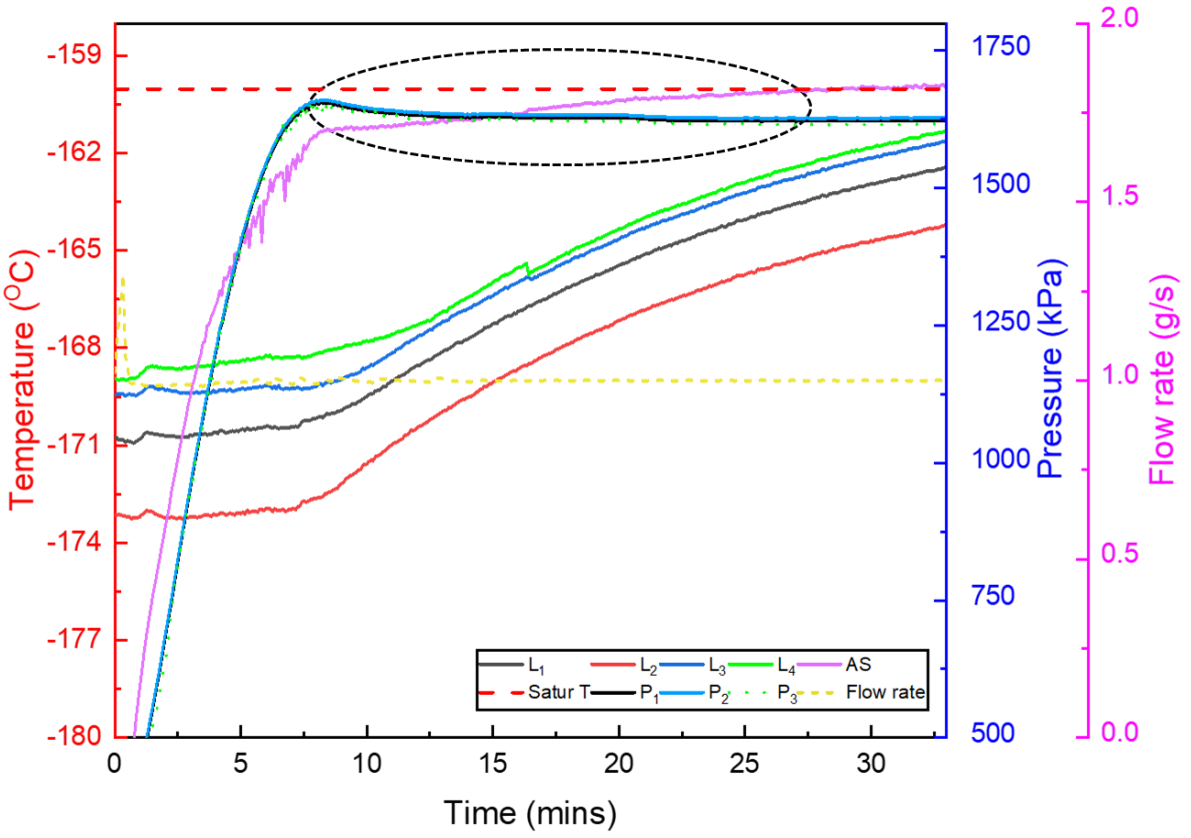


Figure 6.11: System parameters of LHCS temperature, pressure, and flow rate for N_2 condensation process using the sensible cold energy of PCM at an operating pressure of 16.5 barg.

As shown in Figure 6.12, during the condensation process of N_2, the temperature (T_3) of the high-pressure N_2 entering the system is maintained at approximately 10.2℃ and its temperature fluctuates by no more than 0.5℃. However, the outlet temperature (S_1 or T_2) of the cooled N_2 initially trends to rise and then stabilizes at around -152℃, and the average temperature difference between the outlet (cold side) and the inlet (hot side) is about 10℃. As demonstrated in Figure 6.6, since several cylinders at the front of the tandem (cylinder 1 to 3) have some degree of supercooling, this results in a lower N_2 temperature at the outlet. Its temperature gradually equilibrates as this cold energy is consumed. Meanwhile, the pipeline between the SHCS tank outlet and the LHCS inlet is not covered by a vacuum layer, the heat soak from the ambient, therefore, makes the temperature at point T_2 slightly higher than the temperature at point S_1 by about 0.7℃ even if the pipeline is wrapped with the

insulation material. In addition, there is no significant temperature difference between S_5, S_6, and S_7, which are used to study the temperature distribution of a single cylinder at equal intervals along the axial direction. Its average temperature is between the hot side and the cold side, which is around -148℃.

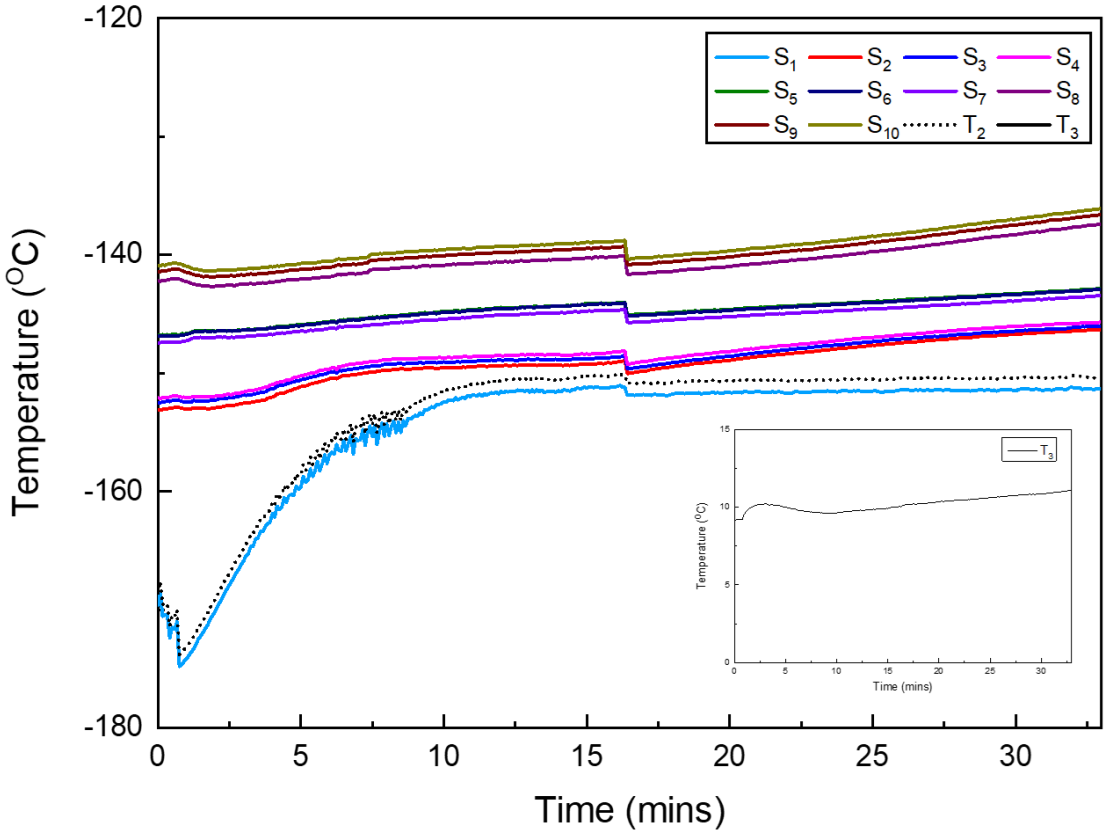


Figure 6.12: The temperature profile of the SHCS tank during the N_2 condensation process at an operating pressure of 16.5 barg using the subcooled period of the PCM.

6.3.2 System condensation rate of N_2 in the phase transition period of the PCM

Before starting the condensation experiment with the latent cold energy of the PCM, the system pressure was reduced several times to ensure that all LN_2 generated in the sensible cold energy period had been removed completed. Besides, the system N_2 flow rate was decreased from 1 g/s to 0.5 g/s to reduce the effect of the gradually decreasing temperature difference between the PCM temperature

and the LN_2 saturation temperature on N_2 condensation.

Figure 6.13 shows system parameters of LHCS temperature, pressure, and flow rate using latent heat of the PCM during the system condensation process. It can be seen that due to the reduction in N_2 flow rate, the new system pressure is maintained at 17 barg, and the corresponding saturation temperature of the LN_2 is increased to -159.5℃. Simultaneously, the AS temperature is observed at around -160.5℃, which is 1℃ below the current saturation temperature of the LN_2. It indicates that the cold N_2 can be liquefied with a condensation rate of 0.5 g/s in the phase transition period of the PCM while the system pressure remains constant at 17 barg. The effective time of N_2 liquefaction ($T_{AS} < T_{saturation}$) is denoted by the black dotted circle in Figure 6.13, which is around 24 minutes. The total amount of N_2 liquefied at a system pressure of 17 barg is 0.72 kg during the latent cold period of the PCM. After 24 minutes of the N_2 condensation process, the AS temperature starts to increase and eventually exceeds the saturation temperature of the LN_2 without showing a downward trend, which implies that the PCM is not capable of providing enough cold energy or temperature difference to liquify N_2 under the existing system conditions. When the system pressure is released at 27 minutes of the condensation process, the AS temperature exhibits the same downward trend that is also observed in the dynamic experiments. However, the difference is that the AS temperature does not remain near the saturation temperature of the LN_2, but tends to rise gradually as the system pressure returns to the set pressure.

The overall temperature of the SHCS tank tends to increase with further heat exchange between the glass beads and the N_2, as shown in Figure 6.14. The outlet temperature (S_1 or T_2) of the cold N_2 is maintained for the first 10 minutes at -153℃, and rises gradually as the process continues. This means

that the cold energy required to liquefy the N_2 is increase as well, thus affecting the overall liquefaction efficiency of the system during the phase transition period of the PCM. In addition, the temperature on the hot side increases considerably faster than that on the cold side, and the average temperature difference between the cold side and the hot side is also enlarged from 10℃ at the start of the experiment to 20℃ at the end of condensation process.

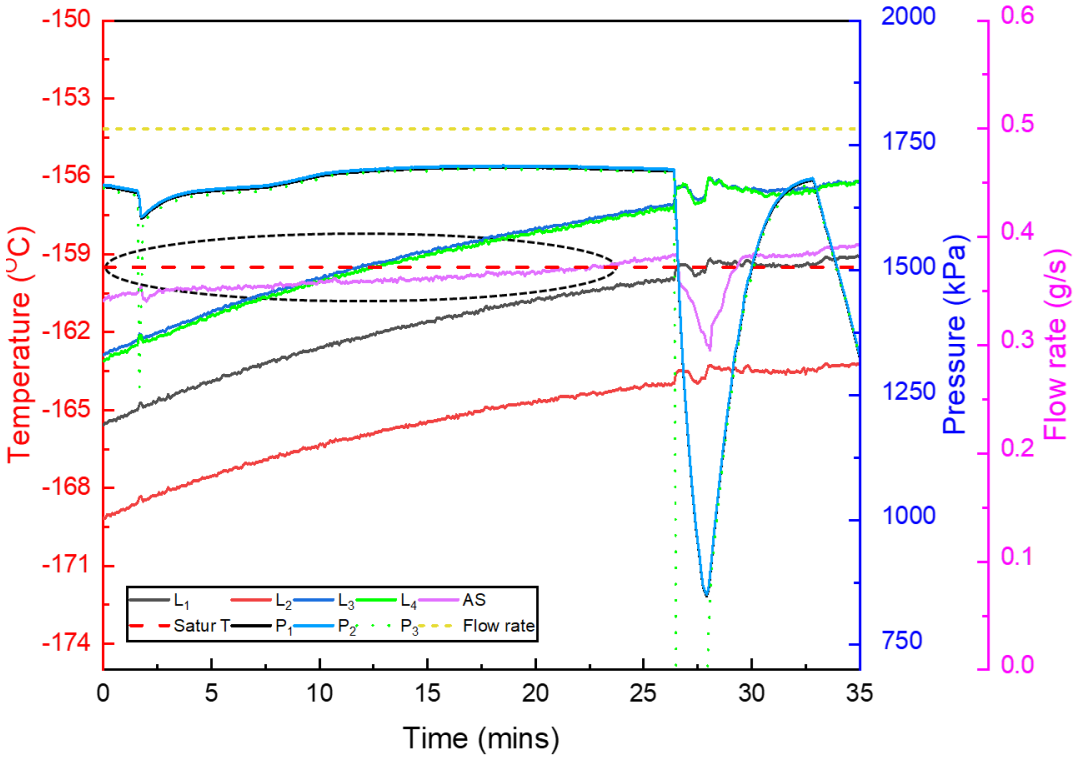


Figure 6.13: System parameters of LHCS temperature, pressure, and flow rate for N_2 condensation process using the latent cold energy of PCM at an operating pressure of 17 barg.

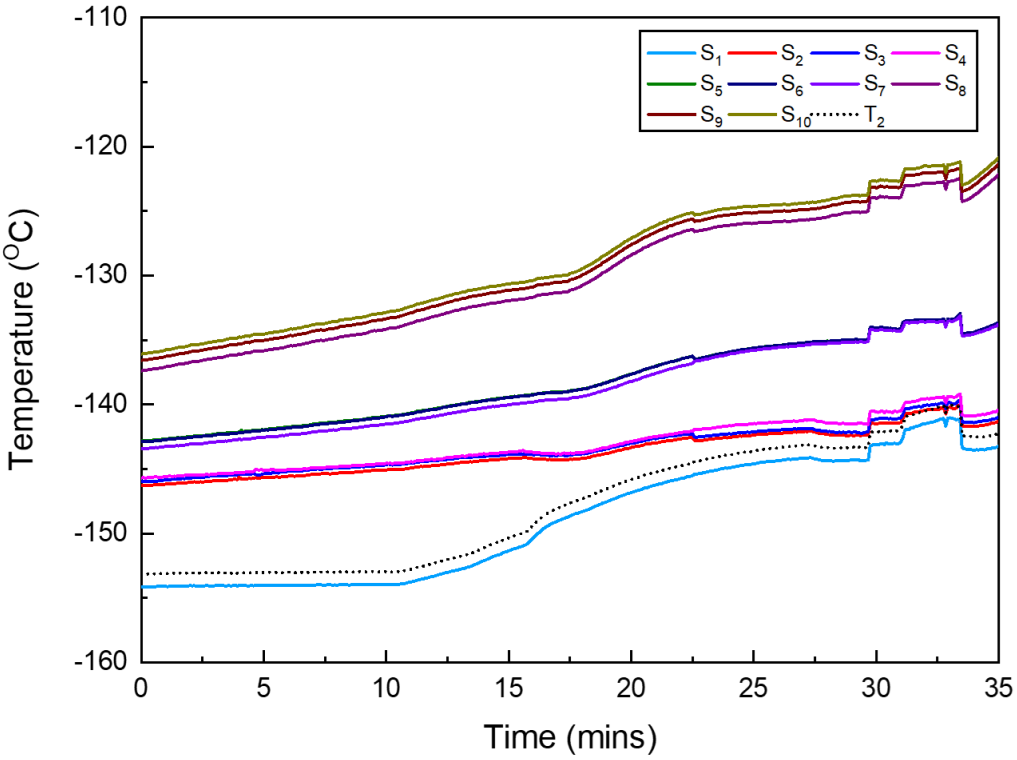


Figure 6.14: The temperature profile of the SHCS tank during the N_2 condensation process at an operating pressure of 17 barg using the phase transition period of the PCM.

6.4 Summary

This chapter presents the experimental results of the high-grade cold energy storage in both LHCS and SHCS units. Both charging and discharging processes were studied. One of the specific tasks was to verify the liquefaction of N_2 during the release of cold energy stored in the CTES materials.

In the system charging process, the working fluid pressure was set at 13 barg and 8.5 barg for cooling the system, respectively. It can be found that when the charging pressure is set at 13 barg, there is a mismatch in the degree of cooling between the PCM and the glass beads, which tend to be overcooled prior to the phase transition of the PCM. Although this issue can be mitigated by changing the path of LN_2 through the system to cool down the LHCS tank individually, a significant amount of cold energy is discharged directly from the system before being stored in the CTES materials. The system

charging pressure, therefore, was reduced to 8.5 barg to bulit a 10℃ temperature difference between the saturation temperature of LN_2 and the PCT of the PCM. The LN_2 flow rate was also decreased from 3 g/s to 2 g/s to increase the heat exchange time between the LN_2 and the CTES materials. The results indicate that the CTES materials can be fully charged within 10 hours using 110 L of LN_2. The PCM is cooled from -95℃ to -165℃ with a cooling rate of 14℃/hr and then takes 2 hours to finalise the phase transition process. The overall temperature of the SHCS tank is maintained at around -150℃ at the end of the charging process, and only the first few cylinders exhibit the overcooling problem during the last hour of the charging process.

In the system discharging process, the verification experiments were implemented under static and dynamic conditions to determine whether high pressure N_2 can be liquefied by heat exchange with the frozen PCM and glass beads at a given system pressure. By monitoring the real-time pressure of the system and the AS temperature at the bottom of the U-shaped tube, different three scenarios were proposed to analyse the possible state of N_2 after heat exchange with materials, namely 1) $T_{AS} < T_{saturation}$, $\dot{m}_{discharging} \cong \dot{m}_{N_2}$; 2) $T_{AS} \approx T_{saturation}$, $\dot{m}_{discharging} \geq \dot{m}_{N_2}$; 3) $T_{AS} > T_{saturation}, \dot{m}_{discharging} > \dot{m}_{N_2}$. Based on the experimental results of N_2 liquefaction validation, further condensation experiments were performed using the sensible cold energy and the latent cold energy of PCM, respectively. During the sensible cold period of PCM, N_2 is liquified at a system pressure of 16.5 barg for a duration of 18 minutes, yielding a total of 1.08 kg of LN_2. For the phase transition period of PCM, the condensation capacity of the system for N_2 progressively decreases as the heat transfer temperature difference provided by the PCM reduced, the N_2 flow rate was therefore adjusted from 1 g/s to 0.5 g/s. The effective time of N_2 liquefaction is approximately 24 minutes, and the mass of the condensed N_2 is 0.72 kg when the system pressure is maintained at 17 barg.

CHAPTER 7

CONCLUSIONS AND RECOMMENDATIONS

7.1 Conclusions

This work focuses on three aspects associated with high-grade cold energy storage based on CTES materials: 1) to screen and determine suitable CTES materials for cryogenic applications; 2) to design and build a laboratory-scale test rig for extremely valuable high-grade cold energy storage/utilisation based on the investigated CTES materials; 3) to verify the performance of the test rig for high-grade cold energy storage/utilisation through system charging and discharging experiments. The main conclusions are summarised as follows:

- The specific heat capacity and thermal conductivity of Borosilicate glass beads (SHS material) have a tendency to decrease with the temperature reduction.

- The results of the DSC measurements indicate that the PCT of 1-Hexene is -138.8℃ with a phase change enthalpy of 156.39 kJ/kg. But the phase transition of 2-methylbutane was not observed in the same DSC measurements. The T-history method, therefore, was used for both 1-Hexene and 2-Methylbutane to further investigate their phase transition behaviours. It can be found that the supercooling degree of 1-Hexene (12℃) is approximately 40% lower than the DSC results, and that of 2-Methylbutane is only 2℃. The melting enthalpy of 2-Methylbutane is obtained by comparing and calculating the under-curve area of the melting process of 1-Hexene and 2-Methylbutane, which is estimated to be 74.29 kJ/kg.

- The expanded graphite (EG) and two different thickeners were mixed separately with pure 1-Hexene to address the low thermal conductivity issue. Both SiO_2-based (3 wt.%) and SEBS-based (2 wt.%) composites with 0.5 wt.% EG enhance the thermal conductivity of solid state 1-Hexene by 34.5% and 38.1% compared with the pure substance, respectively. For liquid state,

the introduction of 0.5 wt.% EG leads to an increase in the thermal conductivity of both optimally modified mixtures by 64.2% and 52.3%, achieving 0.248 W/m·K and 0.230 W/m·K, respectively.

- The long-term stability of 1-Hexene was performed by 100 complete charging and discharging thermal cycles. It shows an acceptable variation (3.16%) in the latent heat after 100 thermal cycles. In addition, the crystalline memory effect of the material due to thermal cycling significantly reduces the time required for recrystallisation, which is beneficial for the practical application of the material. Furthermore, the volume expansion coefficients from solid to liquid phase are 21% and 20% for 1-Hexene and 2-Methylbutane, respectively.

- The flammability of pure PCMs and PCMs modified with two different fire retardants (SiO_2 and TCEP) was studied at ambient temperature. The addition of both fire retardants can effectively inhibit the burning intensity of PCM, and the increment of the LFL is proportional to the amount of SiO_2 added. Compared with the SiO_2, the flame retardancy of the TCEP is not stable in terms of flame retardancy. However, it is likely to be attributed to the better dispersion of SiO_2 in 1-Hexene than in TCEP, the 5% (v/v) TCEP exhibits lower flame retardancy than SiO_2 as the volume of 1-Hexene is increased. SiO_2 is regarded as a more suitable candidate for mitigating the flammability of the PCMs due to its compatibility and environmental advantages.

- The determined thermophysical properties of 3-Methylpentane suggest that it can be a good alternative LHS material at cryogenic applications, especially in terms of compatibility with heat exchange devices due to its similar volume expansion to that of 2-Methylbutane.

- A one-dimensional transient tube model with cylindrical fins was proposed to study the effect of different parameters including fin length, fin thickness, fin gap, and materials on the heat transfer between the HTF and the PCM in the LHCS tank. The simulation results indicate that the heat transfer coefficients for boiling and condensation vary in different patterns with the proportion of vapour in the two-phase flow, but the inner tube diameter and the mass flow rate are positively related to these coefficients. The fin thickness, fig gap, fin length and number of fins are positively correlated with the heat transfer rate. However, different tube materials have a negligible effect on the heat transfer rate.

- An experimental system was designed and built to store and utilise high-grade cold energy by using 2-Methylbutane as LHS material and Borosilicate glass beads as SHS material. This system consists of two processes corresponding to the storage and utilisation of the cold energy, which are: a) system charging process; b) system discharging process. One of the specific tasks was to verify the liquefaction of N_2 during the release of cold energy stored in the CTES materials.

- The system charging experiments were conducted at 13 barg and 8.5 barg, respectively. It can be found that when the charging pressure is set at 13 barg, there is a mismatch in the degree of cooling between the PCM and the glass beads, which tend to be overcooled prior to the phase transition of the PCM. The results of the charging process at 8.5barg show the CTES materials can be fully charged within 10 hours using 110 L of LN_2, and the overcooling problem of the SHS material has been significantly improved.

- In the system discharging experiments, the real-time pressure of the system and the AS temperature at the bottom of the U-shaped tube were used to determine the possible states of N_2

after heat exchange with PCM, as the interior of the LHCS tank is invisible. Three different scenarios are included: 1) $T_{AS} < T_{saturation}$, $\dot{m}_{discharging} \cong \dot{m}_{N_2}$; 2) $T_{AS} \approx T_{saturation}, \dot{m}_{discharging} \geq \dot{m}_{N_2}$; 3) $T_{AS} > T_{saturation}, \dot{m}_{discharging} > \dot{m}_{N_2}$.

- The system condensation capacity of N_2 varies according to the temperature difference between the frozen PCM and the cold N_2. The results indicate that the total amount of LN_2 produced during the sensible cold period of PCM is 1.08 kg at a system pressure of 16.5 barg. For the phase transition period of PCM, the effective time of N_2 liquefaction is approximately 24 minutes under conditions of reducing the system flow rate from 1.0 g/s to 0.5 g/s and increasing the system pressure from 16.5 barg to 17 barg. The mass of liquefied N_2 is 0.72 kg.

7.2 Recommendations and future work

Although this work has obtained some promising results in the cryogenic energy storage filed, there are still many aspects of CTES materials and their applications that deserve to be further investigated. Some recommendations for future work are given in the following:

- This work has successfully applied the hydrocarbons with a few carbon atoms (C_5 and C_6) as cryogenic PCMs. However, the selection of PCM candidates that are appropriate for cryogenic applications remains very limited. More efforts are needed in the development of new material formulations, such as eutectic composite cryogenic PCMs, which can achieve lower phase transition temperatures. Besides, the thermophysical properties of cryogenic PCMs are not as easy to determine as those of room temperature or mid-temperature PCMs. Some properties can only be known through indirect measurements, which makes testing more challenging. Therefore,

more convenient and accurate measurement methods should be developed to facilitate the study of cryogenic PCMs.

- In the configuration of the test rig, the series connection of the LHCS and SHCS tanks enables the maximum amount of high-grade cold energy to be stored in the CTES materials during the charging process. However, the different thermal conductivities of LHS and SHS materials can led to an asynchronous cooling progress, which reduces the efficiency of cold energy storage. Modification work on the test rig can be carried out, such as adding more U-shaped tubes inside the LHCS tank, thus increasing the heat transfer area between the HTF and the PCM.

- The system charging and discharging processes are mainly focused on the experimental study of N_2 liquefaction in this work. The total system efficiency should be further evaluated and studied in both numerical and experimental aspects to gain a more comprehensive understanding of the charging and discharging processes.

Appendix

Appendix A

Modified Bessel Functions of the first and second kinds

Table A.1: Zero-order and first-order Bessel functions of the first and second kinds.

x	$e^{-x}I_0(x)$	$e^{-x}I_1(x)$	$e^{x}K_0(x)$	$e^{x}K_1(x)$
0.0	1.0000	0.0000	∞	∞
0.2	0.8269	0.0823	2.1407	5.8334
0.4	0.6974	0.1368	1.6627	3.2587
0.6	0.5993	0.1722	1.4167	2.3739
0.8	0.5241	0.1945	1.2582	1.9179
1.0	0.4657	0.2079	1.1445	1.6361
1.2	0.4198	0.2152	1.0575	1.4429
1.4	0.3831	0.2185	0.9881	1.3010
1.6	0.3533	0.2190	0.9309	1.1919
1.8	0.3289	0.2177	0.8828	1.1048
2.0	0.3085	0.2153	0.8416	1.0335
2.2	0.2913	0.2121	0.8056	0.9738
2.4	0.2766	0.2085	0.7740	0.9229
2.6	0.2639	0.2046	0.7459	0.8790
2.8	0.2528	0.2007	0.7206	0.8405
3.0	0.2430	0.1968	0.6978	0.8066
3.2	0.2343	0.1930	0.6770	0.7763
3.4	0.2264	0.1892	0.6579	0.7491
3.6	0.2193	0.1856	0.6404	0.7245
3.8	0.2129	0.1821	0.6243	0.7021
4.0	0.2070	0.1787	0.6093	0.6816
4.2	0.2016	0.1755	0.5953	0.6627
4.4	0.1966	0.1724	0.5823	0.6453
4.6	0.1919	0.1695	0.5701	0.6292
4.8	0.1876	0.1667	0.5586	0.6142
5.0	0.1835	0.1640	0.5478	0.6003

5.2	0.1794	0.1614	0.5376	0.5872
5.4	0.1762	0.1589	0.5279	0.5749
5.6	0.1728	0.1565	0.5188	0.5633
5.8	0.1696	0.1542	0.5101	0.5525
6.0	0.1666	0.1520	0.5019	0.5422
6.4	0.1611	0.1479	0.4865	0.5232
6.8	0.1561	0.1441	0.4724	0.5060
7.2	0.1515	0.1405	0.4595	0.4905
7.6	0.1473	0.1372	0.4476	0.4762
8.0	0.1434	0.1341	0.4366	0.4631
8.4	0.1398	0.1312	0.4264	0.4511
8.8	0.1365	0.1285	0.4168	0.4399
9.2	0.1334	0.1260	0.4079	0.4295
9.6	0.1305	0.1235	0.3955	0.4198
10.0	0.1278	0.1213	0.3916	0.4108

Appendix B

Program code of Latent heat cold storge (LHCS) tank

Boiling process

```
%input
%%Geometry
N=5:5:70;%fin number
S=20e-3;%fin gap[2.5e-3 5e-3 10e-3]
t=1.5e-3;%fin thickness
r2=10e-3:10e-3:200e-3;%fin raidus
r1=3e-3;%pipe outer radius
w=1e-3;%pipe wall thickness
r0=r1-w;%pipe inner radius

%%Conditions
T_PCM=130; %PCM Temperature, K, fixed
massflow=1.5e-3; %kg/s
T_in=103;%inlet temperature

%material Properties
k_fin=500; %fin thermal conductivity, fixed
k_tube=500;%tube thermal conductivity
h_PCM=0.19;%PCM thermal conductivity
```

```
%Working Fluid Properties, fixed
rho_l=670.94;%kg/m^3
rho_g=39.184;%kg/m^3
miu_l=6.8993e-5;%Pa*s
miu_g=7.706e-6;%Pa*s
Cp_l=2.4043e3;%J/Kg/K
Cp_g=1.6162e3;%J/Kg/K
k_l=0.094917;%W/m*k
k_g=0.011677;%W/m*k
x=0.9;
sigma_l=0.0034831;%N*m
sigma_g=0.0034831;%N*m

%Initialization
Temp_b=zeros(length(N),length(r2));
Temp_w=zeros(length(N),length(r2));
HeatRate=zeros(length(N),length(r2));
HTC_avg=zeros(length(N),length(r2));
%Calcualtion

for i=1:length(N)
for ii=1:length(r2)
d=2*(r1-w);%inner diameter of tube
G=massflow/(d^2*pi()/4);
L=N(i)*(t+S);%tube length
r2c=r2(ii)+t/2;
Af=2*pi()*(r2c^2-r1.^2);%area surface of the fin
At=(Af+S*r1*2*pi())*N(i);%total area

C1=h_PCM*At*(1-N(i)*Af/At*(1-Fin_Efficiency_Cal(r1,r2(ii),k_fin,h_PCM,t)));
C2=2*pi()*k_tube*L/log(r1/r0);
C3=2*pi()*r0*L*HTC_Boiling(G,d,rho_l,rho_g,miu_l,Cp_l,k_l,x);

T_base=((C1*C3+C1*C2)*T_PCM+C2*C3*T_in)/(C1*C3+C1*C2+C2*C3);
T_wall=(C3*C2*T_in-C1*C2*T_base+C1*C2*T_PCM)/(C3*C2);
%output in loop
    Temp_b(i,ii)=T_base;
    Temp_w(i,ii)=T_wall;
    HTC_avg(i,ii)=HTC_Boiling_Shah(G,d,rho_l,rho_g,miu_l,Cp_l,k_l,x);
    HeatRate(i,ii)=-C3*(T_in-T_wall);
end
end

function [HTC] = HTC_Boiling(G,d,rho_l,rho_g,miu,Cp,k_l,x)
```

```
%HTC_TWOPHASE Summary of this function goes here
%G mass flux, kg/m^2/s
%d diameter of pipe, m
%rho_l rho_g density of liquid and gas phase, kg/m^3
%miu dyanmic viscosity, Pa*s
%Cp thermal capacity, J/Kg/K
%k_l thermal conductivity of liquid phase, W/m/K
%x vapour quality, 0-1

%Froude numbers
Fr=G^2/9.8/rho_l^2/d;
%correction factor
if Fr<0.04
    K_FR=(25*Fr)^-0.3;
else
    K_FR=1;
end

%convection number
Co=K_FR*((1-x)/x)^0.8*(rho_g/rho_l)^0.5;

%convection boiling factor
if Co<1
    Fcb=1.8*Co^-0.8;
else
    Fcb=1+0.8*exp(1-Co^0.5);
end
%velocity
v=G/rho_l;%volume flow rate
%Renold number
Re=v*rho_l*d/miu;
%Prandlt bumber
Pr=Cp*miu/k_l;
%liquid only heat transfer coefficient
h_l=0.023*Re^0.8*Pr^0.4*k_l/d;

%enhancement factor due to the two phase flow
F=Fcb*(1-x);

%two phase flowheat transfer coefficient
HTC=F*h_l;

End
```

Condensation process

```
%input
%%Geometry
N=5:5:70;%fin number
S=20e-3;%fin gap[2.5e-3 5e-3 10e-3]
t=1.5e-3;%fin thickness
r2=10e-3:10e-3:200e-3;%fin raidus
r1=3e-3;%pipe outer radius
w=1e-3;%pipe wall thickness
r0=r1-w;%pipe inner radius

%%Conditions
T_PCM=113; %PCM Temperature, K, fixed
massflow=1e-3; %kg/s
T_in=123;%inlet temperature

%material Properties
k_fin=500; %fin thermal conductivity, fixed
k_tube=500;%tube thermal conductivity
h_PCM=0.19;%PCM thermal conductivity

%Working Fluid Properties, fixed
rho_l=591.16;%kg/m^3
rho_g=79.674;%kg/m^3
miu_l=4.9210e-5;%Pa*s
miu_g=9.1543e-6;%Pa*s
v_l=miu_l/rho_l;%m^2/s
v_g=miu_g/rho_g;%m^/s
Cp_l=3.0676e3;%J/Kg/K
Cp_g=2.5051e3;%J/Kg/K
k_l=0.075026;%W/m*k
k_g=0.016507;%W/m*k
x=0.3;
sigma_l=0.0016033;%N*m
sigma_g=0.0016033;%N*m

%Initialization
Temp_b=zeros(length(N),length(r2));
Temp_w=zeros(length(N),length(r2));
HeatRate=zeros(length(N),length(r2));
HTC_avg=zeros(length(N),length(r2));
%Calcualtion
```

```
for i=1:length(N)
for ii=1:length(r2)
d=2*(r1-w);%inner diameter of tube
G=massflow/(d^2*pi()/4);
L=N(i)*(t+S);%tube length
r2c=r2(ii)+t/2;
Af=2*pi()*(r2c^2-r1^2);%area surface of the fin
At=(Af+S*r1*2*pi())*N(i);%total area

C1=h_PCM*At*(1-N(i)*Af/At*(1-Fin_Efficiency_Cal(r1,r2(ii),k_fin,h_PCM,t)));
C2=2*pi()*k_tube*L/log(r1/r0);
C3=2*pi()*r0*L*HTC_Condenstion(G,d,rho_l,rho_g,miu_l,miu_g,v_l,v_g,Cp_l,Cp_
g,k_l,k_g,sigma_l,sigma_g,x);

T_base=((C1*C3+C1*C2)*T_PCM+C2*C3*T_in)/(C1*C3+C1*C2+C2*C3);
T_wall=(C3*C2*T_in-C1*C2*T_base+C1*C2*T_PCM)/(C3*C2);
%output in loop
    Temp_b(i,ii)=T_base;
    Temp_w(i,ii)=T_wall;

HTC_avg(i,ii)=HTC_Condenstion(G,d,rho_l,rho_g,miu_l,miu_g,v_l,v_g,Cp_l,Cp_g
,k_l,k_g,sigma_l,sigma_g,x);
    HeatRate(i,ii)=-C3*(T_in-T_wall);
end
end

function [HTC,FlowRegime] =
HTC_Condenstion(G,d,rho_l,rho_g,miu_l,miu_g,v_l,v_g,Cp_l,Cp_g,k_l,k_g,sigma
_l,sigma_g,x)
%Kim 2013 Model is a fitted model which should be conservative for
%downward annular condensation
%nitrogen liquification
%Sung-Min Kim,Issam Mudawar, Universal approach to predicting heat transfer
%coefficient for condensing mini/micro-channel flow, International Journal
%of Heat and Mass Transfer, 2013, Vol 56, Issuses 1-2, Pages 238-250

%rho=density in kg/m^3, miu=dynamic viscosity in Pa*S,Cp=specific heat
%capacity in kJ/kgK, k thermal conductivity in W/m^2/K, sigma=surface
%tension in N/m
%_l=liquid phase, _g=gas phase
%x=vapor quality

g=9.8; %Set gravity
%Reynolods numbers
```

```
Re_l=G*(1-x)*d/miu_l;
Re_g=G*x*d/miu_g;
Re_lo=G*d/miu_l;

%Prandtl number
Pr_l=Cp_l*miu_l/k_l;
Pr_g=Cp_g*miu_g/k_g;

%Lockhart-Martinelli parameter, only momentum equilibrium flow is
considered
X_tt=(miu_l/miu_g)^0.1*((1-x)/x)^0.9*(rho_g/rho_l)^0.5;

%Liquid- or vapor-only Suratman number
Su_go=rho_g*sigma_g*d/miu_g^2;

%modified Webber number, in Ref equation 15a and 15b
if Re_l<=1250
    We=2.45*Re_g^0.64/(Su_go^0.3*(1+1.09*X_tt^0.039)^0.4);
else

We=0.85*Re_g^0.79*X_tt^0.157*((miu_g/miu_l)^2*(rho_l/rho_g))^0.084/(Su_go^0
.3*(1+1.09*X_tt^0.039)^0.4);
end

%Two phase multipiler
if Re_l>=2000 && Re_g>=2000
    C=3.9*10^-2*Re_lo^0.03*Su_go^0.1*(rho_l/rho_g)^0.35;
elseif Re_l>=2000 && Re_g<2000
    C=8.7*10^-4*Re_lo^0.17*Su_go^0.5*(rho_l/rho_g)^0.14;
elseif Re_l<2000 && Re_g>=2000
    C=1.5*10^-3*Re_lo^0.59*Su_go^0.19*(rho_l/rho_g)^0.36;
elseif Re_l<2000 && Re_g<2000
    C=3.5*10^-5*Re_lo^0.44*Su_go^0.5*(rho_l/rho_g)^0.48;
end

if Re_l<2000
    ff=16*Re_l^-1;
elseif Re_l>=2000 && Re_l<20000
    ff=0.079*Re_l^-0.25;
elseif Re_l>=20000
    ff=0.046*Re_l^-0.2;
end

if Re_g<2000
```

```
    fg=16*Re_g^-1;
elseif Re_g>=2000 && Re_g<20000
    fg=0.079*Re_g^-0.25;
elseif Re_g>=20000
    fg=0.046*Re_g^-0.2;
end
X=sqrt((ff*v_l*(1-x)^2)/(fg*v_g*x^2));
fai=sqrt(1+C*X+X^2);

%Heat Transfer Coefficient
if We>7*X_tt^0.2  %for annular flow
    HTC=(k_l/d)*0.048*Re_l^0.69*Pr_l^0.34*fai/X_tt;
else %for slug and bubbly flow
    HTC=(k_l/d)*sqrt((0.048*Re_l^0.69*Pr_l^0.34*fai/X_tt)^2+(3.2*10^-
7*Re_l^-0.38*Su_go^1.39)^2);
end
FlowRegime=We/(7*X_tt^0.2);
```

Appendix C

Experimental procedures

The experimental procedures can be divided into three steps: 1) the experimental preparation process; 2) the system charging process, which starts from the LN_2 tank, and ends with the gas heating system; 3) the system discharge process, which starts from the N_2 cylinder and ends with the gas heating system. According to system temperature variations, the experimental procedures for the test rig are depicted in Figure C.1.

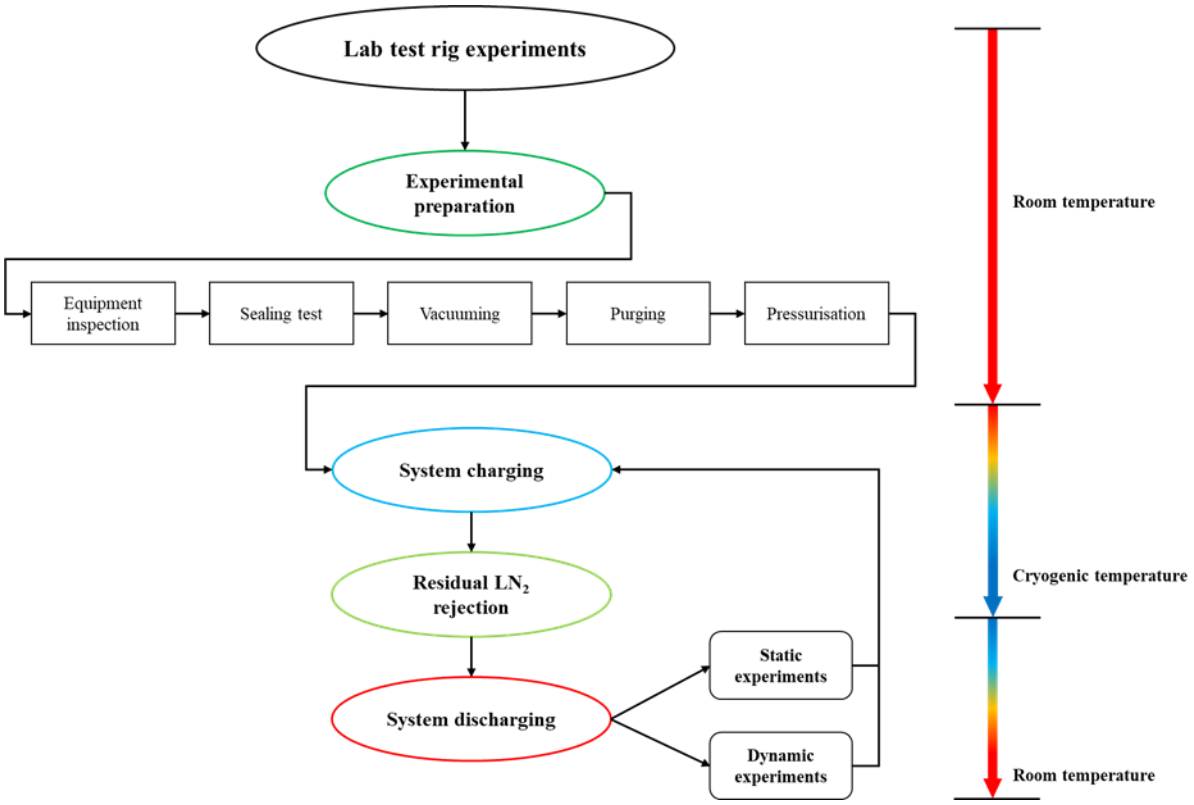


Figure C.1: The experimental procedures for the test rig based on system temperature changes.

Experimental preparation process

Before starting system experiments, the preparation work needs to be carried out to ensure that the experiments run smoothly. The preparation process includes: 1) equipment inspections; 2) system

sealing test; 3) evacuation of LHCS and SHCS tanks; 4) system purging; 5) system pressurizing.

Equipment inspections

The equipment inspections are summarised below:

1) Check and record the amount of LN_2 according to the reading of the electronic contents gauge;
2) Check the amount of N_2 based on the pressure reading of the gas cylinder;
3) Check the connection status between the data acquisition system and the PC (including data logger and mass flow controller software);
4) Check the power connection of the system control panel mainly including solenoid valves and the emergency stop button;
5) Check the water level of the thermostat bath;

System sealing test

The system pressure was increased to 19 barg to perform the sealing test. In this operation, the downstream MFC 1 and the valve 15 were closed to build the system pressure. At the same time, soap bubbles were used at the critical connections of components to verify the system leakage status when the system pressure increased. Once the system pressure was maintained at 19 barg for 10 minutes, the corresponding flow rate reading of MFC 2 was recorded as the system leakage rate, which was 0.052 g/s.

Vacuuming of LHCS and SHCS tanks

In order to reduce the loss of stored cold energy due to heat transfer between the material and its surroundings, two tanks were vacuumed prior to the experiment. As described in Sections 5.2.1 and

5.2.2, the blue-red rubber sleeve was removed from the safety ports of both tanks to connect the vacuum pump.

System purging

Because both processes operated at relatively low temperatures, the pipes and components were dehumidified with N_2 three times before the experiment. In this step, the operating pressure was set to 8 barg, and the mass flow rate of the N_2 was 0.5 g/s.

System pressurisation

In order to avoid the rapid evaporation of LN_2 due to the large pressure difference during the initial stage of the charging process, the system pressure, therefore, was increased to close to that of the LN_2 vessel before LN_2 was introduced into the system. This step also used the N_2 cylinder as the pressure source, the operating pressure at this point was set slightly below the LN_2 vessel pressure, and the mass flow rate of the N_2 was 0.5 g/s.

According to the system flow chart (see Figure 5.1), system purging, and pressurisation operations are as follows:

1) Set and open the pressure regulator (V1);
2) Open the solenoid valve (V2) by its power switch;
3) Set the flow rate 0.5 g/s on mass flow controller (MFC 2);
4) Close the extended spindle globe valve (V11);
5) Open the extended spindle needle valve (V10);
6) Open the extended spindle globe valve (V12);

7) Open the bypass valve (V15) for system purging, close the V15 for system pressurizing;

8) Set the flow rate 0 g/s on mass flow controller (MFC1).

9) Monitor the system pressure no exceed the pressure relief valve setting value.

System charging process

Depending on the temperature variation of the CTES materials, the system charging process has two stages: 1) fluctuation stage; 2) stable decline stage.

In the initial fluctuation stage, LN_2 was mainly used for cooling system pipes and components, such as the U-shaped tube and the flange chamber of the LHCS tank. Therefore, the temperature of CTES materials remained almost constant over a period of time. During this time, the temperature at the bottom of the U-shaped tube also tended to fluctuate up and down. Once the AS temperature reached the saturation temperature of the LN_2 at this operating pressure, the system charging process will move on to the next stage.

The second stage was a steady decrease in the temperature of CTES materials. The cold energy input to the system was adjusted in time by MFC 1 according to the working power of the thermostat bath and the cooling rate of CTES materials. To avoid the issue of the SHS material being overcooled due to different thermal conductivity of PCM and glass beads, two methods were proposed: 1) remove the pipe insulation material between the LHCS and SHCS tanks to ensure that the inlet temperature (T_2) of the SHCS tank is higher than the phase transition temperature of the PCM; 2) adjust the sequence of LN_2 flowing through the system so that it only passes through the LHCS tank to cool down the PCM.

The detailed operations are summarised as follows:

1) Open the power switch of the thermostat bath, and set the heating temperature at 40℃;
2) Open the pressure building valve of the LN_2 vessel;
3) Open the decant valve (V4) on the top of the LN2 vessel;
4) Open the solenoid valve (V6) by its power switch;
5) Close the extended spindle needle valve (V10);
6) Open the extended spindle globe valve (V11);
7) Open the extended spindle globe valve (V12);
8) Close the bypass valve (V15);
9) Set the flow rate 2 g/s on mass flow controller (MFC 1);
10) Monitor the working power of the thermostat bath after each adjustment of LN_2 flow rate;
11) Monitor the system pressure no exceed the pressure relief valve setting value;
12) Remove the pipe insulation material in the event of excessive cooling of glass beads;
13) Change the path of LN_2 through the system, open the extended spindle needle valve (V10);
14) Close the extended spindle globe valve (V11).

Moreover, the residual LN_2 in the system was evaporated by reducing the system pressure at the end of the charging process. This rejection process was conducted several times to ensure that no liquid remained in the system. It is possible to determine whether the remaining LN_2 has been completely evaporated according to the pressure and temperature changes during the system pressure release. For instance, as the system pressure gradually decreases, the temperature at the bottom of the U-shaped tube (AS) tends to decrease due to heat absorption by evaporation of the LN_2. Once its temperature has not dropped significantly, it means that the LN_2 has been completely evacuated. Moreover, the

fluctuations in system pressure (P_1-P_3) can also be used as a criterion, i.e., no obvious increase in system pressure after closing the bypass valve (V15) and the mass flow controller (MFC1).

The detailed operations are summarised below:

1) Close the decant valve (V4) of the LN_2 tank;
2) Keep the solenoid valve (V6) open;
3) Close the extended spindle needle valve (V11);
4) Open the extended spindle globe valve (V10);
5) Open the extended spindle globe valve (V12);
6) Open the bypass valve (V15);
7) Set the flow rate 0 g/s on mass flow controller (MFC 1);
8) Close the bypass valve (V15) once the AS temperature has not dropped.

System discharging process

The system discharging process was classified as static and dynamic experiments according to different operating conditions.

Static experiments

The system static experiment was carried out under sealed conditions with the bypass valve (V15) and the MFC 1 closed throughout. Following the system residual LN_2 rejection process, the system pressure was then raised to the operating pressure. The AS temperature was monitored in real time as soon as the system pressure reached the set point of the N_2 cylinder. Simultaneously, the variation in mass flow rate of N_2 entering the system was recorded during the entire experimental process to

determine the state of the internal gas. Theoretically, the readout of MFC 2 will decrease to 0 as the system pressure increases to the operating pressure, while the reading changes after the system pressure stabilisation and the corresponding AS temperature can be used to detect whether the gas will be liquefied. The detailed operations are summarised below:

1) Set and open the pressure regulator (V1) of N_2 cylinder;
2) Open the solenoid valve (V2) by power switch;
3) Set the flow rate 2 g/s on mass flow controller (MFC 2);
4) Close the extended spindle globe valve (V11);
5) Open the extended spindle needle valve (V10);
6) Open the extended spindle globe valve (V12);
7) Close the bypass valve (V15);
8) Set the flow rate 0 g/s on MFC 1;
9) Record the change in flow rate changes of MFC 2;
10) Monitor the real-time AS temperature and the system pressure; and
11) Always check the operating power of the heating system.

Dynamic experiments

The main difference from the static experiment is that during the dynamic experiment the opening of MFC 1 was adjusted according to the actual PCM temperature and system pressure variations. For instance, the initial value was set to a small flow rate in order to reduce the time required to pressurise the system. Once the system pressure approached a predetermined test value, the flow rate was increased allowing the system pressure to stabilise in dynamic equilibrium. In the subsequent N_2 liquefaction tests, the change in flow rate was dependent on the temperature variation of the PCM.

Besides, the actual AS temperature and the saturation temperature of LN_2 corresponding to actual system pressure were used to evaluate the N_2 liquefaction process. This evaluation process will be further discussed in Chapter 6 based on the experimental results. The detailed operations follow the static experiment except for maintaining the adjustments of MFC 1.

Bibliography

[1] Veziroglu, T. N. (2007). 21st Century's energy: Hydrogen energy system. In *Assessment of hydrogen energy for sustainable development* (pp. 9-31). Springer, Dordrecht.

[2] REN21. (2021). Renewables 2021 global status report. *Paris: REN21 Secretariat*.

[3] Dudley, B. (2021). BP statistical review of world energy 2021, 70th edition. *London, UK*.

[4] UK Government, Industrial decarbonization strategy, 2021. Department for Business, Energy & Industrial Strategy. (2021, April 20). *UK enshrines new target in law to slash emissions by 78% by 2035*. GOV.UK. https://www.gov.uk/government/news/uk-enshrines-new-target-in-law-to-slash-emissions-by-78-by-2035

[5] Verbruggen, A. (2008). Renewable and nuclear power: A common future?. *Energy Policy*, *36*(11), 4036-4047.

[6] Weisser, D., & Garcia, R. S. (2005). Instantaneous wind energy penetration in isolated electricity grids: concepts and review. *Renewable energy*, 30(8), 1299-1308.

[7] Rodrigues, E. M. G., Godina, R., Santos, S. F., Bizuayehu, A. W., Contreras, J., & Catalão, J. P. S. (2014). Energy storage systems supporting increased penetration of renewables in islanded systems. *Energy*, 75, 265-280.

[8] Liquid air in the energy and transport systems. The Centre for Low Carbon Futures;2013. http://bit.ly/liquid-air-full-report-2013.

[9] Smith EM. STORAGE OF ELECTRICAL ENERGY USING SUPERCRITICAL LIQUID AIR n.d.;191.

[10] Energy storage-revolution in the air. Mod Power Syst 2013:32.

[11] GE storage agreement with highview. Mod Power Syst 2014:4.

[12] Strahan D. Liquid air technologies: a guide to the potential. Centre for Low Carbon Futures; 2013.

[13] Morgan, R., Nelmes, S., Gibson, E., & Brett, G. (2015). An analysis of a large-scale liquid air energy

storage system. *Proceedings of the Institution of Civil Engineers-Energy*, 168(2), 135-144.

[14] Hüttermann, L., & Span, R. (2019). Influence of the heat capacity of the storage material on the efficiency of thermal regenerators in liquid air energy storage systems. *Energy*, 174, 236-245.

[15] Sciacovelli, A., Vecchi, A., & Ding, Y. (2017). Liquid air energy storage (LAES) with packed bed cold thermal storage–From component to system level performance through dynamic modelling. *Applied energy*, *190*, 84-98.

[16] Sharma, A., Tyagi, V. V., Chen, C. R., & Buddhi, D. (2009). Review on thermal energy storage with phase change materials and applications. *Renewable and Sustainable energy reviews*, *13*(2), 318-345.

[17] Lane, G. A. (1983). Solar heat storage: Latent heat materials. Volume 1. Background and scientific principles.

[18] Mehling, H., & Cabeza, L. F. (2008). *Heat and cold storage with PCM* (Vol. 308). Berlin: springer.

[19] Abedin, A. H., & Rosen, M. A. (2012). Closed and open thermochemical energy storage: Energy-and exergy-based comparisons. *Energy*, *41*(1), 83-92.

[20] Hauer, A. (2011). Storage technology issues and opportunities. In *Committee on Energy Research and Technology (International Energy Agency), International Low-Carbon Energy Technology Platform, Strategic and Cross-Cutting Workshop "Energy Storage–Issues and Opportunities*.

[21] H Abedin, A., & A Rosen, M. (2011). A critical review of thermochemical energy storage systems. *The open renewable energy journal*, *4*(1).

[22] Abhat, A. (1983). Low temperature latent heat thermal energy storage: heat storage materials. *Solar energy*, *30*(4), 313-332.

[23] Cabeza, L. F., Castell, A., Barreneche, C. D., De Gracia, A., & Fernández, A. I. (2011). Materials used as PCM in thermal energy storage in buildings: A review. *Renewable and Sustainable Energy Reviews*, *15*(3),

1675-1695.

[24] Zhou, D., Zhao, C. Y., & Tian, Y. (2012). Review on thermal energy storage with phase change materials (PCMs) in building applications. *Applied energy*, *92*, 593-605.

[25] Araki, H., Nakabaru, M., & Chino, K. (2002). Simulation of heat transfer in the cool storage unit of a liquid–air energy storage system. *Heat Transfer—Asian Research: Co-sponsored by the Society of Chemical Engineers of Japan and the Heat Transfer Division of ASME*, *31*(4), 284-296.

[26] Sciacovelli, A., Smith, D., Navarro, H., Li, Y., & Ding, Y. (2016). Liquid air energy storage–Operation and performance of the first pilot plant in the world. *Proceedings of ECOS*, 19-23.

[27] Peng, H., Shan, X., Yang, Y., & Ling, X. (2018). A study on performance of a liquid air energy storage system with packed bed units. *Applied Energy*, *211*, 126-135.

[28] Morgan, R., Nelmes, S., Gibson, E., & Brett, G. (2015). Liquid air energy storage–analysis and first results from a pilot scale demonstration plant. *Applied energy*, *137*, 845-853.

[29] Chai, L., Liu, J., Wang, L., Yue, L., Yang, L., Sheng, Y., ... & Tan, C. (2014). Cryogenic energy storage characteristics of a packed bed at different pressures. *Applied Thermal Engineering*, *63*(1), 439-446.

[30] Laughlin, R. B. (2017). Pumped thermal grid storage with heat exchange. *Journal of Renewable and Sustainable Energy*, *9*(4), 044103.

[31] Li, Y., Cao, H., Wang, S., Jin, Y., Li, D., Wang, X., & Ding, Y. (2014). Load shifting of nuclear power plants using cryogenic energy storage technology. *Applied energy*, *113*, 1710-1716.

[32] Hüttermann, L., Span, R., Maas, P., & Scherer, V. (2019). Investigation of a liquid air energy storage (LAES) system with different cryogenic heat storage devices. *Energy Procedia*, *158*, 4410-4415.

[33] Su, W., Darkwa, J., & Kokogiannakis, G. (2015). Review of solid–liquid phase change materials and their encapsulation technologies. *Renewable and Sustainable Energy Reviews*, *48*, 373-391.

[34] Dheep, G. R., & Sreekumar, A. (2014). Influence of nanomaterials on properties of latent heat solar thermal energy storage materials–A review. *Energy conversion and management*, *83*, 133-148.

[35] Sarbu, I., & Sebarchievici, C. (2018). A comprehensive review of thermal energy storage. *Sustainability*, *10*(1), 191..

[36] Zalba, B., Marın, J. M., Cabeza, L. F., & Mehling, H. (2003). Review on thermal energy storage with phase change: materials, heat transfer analysis and applications. *Applied thermal engineering*, *23*(3), 251-283.

[37] Oró, E., De Gracia, A., Castell, A., Farid, M. M., & Cabeza, L. F. (2012). Review on phase change materials (PCMs) for cold thermal energy storage applications. Applied Energy, 99, 513-533.

[38] Li, G., Hwang, Y., Radermacher, R., & Chun, H. H. (2013). Review of cold storage materials for subzero applications. Energy, 51, 1-17.

[39] Mohamed, S. A., Al-Sulaiman, F. A., Ibrahim, N. I., Zahir, M. H., Al-Ahmed, A., Saidur, R., ... & Sahin, A. Z. (2017). A review on current status and challenges of inorganic phase change materials for thermal energy storage systems. *Renewable and Sustainable Energy Reviews*, *70*, 1072-1089.

[40] Lin, Y., Alva, G., & Fang, G. (2018). Review on thermal performances and applications of thermal energy storage systems with inorganic phase change materials. *Energy*, *165*, 685-708.

[41] Yang, L., Villalobos, U., Akhmetov, B., Gil, A., Khor, J. O., Palacios, A., ... & Romagnoli, A. (2021). A comprehensive review on sub-zero temperature cold thermal energy storage materials, technologies, and applications: State of the art and recent developments. *Applied Energy*, 116555.

[42] Lee, J., Jeong, S., Han, Y. H., & Park, B. J. (2010). Concept of cold energy storage for superconducting flywheel energy storage system. *IEEE Transactions on applied superconductivity*, *21*(3), 2221-2224.

[43] Parks, G. S., Moore, G. E., Renquist, M. L., Naylor, B. F., McClaine, L. A., Fujii, P. S., & Hatton, J. A. (1949). Thermal data on organic compounds. XXV. Some heat capacity, entropy and free energy data for nine

hydrocarbons of high molecular weight. *Journal of The American Chemical Society*, *71*(10), 3386-3389.

[44] Messerly, J. F., Guthrie Jr, G. B., Todd, S. S., & Finke, H. L. (1967). Low-temperature thermal data for pentane, n-heptadecane, and n-octadecane. Revised thermodynamic functions for the n-alkanes, C5-C18. *Journal of Chemical and Engineering Data*, *12*(3), 338-346.

[45] Sarier, N., & Onder, E. (2012). Organic phase change materials and their textile applications: an overview. *Thermochimica acta*, *540*, 7-60.

[46] Hägg, C. (2005). *Ice slurry as secondary fluid in refrigeration systems: fundamentals and applications in supermarkets* (Doctoral dissertation, KTH).

[47] Kumano, H., Asaoka, T., Saito, A., & Okawa, S. (2007). Study on latent heat of fusion of ice in aqueous solutions. *International journal of refrigeration*, *30*(2), 267-273.

[48] Kenisarin, M. M. (2014). Thermophysical properties of some organic phase change materials for latent heat storage. A review. *Solar Energy*, *107*, 553-575.

[49] Hasnain, S. M. (1998). Review on sustainable thermal energy storage technologies, Part I: heat storage materials and techniques. *Energy conversion and management*, *39*(11), 1127-1138.

[50] Haynes, W. (2016). *CRC Handbook of Chemistry and Physics, 97th Edition*. CRC Press LLC.

[51] Ke, H. (2017). Phase diagrams, eutectic mass ratios and thermal energy storage properties of multiple fatty acid eutectics as novel solid-liquid phase change materials for storage and retrieval of thermal energy. *Applied Thermal Engineering*, *113*, 1319-1331.

[52] Sharma, R. K., Ganesan, P., Tyagi, V. V., Metselaar, H. S. C., & Sandaran, S. C. (2015). Developments in organic solid–liquid phase change materials and their applications in thermal energy storage. *Energy Conversion and Management*, *95*, 193-228.

[53] Zhang, J., & Li, Y. (2020). Highly Accurate Prediction Method for Thermophysical Properties of Cryogenic

Phase Change Materials. *Chemical Engineering & Technology*, *43*(6), 1167-1175.

[54] PCM Products Ltd. Sub-Zero Eutectic PCM Solutions; n.d. https://www.pcmproducts.net/Eutectic_Refrigeration_PCMs.htm. [Accessed: 17-Apr-2020].

[55] Rubitherm. PCM SP-LINE 2020. https://www.rubitherm.eu/en/index.php/p roductcategory/anorganische-pcm-sp. [Accessed: 17-Apr-2020].

[56] PURETEMP LLC. Puretemp technical data sheets; 2020. https://www.puretemp. com/stories/puretemp-technical-data-sheets. [Accessed: 17-Apr-2020].

[57] PLUSS. savE PCMs product range; 2020. https://www.pluss.co.in/product-rang e-PCM.php. [Accessed: 17-Apr-2020].

[58] Solé, A., Miró, L., Barreneche, C., Martorell, I., & Cabeza, L. F. (2013). Review of the T-history method to determine thermophysical properties of phase change materials (PCM). *Renewable and Sustainable Energy Reviews*, *26*, 425-436.

[59] Menczel, J. D., Judovits, L., Prime, R. B., Bair, H. E., Reading, M., & Swier, S. (2009). Differential scanning calorimetry (DSC). *Thermal analysis of polymers: Fundamentals and applications*, 7-239.

[60] Castellón, C., Günther, E., Mehling, H., Hiebler, S., & Cabeza, L. F. (2008). Determination of the enthalpy of PCM as a function of temperature using a heat-flux DSC—A study of different measurement procedures and their accuracy. *International Journal of Energy Research*, *32*(13), 1258-1265.

[61] Kousksou, T., Jamil, A., El Omari, K., Zeraouli, Y., & Le Guer, Y. (2011). Effect of heating rate and sample geometry on the apparent specific heat capacity: DSC applications. *Thermochimica acta*, *519*(1-2), 59-64.

[62] Günther, E., Hiebler, S., Mehling, H., & Redlich, R. (2009). Enthalpy of phase change materials as a function of temperature: required accuracy and suitable measurement methods. *International Journal of Thermophysics*, *30*(4), 1257-1269.

[63] Rathgeber, C., Schmit, H., Miró, L., Cabeza, L. F., Gutierrez, A., Ushak, S. N., & Hiebler, S. (2018). Enthalpy-temperature plots to compare calorimetric measurements of phase change materials at different sample scales. *Journal of Energy Storage*, *15*, 32-38.

[64] Rathgeber, C., Schmit, H., Miró, L., Cabeza, L. F., Gutierrez, A., Ushak, S. N., ... & Hauer, A. (2015). Analysis of supercooling of phase change materials with increased sample size–Comparison of measurements via DSC, T-History and at pilot plant scale. In *Greenstock 2015-13th IEA ECES Conference* (pp. 14-41).

[65] Yinping, Z., & Yi, J. (1999). A simple method, the-history method, of determining the heat of fusion, specific heat and thermal conductivity of phase-change materials. *Measurement Science and Technology*, *10*(3), 201.

[66] Lazaro, A., Günther, E., Mehling, H., Hiebler, S., Marin, J. M., & Zalba, B. (2006). Verification of a T-history installation to measure enthalpy versus temperature curves of phase change materials. *Measurement Science and Technology*, *17*(8), 2168.

[67] Peck, J. H., Kim, J. J., Kang, C., & Hong, H. (2006). A study of accurate latent heat measurement for a PCM with a low melting temperature using T-history method. *International Journal of Refrigeration*, *29*(7), 1225-1232.

[68] Badenhorst, H., & Cabeza, L. F. (2017). Critical analysis of the T-history method: A fundamental approach. *Thermochimica Acta*, *650*, 95-105.

[69] Hong, H., Kim, S. K., & Kim, Y. S. (2004). Accuracy improvement of T-history method for measuring heat of fusion of various materials. *International Journal of Refrigeration*, *27*(4), 360-366.

[70] Marin, J. M., Zalba, B., Cabeza, L. F., & Mehling, H. (2003). Determination of enthalpy–temperature curves of phase change materials with the temperature-history method: improvement to temperature dependent properties. *Measurement science and technology*, *14*(2), 184.

[71] Tritt, T. M. (Ed.). (2005). *Thermal conductivity: theory, properties, and applications*. Springer Science & Business Media.

[72] Czichos, H., & Saito, T. (2006). *Springer handbook of materials measurement methods* (Vol. 978, pp. 399-429). L. Smith (Ed.). Berlin: Springer.

[73] Palacios, A., Cong, L., Navarro, M. E., Ding, Y., & Barreneche, C. (2019). Thermal conductivity measurement techniques for characterizing thermal energy storage materials–A review. *Renewable and Sustainable Energy Reviews*, *108*, 32-52.

[74] Zhao, D., Qian, X., Gu, X., Jajja, S. A., & Yang, R. (2016). Measurement techniques for thermal conductivity and interfacial thermal conductance of bulk and thin film materials. *Journal of Electronic Packaging*, *138*(4).

[75] Hwang, Y. J., Ahn, Y. C., Shin, H. S., Lee, C. G., Kim, G. T., Park, H. S., & Lee, J. K. (2006). Investigation on characteristics of thermal conductivity enhancement of nanofluids. *Current Applied Physics*, *6*(6), 1068-1071.

[76] Assael, M. J., Antoniadis, K. D., & Wakeham, W. A. (2010). Historical evolution of the transient hot-wire technique. *International journal of thermophysics*, *31*(6), 1051-1072.

[77] Min, S., Blumm, J., & Lindemann, A. (2007). A new laser flash system for measurement of the thermophysical properties. *Thermochimica Acta*, *455*(1-2), 46-49.

[78] Lian, T. W., Kondo, A., Akoshima, M., Abe, H., Ohmura, T., Tuan, W. H., & Naito, M. (2016). Rapid thermal conductivity measurement of porous thermal insulation material by laser flash method. *Advanced Powder Technology*, *27*(3), 882-885.

[79] Chen, R., Huang, X., Zheng, R., Xie, D., Mei, Y., & Zou, R. (2020). Flame-retardancy and thermal properties of a novel phosphorus-modified PCM for thermal energy storage. *Chemical Engineering Journal*, *380*, 122500.

[80] Coronado, C. J., Carvalho Jr, J. A., Andrade, J. C., Cortez, E. V., Carvalho, F. S., Santos, J. C., & Mendiburu, A. Z. (2012). Flammability limits: a review with emphasis on ethanol for aeronautical applications and description of the experimental procedure. *Journal of hazardous materials*, *241*, 32-54.

[81] Le, H., Liu, Y., & Mannan, M. S. (2013). Lower flammability limits of hydrogen and light hydrocarbons at subatmospheric pressures. *Industrial & Engineering Chemistry Research*, *52*(3), 1372-1378.

[82] Gharagheizi, F. (2009). A new group contribution-based model for estimation of lower flammability limit of pure compounds. *Journal of hazardous materials*, *170*(2-3), 595-604.

[83] Crowl, D. A., & Louvar, J. F. (2019). *Chemical process safety: fundamentals with applications, 4th Edition*. Pearson Education.

[84] Albahri, T. A. (2003). Flammability characteristics of pure hydrocarbons. *Chemical Engineering Science*, *58*(16), 3629-3641.

[85] Rowley, J. R., Rowley, R. L., & Wilding, W. V. (2011). Estimation of the lower flammability limit of organic compounds as a function of temperature. *Journal of hazardous materials*, *186*(1), 551-557.

[86] Vidal, M., Wong, W., Rogers, W. J., & Mannan, M. S. (2006). Evaluation of lower flammability limits of fuel–air–diluent mixtures using calculated adiabatic flame temperatures. *Journal of hazardous materials*, *130*(1-2), 21-27.

[87] European Standard EN1839. Determination of the explosion limits and the limiting oxygen concentration (LOC) for flammable gases and vapours. European Standard; 2017.

[88] ASTM E681-09, Standard Test Method for Concentration Limits of Flammability of Chemicals (Vapors and Gases). West Conshohocken, PA, 2015, USA.

[89] ASTM E2079-19, Standard Test Methods for Limiting Oxygen (Oxidant) Concentration in Gases and Vapors, ASTM International, West Conshohocken, PA, 2019, USA.

[90] Takahashi, A., Urano, Y., Tokuhashi, K., & Kondo, S. (2003). Effect of vessel size and shape on experimental flammability limits of gases. *Journal of hazardous materials*, *105*(1-3), 27-37.

[91] Schroder, V., & Molnarne, M. (2005). Flammability of gas mixtures: Part 1: Fire potential. *Journal of hazardous materials*, *121*(1-3), 37-44.

[92] Kind, D. J., & Hull, T. R. (2012). A review of candidate fire retardants for polyisoprene. *Polymer Degradation and Stability*, *97*(3), 201-213.

[93] Sittisart, P., & Farid, M. M. (2011). Fire retardants for phase change materials. *Applied Energy*, *88*(9), 3140-3145.

[94] Zhang, P., Song, L., Lu, H., Wang, J., & Hu, Y. (2010). The influence of expanded graphite on thermal properties for paraffin/high density polyethylene/chlorinated paraffin/antimony trioxide as a flame retardant phase change material. *Energy conversion and management*, *51*(12), 2733-2737.

[95] Chen, L., & Wang, Y. Z. (2010). A review on flame retardant technology in China. Part I: development of flame retardants. *Polymers for Advanced Technologies*, *21*(1), 1-26.

[96] Bocchini, S., & Camino, G. (2010). Halogen-containing flame retardants. *Fire retardancy of polymeric materials*, *2*.

[97] Kashiwagi, T., Shields, J. R., Harris Jr, R. H., & Davis, R. D. (2003). Flame‐retardant mechanism of silica: Effects of resin molecular weight. *Journal of applied polymer science*, *87*(9), 1541-1553.

[98] Huang, H., Tian, M., Liu, L., He, Z., Chen, Z., & Zhang, L. (2006). Effects of silicon additive as synergists of $Mg(OH)_2$ on the flammability of ethylene vinyl acetate copolymer. *Journal of applied polymer science*, *99*(6), 3203-3209.

[99] Huang, H., Tian, M., Liu, L., Liang, W., & Zhang, L. (2006). Effect of particle size on flame retardancy of Mg (OH) 2‐filled ethylene vinyl acetate copolymer composites. *Journal of Applied Polymer Science*, *100*(6),

4461-4469.

[100] Jang, J., Chung, H., Kim, M., & Sung, H. (2000). The effect of flame retardants on the flammability and mechanical properties of paper-sludge/phenolic composite. *Polymer Testing*, *19*(3), 269-279.

[101] Li, Q., Li, C., Du, Z., Jiang, F., & Ding, Y. (2019). A review of performance investigation and enhancement of shell and tube thermal energy storage device containing molten salt based phase change materials for medium and high temperature applications. *Applied Energy*, *255*, 113806.

[102] Gautam, A., & Saini, R. P. (2020). A review on sensible heat based packed bed solar thermal energy storage system for low temperature applications. *Solar Energy*, *207*, 937-956.

[103] Ortega-Fernández, I., Zavattoni, S. A., Rodríguez-Aseguinolaza, J., D'Aguanno, B., & Barbato, M. C. (2017). Analysis of an integrated packed bed thermal energy storage system for heat recovery in compressed air energy storage technology. *Applied energy*, *205*, 280-293.

[104] Ismail, K. A. R., & Stuginsky Jr, R. (1999). A parametric study on possible fixed bed models for pcm and sensible heat storage. *Applied Thermal Engineering*, *19*(7), 757-788.

[105] de Gracia, A., & Cabeza, L. F. (2017). Numerical simulation of a PCM packed bed system: a review. *Renewable and Sustainable Energy Reviews*, *69*, 1055-1063.

[106] Schumann, T. E. (1929). Heat transfer: a liquid flowing through a porous prism. *Journal of the Franklin Institute*, *208*(3), 405-416.

[107] Elouali, A., Kousksou, T., El Rhafiki, T., Hamdaoui, S., Mahdaoui, M., Allouhi, A., & Zeraouli, Y. (2019). Physical models for packed bed: Sensible heat storage systems. *Journal of Energy Storage*, *23*, 69-78.

[108] Davenne, T. R., Garvey, S. D., Cardenas, B., & Simpson, M. C. (2017). The cold store for a pumped thermal energy storage system. *Journal of Energy Storage*, *14*, 295-310.

[109] Khor, J. O., Sze, J. Y., Li, Y., & Romagnoli, A. (2020). Overcharging of a cascaded packed bed thermal

energy storage: Effects and solutions. *Renewable and Sustainable Energy Reviews*, *117*, 109421.

[110] Esence, T., Bruch, A., Molina, S., Stutz, B., & Fourmigue, J. F. (2017). A review on experience feedback and numerical modeling of packed-bed thermal energy storage systems. *Solar Energy*, *153*, 628-654.

[111] Colburn, A. P. (1931). Heat transfer and pressure drop in empty, baffled, and packed tubes1. *Industrial & Engineering Chemistry*, *23*(8), 910-913.

[112] Standish, N., & Drinkwater, J. B. (1970). The effect of particle shape on flooding rates in packed columns. *Chemical Engineering Science*, *25*(10), 1619-1621.

[113] Allen, K. G., Von Backström, T. W., & Kröger, D. G. (2013). Packed bed pressure drop dependence on particle shape, size distribution, packing arrangement and roughness. *Powder technology*, *246*, 590-600.

[114] Phillips, W. F. (1981). Effects of stratification on the performance of solar air heating systems. *Solar energy*, *26*(2), 175-180.

[115] Haller, M. Y., Cruickshank, C. A., Streicher, W., Harrison, S. J., Andersen, E., & Furbo, S. (2009). Methods to determine stratification efficiency of thermal energy storage processes–review and theoretical comparison. *Solar Energy*, *83*(10), 1847-1860.

[116] Ramana, A. S., Venkatesh, R., Raj, V. A. A., & Velraj, R. (2014). Experimental investigation of the LHS system and comparison of the stratification performance with the SHS system using CFD simulation. *Solar energy*, *103*, 378-389.

[117] Lugolole, R., Mawire, A., Okello, D., Lentswe, K. A., Nyeinga, K., & Shobo, A. B. (2019). Experimental analyses of sensible heat thermal energy storage systems during discharging. *Sustainable Energy Technologies and Assessments*, *35*, 117-130.

[118] Yang, B., Bai, F., Wang, Y., & Wang, Z. (2019). Study on standby process of an air-based solid packed bed for flexible high-temperature heat storage: Experimental results and modelling. *Applied Energy*, *238*, 135-146.

[119] Torras, S., Castro, J., Rigola, J., Morales-Ruiz, S., Riccius, J., & Leiner, J. (2019). Multiphysics modeling and experimental validation of low temperature accumulator for cryogenic space propulsion systems. *Aerospace Science and Technology*, *84*, 75-89.

[120] Sang, W. H., Lee, Y. T., Chung, J. D., Kim, S. T., Kim, T., Oh, C. H., & Lee, K. H. (2016). Efficient numerical approach for simulating a full scale vertical ice-on-coil type latent thermal storage tank. *International Communications in Heat and Mass Transfer*, *78*, 29-38.

[121] Arunachalam, S. (2019). Latent heat storage: container geometry, enhancement techniques, and applications—a review. *Journal of Solar Energy Engineering*, *141*(5).

[122] Mosaffa, A. H., Talati, F., Tabrizi, H. B., & Rosen, M. A. (2012). Analytical modeling of PCM solidification in a shell and tube finned thermal storage for air conditioning systems. *Energy and buildings*, *49*, 356-361.

[123] Yamashita, Y. O. S. H. I. H. I. K. O., Hirata, Y. U. U. S. H. I., Iwata, Y. U. K. I. O., Yamazaki, K. I. Y. O. S. H. I., & Ito, Y. U. T. A. K. A. (2004). Performance and heat transfer characteristics of a latent heat storage unit with finned tubes: Experimental study on liquefaction of LNG Boil-off Gas by melting n-pentane as a phase-change material. *Kagaku Kogaku Ronbunshu*, *30*(4), 399-406.

[124] Oró, E., Miró, L., Farid, M. M., Martin, V., & Cabeza, L. F. (2014). Energy management and CO2 mitigation using phase change materials (PCM) for thermal energy storage (TES) in cold storage and transport. *International journal of refrigeration*, *42*, 26-35.

[125] Bista, S., Hosseini, S. E., Owens, E., & Phillips, G. (2018). Performance improvement and energy consumption reduction in refrigeration systems using phase change material (PCM). *Applied Thermal Engineering*, *142*, 723-735.

[126] Joybari, M. M., Haghighat, F., Moffat, J., & Sra, P. (2015). Heat and cold storage using phase change

materials in domestic refrigeration systems: The state-of-the-art review. *Energy and Buildings*, *106*, 111-124.

[127] Glaister, D. S., Bell, K. D., Bello, M., & Stoyanof, M. (1995). The development and verification of a cryogenic phase change thermal storage unit for spacecraft applications. In *Cryocoolers 8* (pp. 927-940). Springer, Boston, MA.

[128] Ding, Y., Tong, L., Zhang, P., Li, Y., Radcliffe, J., & Wang, L. (2016). Liquid air energy storage. In *Storing Energy* (pp. 167-181). Elsevier.

[129] He, T., Chong, Z. R., Zheng, J., Ju, Y., & Linga, P. (2019). LNG cold energy utilization: Prospects and challenges. *Energy*, *170*, 557-568.

[130] Kanbur, B. B., Xiang, L., Dubey, S., Choo, F. H., & Duan, F. (2017). Cold utilization systems of LNG: A review. *Renewable and sustainable energy reviews*, *79*, 1171-1188.

[131] Yamamoto, T., & Fujiwara, Y. (2012). The accomplishment of 100% utilization of LNG cold energy. In *Kuala Lumpur 2012 World Gas Conference*.

[132] Yamamoto, T., Fujiwara, Y., & Kitagaki, S. (2012). Challenges of Advanced Utilization of LNG Cold in Osaka Gas Senboku LNG Terminals. In *Design for Innovative Value Towards a Sustainable Society* (pp. 148-153). Springer, Dordrecht.

[133] Otsuka, T. (2006, June). Evolution of an LNG terminal: Senboku terminal of Osaka gas. In *23rd World Gas Conference, Amsterdam* (pp. 1362-1372).

[134] Ito, Y., Okamoto, H., Nii, T., Yamane, M., & Abuyama, T. (1998). Dynamic simulation of cold energy storage and process control for BOG re-liquefied systems; BOG saiekika system ni okeru doteki kaiseki. *R and D Kobe Seiko Giho (Research and Development, Kobe Steel Engineering Reports), 48*.

[135] Toledo, Mettler (2010). Interpreting DSC curves Part 1: Dynamic Measurements.

[136] Incropera, F. P., DeWitt, D. P., Bergman, T. L., & Lavine, A. S. (2017). *Fundamentals of heat and mass*

transfer (8th ed.). New York: Wiley.

[137] Cengel, Y., & Heat, T. M. (2006). *A practical approach (3rd ed.)*. New York, NY, USA: McGraw-Hill.

[138] Yunus A Çengel, & Ghajar, A. J. (2020). *Heat and Mass Transfer: Fundamentals and Applications (6th ed.)*. McGraw-Hill Education.

[139] Shah, M. M., & MM, S. (1976). A new correlation for heat transfer during boiling flow through pipes. *ASHRAE Trans.* 82(2): 66–86.

[140] Shah, M. M. (1982). Chart correlation for saturated boiling heat transfer: equations and further study. *ASHRAE transactions*, 88(1): 185-196.

[141] Chen, J. C. (1966). Correlation for boiling heat transfer to saturated fluids in convective flow. *Industrial & engineering chemistry process design and development*, *5*(3), 322-329.

[142] Kandlikar, S. G. (1990). A general correlation for saturated two-phase flow boiling heat transfer inside horizontal and vertical tubes. *J. Heat Transfer*, 112:219–28.

[143] Steiner, D., & Schlünder, E. U. (1976). Heat transfer and pressure drop for boiling nitrogen flowing in a horizontal tube: 1. Saturated flow boiling. *Cryogenics*, *16*(7), 387-398.

[144] Steiner, D., & Taborek, J. (1992). Flow boiling heat transfer in vertical tubes correlated by an asymptotic model. *Heat transfer engineering*, *13*(2), 43-69.

[145] Liu, Z., & Winterton, R. H. S. (1991). A general correlation for saturated and subcooled flow boiling in tubes and annuli, based on a nucleate pool boiling equation. *International journal of heat and mass transfer*, *34*(11), 2759-2766.

[146] Qi, S. L., Zhang, P., Wang, R. Z., & Xu, L. X. (2007). Flow boiling of liquid nitrogen in micro-tubes: Part II–Heat transfer characteristics and critical heat flux. *International journal of heat and mass transfer*, *50*(25-26), 5017-5030.

[147] Shahs, M. M. (2006). Evaluation of general correlations for heat transfer during boiling of saturated liquids in tubes and annuli. *HVAC&R Research*, *12*(4), 1047-1063.

[148] Cheng, L., Ribatski, G., & Thome, J. R. (2008). Two-phase flow patterns and flow-pattern maps: fundamentals and applications. *Applied Mechanics Reviews*, *61*(5).

[149] Shah, M. M. (1979). A general correlation for heat transfer during film condensation inside pipes. *International Journal of heat and mass transfer*, *22*(4), 547-556.

[150] Wang, W. W. W., Radcliff, T. D., & Christensen, R. N. (2002). A condensation heat transfer correlation for millimeter-scale tubing with flow regime transition. *Experimental Thermal and Fluid Science*, *26*(5), 473-485.

[151] Park, J. E., Vakili-Farahani, F., Consolini, L., & Thome, J. R. (2011). Experimental study on condensation heat transfer in vertical minichannels for new refrigerant R1234ze (E) versus R134a and R236fa. *Experimental thermal and fluid science*, *35*(3), 442-454.

[152] Kim, S. M., & Mudawar, I. (2012). Flow condensation in parallel micro-channels–Part 2: Heat transfer results and correlation technique. *International Journal of Heat and Mass Transfer*, *55*(4), 984-994.

[153] Derby, M., Lee, H. J., Peles, Y., & Jensen, M. K. (2012). Condensation heat transfer in square, triangular, and semi-circular mini-channels. *International Journal of Heat and Mass Transfer*, *55*(1-3), 187-197.

[154] Kim, S. M., & Mudawar, I. (2013). Universal approach to predicting heat transfer coefficient for condensing mini/micro-channel flow. *International Journal of Heat and Mass Transfer*, *56*(1-2), 238-250.

[155] Dobson, M. K., & Chato, J. C. (1998). Condensation in smooth horizontal tubes, *ASME J. Heat Transfer*, 120 (1), 193-213.

[156] Moser, K. W., Webb, R. L., & Na, B. (1998). A new equivalent Reynolds number model for condensation in smooth tubes, *ASME J. Heat Transfer*, 120 (2), 410-417.

[157] Kim, S. M., & Mudawar, I. (2012). Universal approach to predicting two-phase frictional pressure drop

for adiabatic and condensing mini/micro-channel flows. *International Journal of Heat and Mass Transfer*, *55*(11-12), 3246-3261.

[158] Lockhart, R. W. (1949). Proposed correlation of data for isothermal two-phase, two-component flow in pipes. *Chem. Eng. Prog.*, *45*, 39-48.

[159] Soliman, H. M. (1986). The mist-annular transition during condensation and its influence on the heat transfer mechanism. *International Journal of Multiphase Flow*, *12*(2), 277-288.

[160] Powell, R. L., & Blanpied, W. A. (1954). Thermal conductivity of metals and alloys at low temperatures: a review of the literature.

[161] Woodcraft, A. L. (2005). Predicting the thermal conductivity of aluminium alloys in the cryogenic to room temperature range. *Cryogenics*, *45*(6), 421-431.

[162] Kittel, C. (1949). Interpretation of the thermal conductivity of glasses. *Physical Review*, *75*(6), 972.

[163] Gil, L., Ramos, M. A., Bringer, A., & Buchenau, U. (1993). Low-temperature specific heat and thermal conductivity of glasses. *Physical review letters*, *70*(2), 182.

[164] Stephens, R. B. (1976). Intrinsic low-temperature thermal properties of glasses. *Physical Review B*, *13*(2), 852.

[165] Zaitlin, M. P., & Anderson, A. C. (1974). Thermal Conductivity of Borosilicate Glass. *Physical Review Letters*, *33*(19), 1158.

[166] Dilley, N. R., Black, R. C., Montes, L., Wilson, A., & Simmonds, M. B. (2001). Commercial apparatus for measuring thermal transport properties from 1.9 to 390 Kelvin. *MRS Online Proceedings Library*, *691*(1), 1-6.

[167] McCullough, J. P., Finke, H. L., Gross, M. E., Messerly, J. F., & Waddington, G. (1957). Low temperature calorimetric studies of seven 1-olefins: Effect of orientation disorder in the solid state. *The Journal of Physical Chemistry*, *61*(3), 289-301.

[168] Edelstein, F. (1991). The behavior of cryogenic phase change materials used for IR sensor thermal control in space. *SAE transactions*, 1774-1782.

[169] Zahir, M. H., Mohamed, S. A., Saidur, R., & Al-Sulaiman, F. A. (2019). Supercooling of phase-change materials and the techniques used to mitigate the phenomenon. *Applied Energy*, *240*, 793-817.

[170] Guthrie Jr, G. B., & Huffman, H. M. (1943). Thermal data. XVI. The heat capacity and entropy of isopentane. The absence of a reported anomaly. *Journal of the American Chemical Society*, *65*(6), 1139-1143.

[171] Yaws, C. L. (1995). *Handbook of Thermal Conductivity, Volume 2: Organic Compounds C5 to C7*. Elsevier.

[172] Qureshi, Z. A., Ali, H. M., & Khushnood, S. (2018). Recent advances on thermal conductivity enhancement of phase change materials for energy storage system: a review. *International Journal of Heat and Mass Transfer*, *127*, 838-856.

[173] Mesalhy, O., Lafdi, K., Elgafy, A., & Bowman, K. (2005). Numerical study for enhancing the thermal conductivity of phase change material (PCM) storage using high thermal conductivity porous matrix. *Energy Conversion and Management*, *46*(6), 847-867.

[174] Alshaer, W. G., Nada, S. A., Rady, M. A., Le Bot, C., & Del Barrio, E. P. (2015). Numerical investigations of using carbon foam/PCM/Nano carbon tubes composites in thermal management of electronic equipment. *Energy Conversion and Management*, *89*, 873-884.

[175] Py, X., Olives, R., & Mauran, S. (2001). Paraffin/porous-graphite-matrix composite as a high and constant power thermal storage material. *International Journal of heat and mass transfer*, *44*(14), 2727-2737.

[176] Rao, Z. H., & Zhang, G. Q. (2011). Thermal properties of paraffin wax-based composites containing graphite. *Energy Sources, Part A: Recovery, Utilization, and Environmental Effects*, *33*(7), 587-593.

[177] Lu, W., & Tassou, S. A. (2013). Characterization and experimental investigation of phase change materials

for chilled food refrigerated cabinet applications. *Applied energy*, *112*, 1376-1382.

[178] Craver, C. D., & Coblentz Society. (1982). The Coblentz Society desk book of infrared spectra. Kirkwood, MO (P.O. Box 9952, Kirkwood 63122: The Society.

[179] Park, H. S., & Hong, C. K. (2021). Anion Exchange Membrane Based on Sulfonated Poly (Styrene-Ethylene-Butylene-Styrene) Copolymers. *Polymers*, *13*(10), 1669.

[180] Chen, P., Gao, X., Wang, Y., Xu, T., Fang, Y., & Zhang, Z. (2016). Metal foam embedded in SEBS/paraffin/HDPE form-stable PCMs for thermal energy storage. *Solar Energy Materials and Solar Cells*, *149*, 60-65.

[181] Todros, S., Venturato, C., Natali, A. N., Pace, G., & Di Noto, V. (2014). Effect of steam on structure and mechanical properties of biomedical block copolymers. *Journal of Polymer Science Part B: Polymer Physics*, *52*(20), 1337-1346.

[182] Mengjie, S., Pun, W. M., Swapnil, D., Dongmei, P., & Ning, M. (2017). Thermal stability of organic binary PCMs for energy storage. *Energy Procedia*, *142*, 3287-3294.

[183] Liu, X., Wang, Y., Wang, Z., Cavallo, D., Müller, A. J., Zhu, P., ... & Wang, D. (2020). The origin of memory effects in the crystallization of polyamides: Role of hydrogen bonding. *Polymer*, *188*, 122117.

[184] Xu, J., Ma, Y., Hu, W., Rehahn, M., & Reiter, G. (2009). Cloning polymer single crystals through self-seeding. *Nature materials*, *8*(4), 348-353.

[185] Supaphol, P., & Lin, J. S. (2001). Crystalline memory effect in isothermal crystallization of syndiotactic polypropylenes: effect of fusion temperature on crystallization and melting behavior. *Polymer*, *42*(23), 9617-9626.

[186] Mamun, A., Chen, X., & Alamo, R. G. (2014). Interplay between a strong memory effect of crystallization and liquid–liquid phase separation in melts of broadly distributed ethylene–1-alkene

copolymers. *Macromolecules*, *47*(22), 7958-7970.

[187] Moffat, R. J. (1988). Describing the uncertainties in experimental results. *Experimental thermal and fluid science*, *1*(1), 3-17.

[188] Ripple, D. C., & Garrity, K. M. (2006). Uncertainty budgets for comparison calibrations of thermocouples. *NCSLI Measure*, *1*(1), 28-34.